Determination and Microscopic Study of Incipient Defects in Irradiated Power Reactor Fuel Rods

EPRI

EPRI NP-812
Project 829
Final Report
July 1978

Keywords:
Fuel Rod
Zircaloy
Fission Products
Stress Corrosion Cracking
Hydriding

Prepared by
Battelle-Columbus Laboratories
Columbus, Ohio

ELECTRIC POWER RESEARCH INSTITUTE

Determination and Microscopic Study of Incipient Defects in Irradiated Power Reactor Fuel Rods

NP-812
Research Project 829

Final Report, July 1978

Work Completed, May 1978

Prepared by

V. Pasupathi and J. S. Perrin
BATTELLE'S COLUMBUS LABORATORIES

E. Roberts, E. H. Pilzer, N. R. Metcalf, and G. R. Schmidt
WESTINGHOUSE ELECTRIC CORPORATION
(Report Sections on Point Beach-1 Rods)

H. S. Rosenbaum, U. E. Wolff, and W. L. Bell
GENERAL ELECTRIC COMPANY
(Report Sections on Dresden-3 Rods)

R. F. Mattas, J. E. Sanecki, and L. A. Neimark
(Report Sections on Dresden-3 and Oskarshamn-1 Rods)

Prepared for

Electric Power Research Institute
3412 Hillview Avenue
Palo Alto, California 94304

EPRI Project Manager
J. T. A. Roberts
Nuclear Power Division

EPRI PERSPECTIVE

PROJECT DESCRIPTION

The topic of this report is the examination of the cracks that sometimes occur in power reactor fuel rods in order to find probable causes - as a step toward prevention. Many of the cracks observed have occurred in cores which have experienced power increases within technical specifications but outside the current range of operational recommendations. This type of fuel rod cracking is termed a PCI (pellet-cladding interaction) failure. The potential for such failures increases with increasing rate and size of core power changes. The principal near-term preventative measure has been to make first-time core power increases more slowly. While the total rate of fuel "leakers" has been kept at low levels, the resulting loss of plant output (capacity factor) is significant for some plants. In 1977, fuel "conditioning" to minimize PCI reduced plant capacity by about 1% for PWRs and by about 3% for BWRs, with extremes up to 6% for some BWRs. If oil-fired replacement power is required to cover such capacity reductions, the incremental annual fuel costs can range from $100 million to $400 million. Another incentive for improved tolerance to power changes is to permit more rapid load following - which becomes increasingly important in the 1980s.

PROJECT OBJECTIVES

With these economic incentives, EPRI has mounted a research effort to understand the causative mechanism of PCI failures in power reactor fuel rods and to provide remedies which include changes in design and in materials specifications and optimized reactor operating procedures. Data are being derived from laboratory, power reactor, and test reactor studies, as shown by the Program Tree below.

This report describes current efforts to characterize and, when possible, to classify PCI effects in power reactor fuel rods to help ensure that the parallel studies and tests are simulating the correct range of phenomena. This is a key

part of the power reactor fuel surveillance program, as indicated below.

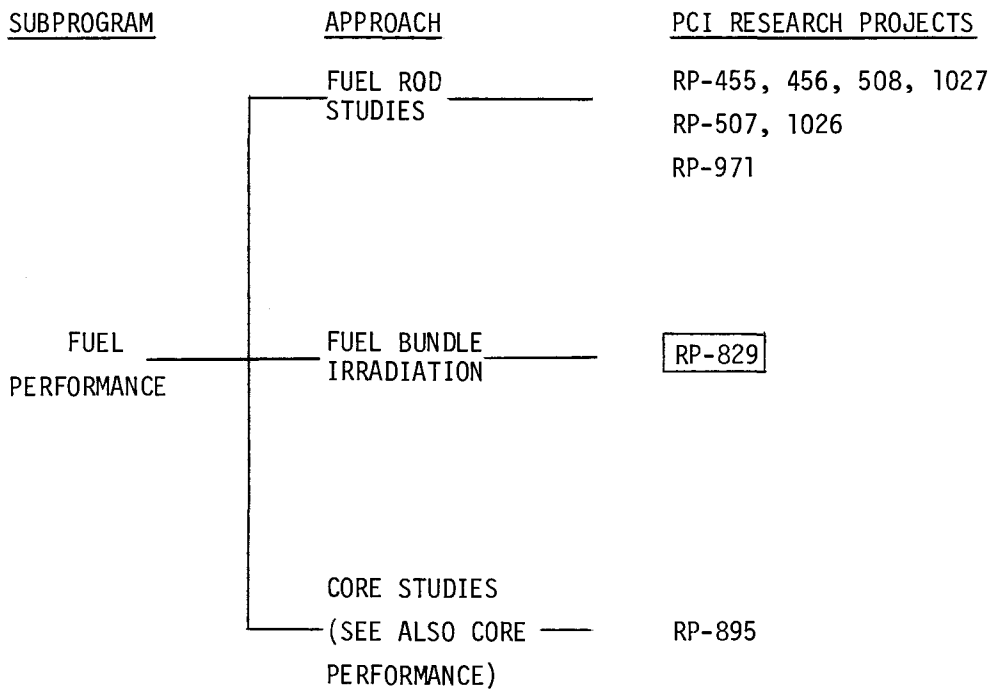

The program to examine PCI failures in power reactor fuel started in 1975 with unpressurized PWR fuel; that work was reported in NP-219 - Evaluation of Fuel Performance in Maine Yankee Core 1. In that fuel the failure mechanism was stress corrosion cracking (SCC) of the Zircaloy cladding by fission products released from the fuel pellets. The second campaign reported here was initiated to fill out the data base on BWR and PWR fuel of more recent design, fabrication, and materials vintage. The primary objective was to verify whether SCC of the Zircaloy cladding is the only, the primary one of several, or simply one of several cracking mechanisms in PCI. A secondary objective of this work was to determine the capabilities of current nondestructive (NDE) techniques to detect incipient (i.e., part-way through-wall) cracks in irradiated fuel rod cladding.

The outcome of this project was significantly impacted by this secondary objective. Current NDE techniques were unable to locate incipient defects in nonleaking, but suspect, fuel rods. The eddy current probes only detected part-way through-wall cracks in fuel rods which also contained through-wall cracks.

Consequently the number of cracks to examine from the available fuel rod population was limited to leaking rods. In only one case was a part-way crack not contaminated through ingress of water into a leaking rod.

CONCLUSIONS AND RECOMMENDATIONS

The limited evidence from this work strongly supports SCC as the primary PCI defect mechanism, with secondary cracks being attributed to hydriding. Additionally, during the course of this work, other examinations of suspect PCI damage in power reactor fuel were made available. We now have an impressive body of evidence supporting SCC as the principal mode of Zircaloy fracture in PCI events, and this reinforces the EPRI program objective of developing design remedies for stress corrosion cracking of Zircaloy. Several remedy concepts are already under irradiation in test reactors, and a power reactor demonstration program is planned to start in 1979. As a result, we expect to have a firm basis for specifying minor modifications to fuel designs as early as 1980, and greater changes in design and materials specifications several years later.

J. T. A. Roberts, Program Manager
Systems and Materials Department
Nuclear Power Division

ABSTRACT

This final report presents the results of nondestructive and destructive examinations carried out on the Point Beach-1 (PWR) and Dresden-3 (BWR) candidate fuel rods selected for the study of pellet-clad interaction (PCI) induced incipient defects. In addition, the report includes results of examination of sections from Oskarshamn-1 (BWR) fuel rods.

The nondestructive examination conducted on the candidate rods included profilometry, gamma scanning for gross gamma activity and Cs-137 activity, and eddy current scans using encircling coil and probe coil systems. The destructive examinations consisted of fission gas collection and analysis and metallography.

Eddy current examination of Point Beach-1 rods showed indications of possible incipient defects in the fuel rods. The profilometry and the gamma scan data also indicated that the source of the eddy current indications may be incipient defects. No failed rods or rods with incipient failure were found in the sample from Point Beach-1. It was inferred that the eddy current techniques presently available are not capable of unambiguously detecting tight PCI cracks in unfailed rods. An evaluation of all the data obtained showed that the candidate fuel assembly contained no more than eight failed rods with 93 percent probability. This estimated number of failed fuel rods is less than that initially supposed. Despite the lack of success in finding incipient defects and failed rods, the mechanism for fuel rod failures in Point Beach-1 is postulated to be PCI-related, with high startup rates and fuel handling being the key elements.

Nine out of the 10 candidate fuel rods from Dresden-3 (BWR) were failed, and all the failed rods had leaked water so that the initial mechanism was obscured. Examination of clad inner surfaces of the specimens from failed and unfailed rods showed fuel deposits of widely varying appearance. The deposits were found to contain uranium, cesium, and tellurium. The amount and the type of deposits indicated lower levels of fission product activity in comparison to those of the

Maine Yankee fuel rods examined in an earlier EPRI program. Transmission electron microscopy of clad specimens showed evidence of microscopic strain. Metallographic examination of fuel pellets from the peak transient power location showed extensive grain boundary separation and axial movement of the fuel indicative of rapid release of fission products.

Examination of Oskarshamn clad specimens at ANL did not show any stress corrosion crack (SCC) type defects. The defects found in the examinations appear to be related to secondary hydriding. The primary defects examined by ASEA-Atom at Studsvik, however, showed the failure mode to be PCI-SCC mechanism. The clad inner surface of the Oskarshamn specimens also showed uranium-rich deposits of varying features.

ACKNOWLEDGMENTS

The authors gratefully acknowledge the help of the following people and organizations in the various phases of this progam.

Battelle's Columbus Laboratories

V. W. Storhok and R. W. Klingensmith for program direction.

A. Parsons, P. Tomlin, P. D. Faust, M. Berchtold for nondestructive examination of fuel rods.

E. H. Sands and W. E. Bruce for metallography.

Argonne National Laboratory

R. Holdsworth and D. Donahue for specimen sectioning.

A. Baudino for photo processing.

Westinghouse Electric Corporation

Westinghouse NFD personnel for program coordination at reactor site.

P. J. Sipush for power history data.

J. Wonn for ultrasonic testing.

J. M. Ludwiczak and J. R. Schettig for program interface with Point Beach.

Wisconsin Electric Power Company personnel for project implementation at reactor site.

General Electric Company

R. Spicka (San Jose) and H. R. Strickler (Morris, Ill.) for fuel assembly shipment.

ASEA-Atom--G. Vesterlund for help in Oskarshamn-1 fuel rod studies.

Commonwealth Edison Company

W. M. Kiefer, L. D. Butterfield and A. S. Pallott for some of the reactor data.

J. G. Toscas and J. G. Wulf of the Dresden Nuclear Power Station for their help with work at the reactor site.

General Electric Company, Nuclear Energy Engineering Division

D. O. Sheppard, J. R. Ingvoldstad and N. H. Skarshaug for their efforts in fuel rod selection.

L. D. Noble, B. P. Sarin, L. C. Paulson and D. K. Kerwin for help in calculating and evaluating power histories.

R. E. Smith and D. L. Orton for hot cell metallography and specimen preparation

R. W. Warner and A. D. Gardea for help with the electron microscopy operations.

CONTENTS

Section		Page
1	INTRODUCTION	1-1
	BACKGROUND	1-1
	PROJECT DESCRIPTION	1-2
	TECHNICAL WORKSCOPE	1-3
	Phase I. Selection, Acquisition, and Shipment of Fuel Rods	1-3
	Phase II. Nondestructive Examination	1-5
	Phase III. Destructive Examination and Basic Studies	1-5
	Destructive Examination	1-5
	Basic Studies at GE and ANL	1-5
	Phase IV. Final Data Development, Evaluation, and Reporting	1-6
2	SUMMARY, RESULTS, AND CONCLUSIONS	2-1
	SUMMARY	2-1
	Point Beach-1 Fuel Rods	2-1
	Dresden-3 Fuel Rods	2-1
	Oskarshamn-1 Fuel Rods	2-2
	RESULTS	2-2
	CONCLUSIONS	2-6
	Point Beach-1 Fuel Rod Studies	2-6
	Dresden-3 Fuel Rod Studies	2-6
	Oskarshamn Fuel Rod Studies	2-7
3	DESCRIPTION OF THE WORK	3-1
	POINT BEACH-1 FUEL ROD EXAMINATIONS	3-1
	Introduction	3-1
	Point Beach Unit 1 General Core and Fuel Description	3-2
	Point Beach Unit 1 Region-4 Operating History	3-2
	Reactor Cycle 2	3-2
	Reactor Cycle 3	3-4

CONTENTS (CONTINUED)

Section		Page
3	On-Site Examination at the End of Cycle 3	3-12
	Visual Inspection	3-12
	Fuel Assembly Leak Test	3-12
	Selection of Fuel for the Postirradiation Examination Program	3-15
	Hot Cell Examinations	3-19
	Initial Nondestructive Screening of Fuel Rods	3-19
	Further Nondestructive Examination of Candidate Rods	3-22
	Selection of Samples for Destructive Examinations	3-36
	Destructive Examination	3-43
	Ultrasonic Testing of Point Beach Assembly D-14	3-51
	Additional Fuel Rod Puncture	3-54
	DRESDEN-3 FUEL ROD STUDIES	3-63
	Introduction	3-63
	Rod Selection	3-64
	Examinations of Candidate Fuel Rods	3-65
	Selection of Specimens for Microscopic Study	3-70
	Eddy Current Inspection	3-82
	Metallurgical, Fractographic, and Chemical Studies (GE-VNC)	3-83
	Macroexamination of Clad Surfaces	3-83
	Sampling and Experimental Procedures	3-87
	Results	3-97
	Fractographic and Chemical Studies (ANL)	3-166
	Characterization of Cladding Inner Surface	3-170
	Defect Fractography	3-183
	Pellet-Pellet Interface (Fuel Microstructure)	3-188
	Data Correlations	3-192
	Nondestructive and Destructive Tests	3-192
	Defects and Fuel Power History	3-193
	EXAMINATION OF CLADDING FROM THE OSKARSHAMN-1 POWER RAMP EXPERIMENT	3-193
	Introduction	3-193
	Selection of Specimens	3-199
	Examinations and Results	3-202
	Surface Characterization	3-205
	Fractographic Examination	3-229

CONTENTS (CONTINUED)

Section		Page
4	GENERAL DISCUSSION	4-1
	POINT BEACH-1 FUEL ROD STUDIES	
	Selection of Fuel Rods for Examination	4-1
	Nondestructive Examination Results	4-2
	Destructive Examination	4-4
	Search for a Failed Fuel Rod	4-6
	Analysis of Puncture Data	4-8
	DRESDEN-3 FUEL RODS	4-13
	Rod Selection	4-13
	Eddy Current	4-14
	Fission Gas Release	4-15
	Deposits on the Inner Surface of Cladding and Chemical Interactions	4-15
	Fractography	4-16
	Hydride Particles	4-17
	TEM--Microstructural Evidence of Strain	4-18
	Pellet-Pellet Interface	4-19
	OSKARSHAMN-1 CLADDING STUDIES	4-19
	Clad Inner Surface Characterization	4-19
	Fractographic Characterization	4-21
5	REFERENCES	5-1
	APPENDIX A POINT BEACH UNIT 1, CYCLE 3 ASSEMBLY AND CORE COMPONENT DETAILS	A-1
	APPENDIX B POINT BEACH UNIT 1, CYCLE 3 CORE LOADING AND OPERATIONAL DATA	B-1
	APPENDIX C POINT BEACH UNIT 1, REGION 4, CHARACTERIZATION DATA	C-1
	APPENDIX D POINT BEACH UNIT 1, CYCLE 3 HOT CELL DATA	D-1
	APPENDIX E IMAGING OF ZIRCONIUM HYDRIDE IN ZIRCALOY WITH BACKSCATTERED ELECTRONS	E-1

Blank Page

FIGURES

Figure		Page
1.2-1	Determination and Microscopic Study of Incipient Defects in Irradiated Power Reactor Fuel Rods	1-4
2.2-1	Relationship Between Power Change ΔP and Burnup for Failure-No Failure Condition	2-4
2.2-2	Relationship Between Peak Power (P_{max}) and Burnup for Failure-No Failure Condition	2-5
3.1-1	On Line Gamma Monitor Tube Response to Reactor Power During Point Beach Unit-1, Cycle 3, Startup	3-5
3.1-2	Local Rod Powers in Region 4 Fuel During Cycle 3 Startup	3-6
3.1-3	Local Rod Powers Due to Part Length Control Rod Maneuvers During Cycle 3 Startup	3-9
3.1-4	Point Beach Unit 1: Cycle 3 Power History	3-10
3.1-5	Point Beach Unit 1: Cycle 3 I^{131} Coolant Activity	3-11
3.1-6	Point Beach Unit 1 End of Cycle 3 Leak Test Results	3-14
3.1-7	Rod Average Power at Beginning of Cycle 3 (kW/m)	3-18
3.1-8	Eddy Current Scan of Rod 045 Showing a Coincidence of a Possible Incipient Defect Signal and a Ridge Signal at ~ 280 cm From Rod Bottom	3-21
3.1-9	Appearance of Gamma Acitivity Profile from Gross Gamma Scan on Point Beach Rod I-13, Assemble D-14, Showing Fuel Stack Gaps and a Fractured Pellet	3-25
3.1-10	Appearance of Typical Gamma Activity Profile From Gross Gamma Scan and Cs-137 Scan on Point Beach-1 Rod 045	3-26
3.1-11	Diametral Measurements of Point Beach-1 Rod 037 at BOL, EOC-2 and EOC-3	3-30
3.1-12	Fuel Rod Diameter Profiles at End of Life (Reactor Cycle 3) Point Beach-1	3-31
3.1-13	Examples of Clad Ridging Observed in the Spiral and Linear Diameter Profile Traces from Rod 045	3-34
3.1-14	Spiral Diameter Trace Depicting an Area of Localized Diameter Increase Within a Generally Oval Region. Point Beach-1 Rod K-6	3-35
3.1-15	Encircling Coil and Probe Eddy Current Responses for Point Beach-1 Rod 045 at 323.5 cm (127.8 in.) from the Bottom of the Rod	3-37

FIGURES (Continued)

Figure		Page
3.1-16	Encircling Coil and Probe Eddy Current Responses for Point Beach-1 Rod A-1 at ~ 237 cm (93.3 in.) from Rod Bottom	3-38
3.1-17	Probe Coil Eddy Current Indication Observed at the Location of Fuel Stack Gap and Rod Diameter Increase in Point Beach-1 Rod 045	3-39
3.1-18	Average Power of Rod 045 of Assembly D-40 During Reactor Cycles 2 and 3	3-41
3.1-19	Average Power of Rod A-1 of Assembly D-14 During Reactor Cycles 2 and 3	3-42
3.1-20	Examples of Fuel-Clad Bonding Observed in Rod 045 at ~ 280 cm (~ 110 in.) from Rod Bottom	3-47
3.1-21	Examples of Apparent Pitting Corrosion Observed in Point Beach-1 Rod 045 at ~ 280 cm (110 in.) from Rod Bottom	3-49
3.1-22	Appearance of the Metallic Particle at the Center of Eddy Current Indication Observed in the Point Beach -1 Rod A-1 at ~ 237 cm (93.3 in.) from Rod Bottom	3-50
3.1-23	Nonfailed Standard Rod Ultrasonic Tested in Water (Completely Immersed)	3-53
3.1-24	Punctured Standard Rod Tested Under the Same Conditions as in Figure 3.1-23	3-53
3.1-25	Ultrasonic Test Results on Point Beach Assembly D-14	3-55
3.1-26	Location of Punctured Rods in Point Beach Assembly D-14	3-57
3.1-27	Probability of Finding at Least One Perforated Rod for an Assumed Number of Perforated Rods in the Assembly as a Function of the Number of Sampled Rods	3-59
3.2.1	Probe Coil Eddy Current Chart Showing a Defect Indication on Dresden-3 Rod KB-5249 at ~ 35 cm	3-68
3.2-2	Appearance of the Through-Wall Crack in the Specimen from Rod KB-5249 Near the Center of the Eddy Current Signal at 35.7 cm (14 in.) from Rod Bottom	3-71
3.2-3a	Axial Burnup Profile of Rod KG-0113 (DD-0710, A7)	3-72
3.2-3b	Axial Distribution of Transient Power and Maximum Previous Power for Rod KG-0113 (DD-0710, A7)	3-73
3.2.3c	Power History at Node 2 for Rod KG-0113 (DD-0710, A7)	3-74
3.2-4a	Axial Burnup Profile of Rod KE-2225 (DD-0706, G6)	3-75
3.2-4b	Axial Distribution of Transient Power and Maximum Previous Power for Rod KE-2225 (DD-0706, G6)	3-76
3.2-4c	Power History at Node 2 for Rod KE-2225 (DD-0706, G6)	3-77
3.2-5a	Axial Burnup Profile of Rod KD-0451 (DD-0021, A1)	3-78

FIGURES (Continued)

Figure		Page
3.2.5b	Axial Distribution of Transient Power and Maximum Previous Power for Rod KD-0451 (DD-0021, A1)	3-79
3.2.5c	Power History at Node 2 of Rod KD-0451 (DD0021, A1)	3-80
3.2-6	Cutting Diagrams	3-81
3.2-7	Comparison of (a) Weak and (b) Strong Eddy Current Indications--ANL	3-84
3.2-8	Macrophotographs of Cladding Sections from Rod KD-0451	3-86
3.2-9	Macrophotographs of Outside Surface of Cladding Section 19 from Rod KE-2225	3-88
3.2-10	Macrophotographs of One-Half of Inside Surface of Cladding Section 3 from Rod KE-2225	3-89
3.2-11	Macrophotographs of Inside Surface of Cladding Sections from Rod KE-2225	3-90
3.2-12	Unirradiated Zircaloy-2 Tube Section Tested with Expanding Mandrel	3-91
3.2-13	Section 5, 14.5 to 15 Inches from Bottom of Rod KE-2225, after Expanding Mandrel Test	3-92
3.2-14	Section 5, 10 to 11 Inches from Bottom of Rod KD-0451, Flattened	3-94
3.2-15	Section 5, 11-1/2 to 12-1/2 Inches from Bottom of Rod KE-2225, Flattened	3-95
3.2-16	Rod KE-2225, Crack A; Overview of all SEM Micrographs	3-99
3.2-17	Rod KE-2225, Whole Fracture Surface of Crack A	3-101
3.2-18	Rod KE-2225, Crack A; Area of Crack Penetration (Stereo Pair)	3-103
3.2-19	Rod KE-2225, Crack A; Lower Part of Figure 3.2-18	3-104
3.2-20	Rod KE-2225, Crack A; Upper Part of Figure 3.2-18 (Stereo Pair)	3-105
3.2-21	Rod KE-2225, Crack A; Area of Part-through Crack Penetration	3-107
3.2-22	Rod KE-2225, Crack A; Parts of Figure 3.2-21	3-109
3.2-23	Rod KE-2225, Crack B; Overview of all SEM Micrographs	3-111
3.2-24	Rod KE-2225, Whole Fracture Surface of Crack B	3-113
3.2-25	Rod KE-2225, Crack B (See Figure 3.2-23 for Location)	3-115
3.2-26	Rod KE-2225, Crack B; Part of Figure 3.2-21 Near Inside Cladding Surface, Stress Corrosion Fracture	3-117
3.2-27	Rod KE-2225, Crack B; Part of Figure 3.2-21 at Crack Tip (Stereo Pairs)	3-118
3.2-28	Rod KE-2225, Crack B, Part of Figure 3.2-27 at Crack Tip (Stereo Pairs)	3-119

FIGURES (Continued)

Figure		Page
3.2-29	Rod KE-2225, Crack B; Part of Figure 3.2-21, Near Outside Surface of Cladding, Quasi-Cleavage and Ductile Dimples	3-120
3.2-30	Rod KE-2225, Crack B; Area Near Crack Tip (See Figure 3.2-23 for Location)	3-121
3-2-31	Rod KE-2225, Crack B; Near End of Incipient Crack (See Figure 3.2-23 for Location)	3-122
3.2-32	Rod KE-2225, Section 5C, Flattened	3-124
3.2-33	Rod KE-2225, Section 5C; Ductile Fracture Surface	3-125
3.2-34	Rod KE-2225, Section 5D, Flattened	3-127
3.2-35	Rod KE-2225, Section 5D, Flattened; Area Near Center of Figure 3.2-34	3-129
3.2-36	Rod KE-2225, Section 5D, Flattened; Area in Center of Figure 3.2-35	3-130
3.2-37	Rod KE-2225, Section 5D, Flattened; Area Including Location of Fuel Pellet-To-Pellet Interface	3-131
3.2-38	Rod KE-2225, Section 5D; Area of Figure 3.2-37b; X-Ray Maps	3-132
3.2-39	Rod KE-2225, Section 5D; Area of Figure 3.2-37c; X-Ray Maps	3-133
3.2-40	Rod KE-2225, Section 5A; Interaction Layer on Inside Cladding Surface	3-134
3.2-41	Rod KD-0451, Section 5A, Flattened	3-135
3.2-42	Rod KD-0451, Section 5A, Flattened; Area Marked in Figure 3.2-41	3-137
3.2-43	Rod KD-0451, Section 5B, Flattened	3-138
3.2-44	Rod KD-0451, Section 5B, Left Half of Area in Figure 3.2-43c; X-Ray Maps	3-139
3.2-45	Rod KD-0451, Section 6, Flattened	3-140
3.2-46	Rod KD-0451, Section 6, Area of Figure 3.2-45b; X-Ray Maps	3-142
3.2-47	Rod KD-0451, Section 15, Flattened	3-143
3.2-48	Rod KD-0451, Section 15, Area of Figure 3.2-47c; X-Ray Maps	3-144
3.2-49	Rod KE-2225, Section 5, Metallographic Cross Section 11.5 to to 12.5 Inches from Bottom of Rod, Unetched	3-145
3.2-50	Rod KE-2225, Section 5, Metallographic Cross Section 14.3 to 14.5 Inch from Bottom of Rod	3-146
3.2-51	Rod KE-2225, Section 5, Metallographic Cross Section Through Crack A, Etched	3-147
3.2-52	Rod KE-2225, Section 5, Metallographic Cross Section Through Crack A, at Outside Cladding Surface, Etched	3-148
3.2-53	Rod KE-2225, Section 5, 11-1/2 to 12-1/2 Inches from Bottom of Rod, Longitudinal Metallographic Section, Etched	3-149

FIGURES (Continued)

Figure		Page
3.2-54	Rod KD-0451, Section 5, Metallographic Cross Section 10 to 11 Inches from Bottom of Rod, Unetched; Fuel Bonded to Cladding with Smooth Interaction Layer	3-151
3.2-55	Rod KD-0451, Section 16, Metallographic Cross Section 117 to 118 Inches from Bottom of Rod, Unetched	3-152
3.2-56	Microstructures of Fuel Rod KD-0451 Showing Mixed Unrecrystallized and Recrystallized Portions	3-153
3.2-57	Corduroy Image Effects in Fuel Rod KD-0451	3-154
3.2-58	$\bar{c} + \bar{a}$ Dislocations in Unrecrystallized Areas of Fuel Rod KD-0451 Observed with Basal Planes Diffracting	3-155
3.2-59	"Black Spot" Radiation Damage in Recrystallized Portion of Fuel Rod KD-0451, Section 7	3-156
3.2-60	Hydrides in High Power and High Burnup Regions of Fuel Rod KD-0451	3-157
3.2-61	Faint Dislocation Channels in Fuel Rod KD-0451, Section 7	3-159
3.2-62a	Continuous Grain-to-Grain Features Exhibiting Anomalous Electron Transparency in Thick Foil Regions of Fuel Rod KD-0451, Section 7	3-160
3.2-62b	Similar to Figure 3.2-62a, Arrows Indicate Continuation	3-161
3.2-63	Optical Images of Transmission Electron Microscopy Specimens from Fuel Rod KD-0451 Showing Stringerlike Features in the Axial Direction of the Cladding	3-162
3.2-64	a. Unrecrystallized, b. Recrystallized Regions of Fuel Rod KE-2225	3-163
3.2-65	Twins and Hydrides in Ramp Region of Fuel Rod KE-2225	3-164
3.2-66	Continuous Grain-to-Grain Features in Fuel Rod KE-2225	3-165
3.2.67	Opitcal Images of Same Features of Fuel Rod KE-2225 as Shown in Figure 3.2-63	3-167
3.2-68	SEM Backscattered Electron Images of Stringerlike Features of Fuel Rod KE-2225	3-168
3.2-69	Cutting Diagram for ANL Dresden-3 Specimens from Rod KE-2225 (DD706-G6)	3-169
3.2-70	Clam Shell Sections of Specimen ANL $4 Showing Location of ECI	3-171
3.2-71	Inner Surface of Specimens (a) ANL #2, (b) ANL #4, and (c) ANL #6	3-172
3.2-72	SEM Composite of Specimen ANL #4 Showing Location of ECI	3-174
3.2-73	Dark Line Corresponding to Fuel Cracks	3-175
3.2-74	Pellet-Pellet Interface	3-176
3.2-75	Fuel Particle Adhering to Inner Surface. Area C, Fig. 3.2-72	3-177

FIGURES (Continued)

Figure		Page
3.2-76	Cracks Located at Sites of Surface Mounting, Area D, Figure 3.2-72	3-179
3.2-77	Defect Structures Observed in Area of ECI	3-180
3.2-78	Close-Ups of (a) Area 1, Figure 3.2-77a and (b) Area 2, Figure 3.2-77a	3-181
3.2-79	Close-Ups of Area of Oxide Surface Cracking (a) Area 1, Figure 3.2-77c, (b) Middle of (a)	3-182
3.2-80	(a) Area G, Figure 3.2-72 after Ultrasonic Cleaning, (b) Area H, Figure 3.2-72 after Ultrasonic Cleaning; (c) Area 1 in (a); (d) Area 2 in (b)	3-184
3.2-81	(a) Area G, Figure 3.2-72 after 3-Point Bending; (b) Area H, Figure 3.2-72 after 3-Point Bending; (c) Area 1 in (a)	3-185
3.2-82	Map of Fracture Surface Exposed by 3-Point Bending Between Areas G and H of Figure 3.2-72	3-186
3.2-83	Map of Area 1 of Fracture Map of Figure 3.2-82 Undistinguished Area (A), Brittle Area (B), and Ductile Area (C)	3-187
3.2-84	Composite Photograph of Specimen PPI-1	3-189
3.2-85	Composite Photograph of Specimen PPI-2	3-190
3.2-86	Microstructure of Fuel from Figures 3.2-84 and 3.2-85	3-191
3.3-1	Control Rod Position and Turbine Condensor Off-Gas Activity During the Ramp Experiment in Oskarshamn -1	3-194
3.3-2	Location of Failed Fuel Assemblies in Oskarshamn-1 Core After the Ramp Experiment	3-196
3.3-3	Axial Power Profile as a Function of Control Rod Position	3-197
3.3-4	Number of Failed Rods Per Axial Node (Based on Eddy Current Examination) in the Group of 45 Rods Which May Have Failed Due to the Ramp Experiment	3-198
3.3-5	Primary PCI Cracks Observed in Oskarshamn-1 Fuel Rods	3-200
3.3.6	Locations of Eddy Current Indications and the Specimens Selected for Examination at ANL	3-203
3.3-7	(a) Inner Surface of Specimen 11K (~ 1.5X) (b) Inner Surface of Specimen 11K taken in SEM	3-206
3.3-8	Fuel Particles on Inner Surface of Specimen 11K	3-207
3.3-9	(a) Wormlike Growths on Specimen 10K; (b) Close-Up of Wormlike Growths; (c) Nodular Surface on Specimen 10K	3-208
3.3-10	(a) Cracks on Inner Surface of Specimen 11K; (b) Cracks on Inner Surface of Specimen 14K; (c) Cracks Produced by Flattening Specimen 14K	3-210
3.3-11	(a) Inner Surface of Specimen 15K (~ 3X); (b) Inner Surface of Specimen 15K taken in SEM	3-211

FIGURES (Continued)

Figure		Page
3.3-12	(a) UO_2 Line Deposits on Specimen 15K (60X); (b) UO_2 Particles on Specimen 16K (700X)	3-213
3.3-13	Inner Surface of Specimen 4K; Defect is Located at Area A	3-214
3.3-14	(a) White Line Deposit from Specimen 4K (Area B, Fig. 3.3-13); (b) Close-Up of (a)	3-126
3.3-15	Through-Wall Crack Associated With Defect, (Area A, Figure 3.3-13) in Specimen 4K	3-217
3.3-16	Fracture Surface of Defect on Inner Surface of Specimen 4K (Area A, Fig. 3.3-13)	3-218
3.3-17	Second Defect on Inner Surface of Specimen 4K	3-218
3.3-18	(a) Crack Associated with Defect Shown in Area A, Figure 3.3-17, and (b) Uranium Map of (a)	3-219
3.3-19	Inner Surface of Specimen 8K (~ 2.5X)	3-220
3.3-20	(a) Light Strip on Inner Surface of Specimen 8K (200X), and (b) Close-Up of (a) (2000X)	3-221
3.3-21	Cracks Located Along PPI of Specimen 8K	3-222
3.3-22	Inner Surface of Specimen 2K (~ 2.5X); Defect is Located at Area A	3-224
3.3-23	SEM Composite of Specimen 2K	3-225
3.3-24	Uranium Containing Deposit on Inner Surface of Specimen 2K (Area A, Fig. 3.3-23)	3-226
3.3-25	Circular Cracks Near Large Uranium Containing Deposit on Inner Surface of Specimen 2K (Area B, Fig. 3.3-23)	3-227
3.3-26	(a) Circular Deposit Containing a High Uraniun Concentration (Area D, Figure 20); (b) Uranium Map of (a)	3-228
3.3-27	Surface Oxide Flaking Near Uranium-Rich Deposit (Area E, Figure 3.3-23)	3-230
3.3-28	Defect Site of Specimen 2K (Area A, Figure 3.3-22 and Area 6, Figure 3.3-23)	3-230
3.3-29	Fracture Surface of Defect from Specimen 2K	3-231
3.3-30	Through-Wall Crack Surface Near Outside of Specimen 2K	3-231
3.3-31	Fracture Along Circumferential Cracks in Specimen 8K	3-232
3.3-32	Fracture Map from Specimen 8K of Area A, Figure 3.3-31	3-233
3.3-33	Fracture Map from Specimen 8K of Area A, Figure 3.3-32	3-234
3.3-34	Fracture Through Pit and Longitudinal Crack of Specimen 4K, Figure 3.3-17	3-236
3.3-35	Fracture Map from Specimen 4K of Area A, Figure 3.3-34	3-237

FIGURES (Continued)

Figure		Page
3.3-36	Fracture Maps from Specimen 4K of (a) Area A, Figure 3.3-35, and (b) Area B, Figure 3.3.-35	3-238
3.3-37	Surface Oxide of Specimen 14K	3-239
3.3-38	Appearance of Fracture Surface Near Clad Inner Surface of Oskarshamn-1 Fuel Rods	3-242
4.1-1	Power Increase During Cycle 3 Startup of Punctured Fuel Rods Point Beach-1, Fuel Assembly D-14	4-11
A-1	Point Beach Unit 1, Core and Fuel Assembly Cross Section	A-3
A-2	Point Beach Unit 1 Fuel Assembly	A-5
A-3	Point Beach Unit 1, Cycle 3, Axial Grid Locations with Respect to Fuel and Control Rod Position	A-7
B-1	Region 4 in Point Beach Unit 1, Cycle 2	B-3
B-2	Point Beach Unit 1 : Relative Axial Power Distribution at the End of Cycle 2	B-4
B-3	Point Beach Unit 1 : Cycle 2 Power History	B-5
B-4	Point Beach Unit 1 : Cycle 2 I^{131} Coolant Activity	B-6
B-5	Point Beach Unit 1 : Cycle 2 I^{131} Coolant Activity Ratio	B-7
B-6	Region 4 in Point Beach Unit 1, Cycle 3	B-8
B-7	Reactor Power and Control Rod Maneuvers During Point Beach Unit 1, Cycle 3 Startup	B-9
B-8	Local Powers During Cycle 3 Startup	B-10
B-9	Local Powers During Cycle 3 Startup	B-11
B-10	Point Beach Unit 1: Cycle 3 I^{131}/I^{133} Coolant Activity Ratio	B-12
C-1	Assembly D-14, Distribution of Clad Lots and Pellet Groups	C-9
C-2	Assembly D-14, Rod Average Power, kW/m, at the End of Cycle 2	C-12
C-3	Assembly D-14, Rod Average Burnup (MWD/MTU) at the End of Cycle 2	C-13
C-4	Assembly D-14, Rod Average Power, kW/m, at the Beginning of Cycle 3	C-14
C-5	Assembly D-14, Rod Average Burnup (MWD/MTU) at the End of Cycle 3	C-15
C-6	Preirradiation Spiral Profilometry Trace, Rod 045	C-20
C-7	Transverse Macrostructure of a Fuel Pellet. Fuel Group 48	C-22
C-8	Typical Microstructure of a Fuel Pellet in the As-Polished Condition. Fuel Group 48	C-23
E-1	Backscattered Electron Yield Versus Atomic Number	E-4
E-2	Schematic of Paired Backscattered Electron Signals from Simple Specimens	E-6
E-3	Schematic of Solid State Pair Detector and Associated Electronics	E-7

TABLES

Table		Page
3.1-1	Pertinent Core Characteristics, Fuel Rod Characteristics, and Design Parameters for Point Beach Unit 1, Cycle 3	3-3
3.1-2	Summary or Rod Average Power, Burnup, and Power Increase of Selected Fuel Assemblies at the Beginning of Cycle 3	3-16
3.1-3	Ten Point Beach Unit 1 Candidate Rods Selected for Further Studies	3-23
3.1-4	Point Beach Unit 1 Axial Gap Data Summary	3-27
3.1-5	Profilometry Data Summary on Point Beach Unit 1 Rods	3-29
3.1-6	Summary of Eddy Current Test Results from Point Beach Unit 1 Rod	3-33
3.1-7	Fission Gas Release and Void Volume Data Obtained on Point Beach Unit 1 Fuel Rods	3-44
3.1-8	Summary of Point Beach Unit 1 Fuel Rod Metallography Data	3-49
3.1-9	Representativeness of Rods Selected for Puncture in Point Beach Unit 1 Fuel Assembly D-14	3-58
3.1-10	Probability of Perforated Rods Remaining in a Given Subgroup of Fuel Rods in Assembly D-14	3-60
3.2-1	Summary of Initial NDE Data and Power Histories	3-66
3.2-2	Fission Gas and Void Volume in Dresden Unit 3 Fuel Rods	3-69
3.2-3	Eddy Current Data Summary from Rod KG-0113	3-85
3.3-1	Data on Fuel Rods in RP829-5	3-201
3.3-2	Operating History of Oskarshamn Specimens Examined at ANL	3-204
3.3-3	Oskarshamn Oxide Characterization	3-240
4.1-1	Summary of Perforation Probability Analysis of Punctured and Eddy Current Tested Rods	4-9
C-1	Point Beach Unit 1, Region 4, Leak Test Results	C-3
C-2	Number of Fuel Rods Per Given Combination of Pellet Group and Cladding Lot Assembly D-14	C-6
C-3	As Fabricated Cladding Properties, Fuel Assembly D-14	C-7
C-4	As Fabricated Fuel Properties, Fuel Assembly D-14	C-8
C-5	Pertinent Fuel Rod Information for the Selected Rods of Assembly D-14	C-10
C-6	Pertinent Fuel Rod Information for the Selected Rods of Assembly D-40	C-11

TABLES (Continued)

Table		Page
C-7	Summary of Preirradiation and Postirradiation Information Available on Removable Rods Shipped to BMI Hot Cell Facilities	C-17
C-8	Zircaloy-4 Tube Inside Diameter of the Removable Rods, Rod Number 045	C-18
C-9	Zircaloy-4 Tube Outside Diameter of the Removable Rods	C-19
C-10	Dimensional Analysis of Fuel Pellets of Removable Rod 045	C-21
C-11	Plenum Length and Rod Length of Removable Rods 045	C-24
C-12	343°C (650°F) Tensile Properties of One Cycle Zircaloy-4 Cladding	C-26
C-13	Fission Gas Release of the Removable Rods	C-27
D-1	Point Beach-1 Rod NDE Data Summary at Locations of Eddy Current Indications	D-3
D-2	Initial Puncture and Fission Gas Release Data	D-2
D-3	Fuel Rod Puncture Results Pressure Readings	D-9

Section 1

INTRODUCTION

This document is the final report on "Determination and Microscopic Study of Incipient Defects in Irradiated Power Reactor Fuel Rods". Four other reports have been issued under this program. The first three were irradiation history data packages on Point Beach-1 fuel rods by Westinghouse (1), Dresden-3 fuel rods by General Electric (2), and Oskarshamn-1 fuel rods by ASEA-Atom (3). The fourth is an interim report on the hot cell examination of the Point Beach and Dresden fuel rods by Battelle's Columbus Laboratories (BCL) (4).

1.1 BACKGROUND

Reported fuel rod failures in commercial power reactors have been traced to three main sources, namely, hydriding of Zircaloy cladding, clad creepdown and collapse, and pellet-clad interaction (PCI). The first two causes of fuel failure have been essentially eliminated or made statistically insignificant by design and process changes in fuel manufactured since 1972.

However, the third cause, failure of cladding by pellet-clad interaction (PCI), still remains a concern to fuel rod integrity. Recognition of this problem is reflected in reactor operational procedures that were introduced by fuel vendors for utility application to reduce the risk of any unacceptable power increase to old or reshuffled fuel rods.

These procedures, while workable, can be expensive in terms of lost plant output. Therefore, a strong incentive exists to provide a more quantitative understanding and control of the PCI phenomena which will enable operating restrictions to be relaxed and eventually removed.

Substantial R&D and analytical efforts are being directed to understanding the fundamental phenomena of PCI. One of the goals of the EPRI Fuel Performance Program (5) is to determine the mechanism of PCI and to provide remedies that include both optimized material design changes and reactor operating procedures.

The majority of these data will come from laboratory and test reactor studies. In order to apply this fundamental data base, therefore, there must be a parallel effort to characterize and, if possible, classify PCI effects in power reactor fuel rods. The EPRI program to examine PCI failures in power reactor fuel was started in 1976 with an unpressurized PWR fuel that had not been subjected to either large or rapid power swings (6). This study of the Maine Yankee fuel showed that deleterious interactions between the fuel pellet and Zircaloy cladding did not have to follow large or rapid power changes; they could also occur in the low stress, highly corrosive (from fission product) conditions caused by fuel clad gap heat transfer degradation (7). The appearance of the cladding cracks examined was typical of stress corrosion cracks (SCC) produced in the laboratory and in test reactor ramp experiments. It therefore appeared as though SCC might be the dominant fracture mode for Zircaloy cladding in the variety of PCI events that could occur during normal and off-normal (as typified by test reactor ramps to $\geq$ 600 w/cm at ~ 100 w/cm/min ramp rates) conditions. However, more data on the PCI characteristics of fuel of current design was clearly required to fill out the data base and to justify a major R&D effort on remedies for Zircaloy SCC. A second campaign was therefore initiated to locate BWR and PWR fuel that had suspect PCI damage and to conduct detailed examination of these fractures. That campaign is the topic of this report.

1.2 PROJECT DESCRIPTION

The purpose of the effort was to identify incipient defects* in fuel rods that had been subjected to a power reactor duty cycle likely to produce strong PCI, and to conduct a detailed macro- and micro-examination of such "uncontaminated" defects with the objective of determining the rate controlling fracture mechanism(s). Another objective of the project was to evaluate or assess the capabilities of current nondestructive techniques to detect incipient defects in irradiated fuel rod cladding.

Because vendor's recommendations were in operation, a compromise had to be reached between older fuel, operated prior to the limitations but characterized by a higher defect probability, and new fuel, operated after the limitations but

---

* Incipient defects are defined as cracks originating on the clad inner surface but which have not penetrated the wall thickness.

essentially defect free. The final choice was made to examine rods from (1) a 14 x 14 PWR fuel assembly from Point Beach-1, which had apparently defected during a reactor startup over ten times faster than that now recommended; (2) a set of early 7 x 7 BWR fuel assemblies from Dresden-3, which had failed as a result of a control rod withdrawal error; and (3) a new 8 x 8 BWR fuel assembly from Oskarshamn-1, Sweden, which had defected as a result of an intentional control rod withdrawal experiment (8).

A contractor group, consisting of the Columbus Laboratories of Battelle Memorial Institute (BCL, RP829-1), Westinghouse (W, RP829-2), General Electric (GE, RP829-3), Argonne National Laboratory--Materials Science Division (ANL-MSD, RP829-4), and ASEA-Atom (RP829-5), was assembled to conduct the various phases of this project. Figure 1.2-1 shows integration into the total project, as originally planned, and the relationship to other similar projects sponsored by EPRI, NRC, and DOE.

1.3 TECHNICAL WORKSCOPE

The technical portion of the project was conducted in four phases.

- Phase I. Selection, Acquisition, and Shipment of Fuel Rods
- Phase II. Nondestructive Examination of Fuel Rods and Selection of Rods and Samples for Destructive Examination
- Phase III. Destructive Examination and Basic Studies
  - (a) Destructive Examination of Selected Rods at Battelle
  - (b) Basic Studies at GE and ANL
- Phase IV. Final Data Development, Evaluation, and Reporting; Waste Disposal.

An overview of these four phases follows.

1.3.1 Phase I. Selection, Acquisition, and Shipment of Fuel Rods

General Electric performed on-site nondestructive examination (NDE) of the Dresden-3 fuel rods and selected 10 rods judged to have a high probability of having PCI defects. These rods were believed to be unfailed based on visual and ultrasonic inspection. The rods selected were in symmetric position to other failed rods whose failures were in the region of transient power increase. These rods were shipped to the BCL Hot Laboratory facility.

RP829 Project Structure

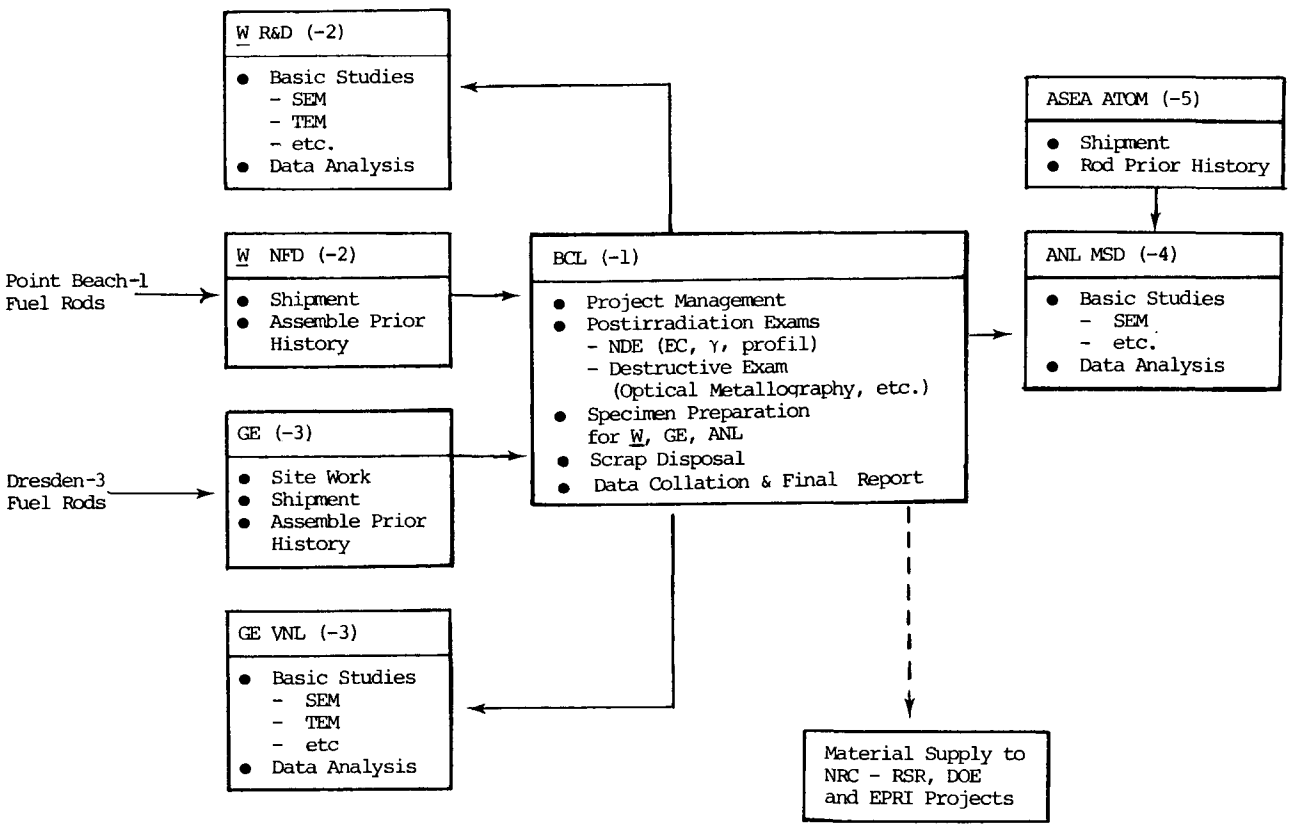

Figure 1.2-1. Determination and Microscopic Study of Incipient Defects in Irradiated Power Reactor Fuel Rods

Westinghouse identified fuel rods at Point Beach-1 believed to have a high probability of PCI defects. In cooperation with the reactor personnel, Westinghouse arranged for the shipment of a complete 14 x 14 fuel assembly and 13 additional rods from the reactor site to the BCL Hot Laboratory facility. After initial screening at BCL, 10 candidate rods were selected for detailed examination.

ASEA-Atom performed detailed NDE work on rods removed from Oskarshamn-1 reactor. Selected samples were shipped directly to ANL for basic studies.

1.3.2 Phase II. Nondestructive Examination

The objective of the nondestructive examination was to locate incipient defects on the inner surfaces of cladding of the rods selected from Point Beach-1 and Dresden-3. The techniques used included profilometry, gamma scanning, and eddy current tests.

At the conclusion of the BCL NDE effort, working sessions involving BCL and program participants were conducted to review the NDE data, and select rods and samples for further studies.

1.3.3 Phase III. Destructive Examination and Basic Studies

1.3.3.1 Destructive Examination. The primary objective of the destructive examination conducted by BCL was to confirm the existence of incipient cracks and to establish a correlation between the NDE signals and the character of the incipient cracks. This correlation was to be established via metallographic examination. The other important objective of the destructive examination was to characterize the fuel rod to provide background information on fuel rod performance. The destructive examination carried out included fission gas release and rod void volume measurements, sectioning, and metallographic examination.

1.3.3.2 Basic Studies at GE and ANL. Selected fuel rod and cladding sections from Dresden-3 fuel rods were shipped to GE and ANL for further studies. It was originally planned to conduct basic studies on Point Beach rod sections at Westinghouse also. However, the destructive examinations on the Point Beach-1 fuel rods failed to show any cladding defects. Thus, no suitable samples were available for basic studies, and the work scope of the program was changed accordingly.

The objective of the basic studies at ANL were to (1) evaluate a pulsed eddy current system for detecting the incipient defects identified by NDE work at BCL, (2) determine the physical and chemical characteristics of the cladding inner surface by SEM, (3) evaluate volatile fission product distribution at pellet interfaces and (4) perform fractography of incipient crack surfaces by SEM. The samples studied under this part of the program included those from Dresden-3 as well as those from Oskarshamn-1 reactor.

The objectives of the basic studies carried out at GE were to characterize the clad inner surface and incipient crack surface using SEM. The samples were examined for evidence of fuel bonding and fuel fission product/Zircaloy interaction. Transmission electron microscopy of clad specimens was conducted to look for evidence of plastic strain caused by PCI.

1.3.4 Phase IV. Final Data Development, Evaluation, and Reporting

At the conclusion of the experimental work all the data collected in the various phases of the project were evaluated. The following sections of this final report include experimental results, data evaluation, and conclusions and recommendations.

Section 2

SUMMARY, RESULTS, AND CONCLUSIONS

2.1 SUMMARY

A detailed postirradiation examination of selected fuel rods from PWR and BWR reactors was carried out at BCL Hot Laboratories, General Electric-Vallecitos Nuclear Center, and Argonne National Laboratory. The rods and rod sections selected for the study were from the Point Beach-1 PWR, Dresden-3 BWR, and Oskarshamn-1 BWR and were believed to contain pellet clad interaction/stress corrosion cracking (PCI/SCC) related defects. The object of the study was to identify rod locations containing PCI-related incipient defects and conduct a detailed examination of the defects. The highlights of the results of these studies are summarized in the following sections.

2.1.1 Point Beach-1 Fuel Rods

A total of 43 rods from Point Beach-1 were investigated. These were all from assemblies which had been irradiated in a previous cycle, had been subjected to a severe start-up ramp, and were leaking (as shown by coolant sampling).

Exhaustive nondestructive examinations of 10 of these rods showed no failures and no incipient failures. Subsequently in an attempt to locate a failed fuel rod, a total of 46 fuel rods were punctured and the internal pressure was measured. All of them were found to be unfailed. It is concluded that the fuel rods which failed are (1) much fewer in number than had been presumed (probably fewer than eight per assembly) and (2) randomly distributed both in location and with respect to parameters such as burnup, power level, rate of power increase, pellet group, and cladding lot.

2.1.2 Dresden-3 Fuel Rods

Ten fuel rods from five assemblies from Dresden-3 were studied. All showed no indication of failures by ultrasonic examination and visual inspection. Nine exhibited eddy current indications of potential incipient cladding defects. Ultimately it was determined that nine of the rods had failed. No incipient defects were

found in the one unfailed rod. All the defects in the failed rods showed evidence of water entry which obscured in all but one instance the initial mechanism of failure. The fracture surface of this one crack exhibited typical cleavage and fluting features of stress corrosion cracking (SCC). Therefore, the results are consistent with PCI-SCC failure but do not establish that hypothesis. Nondestructive examination results correlated reasonably well with existence and location of through-wall cracks. No incipient defects of primary nature were found.

2.1.3 Oskarshamn-1 Fuel Rods

In 1975 Oskarshamn ran a controlled experiment to investigate the PCI susceptibility of preirradiated fuel to power ramping. Selected rods were examined nondestructively and destructively at Oskarshamn. Segments of six rods representing the extremes of the Oskarshamn experiment were examined at ANL by the scanning electron microscope under this project (RP829). No typical SCC defects were observed by ANL, rather the cracks appeared to be of hydride origin. ASEA at Oskarshamn reported a primary PCI defect that exhibit SCC features; therefore it is tentatively concluded that the defects observed in this work were secondary ones.

2.2 RESULTS

- Incipient defects were not discovered in any of the unfailed fuel rods. It is inferred that presently available techniques are not capable of detecting fine, tight, PCI-related incipient defects in unfailed fuel rods.

  The defects (both primary and secondary) discovered in this program were limited to those in failed fuel rods. It was found that the secondary effects from water ingress do obscure the evidence for fracture mode. The crack initiation process, therefore, could not be clearly established. The possibility of crack initiation at pits or hydride patches followed by propagation by SCC mechanism cannot be excluded (9). Such a mechanism could account for failures in fuel rods that did not see significant power ramps.

- Investigation of Point Beach-1 fuel rods failed to uncover any cladding defects. The available evidence, though circumstantial, show that PCI defects can result from fuel handling during refueling shutdowns followed by high reactor startup rates. Since the amount of fuel handling during shutdowns cannot be eliminated or reduced, it seems that the only way to avoid startup failures is to reduce the rate of power increase during the postrefueling startups. The fact that a large number of PWRs which experienced very slow postrefueling startup rates have shown negligible fuel rod failures tends to support the above hypothesis.

- The only primary defects examined in this program came from failed Dresden-3 rods. The evidence for stress corrosion cracking mechan-

ism is predominant despite secondary effects from water ingress. The cracks observed in the BCL and GE-VNC work showed all the characteristics of SCC cracks, namely, normal-to-clad-wall with branching, located at peak power positions, associated with negligible clad strain, cleavage and fluting on the crack surface, fission product activity near the crack, etc.

- The observed level of fission product activity on the inner surface of the cladding from Dresden and Oskarshamn rods was considerably less than that observed in the Maine Yankee fuel rods. The type of fuel deposits observed on the clad inner surface were believed to be more similar to H. B. Robinson fuel rods than Maine Yankee rods. It must, however, be remembered that these rods were failed rods and ingress water could have caused significant redistribution of fission products. The low level of fission product activity probably implies the cracks in these rods formed at high stresses (9).

- Appearance of fuel microstructures at peak power positions in the Dresden-3 rods suggests that the release of fission products occurred at a very rapid rate. Extensive separation of grain boundaries and significant movement of fuel into the dishes are believed to be the result of fast transients. Similar structures have been observed in power ramp tests and direct electrical heating experiments (10, 11).

- The power history of the rods involved in this program was studied to determine if a correlation between fuel rod failure frequency and power ramp history could be obtained. Unfortunately from the limited amount of data available it is not possible to develop a quantitative correlation. However, the data do show some qualitative trends.

  Figure 2.2-1 shows the relationship between the power change (ΔP) and burnup for the rod axial location which experienced the power ramp. Here ΔP is defined as the difference between the maximum power during the ramp and the previous maximum power for that location. Figure 2.2-2 shows a similar plot of local rod peak power (P_{max}) during ramp versus local burnup. In both figures failed and unfailed rods are indicated to show the frequency of fuel rod failures for the given power history condition.

  The Point Beach-1 rods represent rods of normal PWR operating history, namely low ΔP and low P_{max} conditions. Although no failed fuel rods were identified, the fuel assembly studied was a leaker and the data obtained show that low level random failures can occur under these conditions. The Dresden-3 rods represent off-normal power transient conditions, such as accidental rapid withdrawal of control rods, with high ΔP and P_{max} values. The data show that high frequency of failures occurs under these conditions. The rods from Oskarshamn-1 also represent an off-normal operating history with an intentional power ramp near end-of-life. The levels of ΔP and P_{max} for these rods represent both Point Beach-1 and Dresden-3 conditions. These rods also show high failure frequency.

  Examination of Figures 2.2-1 and 2.2-2 show a clear separation of data between the low and the high failure frequency conditions.

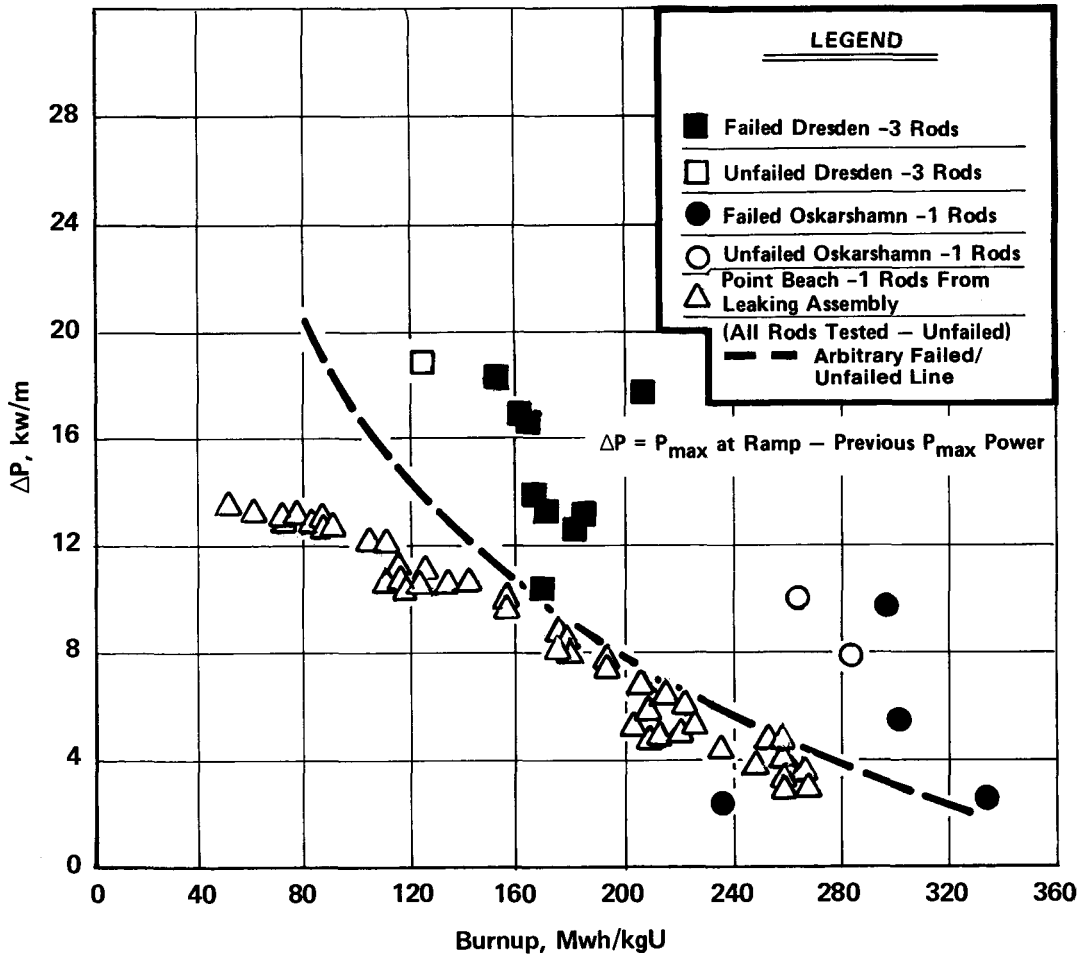

Figure 2.2-1. Relationship Between Power Change ΔP and Burnup for Failure-No Failure Condition

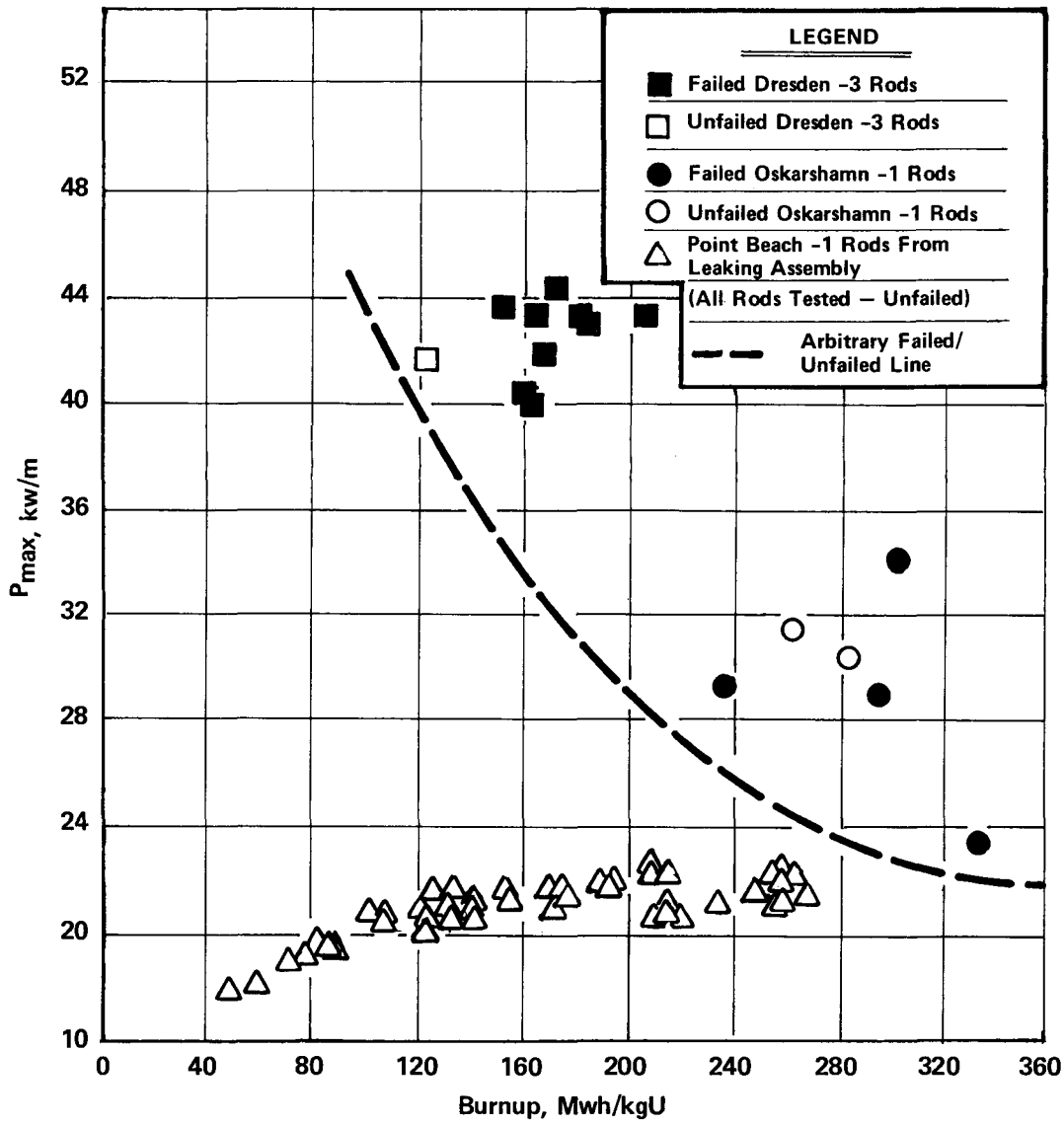

Figure 2.2-2. Relationship Between Peak Power (P_{max}) and Burnup For Failure-No Failure Condition

It is to be noted that the Dresden-3 and Oskarshamn-1 rods selected for the program were expected to contain cladding defects. In this sense the data from these rods are biased towards high failure frequency. Thus, any quantitative correlation derived can be misleading. However, qualitative trends can be identified as shown by the dashed lines in Figures 2.2-1 and 2.2-2 representing fail-no fail conditions.

2.3 CONCLUSIONS

2.3.1 Point Beach-1 Fuel Rod Studies

1. Detailed hot cell examination of removable and standard fuel rods from Region 4 of Point Beach-1 after two cycles of irradiation did not provide any evidence of unusual performance characteristics. Pellet stability, pellet structure, clad creepdown, ovality and ridging, clad hydrogen uptake, and fuel rod fission gas release all appeared normal.

2. Attempts to locate an incipient defect in a nonfailed rod removed from a known leaking assembly proved inconclusive. Currently available nondestructive techniques appear inadequate to provide unambiguous data related to presence of incipient defects in unfailed fuel rods.

3. From puncturing and the measurement of internal pressure in a large sample of representative fuel rods in a known leaking assembly, the location of a failed fuel rod could not be determined. The puncture data suggest that the number of failed fuel rods in the examined fuel assembly is substantially less than initially supposed. Furthermore, the data show that for a few failed rods to remain undetected in the fuel assembly, their distribution must be essentially random and independent of power history and fabrication characteristics. It is concluded that, with 93 percent probability, fuel Assembly D-14 contained no more than eight failed rods.

4. While no definitive data has been obtained from the present program to unambiguously determine the cause of the Point Beach-1, Cycle 3 startup failures, the data are nevertheless generally consistent with the postulated mechanism of pellet-clad interaction. It is argued that as a result of the relocation of fragmented pellets into the pellet-clad diametral gap during fuel handling and the subsequent postfueling rapid rate of reactor startup, pellet-clad interaction failures occurred.

2.3.2 Dresden-3 Fuel Rod Studies

1. The nondestructive and destructive examination of the Dresden-3 fuel rods indicated that 9 out of 10 candidate fuel rods were failed. All the rods had been presumed to be unfailed based on the data from the on-site examination at Dresden. It appeared that the failed rods sealed themselves during subsequent operation.

2. Profile and gamma scan data on the 10 candidate rods showed no major anomalies or unusual features. Eddy current tests showed defect indications in all of the nine failed fuel rods. No indications were observed in the unfailed fuel rod.

3. Metallographic examination of two samples from one of the failed fuel rods at the locations of eddy current indications showed cladding defects in both samples. The stronger of the two indications corresponded to a through-wall crack in the cladding. The crack was filled with corrosion products. The appearance of the crack was similar to PCI induced stress corrosion cracking of the cladding. The through-wall crack is believed to be the primary clad defect in the fuel rod. The other sample exhibited a large hydrided area with cracks, presumably due to secondary hydriding at the location of the eddy current indication.

4. Examination of inner surfaces of the cladding showed deposits of widely varying features such as beads or nodules. The deposits were found to be rich in uranium with small amounts of cesium and tellurium present.

5. SEM examinations of cladding at the location of a strong eddy current indication showed a through-wall crack and a part-wall crack. The crack surfaces were sufficiently oxidized to obscure important features. However, in areas which were clean, features typical of SCC (cleavage and fluting) were observed.

6. Transmission electron microscopy of the cladding specimens showed what are believed to be partially healed dislocation channels. The observation of the dislocation channels showed the PCI event to have produced clad strains on a microscopic scale.

7. Examination of fuel microstructure in the region of peak transient power shows local fuel swelling at a pellet dish. The mechanism involved separation of grain boundaries. This structure suggests that the transformation was associated with a rapid transient release of fission product.

2.3.3 Oskarshamn Fuel Rod Studies

1. No characteristic SCC defects were found in the Oskarshamn specimens examined at ANL. In one case where evidence of pellet-cladding mechanical interaction was found together with a small quantity of cesium, an SCC defect did not result.

2. The defects found in the ANL examination appear to be related to hydrides in the cladding. The extensiveness of hydride-type features suggests that they developed after initial rod failure. The ASEA sponsored examination program at Studsvik did, however, locate what can be regarded as the primary PCI defect, and, as was the case in the Dresden examination, SCC features were observed on the fracture surface. The fracture surfaces showed typical cleavage and fluting features obtained in laboratory iodine SCC tests on cladding from these rods (12).

3. Contrary to what would be expected, there was little correlation between rod operating history and the appearance of the cladding inner surfaces. Macroscopically, cladding from failed rods appeared different from unfailed rods; however, microscopically, there appeared to be no significant difference. Ingress water was the likely cause for local change in the character of uranium-containing deposits believed to be near the site of the rod's through-wall defect. Water ingress is also believed to be related to zirconium oxide separation from the substrate in the highest power rod examined.

4. Defects, of various types, were found during the SEM examinations which could be correlated with the eddy current indications. No defects were found in specimens that had no eddy current indications.

Section 3

DESCRIPTION OF THE WORK

3.1 POINT BEACH-1 FUEL ROD EXAMINATIONS

3.1.1 Introduction

The possiblity of fuel rod perforations occurring at relatively low power levels during reactor startups is a concern to fuel rod integrity. During the spring 1974 postrefueling Cycle 3 startup of the Point Beach Unit 1 reactor, a significant increase in radioactivity in the coolant occurred. This increase of coolant activity appeared to be associated with the startup procedure and the rate of return of the reactor to power.

To improve the understanding of fuel performance limitations and causes of failure during reactor startups, a postirradiation examination of the Point Beach Unit 1 fuel rods was undertaken in this program. The postirradiation examination was limited to Region 4 fuel which was the only previously irradiated fuel region in the Point Beach Unit 1 core at the startup of reactor Cycle 3. The initial scope of the program was to identify incipient defects in nonperforated fuel rods and to conduct macro- and microexaminations of such uncontaminated defects. The objective of the examinations was to determine the conditions that result in perforation of the cladding and to provide additional information to help elucidate the rate controlling failure mechanism.

As the program evolved, the objectives progressively changed as neither a fuel rod containing an incipient defect nor subsequently, a fuel rod containing a through crack could be detected; the examinations utilized a combination of both nondestructive techniques and destructive puncturing/internal pressure checks on a large selected sample of fuel rods.

In this Section the preirradiation information, operating history, interim, and final postirradiation examination results of the Point Beach Unit 1, Region 4, fuel are discussed. Interim reports of this work with the exception of the final postirradiation examination results have been previously published (1).

3.1.2 Point Beach Unit 1 General Core and Fuel Description

Point Beach Unit 1, a pressurized light-water reactor designed by Westinghouse and located at Two Creeks, Wisconsin, is owned and operated by Wisconsin-Electric Power Company.

The core consists of 121 fuel assemblies, each fuel assembly being arranged as a 14 x 14 rod cluster (details are provided in Appendix A). The fuel assembly consists of 179 fuel rods, 16 guide thimbles, and an instrumentation thimble. The fuel rod consists of slightly enriched UO_2 pellets, clad in Zircaloy-4. The guide thimbles are designed to accommodate control rod clusters.

In the Point Beach reactor, there are 33 full-length control rod clusters as well as four part-length control clusters in the core. The various control rod clusters are moved in symmetrically located groups called banks. Banks A, B, C, and D, termed the control groups, are generally moved in a fixed sequential pattern to control the reactor at power (hot zero power to hot full power). The remaining rods, Bank S, are termed the shutdown group. Further details are provided in Appendix A and Reference 1.

3.1.3 Point Beach Unit 1 Region-4 Operating History

3.1.3.1 Reactor Cycle 2. Pertinent core parameters and nominal design information for Region 4 of the Point Beach Unit 1 reactor are given in Table 3.1-1.

Region 4 (containing 40 assemblies) was inserted in the Point Beach Unit 1 core as a fresh fuel region at the beginning of reactor Cycle 2. During Cycle 2, most of the Region 4 assemblies operated at low power levels typical of reload fuel in a PWR. Rod average burnups at the end of reactor Cycle 2 ranged from 2,000 to 13,000 MWD/MTU (fast fluence, greater than 1 MeV, of 3.4×10^{20} to 2.2×10^{21} n/cm^2.*) Details of the average power and average burnup** of each assembly, and the axial power distribution at the end of Cycle 2,** are given in Appendix B; the Cycle 2 power history and the iodine coolant activity are shown in Appendix B.

---

* The fast fluence (greater than 1 MeV) for Region 4 during Cycle 2 can be approximated as fast fluence, $n/cm^2 = 1.69 \times 10^{17} \times$ MWD/MTU.

** As calculated by the W nuclear design computer code.

Table 3.1-1

PERTINENT CORE CHARACTERISTICS, FUEL ROD CHARACTERISTICS, AND DESIGN PARAMETERS FOR POINT BEACH UNIT 1, Cycle 3

Core Characteristics

Rated Power	1518.5 MWt_2
System Pressure	15.51 MN/m^2 (2250 psia)[a]
Average System Temperature	298°C (570°F)

Fuel Rod Characteristics and Design Parameters

Cladding	Zr-4	
Total Rod Length	3.86 m	(152 in.)
Fuel Stack Length	3.66 m	(144 in.)
Plenum Length	0.164 m	(6.45 in.)
Fuel Density	94 percent of theoretical density	
Fuel Enrichment	3.03 percent U^{235}	
Pellet Diameter	0.930 cm	(0.366 in.)
Pellet Length	1.52 cm	(0.600 in.)
Pellet Configuration	Dished	
Cladding OD	1.07 cm	(0.422 in.)
Cladding Thickness	0.0617 cm	(0.0243 in.)
Fuel/Clad Gap	0.019 cm	(7.5 mils)
Rod Internal Pressure, Cold	2.65 MN/m^2	(385 psia)
Gas Fill	He pressurized + 1 atm air	
Rod Average Power	18.7 kW/m	(5.70 kW/ft)

[a]While design pressure is 15.51 MN/m^2 (2250 psia), during reactor Cycle 3, Point Beach Unit 1 operated at a reduced system pressure of 13.78 MN/m^2 (2000 psia). The average system temperature was not changed.

Some coolant activity was evident in Cycle 2. The activity, in part, is attributed to fretting and vibration failure of three rods of a Region-4 assembly that operated next to a leaking baffle joint. However, the failures were not observed until the end of Cycle 3 refueling outages. In Cycle 2 a few visible defects were also observed during the end-of-Cycle 2 on-site examination on the twice-burned Region 2 and Region 3 assemblies. Both of the latter regions were discharged at the end of Cycle 2.

The second cycle core average burnup was 9960 MWD/MTU.

3.1.3.2 Reactor Cycle 3. During Cycle 3 of the Point Beach Unit 1 reactor, Region 4* was the only previously irradiated region in the core. During this cycle, Region 4, in general, operated in higher power positions than in the previous cycle as a result of the fuel management scheme. Fuel assembly locations in the core are provided in Appendix B.

During the initial approach to power on June 8, 1974, following the refueling outage, the gamma monitor (GM) tube readings on the letdown line indicated an increase in the level of coolant activity. This is illustrated in Figure 3.1-1.** A significant activity increase occurred following a rapid power increase from 50 to 70 percent of full power, at rod average powers of 10 to 16 kW/m (3 to 5 kW/ft). Subsequent radiochemical analysis of coolant samples confirmed the high levels of coolant activity and indicated that a significant number of fuel rod perforations appeared to have occurred during startup; correspondingly, these were termed start-up failures.

The first power increase on June 8, 1974, from zero to 32 percent of full power (Figure 3.1-2) was achieved by withdrawing control group D bank approximately 45 steps. Although the rate of power increase was high, the reactor had already

---

* In addition to the 40 Region-4 assemblies, there were four assemblies of Regions 4A and 4B. These were of lower enrichment than Region-4 assemblies. Their relative power in Cycle 2 was 1.15; their burnup at the end of Cycle 2 was 11,390 MWD/MTU. Their relative power in Cycle 3 was 0.94. Only one of those was leak tested at the end of Cycle 3 and was classified as nonperforated. Region 4A and 4B assemblies are not mentioned henceforth for simplicity.

** The later peak in activity was due to the purification system being shut off for 10 hours.

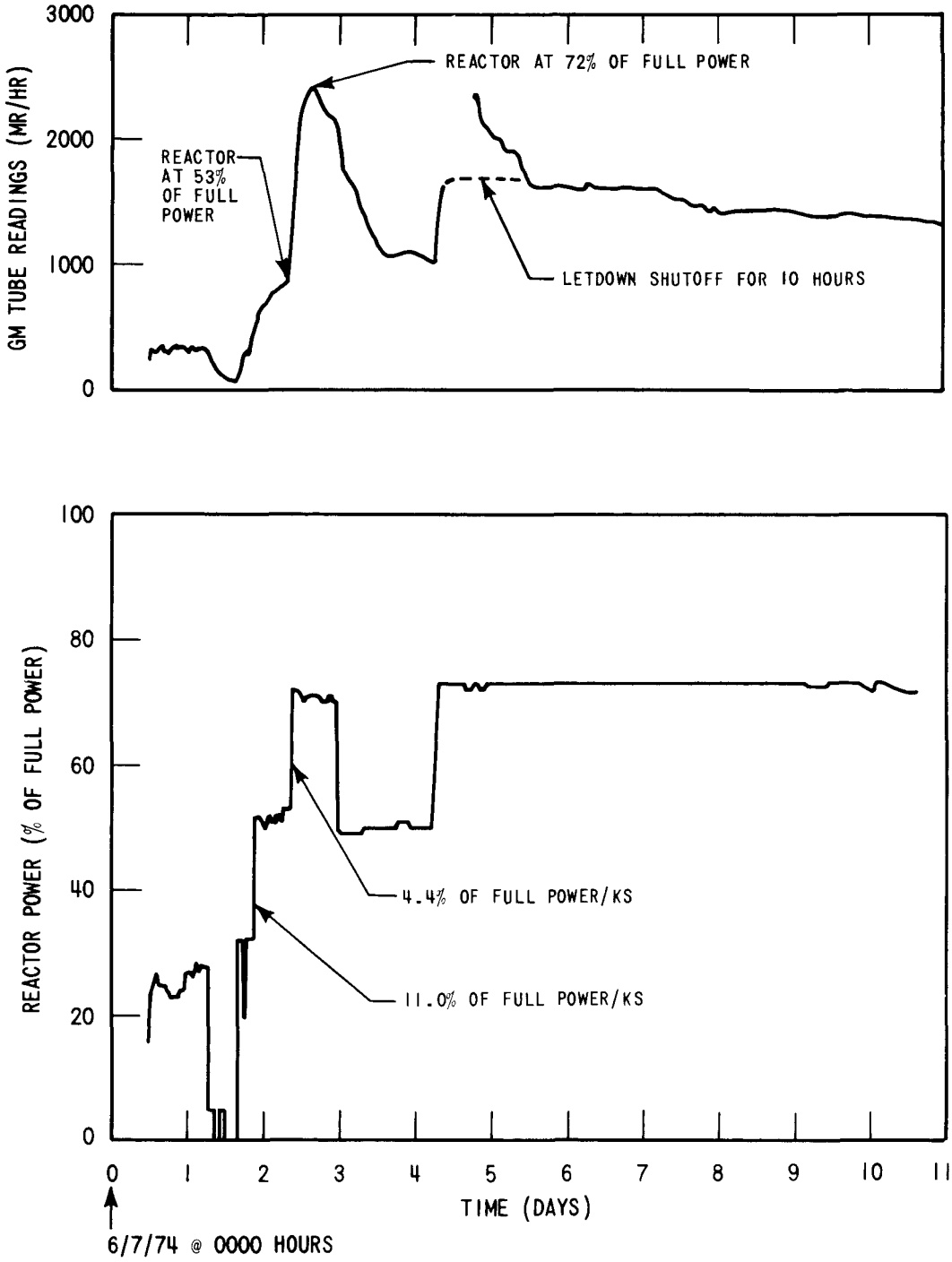

GM Tube Response to Reactor Power During Point Beach Unit 1 Cycle 3 Startup

Figure 3.1-1. On Line Gamma Monitor Tube Response to Reactor Power During Point Beach Unit-1, Cycle 3, Startup

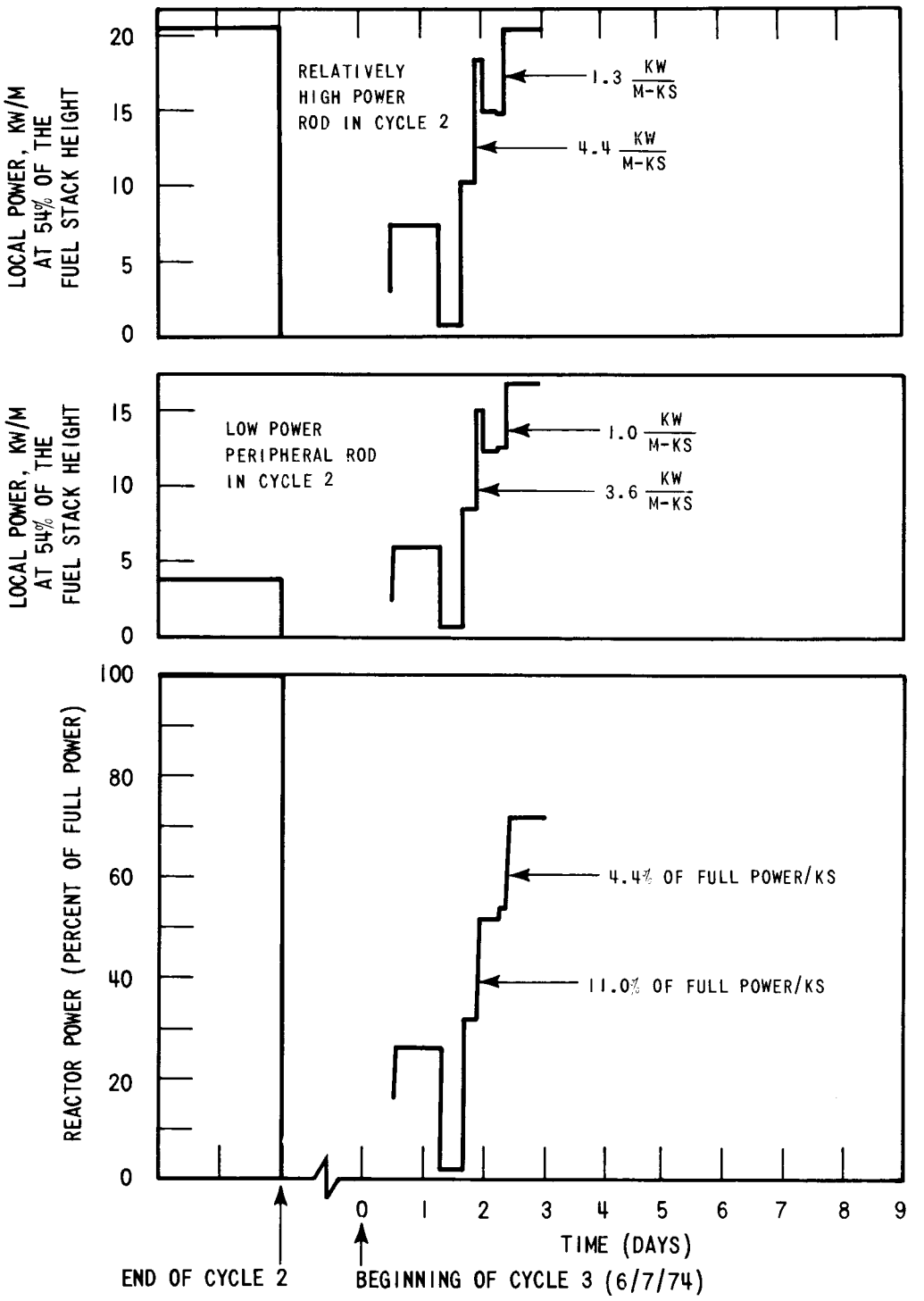

Figure 3.1-2. Local Rod Powers in Region 4 Fuel During Cycle 3 Startup

operated near that power level (23 to 28 percent of full power) for 18 hours on June 7 and early on June 8. The power was increased further, from 32 to 52 percent of full power, on June 8 between 2030 and 2100 hours. This power increase was achieved rather rapidly by withdrawing group D bank 26 steps; the rate of power increase was 11 percent of full power per kilosecond (40 percent of full power per hour). During this period, the activity in the coolant, as evident from the on-line gamma monitor readings, increased slowly. At the steady reactor level of 52 percent of full power, the part-length rod bank was withdrawn from 40 steps to 73 steps on June 8 at about 2400 hours.* The withdrawal probably lasted 82 seconds; this control rod maneuver caused local power shifts, but no substantial change in the rate of coolant activity increase.

On June 9, the reactor power was increased from 53 to 72 percent of full power between 0830 and 0940 hours. The power increase rate was 4.4 percent of full power per kilosecond (16 percent of full power per hour). The power increase was achieved by boron dilution. Thus, this power increase was experienced uniformly across the core. By June 9, 0900 hours, the coolant activity appeared high from the GM tube readings.

The presence of the control rods in the reactor during the startup caused higher axial power peaking factors than would have been obtained with an all-rods-out condition. The power history and control rod maneuvers during the startup period are provided in Appendix B. Local powers and local rates of power increase at several elevations have been evaluated for a sample of Region 4 fuel rods for the time span preceding the first indication of the coolant activity increase (June 9, 0900 hours).

As an example, the local power history of a low power rod (which operated near the reactor periphery in Cycle 2) and a higher power rod (which operated near the center of the core in Cycle 2) is described in Figure 3.1-2 for the axial elevation at 54 percent of the fuel stack height. This axial station was the peak power location on June 8 at 2100 hours, immediately following the power increase

---

* The exact time of withdrawal was not recorded; it occurred between 2300 and 2400 hours. The rate of withdrawal of the part-length rod bank is 0.635 cm/sec. Thus, if the bank were withdrawn in a single action (with no dwell time at intermediate steps) the withdrawal would have lasted 82 seconds. The reactor engineer confirmed that that was the most probable mode of withdrawal.

to 52 percent of full power. Appendix B gives comparable power histories for the axial station of 28 percent and 64 percent of the fuel stack height. The axial location of 28 percent of fuel stack height was the peak power location on June 8 at 2400 hours immediately following the part-length rod bank withdrawal at constant power; the axial location of 64 percent of fuel stack height was the peak power location on June 9 at 0940 hours, immediately following the power increase to 72 percent of full power.

The local power history of a rod from a part-length rod bank assembly in Cycle 3 at 28 percent of fuel stack height is illustrated in Figure 3.1-3. This location was uncovered by the part-length rod bank during the maneuver at constant power, at 52 percent of full power (June 9, 2400 hours). At this location, the part-length rod bank assemblies sustained the highest rate of local power increase experienced in the core; the local rate of power increase was 106.0 kW/m-Ksec (116.3 kW/ft-hr). Increase in local power was approximately 8.7 kW/m (2.6 kW/ft).

The power history and coolant activity for Cycle 3 are given in Figures 3.1-4 and -5. Iodine ratios during the cycle are provided in Appendix B. The iodine coolant activity achieved steady-state approximately 30 days after the reactor startup. At the time, the I^{131} coolant activity reached 0.8-1.0 μCi/gm, a level six times higher than that at the end of Cycle 2. The I^{131}/I^{133} coolant activity ratio reached 0.4, as compared to 0.15 at the end of Cycle 2.* The activity decreased

---

* Since I^{131} has a half-life of 6.95×10^5 sec (8.05 days), and I^{133} has a half-life of 7.49×10^4 sec (20.8 hours), the iodine activity ratio, I^{131}/I^{133}, can be used as an indicator of the release rate of iodine, and can therefore suggest the types of defects that are involved. An instantaneous release of iodines will result in a steady-state iodine coolant activity ratio of:

$$\frac{I^{131}}{I^{133}} = \frac{\gamma_1}{\gamma_3} \times \frac{\lambda_1}{\lambda_3} \times \frac{(\lambda_3 + \beta)}{(\lambda_1 + \beta)} \simeq 0.1$$

where

γ_1 = yield fraction of I^{131} = 0.29
γ_3 = yield fraction of I^{133} = 0.69
λ_1 = decay constant of I^{131} = 9.96×10^{-7} sec^{-1}
λ_3 = decay constant of I^{133} = 92.5×10^{-7} sec^{-1}
β = cleanup rate constant = 2.0×10^{-5} sec^{-1} .

Activity ratios of ≃ 0.1 therefore indicate that a large portion of the iodines is generated by washed-out fuel and released instantaneously.

When microcracks perforate the cladding of fuel rods, the iodines experience extremely long delay from the time they are generated to the time they are released to the coolant. As a result, most of the I^{133} decays and the relative ratio of I^{131} to I^{133} increases by as much as a factor of 10.

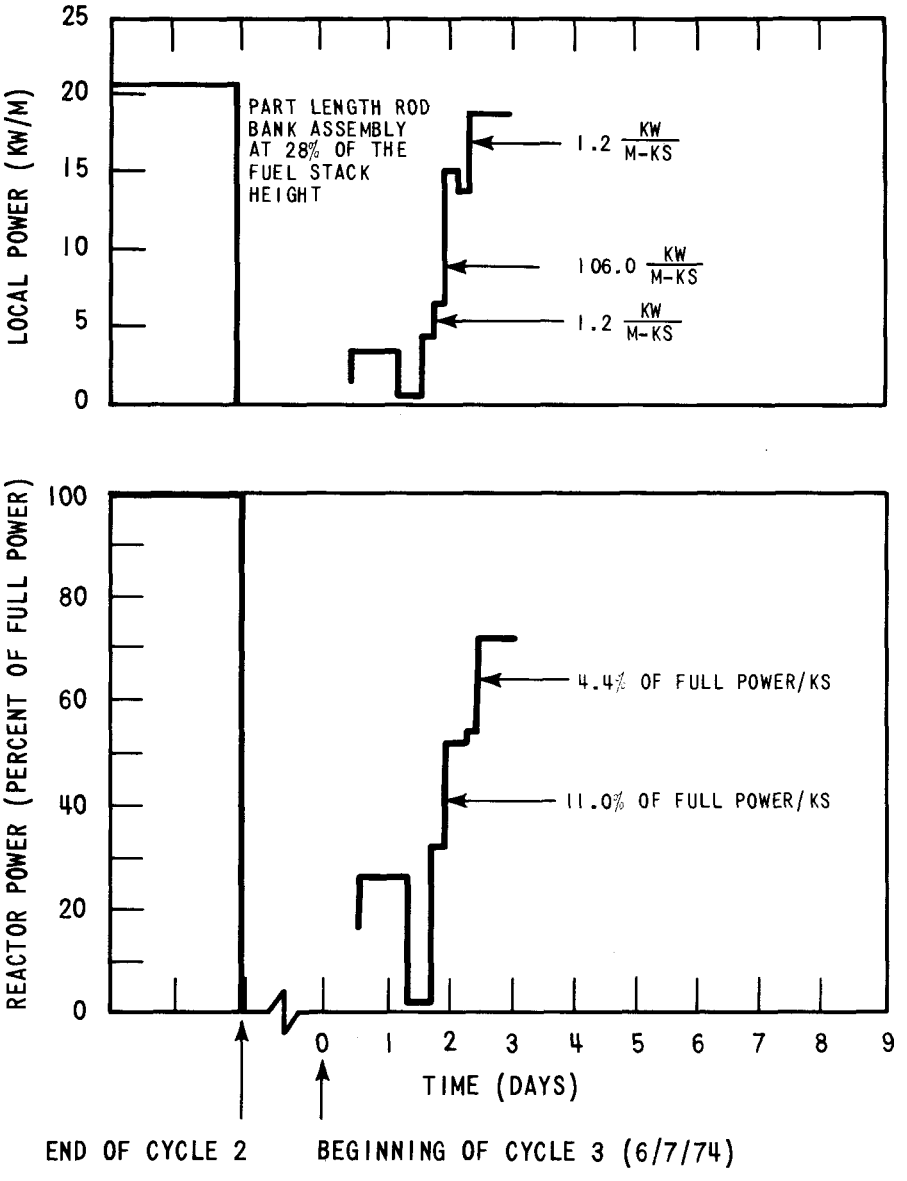

Figure 3.1-3. Local Rod Powers Due to Part Length Control Rod Maneuvers During Cycle 3 Startup

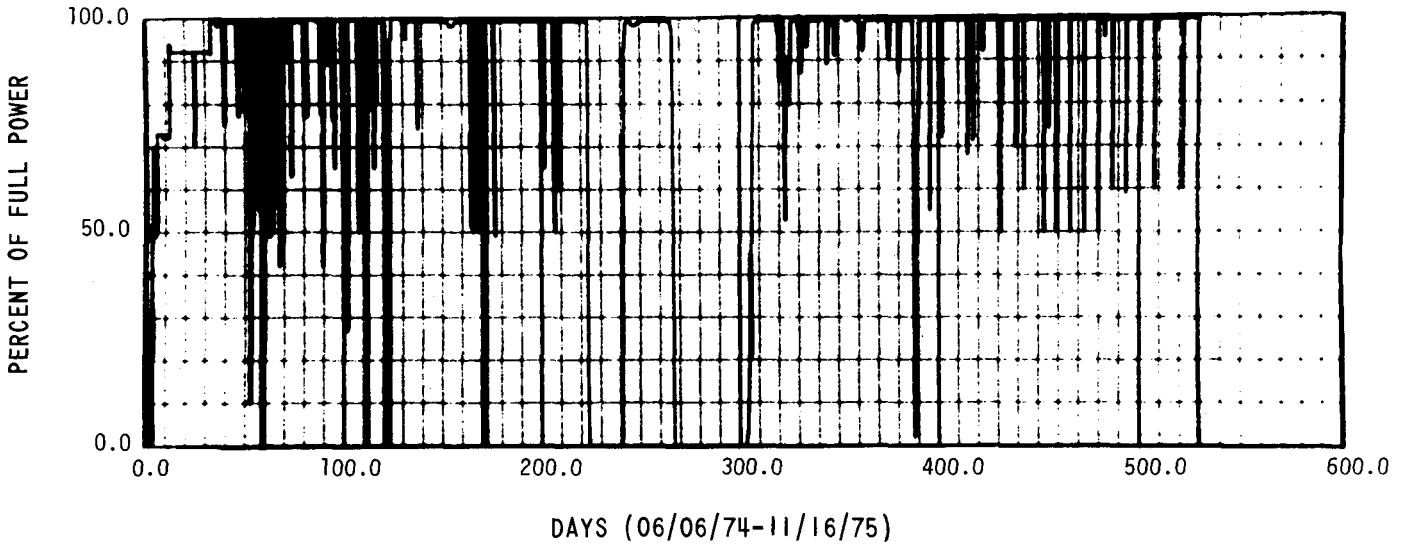

Figure 3.1-4. Point Beach Unit 1: Cycle 3 Power History

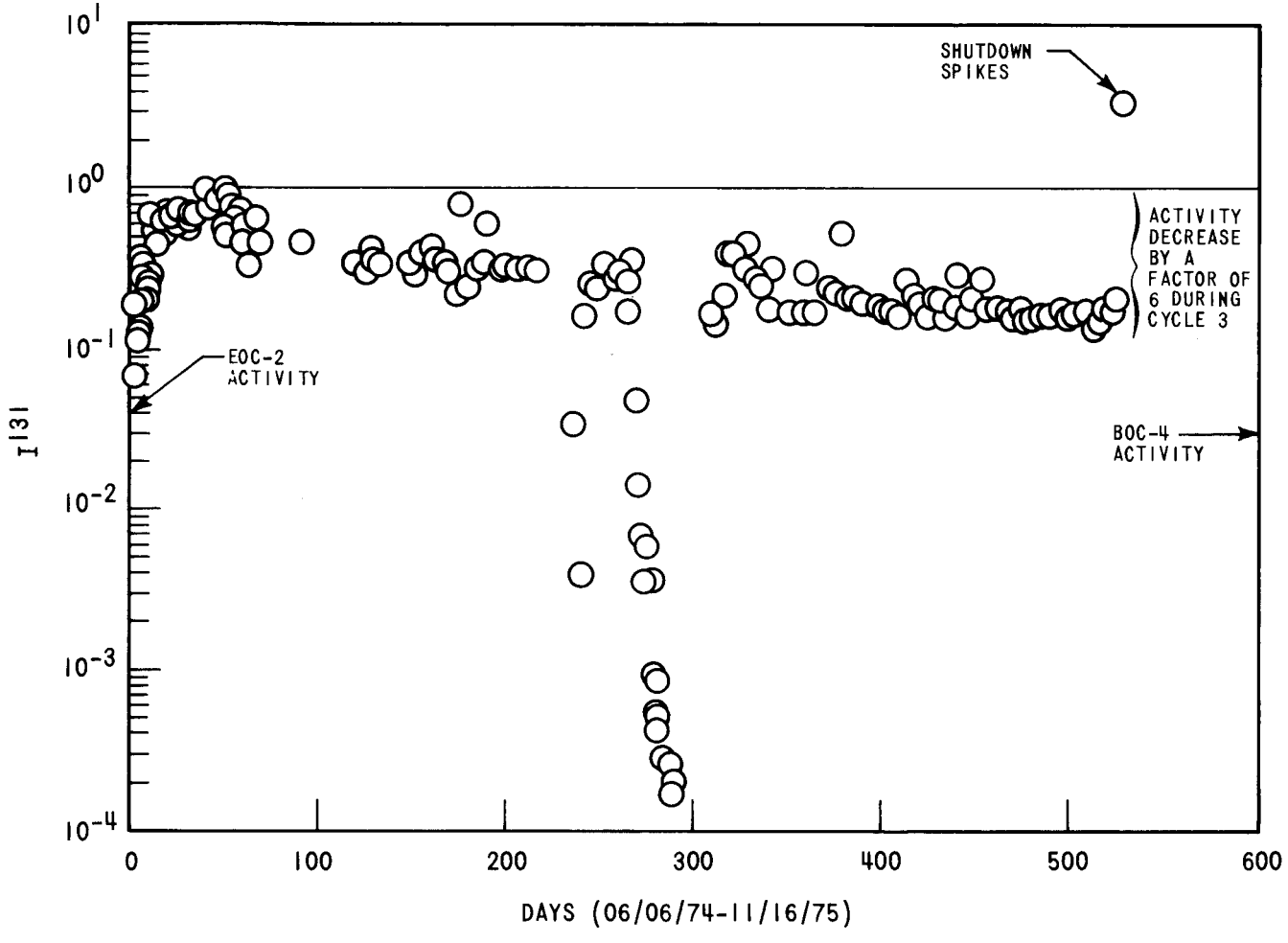

Figure 3.1-5. Point Beach Unit 1: Cycle 3 I^{131} Coolant Activity

with time, however, until at the end of Cycle 3 (following 500 days of operation), the I^{131} coolant activity and the I^{131}/I^{133} coolant activity ratio had almost returned to the levels which prevailed at the end of Cycle 2. The fall in coolant activity, and the associated change of the I^{131}/I^{133} ratio, is suggestive of sealing of small defects which are believed to have formed during the cycle startup. Rehealing of microcracks has been observed on W test fuel (13). Within the described trend of progressively decreasing activity during the cycle, the coolant activity followed the reactor power closely.

The Cycle 3 core average burnup was 14,750 MWD/MTU.

3.1.4 On-Site Examination at the End of Cycle 3

3.1.4.1 Visual Inspection. Following the end-of-Cycle-3 refueling shutdown, 39 discharged Region-4 assemblies were visually inspected on all four faces by W and WEP personnel. Except for one assembly, no defected rods or anomalous conditions were observed. Generally, the lower halves of the fuel rods were uniformly dark and semilustrous with occasional narrow circumferential bands at pellet-length intervals. The upper portions of the rods had a smooth light gray to white appearance on a major portion of their surfaces. The transitions zones, usually beginning between Grids 3 and 4 (from the bottom end), appeared to be mottled areas of mixed light and dark coloration.

One assembly (D-03) was found to have three damaged rods on the 180-degree face at the corner of the 180-degree and the 90-degree faces. Two of the rods were broken and contained large holes directly opposite the grid springs. The cause of damage was identified as high-velocity coolant crossflow leaking through gaps in the corner joint of the core baffle resulting in excessive rod vibration and fretting. Much of the coolant activity remaining in the core at the end of reactor Cycle 3 is believed to be due to this assembly.

3.1.4.2 Fuel Assembly Leak Test. Region 4 was the only previously irradiated region in the core at the beginning of Cycle 3 and was believed to be the region containing the perforated fuel rods. All Region-4 assemblies and two assemblies

from Region 5 and Region 6 were leak tested by Point Beach personnel* at the end of Cycle 3. Detailed leak test data is provided in Appendix C. The two Region 5 and 6 assemblies were believed to be free of perforated fuel rods and were leak tested to provide nonperforated standards.

The I^{131} activity leak test results were corrected for decay to December 8, 1975 (the date leak testing began). Figure 3.1-6 shows a cumulative probability plot of the I^{131} activity readings. Two normal distributions are observed as shown by the two straight lines. It is believed that the higher distribution (corrected I^{131} activity of 4.0×10^{-4} and higher), which includes about half of the assemblies, represents the majority of assemblies containing perforated fuel rods (leaking assemblies).

Significant observations concerning the leak-test results are as follows:

- During the end of Cycle 2 refueling shutdown, four Region 4 assemblies were transferred temporarily from the primary containment to the spent fuel pit. All four of these assemblies were classified as leaking assemblies (D-14, D-40, D-20, D-39).
- Of seven assemblies that experienced no power increase from Cycle 2 to Cycle 3, as well as no additional handling beyond that required for fuel management purposes, none was classified as a leaking assembly. (Assemblies D-25, D-22, D-36, D-11, D-01, D-10, and D-08)
- Conditions due to position in the core (peak power assemblies, assemblies in Group D Bank or part-length rod banks) appeared to have little effect on the leak test results.

---

* The fuel-assembly leak consisted of:

- Placing an assembly in a container within the spent fuel pit.
- Filling the container with demineralized water while the spent fuel pit water was being expelled.
- Circulating the water within the container for a predetermined duration.
- Sampling the container's water.

The fuel assembly leak test can generally identify the leaking assemblies. However, the leak-test results cannot be interpreted in terms of the number of perforated fuel rods in a leaking assembly.

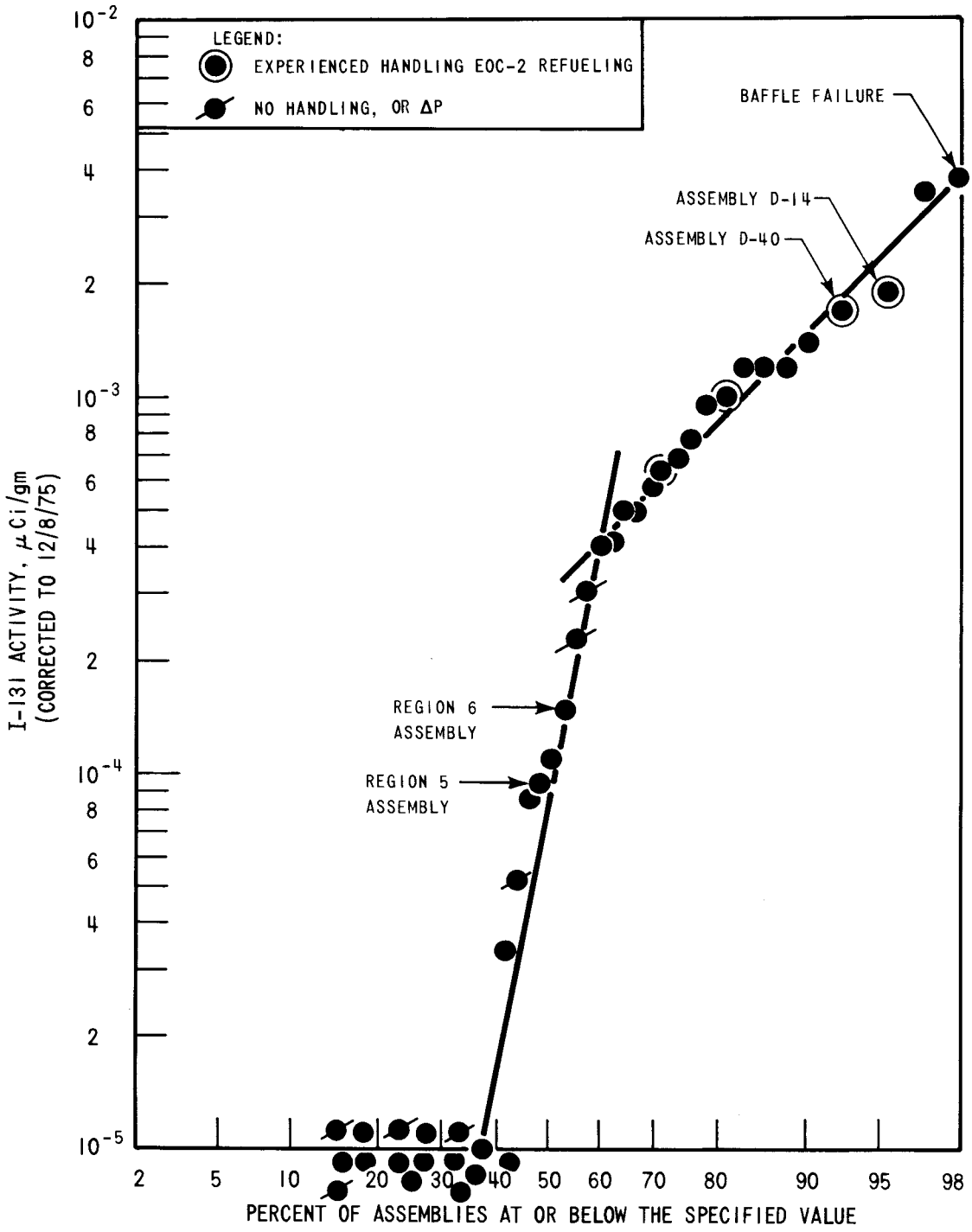

Figure 3.1-6. Point Beach Unit 1 End of Cycle 3 Leak Test Results

3.1.4.3 Selection of Fuel for the Postirradiation Examination Program. To understand the criteria adopted for selecting a fuel assembly for destructive postirradiation examination under this program, it is useful to briefly examine the believed cause of the Point Beach Unit 1 startup failures. As a fuel rod operates in reactor, it is postulated that the fuel, fragmented by thermally induced cyclic stresses, and the cladding, achieve a quasi-steady-state condition wherein the fuel fragments contact the cladding at intermittent points even at low burnups. During a shutdown or a power increase upon the next startup, the situation may change little if the fuel rod does not experience much interim handling and even a fast return to power will probably not result in high stresses being applied to the cladding. However, handling, such as that associated with a transfer from the primary containment to the spent fuel pit, can cause irreversible relocation of fuel fragments in the cold condition. Upon return to power at rapid rates the fuel fragments can, through thermal expansion, produce sufficiently high stress in the cladding to cause local failure even at low power levels.

Similar observations concerning handling and failure probability were made by Atomic Energy of Canada, Ltd. (AECL). From tests in the National Reactor Universal (NRU) reactor (14), AECL concluded that extensive handling of fuel rods during interim hot cell inspections significantly increased the probability of failure during the subsequent postexamination reactor startup.

Consistent with this understanding of the potential cause of the Point Beach Unit 1, Cycle 3, startup failure, the following criteria were applied to the selection of a fuel assembly for destructive examination. It was judged that the selected assembly should:

- Display high activity readings from the end-of-Cycle 3 leak test.
- Belong to the group of assemblies which had been transferred temporarily from the primary containment to the spent fuel pit during the reloading operation prior to Cycle 3.
- Contain rods that had experienced a wide range of local power increase from Cycle 2 to Cycle 3 prior to the indication of the coolant activity increase.
- Contain a wide range of rod burnups at the beginning of Cycle 3.
- Contain several cladding lots and fuel pellet groups (for the purpose of comparison among them).

Table 3.1-2

SUMMARY OR ROD AVERAGE POWER, BURNUP, AND POWER INCREASE OF SELECTED FUEL ASSEMBLIES AT THE BEGINNING OF CYCLE 3

	Rod Average Burnup at BOC3,[a] MWD/MTU	Rod Average Power at EOC2,[b] kW/m (kW/ft)	Rod Average Power at BOC3 at % of Full Power, kW/m (kW/ft) 50%		100%		No. of Rods that Experienced Rod Average Power Increase at 50 % Full Power
Assembly D-31							72
Highest Burnup Rod[c]	10,976	19.21 (5.86)	11.67	(3.56)	23.34	(7.12)	
Lowest Burnup Rod	2,033	4.15 (1.27)	11.30	(3.44)	22.59	(6.89)	
Assembly D-14							61
Highest Burnup Rod	10,751	19.11 (5.83)	11.49	(3.50)	22.98	(7.01)	
Lowest Burnup Rod							
Assembly D-40							11
Highest Burnup Rod	13,012	22.41 (6.88)	11.72	(3.58)	23.45	(7.15)	
Lowest Burnup Rod	4,800	9.12 (2.78)	11.76	(3.59)	23.53	(7.17)	

[a] Beginning of Cycle 3

[b] End of Cycle 2

[c] At the beginning of Cycle 3

Table 3.1-2 summarizes power history characteristics of the three most important candidate fuel assemblies selected using the above criteria. Assembly (D-14) was selected for shipment to BCL hot cell for destructive examination.

Details of the as-built characteristics of the fuel rods in D-14, as determined from retrieval of the W traceability file, are provided in Appendix C. Further details of the power history of the fuel rod are also provided.

Thirty rods from the standard fuel assembly D-14 were selected for initial nondestructive screening at the BCL hot cell. These rods were selected to provide a broad range of fuel rod characteristics (cladding lots, fuel groups, etc.). A summary of the power/history characteristics of the fuel rods in Assembly D-14 is provided in Figure 3.1-7. This figure illustrates for fuel Assembly D-14, that "low power" rods in Cycle 2 experienced large power increases at the beginning of reactor Cycle 3. Since significant coolant activity increases became apparent in Cycle 3 at reactor power levels in excess of 50 percent of full power, all rods having a value greater than two for the ratio of BOC-3 to EOC-2 power experienced a power increase at the time failures became evident; 20 of the 30 standard rods selected from fuel Assembly D-14 were of this category. Pertinent details of all rods selected for the initial screening examinations are provided in Appendix C.

Region 4 of the Point Beach-1 reactor also included a test assembly (D-40) which contained several characterized removable rods of the standard Region 4 design.* These rods were designed to be removed from the assembly during the refueling shutdowns, nondestructively examined, then returned to the assembly for further irradiation. As is evident from the leak test data, this fuel assembly was also judged to contain perforated fuel rods. Hence, because of the detailed characterization previously undertaken by W on these rods, selected removable rods were also identified for shipment to the hot cell.

In reactor Cycle 2, Assembly D-40 operated at an average power of 19.0 kW/m (5.8 kW/ft). The assembly average burnup at the end of this cycle was 9,510 MWD/MTU. In Cycle 3, the assembly operated at an average power of 22.0 kW/m (6.7 kW/ft). Consequently, very few rods had operated in excess of their previous power

---

* Details of preirradiation characterization are given in Appendix C.

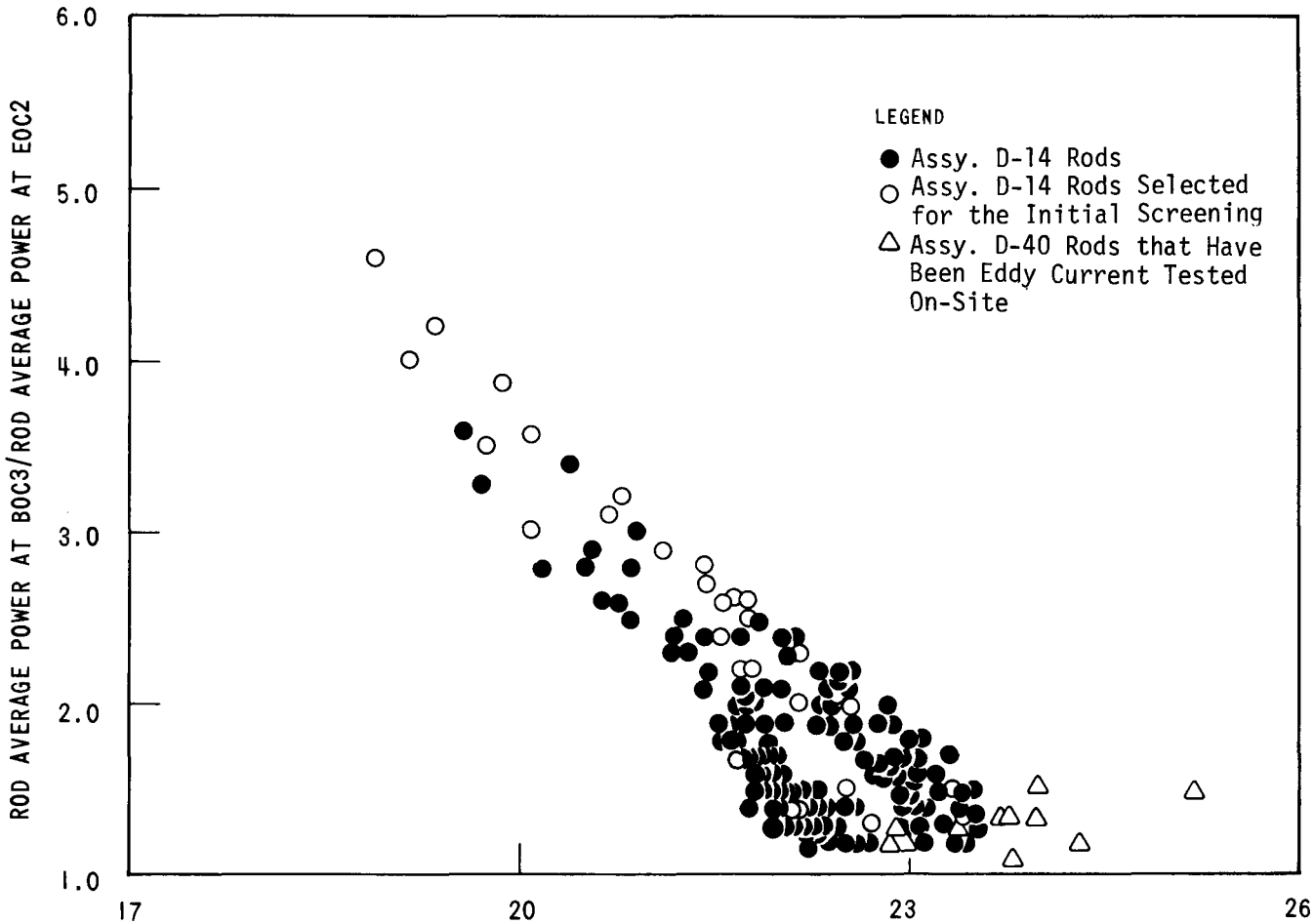

Figure 3.1-7. Rod Average Power at Beginning of Cycle 3 (kW/M)
The Rod Power Increase from the End of Cycle 2 to the Beginning of Cycle 3 Versus Assembly D-14 and the Removable Rods of Assembly D-40

level at the time failure became significant in the core (Table 3.1-2). The end-of-life assembly average burnup was 26,400 MWD/MTU.

Selected rods from Assembly D-40 were given limited nondestructive examination on-site and were destructively examined in detail in the BCL hot cell facilities at the end of Cycle 2. Nondestructive examination was conducted on-site at the end of Cycle 3. End-of-Cycle 2 hot cell examination included puncturing for fission gas release measurements, sectioning, and Zircaloy mechanical testing. Details of the end of (reactor) Cycle 2 hot cell examinations are provided in Appendix C.

End-of-Cycle 3 on-site examination of the Region 4 removable fuel rods included visual examination, dimensional measurements, and encircling coil eddy current testings. None of the tested removable rods was believed to be perforated. However, several rods exhibited low-strength eddy current signals suggestive of possible incipient cracks or roughness of the clad internal surface. Following evaluation of this data, 13 removable rods were selected and shipped to BCL hot cell facilities. Two of these rods operated for only one reactor cycle and were intended to represent 1 Cycle exposure (similar to Region 4, just prior to the occurrence of the startup failures). Characteristics of the selected removable rods are provided in Appendix C.

3.1.5 Hot Cell Examinations

3.1.5.1 Initial Nondestructive Screening of Fuel Rods. The candidate fuel Assembly D-14 was of standard Point Beach-1 14 x 14 fuel assembly design with no provision for withdrawal of fuel rods without removal of the upper nozzle. The removal of the upper nozzle was carried out in the BCL Hot Laboratory pool by drilling out the welds joining the top nozzle to the guide thimble tubes. This provided access to all fuel rods. The procedure has been described previously (4).

The 30 fuel rods, selected for preliminary nondestructive evaluation, as described in Section 3.1.4.3, were removed from the fuel assembly and transferred into the hot cell. These rods, together with the 13 removable rods from fuel Assembly D-40, were screened utilizing an encircling coil eddy current system set at an excitation frequency of 500 kHz. The system was qualified through use of a standard

Zircaloy tube containing machined simulated defects. An internal machined defect of depth equal to 15 to 20 percent of the wall thickness could be detected by this equipment; further details have been published in Reference 4. The preliminary screening was intended to identify 10 rods which warranted further detailed nondestructive examination.

The encircling eddy current charts were examined both for the occurrence of defects and for the extent of clad ridging along the rod. Clad ridging was examined because it represents a form of pellet-clad interaction.

Highlights of the results from the eddy current examination are as follows:

1. Twenty-eight of the 43 rods that were tested displayed one or more signals which could possibly be due to incipient defects.

2. A total of 85 potential incipient defect signals were found, up to 11 per rod. Most incipient defect signals appeared to be located at pellet interfaces.

3. None of the rods were characterized as perforated, based on comparison with a through-hole indication on the standard tube.

4. Ridging signals, of varying frequency and extent were evident. However, while some rods appeared to be ridged at every pellet interface for a large portion of their length, other rods showed little evidence of ridging. Signals, indicative of local diameter increases, were also found in 11 cases.

5. In general, the occurrence of ridging signals was unrelated to the occurrence of incipient defect signals. However, in several cases, a fairly large ridge signal and incipient defect signal coincided.

6. Several rods exhibited very small signals, similar to incipient defect signals, at pellet length intervals. This phenomenon occurred on several rods and sometimes extended for 50 cm (20 inches) at one stretch. These signals probably represent fuel clad bonding or clad deformation or both at pellet interfaces. The tendency of fuel/clad bonding to produce signals indicative of an incipient defect has been observed during the joint CE/EPRI Fuel Evaluation Performance Program (6).

An example of the encircling coil eddy current signal is given in Figure 3.1-8 for the removable rod 045. This rod was subsequently destructively examined in the program. The figure illustrates the coincidence of an incipient defect signal on the horizontal (H) channel with a ridge signal on the vertical (V) channel at the 278.6 cm (10.97 inches) location from the bottom of the fuel rod.

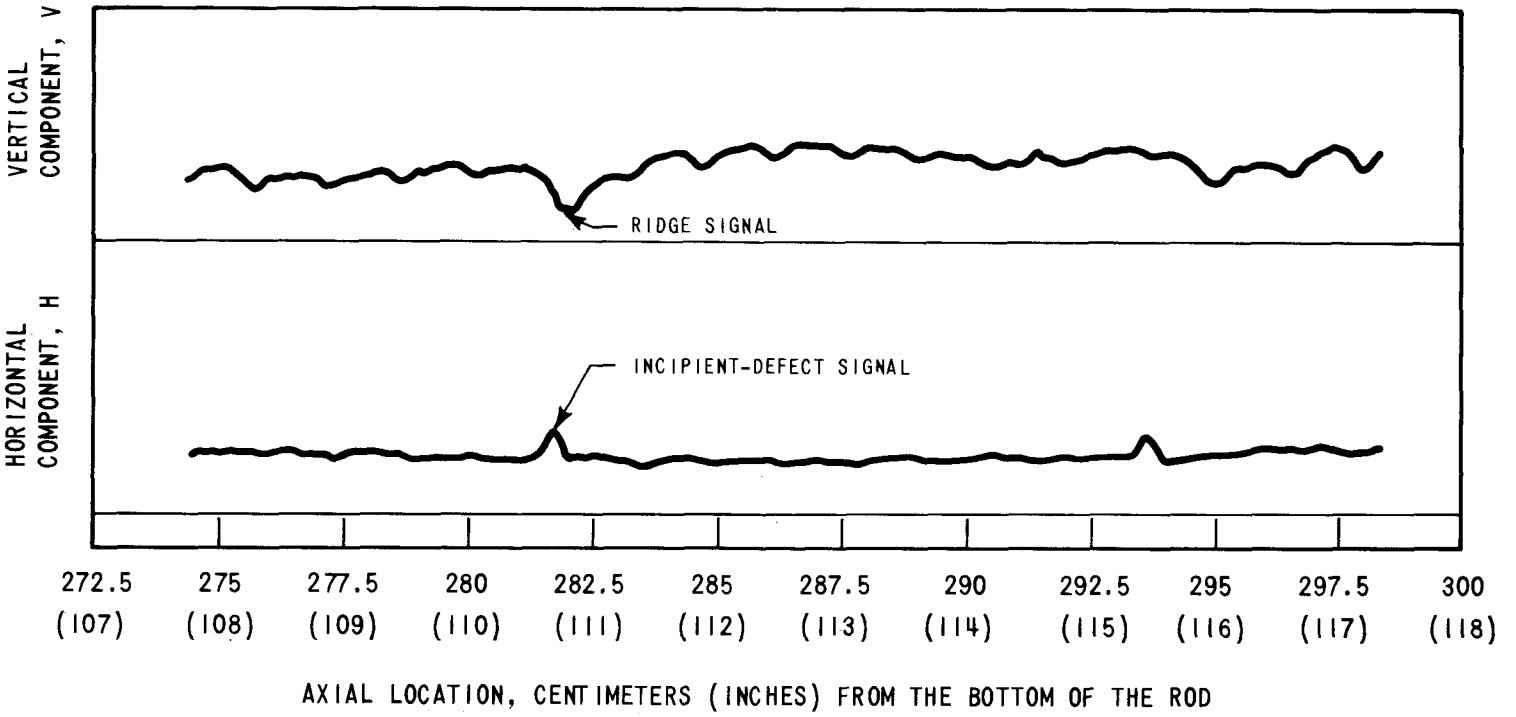

Figure 3.1-8. Eddy Current Scan of Rod 045 Showing a Coincidence of a Possible Incipient Defect Signal and a Ridge Signal at ~ 280 cm From Rod Bottom

In selecting the candidate rods for more detailed examination, it was necessary to confirm that the rods were not perforated. Therefore, two rods displaying strong potential defect signals were selected and punctured. One of the rods, B-11, contained eleven potential incipient defect signals, three of which had some vertical (V) component, which was judged to be representative of very deep incipient defects. The second rod, (removable) rod 045, contained nine incipient defect signals, one of which had some vertical (V) component. Gas collection and analysis showed the correct amount of fill gas and no detectable amounts of hydrogen or water vapor. These results confirmed that the rods were intact and that none of the eddy current signals was representative of a through defect. Results from the puncture analysis are further discussed in Section 3.1.5.4.1.

The selection of 10 candidate rods for further nondestructive screening was based on the number of potential incipient defect signals on each rod, and their relative signal strength. The selection included rods with special features such as a high V/H ratio, potential incipient defect signals at pellet interfaces, and a coincidence of a ridge with a potential incipient defect signal. The 10 candidate rods thus selected are listed in Table 3.1-3. Two removable rods from fuel Assembly D-40, and eight standard rods from fuel Assembly D-14 were selected.

3.1.5.2 Further Nondestructive Examination of Candidate Rods. The 10 candidate rods were subjected to additional nondestructive examinations involving gamma scanning, profilometry and probe eddy current measurements. The gamma scanning included both gross gamma activity and Cs-137 activity profiles. The examination methods have been previously described (4).

3.1.5.2.1 Gamma scanning. System description. The BCL Hot Laboratory gamma scanner measures through a Ge(Li) counting detector the gross gamma and specific isotopic gamma activity along the length of a fuel rod. The signal from the Ge(Li) detector is fed into amplifiers and to an analyzer which records all counts in a specific energy range. For Cs-137 gamma activity scans, the single channel low level discriminator voltage is set and calibrated for the 0.663 MeV level. For gross gamma scanning of the rod, the analyzer uses a low level discriminating circuit to record all counts of energy greater than 0.5 MeV; following setup and calibration of the equipment, the 10 rods were gamma scanned from top to bottom at a rate of 5 cm/min. The collimator slit was set at 0.25 mm (0.010 inch).

Table 3.1-3

TEN POINT BEACH UNIT 1 CANDIDATE
RODS SELECTED FOR FURTHER STUDIES

Rod No.	Assembly Number	Number of Incipient Defect	Range of Signal Strengths Divisions
A-1	D-14	3	4-6.5
K-6	D-14	3	4.5-6.5
E-3	D-14	3	3
A-9	D-14	2	5
K-9	D-14	2	3-9
I-13	D-14	3	4-7
B-11	D-14	11	2-5
F-13	D-14	6	2.5-8
045	D-40	9	2.5-10
039	D-40	4	2.5-5

Scope and Results

The 10 Point Beach candidate rods were scanned over their length for the gross gamma and Cs-137 gamma activity.

From the gamma scan charts, few anomalies such as large axial gaps in the fuel column or highly fragmented pellets were evident. Fuel pellet interfaces were clearly evident from small periodic depressions in the gamma activity due to pellet dishing. Figure 3.1-9 shows an example of the gross gamma activity profile for a standard rod (I-13) in the region of fuel stack gaps and fractured pellets.

Representative gamma scan profiles for both gross gamma and Cs-137 gamma activity are given for removable rod 045 in Figure 3.1-10. Both charts show activity depressions at pellet interfaces. The similarity of the gross gamma and Cs-137 gamma scan data suggests that gross migration of fission product Cs to pellet interfaces, as observed in some of the Maine Yankee Core-1 fuel rods, (6, 7) did not occur in the Point Beach rods.

All the fuel rods studied tended to show small gaps in the fuel stacks, predominantly at pellet interfaces. The widths of gaps were calculated assuming that the area of the gamma activity depression at the gap is proportional to the volume of missing fuel. This technique has been previously used by W and qualified by using a standard prepared from irradiated fuel pellets and containing known gaps. The maximum width of a single gap observed in the 10 rods was 0.62 cm (0.244 inch) and the maximum cumulative length of all the gaps in any one rod was 1.52 cm (0.599 inch). Table 3.1-4 summarizes the gap data for the removable rod 045 and the standard rod A-1 both of which were destructively examined in the program (Section 3.1.5.4). Full details for all 10 rods have been previously published (4).

The stack length changes in the characterized rods 039 and 045 (known preirradiated fuel column lengths) were 0.305 cm (0.21 inch) and -0.71 cm (0.279 inch), respectively. The corresponding density changes (assuming isotropic densification) were 0.24 v/o and -0.57 v/o, respectively. Thus, fuel densification during irradiation was small.

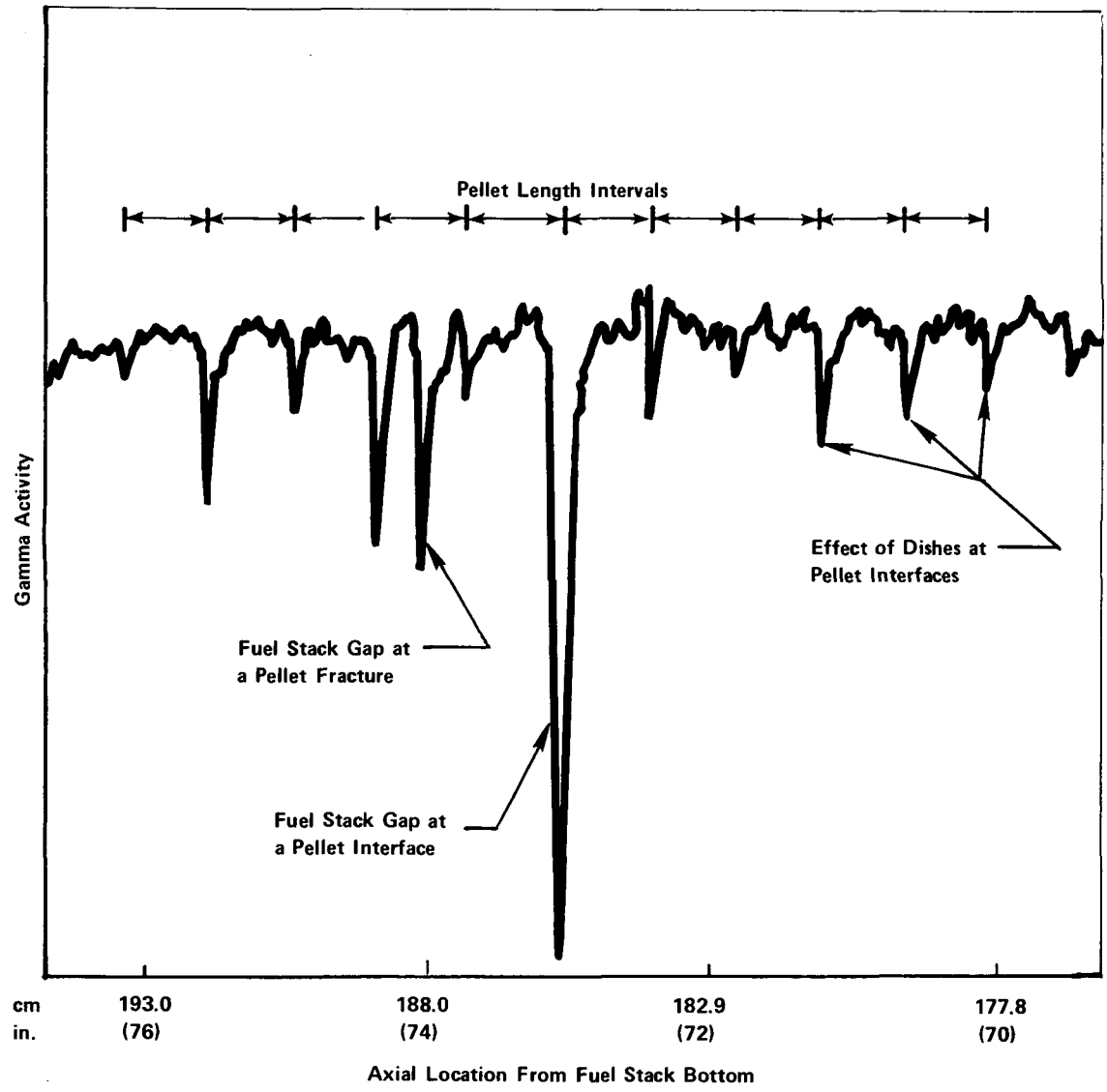

Figure 3.1-9. Appearance of Gamma Activity Profile from Gross Gamma Scan on Point Beach Rod I-13, Assembly D-14, Showing Fuel Stack Gaps and a Fractured Pellet

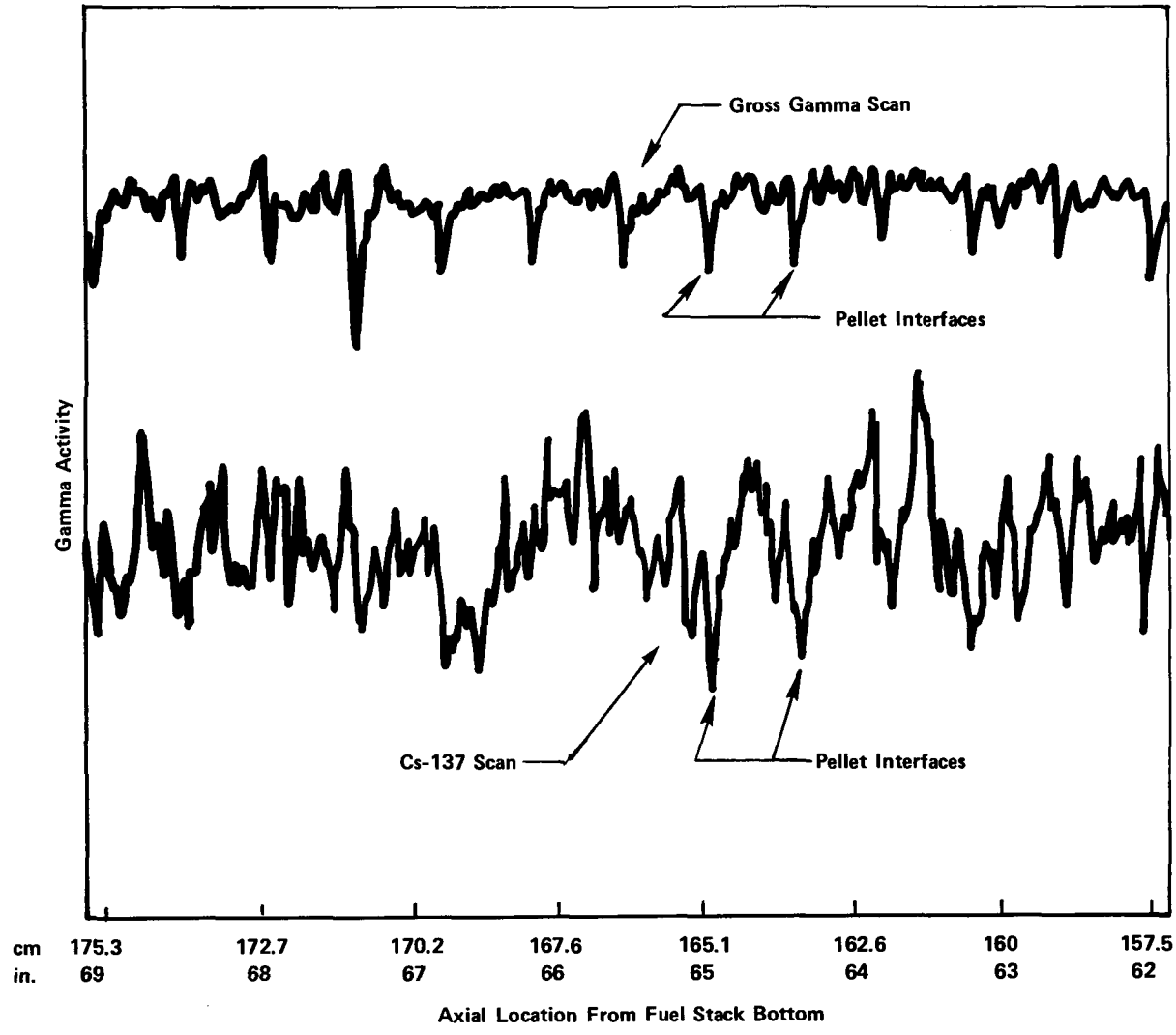

Figure 3.1-10. Appearance of Typical Gamma Activity Profile From Gross Gamma Scan and Cs-137 Scan on Point Beach-1 Rod 045

TABLE 3.1-4 POINT BEACH UNIT 1 AXIAL GAP DATA SUMMARY

(For Rods Destructively Examined)

Rod No.	Rod Average Burnup, MWD/MTU	Axial Location of Gaps* cm	Axial Location of Gaps* in.	Gap Size cm	Gap Size in.	Total Length of Gaps cm	Total Length of Gaps in.	Fuel Stack Length with Gaps+, cm	Fuel Stack Length with Gaps+, in.	Actual Stack Length cm	Actual Stack Length in.
A-1	15563	19.56	7.7	0.033	0.013						
		53.75	21.16	0.064	0.025						
		56.59	22.28	0.043	0.017						
		240.67	94.75	0.043	0.017						
		244.40	96.22	0.061	0.024						
		256.24	100.88	0.028	0.011						
		257.18	101.25	0.043	0.017						
		258.78	101.88	0.053	0.021						
		260.27	102.47	0.074	0.029						
		261.85	103.09	0.018	0.007						
		276.78	108.97	0.025	0.010						
		278.21	109.53	0.025	0.010						
		279.81	110.16	0.013	0.005						
		299.87	118.06	0.048	0.019						
		308.92	121.62	0.036	0.014						
		310.36	122.19	0.086	0.034						
		311.30	122.56	0.198	0.078	0.892	0.351	365.918	144.062	365.026	143.711
045	29365	4.78	1.88	0.041	0.016						
		47.14	18.56	0.069	0.027						
		57.38	22.59	0.036	0.014						
		70.71	27.84	0.023	0.009						
		100.48	39.56	0.025	0.010						
		102.01	40.16	0.018	0.007						
		105.08	41.37	0.036	0.014						
		116.76	45.97	0.018	0.007						
		145.72	57.37	0.028	0.011						
		156.29	61.53	0.020	0.008						
		210.26	82.78	0.061	0.024						
		222.17	87.47	0.013	0.005						
		278.61	109.69	0.056	0.022						
		281.79	110.94	0.020	0.008						
		290.50	114.37	0.048	0.019						
		326.31	128.47	0.051	0.020						
		335.36	132.03	0.259	0.102						
		338.53	133.28	0.033	0.013						
		343.87	135.38	0.036	0.014	0.889	0.350	367.822	144.812	366.933	144.462

+ From gross gamma scan.

*Axial locations are from bottom of rod

3.1.5.2.2 Profilometry. System description and procedure. Fuel rod profilometry was performed to detect and characterize any local fuel rod diameter change and to determine the extent of cladding ovality and creepdown over the full length of the fuel rods. The Battelle profilometer used for this work consists of two linear variable differential transducers (LVDT) placed 180 degrees apart which move axially along the fuel rod. Details of the test equipment and calibration procedure have been previously published (4).

Scope and Results. The 10 candidate rods were profiled over the full length in the standard rotating mode to obtain a spiral trace of the fuel rod diameter. In addition, linear diameter scans (in the nonrotating model) were obtained on two of the fuel rods at four different azimuthal orientations (0-180°, 45-225°, 90-270°,135-315°). Highlights of the examination are as follows:

Cladding Creepdown. All rods exhibited cladding creepdown, a range of 0.045 to 0.081 mm (1.8 to 3.2 mils) being measured. The data are summarized in Table 3.1-5. Comparing the 10 rods for this range of burnup (15,563 to 29,365 MWD/MTU), no clear trend of final creepdown with burnup was apparent. However, clad creepdown of the Region 4 fuel rods appears to have continued through Cycle 3 of the reactor (Cycle 2 for the fuel rods) as is evident from the on-site profilometry data shown in Figure 3.1-11 for removable fuel rod 037 (not examined in this program). Figure 3.1-12 illustrates the axial creepdown profile along the removable rod 045 and the standard rod A-1 (both rods were destructively examined in the program). All axial profiles show the trend of increasing creepdown along the mid sections of the fuel rod where the heat flux and neutron flux are greatest.

Ovality. The diameter scans showed the fuel rods to have variable ovalities (maximum minus minimum diameter) over their length. The minimum ovality measured was approximately 0.012 mm (0.5 mils) while the maximum ovality ranged to 0.24 mm (9.8 mils). Table 3.1-5 shows the extent and location of maximum ovality in the 10 candidate rods. For the two rods 045 and A-1, the range of ovality is also evident from Figures 3.1-11 and -12. These levels of ovality are typical for fuel rods exhibiting light densification.

TABLE 3.1-5 PROFILOMETRY DATA SUMMARY ON POINT BEACH UNIT 1 RODS

Rod No.	Rod Average Burnup/MWD/MT	Min. Average Rod Dia. cm	Min. Average Rod Dia. in.	Location Range* cm	Location Range* in.	Rod Dia. at 371 cm (146 in.) cm	Rod Dia. at 371 cm (146 in.) in.	Maximum Clad Creep** mm	Maximum Clad Creep** mils	Rod Max Ovality/ Axial Location* mm/cm	Rod Max Ovality/ Axial Location* mils/in.
045	29365	1.0630	0.4185	101-280	40-110	1.0703	0.4214	0.074 (.081)***	2.9 (3.2)***	0.211/338	8.3/133
039	26878	1.0655	0.4195	229	90	1.0701	0.4213	0.045 (.061)***	1.8 (2.4)***	0.175/198	6.9/78
K-9	26374	1.0630	0.4185	229	90	1.0693	0.4210	0.064	2.5	0.239/325	9.4/128
B-11	20927	1.0660	0.4197	101.229	40/90	1.0713	0.4218	0.053	2.1	0.249/333	9.8/131
E-3	20580	1.0655	0.4195	178	70	1.0706	0.4215	0.051	2.0	0.137/231	5.4/91
F-13	24550	1.0650	0.4189	178	70	1.0706	0.4215	0.066	2.6	0.117/130	4.6/51
A-1	15563	1.0655	0.4195	152	60	1.0719	0.4220	0.064	2.5	0.198/229	7.8/90
I-13	25067	1.0630	0.4185	178	70	1.0693	0.4210	0.064	2.5	0.221/325	8.7/128
A-9	19288	1.0633	0.4198	203/229	80/90	1.0716	0.4219	0.053	2.1	0.168/224	6.6/88
K-6	25149	1.0642	0.4190	152.229	60/90	1.0703	0.4214	0.061	2.4	0.193/348	7.6/137

*From rod bottom

**In calculating the diameter decrease for standard rods, the measured diameter at 371 cm (146 in.) location in the plenum region was used as the preirradiated rod diameter. The profilometry trace at this location showed the rod to have very low ovality comparable to an unirradiated fuel rod. Thus, it was believed that the diameter at 371 cm would be a good representation of as fabricated rod diameter.

***Based on preirradiation rod diameter for the characterized rod.

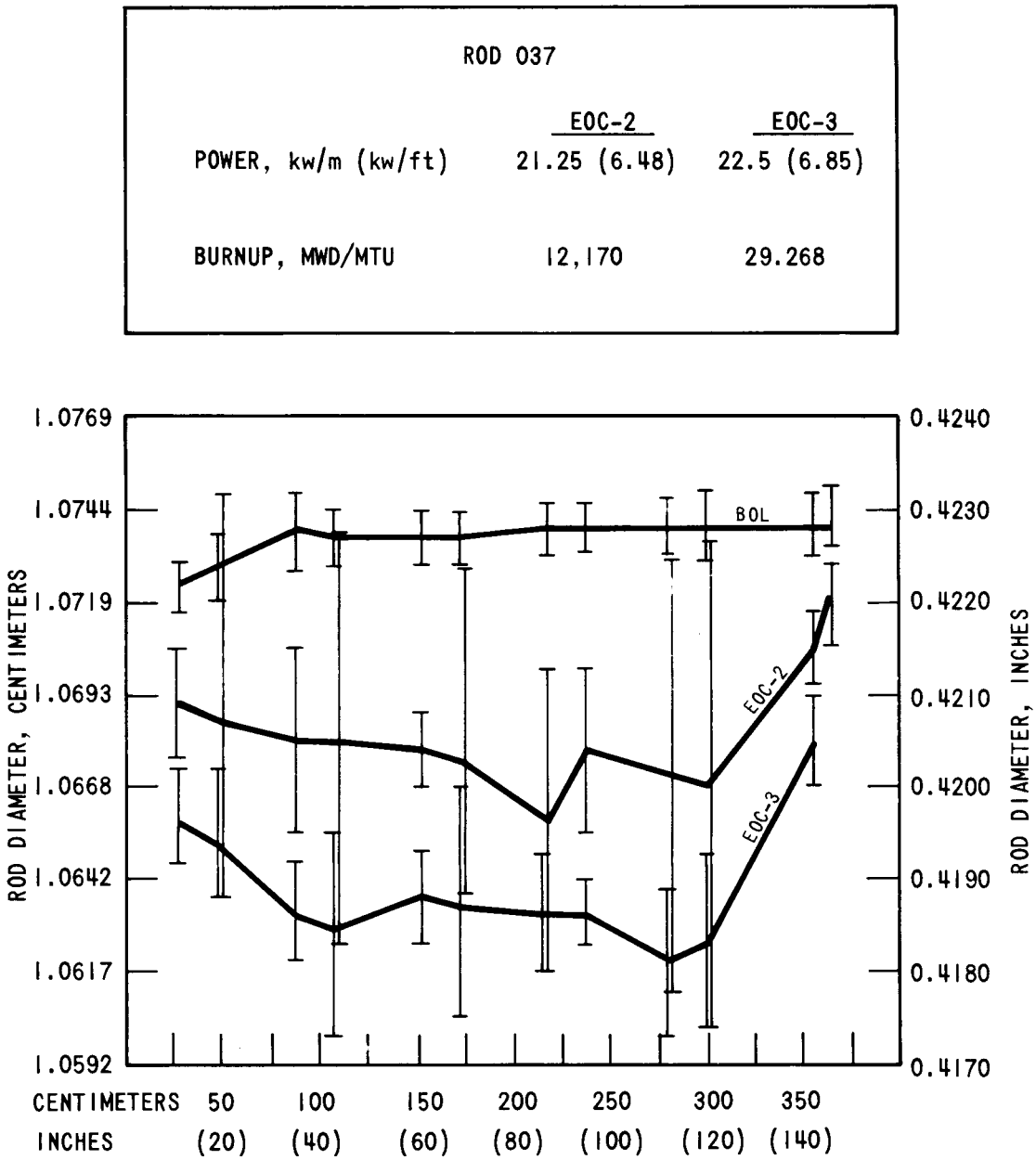

Figure 3.1-11. Diametral Measurements of Point Beach-1 Rod 037 at BOL, EOC-2 and EOC-3

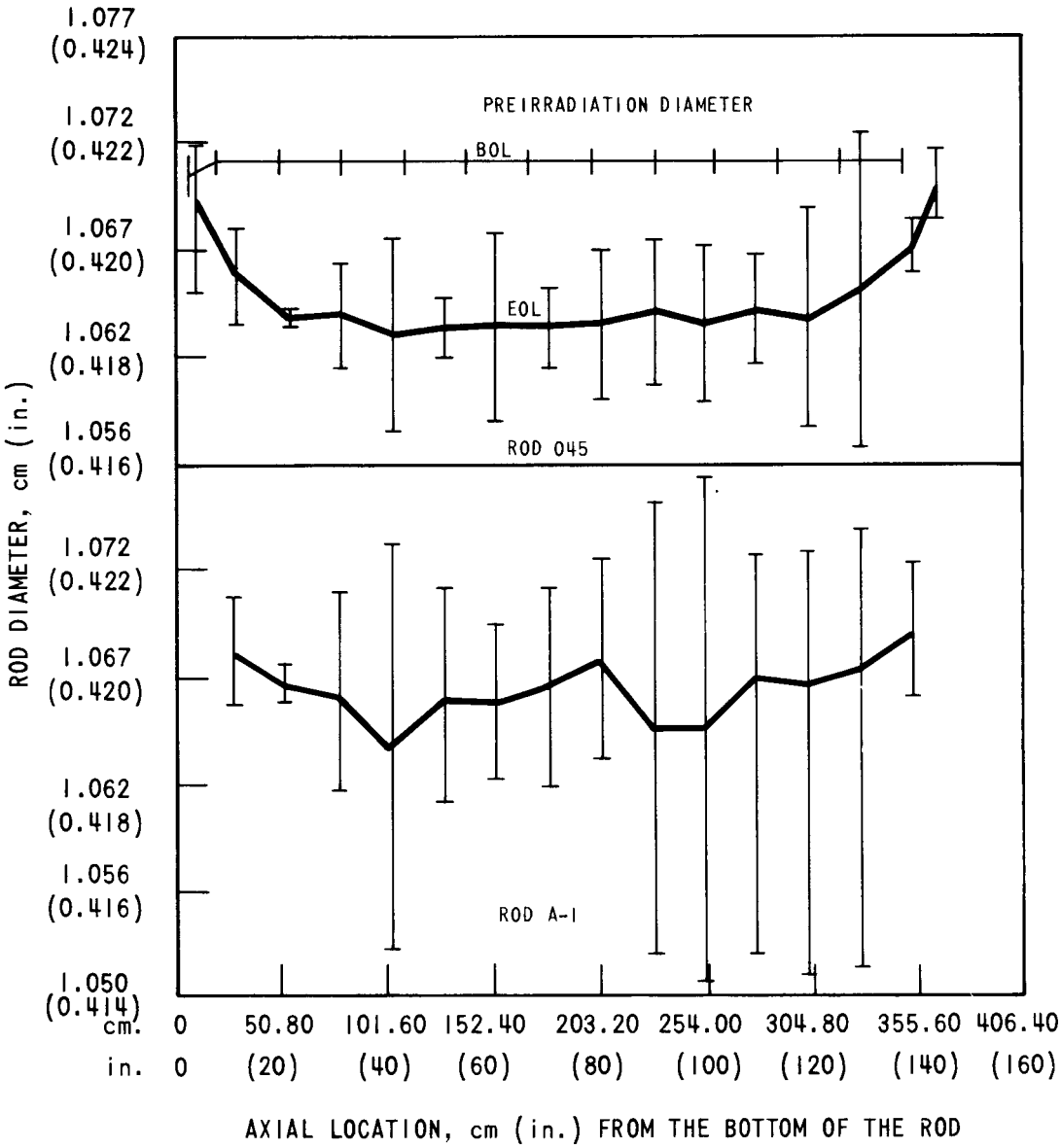

Figure 3.1-12. Fuel Rod Diameter Profiles at End of Life (Reactor Cycle 3) Point Beach-1

Ridging. All fuel rods profiled showed some evidence of clad ridging at fuel pellet interfaces. The ridge heights and locations appeared to vary significantly. The maximum diametral ridge height was estimated to be 0.014 mm (0.6 mil). Evaluation of ridge data from sister rod 037 (1) indicates that in general the ridge height increased only a little (i.e., 0-0.007 mm) during the second cycle of operation (reactor Cycle 3). Figure 3.1-13 shows examples of clad ridging observed in the spiral and linear diameter traces on rod 045. It is to be noted that in general the location of the ridges from both types of profilometry measurement coincide reasonably well. The ridges occur at pellet length intervals. The spiral profilometry data in Figure 3.1-13 also clearly illustrates the ovality of rod 045; it is of interest to note that the ridges are clearly discernable (though small) even where the cladding is oval. In several instances, evidence of local diameter increases, possibly due to wedged or cocked pellets, was observed. An example is illustrated in Figure 3.1-14. Further details of the profilometry data may be obtained from Reference 4.

3.1.5.2.3 Eddy current inspection. System description and procedures. Eddy current inspection of the 10 candidate rods included both encircling coil and probe coil eddy current systems. The encircling coil system uses an annular shaped coil while the probe coil system uses a contoured coil. The probe coil offers improved sensitivity in the location of incipient defects compared to the encircling coil technique. Details of the two eddy current systems have been previously published (4).

Scope and Results. After scribing axial location markers on the 10 candidate rods so that the defect indications could be located more accurately, the fuel rods were again eddy current tested using the same encircling coil system as used in the initial screening process. Following this work, the rods were then tested using the probe eddy current system to provide comparative data. In most cases, probe eddy current tests were run only on segments of rods [approximately 90 cm (35 inches) long] showing encircling coil defect indications.

Table 3.1-6 summarizes the results from encircling coil and probe coil measurements for the two rods, 045 and A-1, which were subsequently selected

Table 3.1-6 SUMMARY OF EDDY CURRENT TEST RESULTS FROM POINT BEACH UNIT 1 ROD
(For Rods Destructively Examined)

Rod No.	Eddy Current Indications					
	Encircling Coil Location			Probe Coil Location+		
	cm	in.	Strength*	cm	in.	Orientation**
045	46.8	18.44	W	48.5	19.1	225°
	105.1	41.38	M	121.2	47.7	135°
	--	--		146.6	57.7	135-180°
	--	--		161.5	63.6	135-0°
	--	--		191.0	75.2	90-135°
	210.2	82.75	M	217.4	85.6	315°
	--	--		223.3	87.9	220°
	--	--		239.5	94.3	225°
	278.6	109.69	S	278.6	109.7	0-225°
	290.7	114.44	S	291.3	114.7	90-180°
	--	--		293.9	115.7	180°
	323.4	127.31	S	323.3	123.3	0-225°
	324.8	127.88	W	325.1	128.0	135-315°
	333.9	131.44	M	334.0	131.5	315°
	342.7	134.94	M	--	--	--
A-1	--	--	M	236.0	92.9	0-45°
	245.26	96.56		244.6	96.3	0-360°
	309.2	121.75	W	309.6	121.9	0-360°
	311.2	122.5	M	311.4	122.6	360°

* Signal Strength W = Weak
M = Medium
S = Strong

+ Locations are from rod bottom.

** Orientation was set such that the first letter of the rod identification number was designated as 0°. Azimuthal orientation of other points are obtained as shown below.

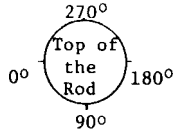

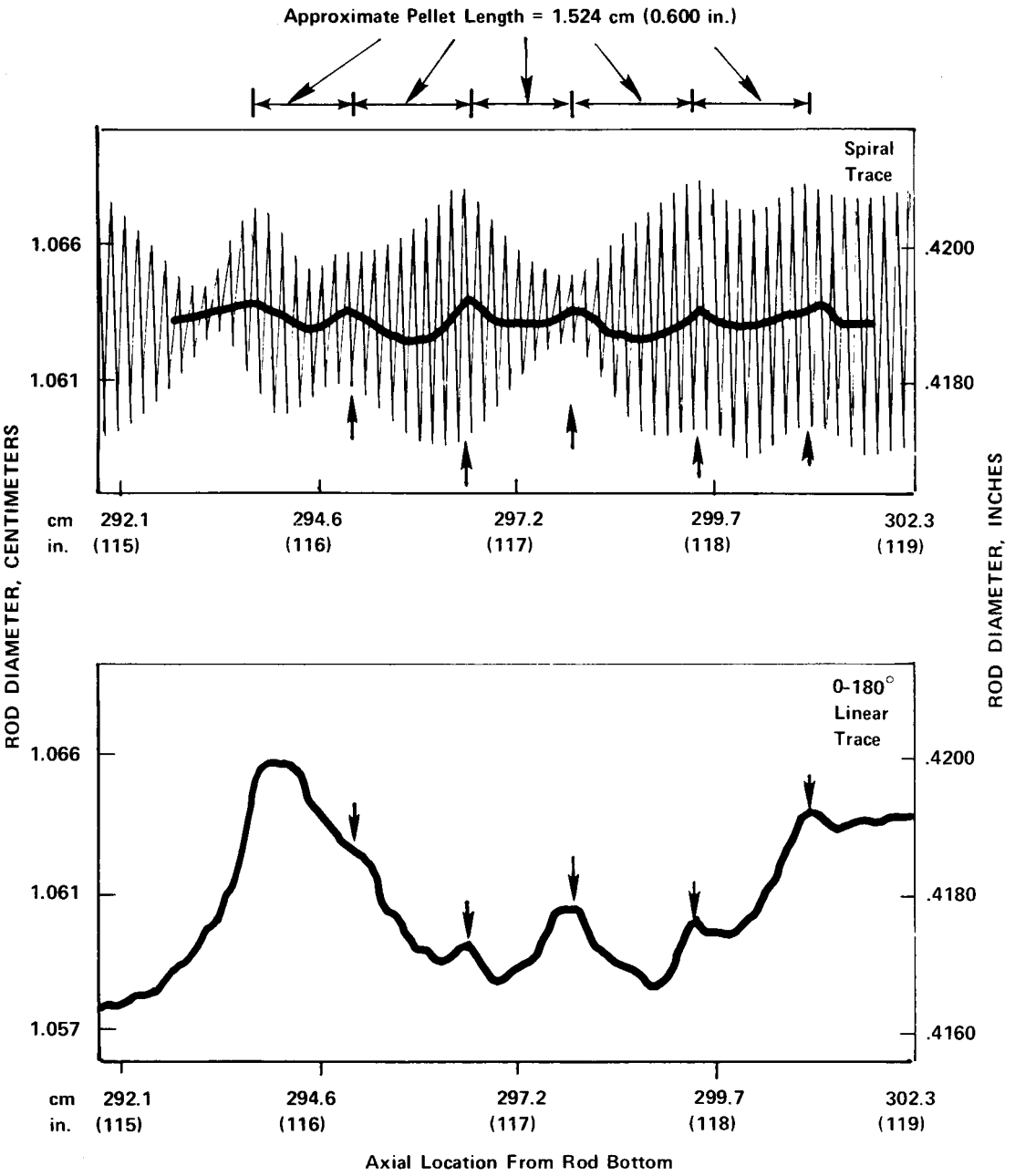

Figure 3.1-13. Examples of Clad Ridging Observed in the Spiral and Linear Diameter Profile Traces from Rod 045

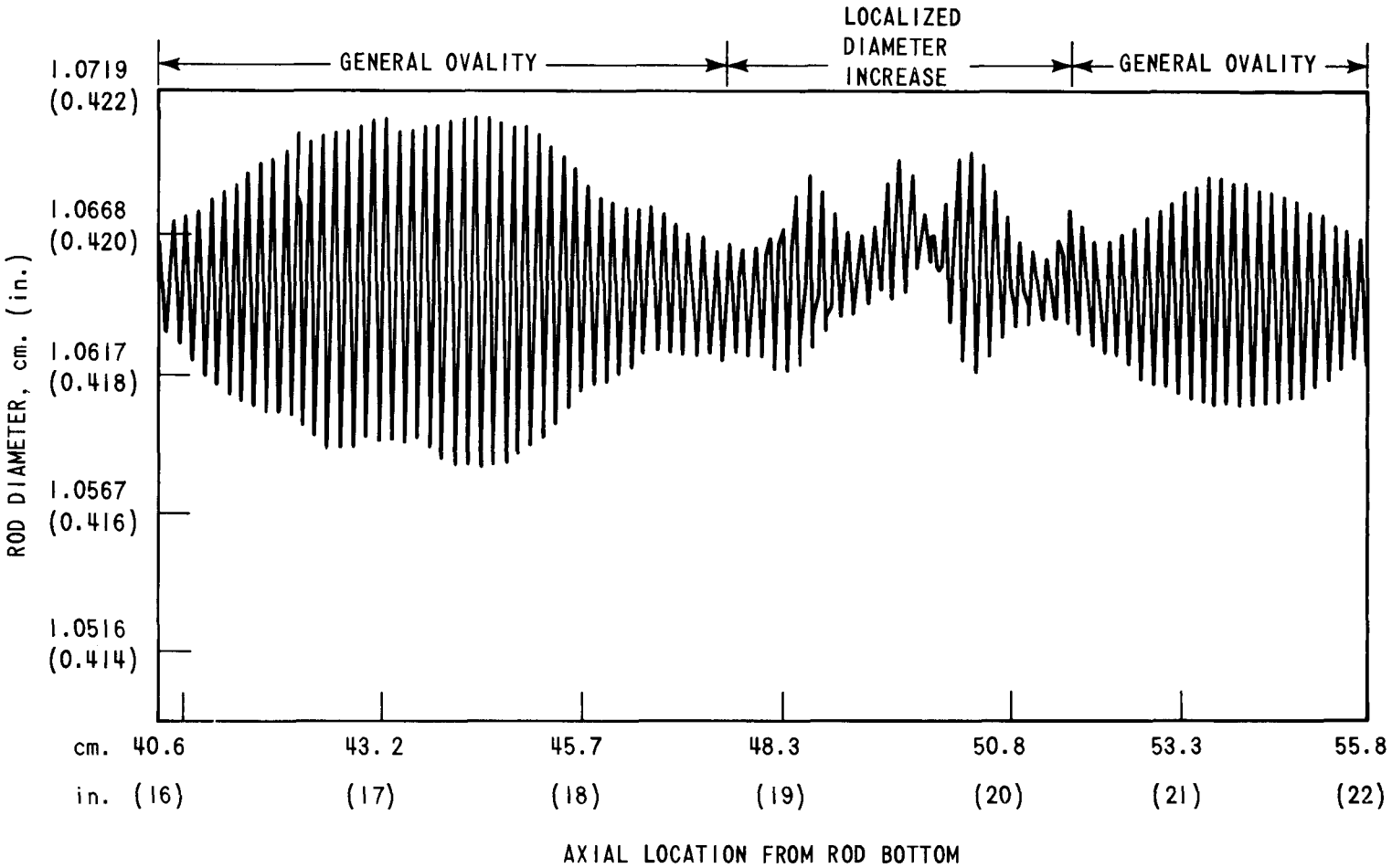

Figure 3.1-14. Spiral Diameter Trace Depicting an Area of Localized Diameter Increase Within a Generally Oval Region. Point Beach-1 Rod K-6

for destructive examination. These rods provide representative data, but details on all 10 rods may be obtained from Reference 4.

The data show, in general, that the axial location of encircling and probe eddy current signals of potential incipient defects compare favorably. It is to be noted, however, that the probe provided a greater number of potential incipient defect signals, possibly as a consequence of its higher sensitivity, although in a few isolated instances "weak" encircling coil signals were not repeated by the probe.

Figures 3.1-15 and -16 show examples of interesting contrasting observations. Figure 3.1-15 compares the encircling and probe eddy current signals for the 323.5 cm (127.3 inch) axial location of the removable rod 045. For this potential defect, the probe provided signals at all azimuthal orientations suggestive of several coexisting radially oriented incipient defects; a clear encircling eddy current signal was evident. In Figure 3.1-16 which compares the encircling and probe eddy current signals from the 237 cm (93.3 inch) axial location of standard fuel rod A-1, the probe data suggest that the potential incipient defect is highly sensitive to azimuthal orientation, and as such, is unable to influence the response of the encircling coil eddy current system. As will be described in Section 3.1.5.4, both of these fuel rods were subsequently sectioned and metallographically examined to determine the cause of the eddy current signals.

In comparing both types of eddy current signals with profilometry and gamma scan data, it is apparent that local clad bulges, believed to be due to pellet wedging and associated hang up of the fuel column (resulting in small axial gaps), also result in signals symptomatic of potential defects. An example is illustrated for rod 045 in Figure 3.1-17. This section of the fuel rod was also subsequently examined metallographically.

3.1.5.3 Selection of Samples for Destructive Examinations. A summary of NDE data for all candidate fuel rods is provided in Apendix D. From examination of all the available data, two fuel rods, 045 and A-1, were judged to be representative of the Point Beach Region-4 fuel rods and offered the greatest potential for successfully locating and characterizing an incipient defect. Rod 045 was the highest burnup removable rod in the program and operated at a rod average power level of 21.38 kW/m (6.52 kW/ft) at the end of reactor Cycle 2. At the

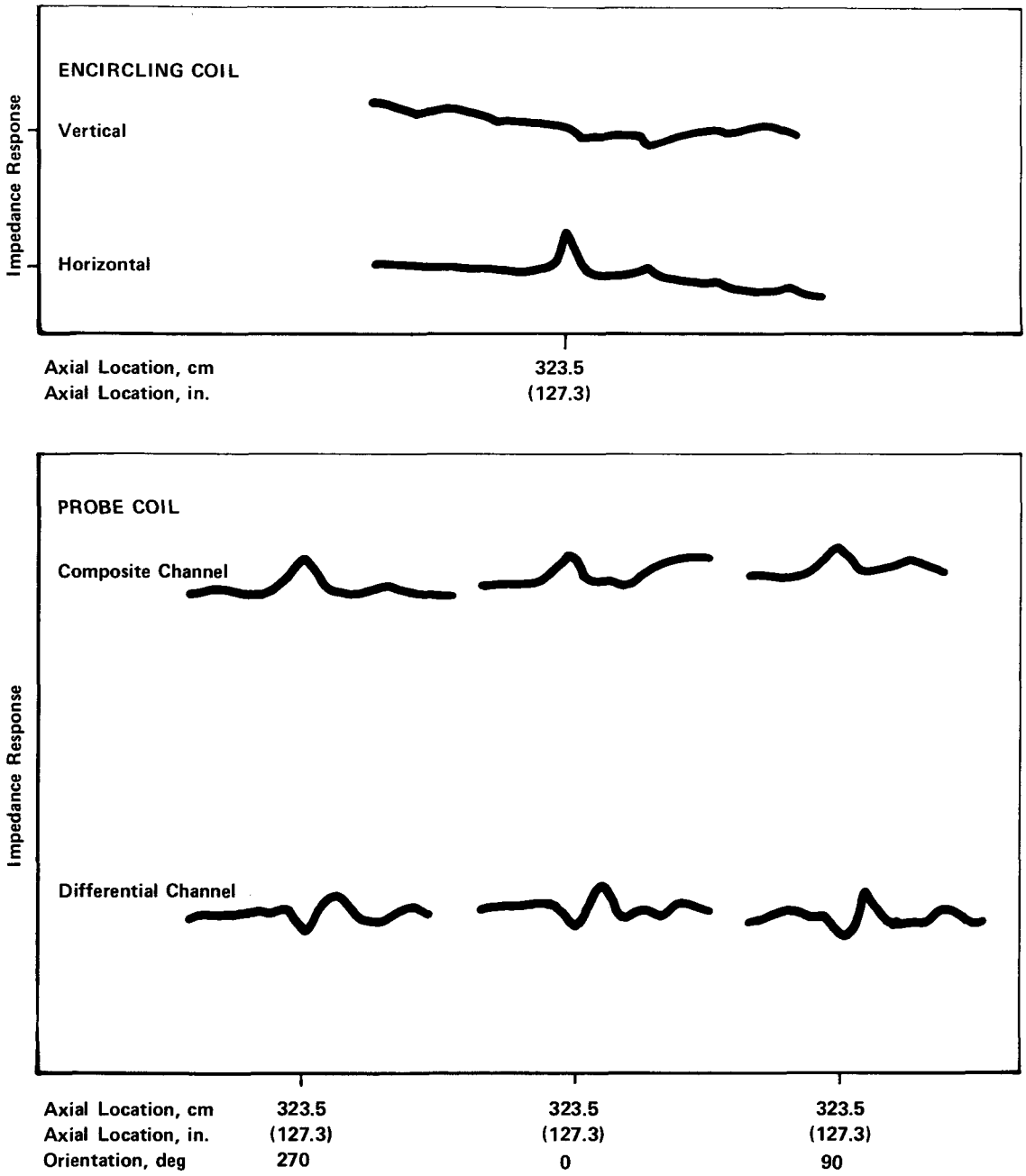

Figure 3.1-15. Encircling Coil and Probe Eddy Current Responses for Point Beach-1 Rod 045 at 323.5 cm (127.8 in.) from the Bottom of the Rod

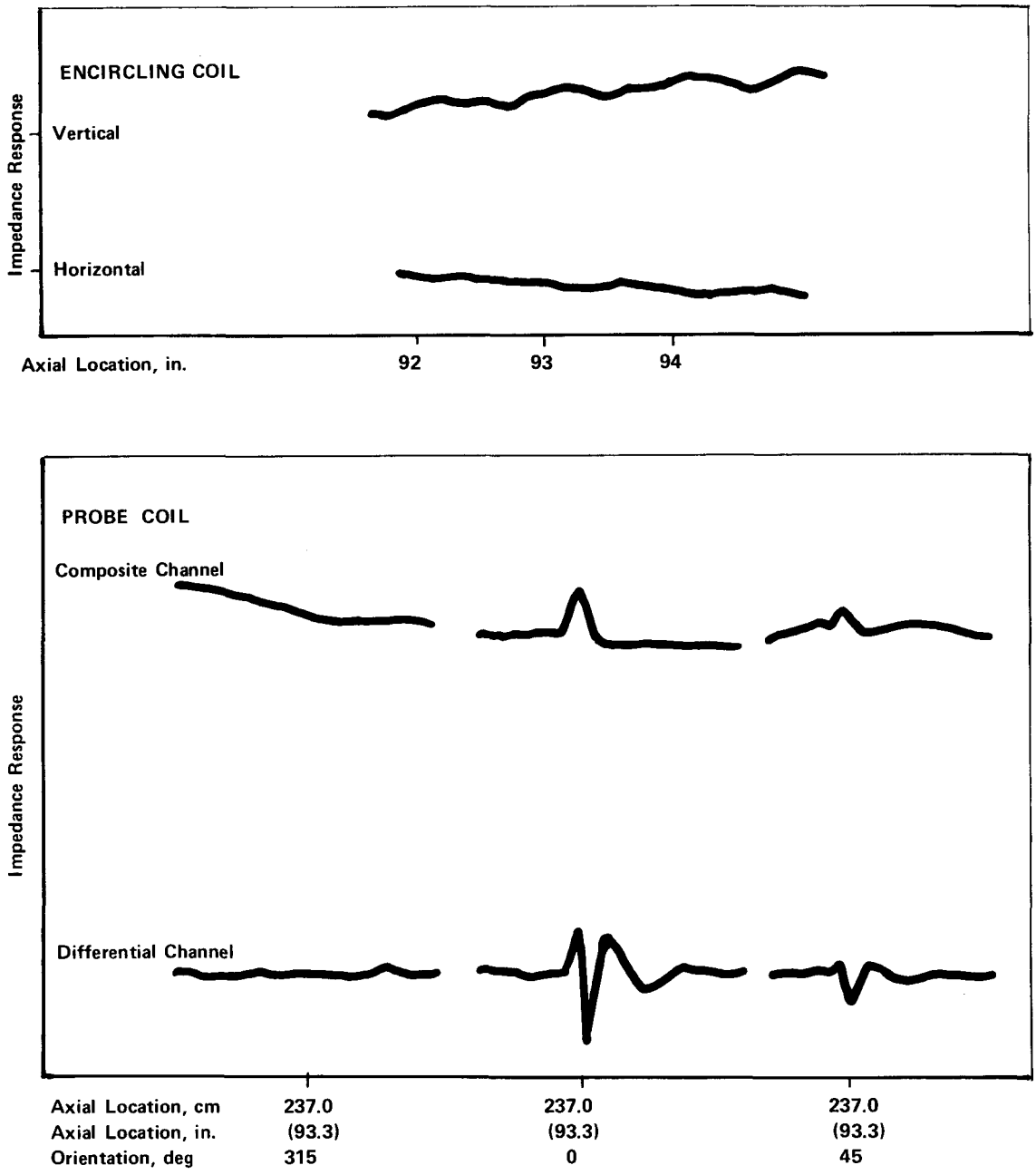

Figure 3.1-16. Encircling Coil and Probe Eddy Current Responses for Point Beach-1 Rod A-1 at ~ 237 cm (93.3 in.) from Rod Bottom

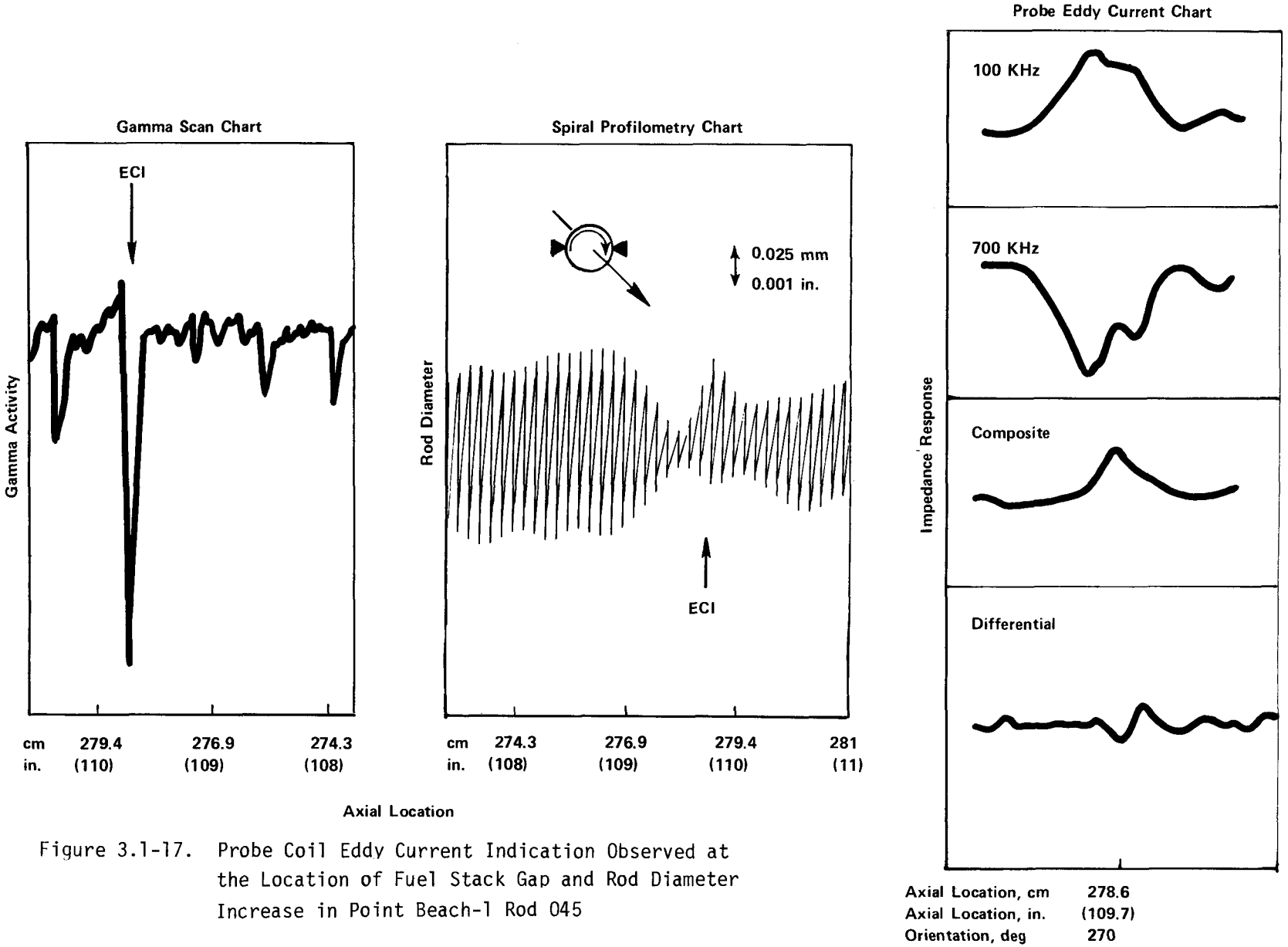

Figure 3.1-17. Probe Coil Eddy Current Indication Observed at the Location of Fuel Stack Gap and Rod Diameter Increase in Point Beach-1 Rod 045

beginning of Cycle 3 when failure in the core was first detected, the rod average power level increased only slightly at reactor full power to 23.77 kW/m (7.25 kW/ft). In contrast, rod A-1, which was irradiated in the standard assembly D-14, operated at only low power during Cycle 2, and subsequently experienced a power increase of 14.75 kW/m (4.5 kW/ft) during the Cycle 3 startup. The power histories are provided in Figures 3.1-18 and -19; further details may be found in Appendix B.

The selection of fuel samples from these two rods for metallographic examination was based on correlations of eddy current signals with fuel stack gaps, sharp local diameter increases of the cladding, and peak power locations. Details of the samples selected are provided below.

Rod 045. Five samples were investigated by metallography and three of these were examined in detail and selected as follows:

Axial location 323.4 cm (125.3 inches):	Observation of a strong eddy current indication (See Figure 3.1-15). Probe indication at each azimuthal orientation.
Axial location 278.6 cm (109.7 inches):	Observation of a strong eddy current indication, which correlated with a sharp local diameter increase and a pellet lockup as indicated by a fuel stack gap (See Figure 3.1-17). Probe indication at the azimuthal position of the cladding bulge.
Axial location 290.7 cm (114.4 inches):	Observation of a strong eddy current indication at a location of a small local diametral increase and a pellet lockup. Probe indication at each azimuthal orientation.

Rod A-1. The following sample was examined from this rod.

Axial location 236.0 cm (92.9 inches):	Probe eddy current indication only (no coil EC signal) which coincided with peak power location (64

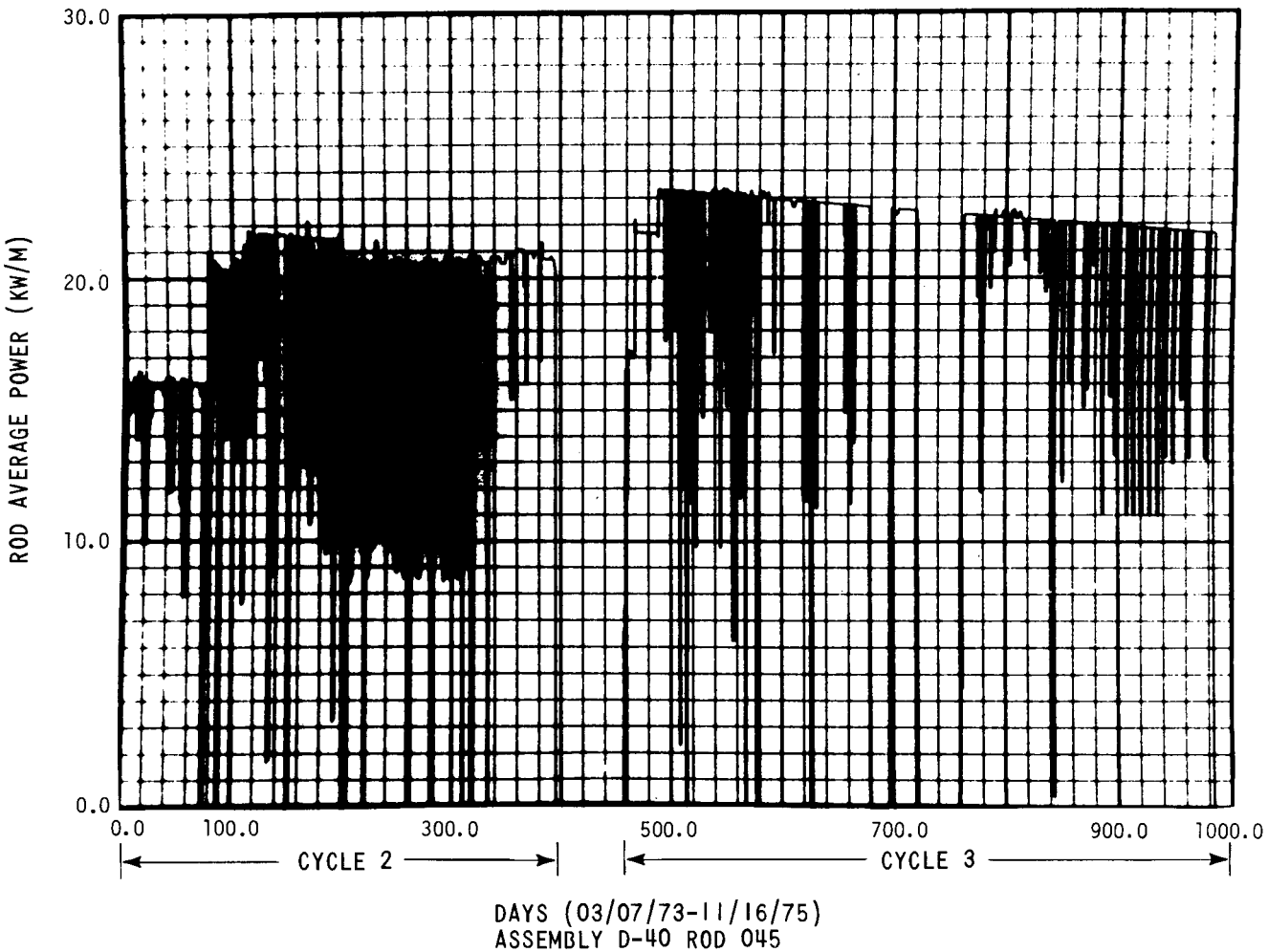

Figure 3.1-18 Average Power of Rod 045 of Assembly D-40 During Reactor Cycles 2 and 3

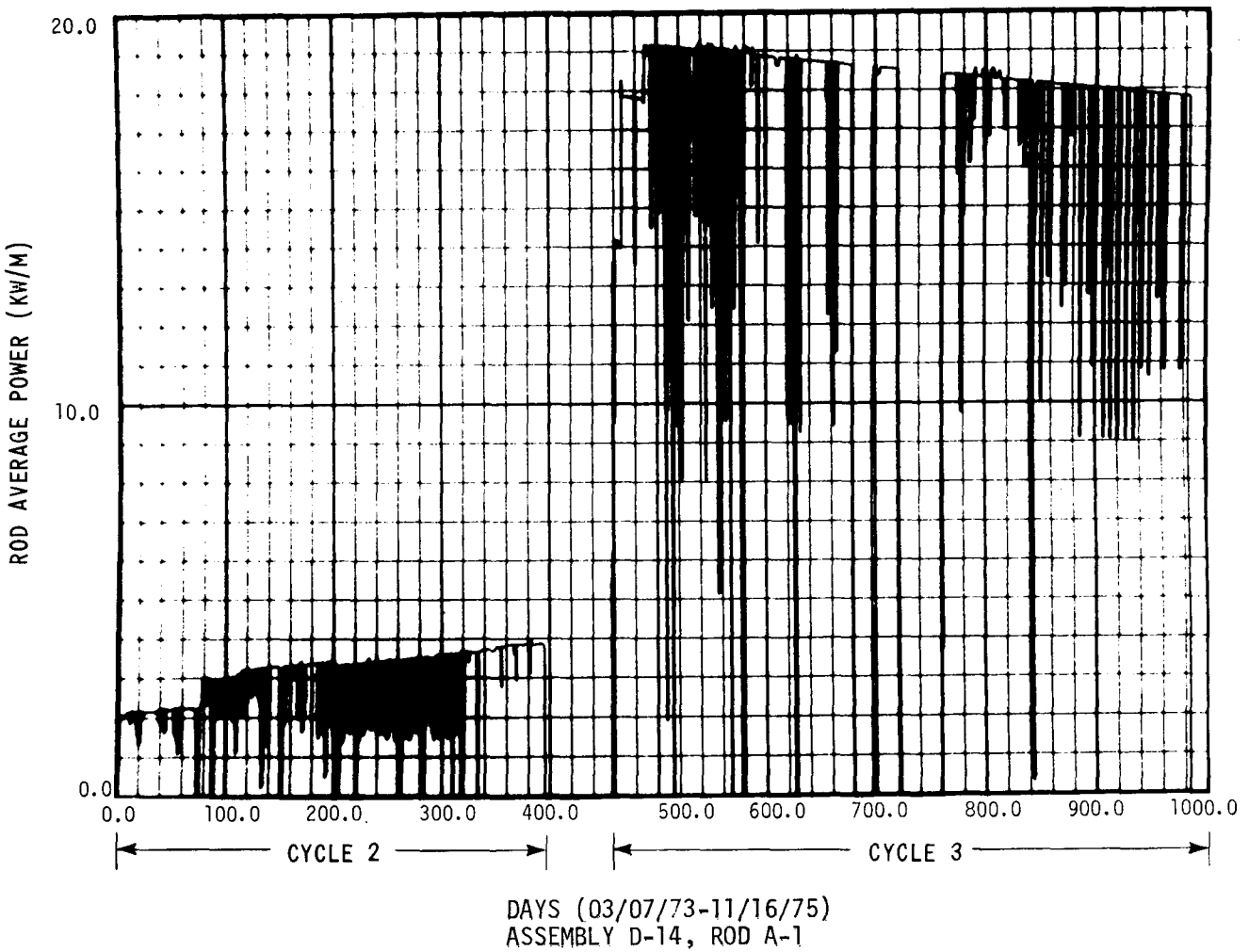

Figure 3.1-19 Average Power of Rod A-1 of Assembly D-14 During Reactor Cycles 2 and 3

percent of fuel column height; see Section 3.1.3.2 (See Figure 3.1-16). Probe indication unique to one azimuthal orientation.

3.1.5.4 Destructive Examination. The primary objective of the destructive examinations was to confirm the existence of incipient cracks and to characterize their structure through metallographic examination. The destructive examinations consisted of:

1. Fuel rod puncture for fission gas collection and fuel rod internal volume measurement
2. Fuel-clad metallography.

Fuel rods 045 (from fuel assembly D-40), A-1, B-11, and M-14 (from fuel assembly D-14) were selected for fission gas analysis; rods 045 and A-1 were subsequently sectioned and metallographically examined. Rods 045, A-1, and B-11 were originally selected for puncture because of their potential for incipient defection as indicated by the eddy current tests; rod M-14 was selected because of unusual end plug markings.

3.1.5.4.1 Fission gas collection and analysis. The objectives of performing fission gas collection and analysis were (a) to determine if the fuel rods were unfailed, and (b) to obtain fractional fission gas release data.

The selected fuel rods (045, A-1, B-11, and M-14) were punctured, the released gases were collected and their volumes measured using the BCL Hot Laboratory fission gas collection system. Details of the procedure have been described previously (4).

Table 3.1-7 shows the gas release and void volume data obtained from the four rods; none of the rods was failed. Also shown in the table are the calculated total fission gas generated and the fractional fission gas release measured. The data show good agreement among the rods. The fractional gas release observed is in the range expected for a typical commercial PWR fuel rod operating at these power levels and to the achieved burnups. The amount of helium collected from the rods is also reasonably consistent with the preirradiated fuel rod internal pressure of 2.65 Mn/m^2 (385 psia). The low

Table 3.1-7

FISSION GAS RELEASE AND VOID VOLUME DATA
OBTAINED ON POINT BEACH UNIT 1 FUEL RODS

Rod No.	Rod Avg. Burnup, MWD/MTU	Fuel Rod Void Volume, cc	Total Vol. of Gas Collected from Rod, STP cc	Gas Composition, vol. percent								Vol. of (Xe + Kr) Released, STP cc	Vol. of (Xe + Kr) Generated[a], STP cc	Percent Fission Gas Released
				H_2	He	H_2O	N_2	O_2	Ar	Kr	Xe			
B-11	20927	24.34	628.67	<.01	88.75[b]	<0.1	6.3[b]	1.69	1.2	0.23	1.79	12.7	1404	0.9
045	29365	23.08	574.39	<.01	97.5	<0.1	0.1	0.06	--	0.20	1.68	10.8	1970	0.55
A-1	15563	26.28	565.52	<.01	98.7	<0.1	0.1	0.04	0.74	0.05	0.41	2.6	1044	0.25
M-14	26120	20.56	542.42	<.01	86.2[b]	<0.1	9.1[b]	2.6[b]	1.2	0.10	0.85	5.15	1752	0.29

[a]Based on 0.3 atoms of (Xe + Kr) generated per fission; assuming 4000 MWD/MTU = 10^{20} fiss/cc.

[b]Some air contamination occurred.

fractional gas releases observed indicate that the temperature experienced by the fuel in these rods was not high enough to cause significant redistribution and release of fission products. The observation is consistent with the conclusions reached from the Cs-137 gamma scan data. In contrast, the Maine Yankee Core-1 fuel rods exhibiting incipient PCI-related cladding cracks showed a significantly higher fission gas release fraction (11-15 percent), and for these rods a correlation of the presence of incipient cladding cracks to high gas release and Cs redistribution was suggested (6).

3.1.5.4.2 Metallographic Examination. Fuel rod sections were obtained from rods 045 and A-1 at the axial locations defined in Section 3.1.5.3. Details of the sectioning are described in the interim report (4). Generally, the specimens were ground and polished incrementally to permit examination of many surfaces. Each surface was examined both in the as-polished condition and after being etched to reveal the hydride concentration and orientation in the cladding. Four out of the six sections cut from the fuel rods were examined in steps up to or beyond the location of the center of eddy current indications. The other two sections were of lower significance and were examined only at four levels with the last surface examined being ~ 2 mm (0.080 inch) away from the center of eddy current indications. The salient features observed on each specimen surface were documented by photography.

Table 3.1-8 summarizes details of the metallographic samples examined from the two rods. Important aspects of the examination are as follows:

Rod 045. A total of 64 surfaces was examined on the five specimens from rod 045. The examination revealed no anomalies in the cladding in any of the five specimens. As expected for these burnups, pieces of fuel were found bonded to the clad inner surface. However, the extent of fuel bonding was small and varied significantly from one surface to another with respect to location and amount. Figure 3.1-20 shows examples of fuel bonding observed in the specimen obtained from the 279.55 cm (110.06 inch) axial location. The appearance of the bonded fuel region was similar to that observed in the Maine Yankee Core-1 fuel rods (6, 7) which had experienced high fission gas release--namely, Zircaloy followed by a ZrO_2 layer (~ 7 μm in thickness) followed by UO_2 fuel. Occasionally,

Table 3.1-8

SUMMARY OF POINT BEACH UNIT 1 FUEL ROD METALLOGRAPHY DATA

Rod No.	Axial Location of Sample[a], cm (in.)	Location of Eddy Current Indication[a], cm (in.)	Total Length of Sample Examined, cm (in.)	No. of Surfaces Examined	Key Observations
045	277.6-279.55 (109.31-110.06)	278.64 (109.7)	1.468 (0.5778)	24	Fuel bonding to various degrees pitting Corrosion on clad inner surface depth ~15μ.
045	289.41-291.31 (115.94-114.69)	114.44 (290.68)	1.005 (0.396)	14	Ditto
045	322.27-324.18 (126.88-127.63)	323.37 (127.31)	1.092 (0.430)	18	Small amount of fuel bonding
045	324.18-326.09 (127.63-128.38)	324.82 (127.88)	0.500 (0.197)	4	Sample was abandoned before the location of the eddy current indication was reached.
045	341.48-343.38 (134.44-135.19)	342.70 (134.92)	0.452 (0.178)	4	Sample was abandoned before the location of the eddy current indication was reached.
A-1	235.20-237.74 (92.6-93.6)	236.98 (93.3)	0.76 (0.3)	2	Large metallic particle (0.6 x 0.76 mm) at pellet periphery. The location of the particle was at the orientation indicated by probe coil system

[a] From bottom of rod.

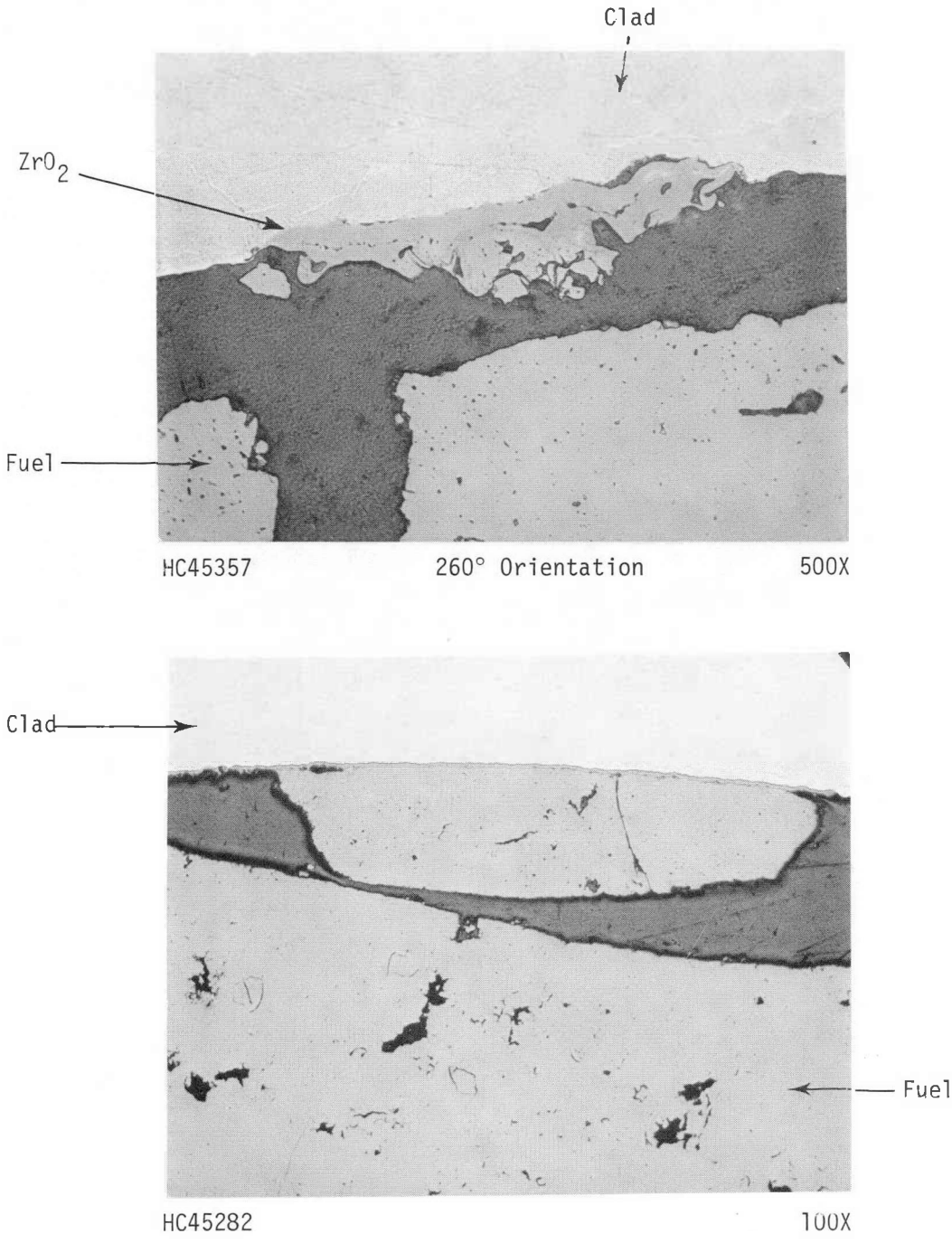

Figure 3.1-20 Examples of Fuel-Clad Bonding Observed In Rod 045 at ~ 280 cm (~ 110 in.) from Rod Bottom

a thin dark layer was observed between the fuel and the zirconium oxide layer. The dark gray cesium-rich zone observed in the Maine Yankee fuel rods was not apparent in any of the Point Beach rods in the bonded fuel region. Another feature of interest, observed in the samples from the 279.5 cm (110.06 inch) and 291.3 cm (114.7 inch) axial locations was the apparent pitting attack on the clad inner surface. In places the pits had a depth of ~ 18 μm. Figure 3.1-21 shows examples. The examinations demonstrated that the eddy current signals observed were not due to incipient defects in the cladding.

All clad samples from rod 045 exhibited very low concentrations of hydride precipitate (< 80 ppm); the levels were typical of Zircaloy-4. The hydride precipitates were in general randomly oriented and uniformly distributed around the cladding circumference.

For the fuel pellets, no significant features were apparent in any of the samples examined. The fuel showed no equiaxed grain growth, indicating that the centerline temperatures experienced during irradiation were rather low (< 1300°C), consistent with the low gas release data.

Rod A-1. The sample from Rod A-1, which exhibited a strong probe coil eddy current indication, was examined on two surfaces. On the first surface, a large metallic inclusion was observed close to the fuel pellet periphery. This is shown in Figure 3.1-22. The specimen was ground further to the location of the center of the eddy current signal and the particle was again observed. Since the location of the particle was in excellent agreement with the azimuthal orientation of the signal indicated by the probe coil, it was concluded that the particle was the source of the eddy current signal and the examination was discontinued.

These metallographic examinations suggest that the eddy current indications (both encircling and probe) of potential cladding defects can be misleading. Extensive examination of samples obtained at the locations of eddy current indications revealed no cladding defects.

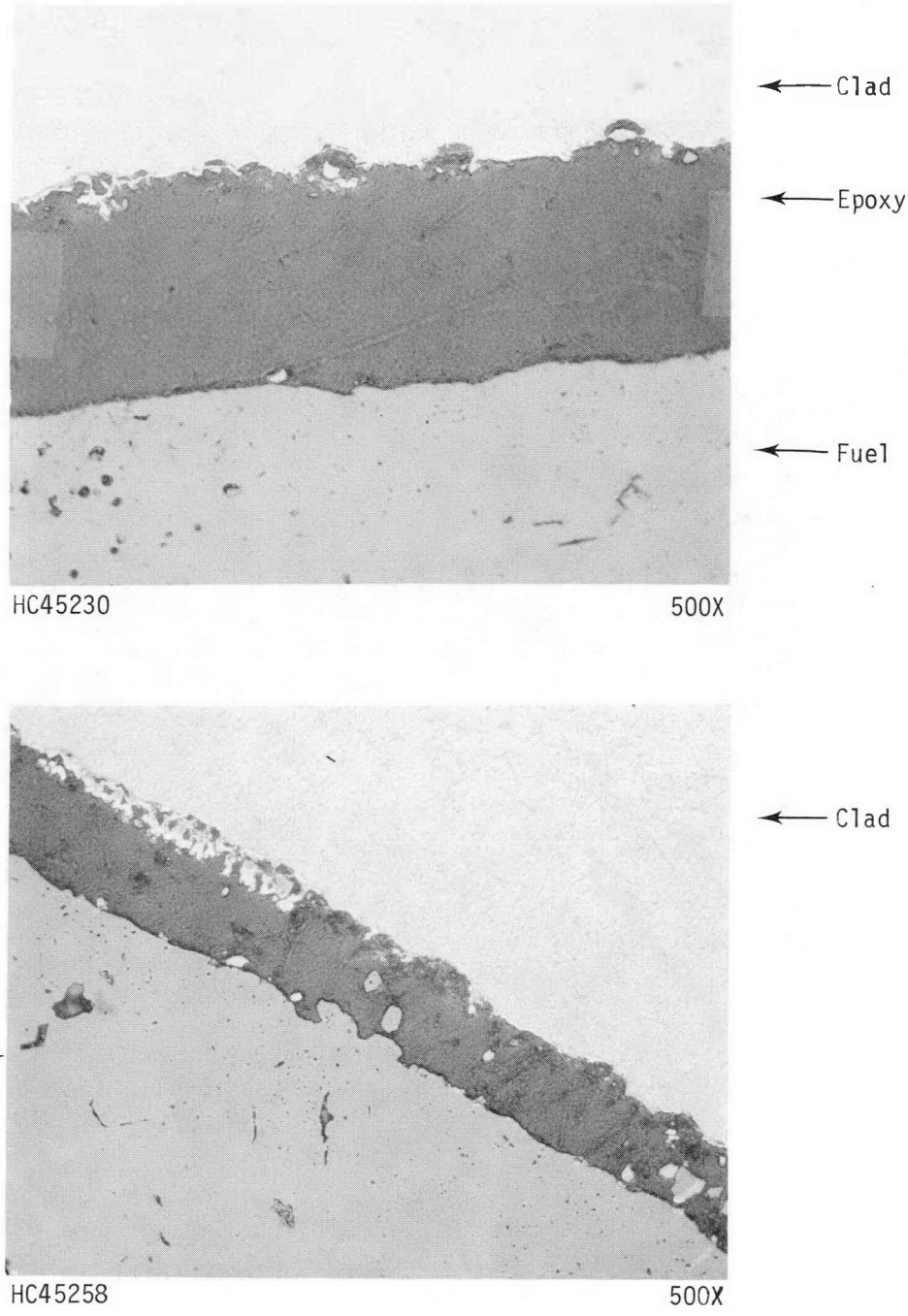

Figure 3.1-21 Examples of Apparent Pitting Corrosion Observed In Point Beach-1 Rod 045 at ~ 280 cm (110 in.) From Rod Bottom

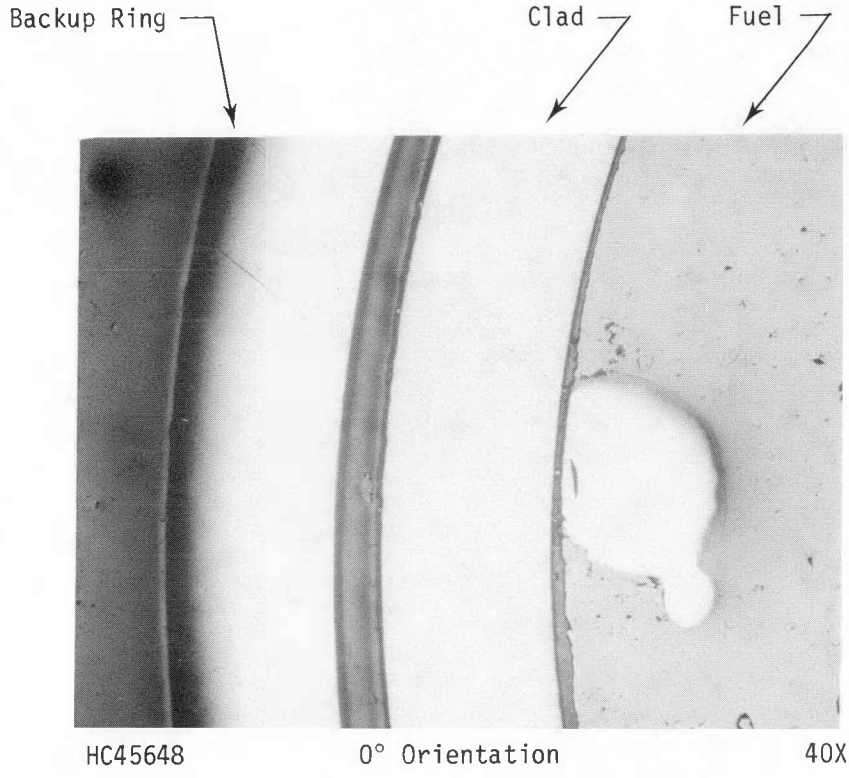

Figure 3.1-22 Appearance of the Metallic Particle at the Center of Eddy Current Indication Observed in the Point Beach-1 Rod A-1 at ~ 237 cm (93.3 in.) from Rod Bottom

It therefore appeared that attempts to confirm the presence of an incipient defect through metallographic examination of rod sections displaying suspect eddy current signals had only low probability of success. Consequently, since fuel assembly D-14 was known to be leaking, future effort in the program was directed toward attempting to locate a perforated rod in the assembly. It was anticipated with this approach that following the successful identification and characterization of a perforated fuel rod, the information would prove valuable in seeking and hopefully characterizing an incipient defect in a nonfailed sister rod.

3.1.5.5 Ultrasonic Testing of Point Beach Assembly D-14. In an attempt to locate perforated fuel rods in fuel Assembly D-14 using ultrasonic equipment, two separate campaigns were undertaken in the pool of the BCL Hot Laboratory utilizing W equipment. The equipment and technique used was of an experimental nature and had not been previously used in full length PWR fuel rods. Nevertheless, in view of the prior success obtained by W with the equipment on shorter experimental rods, and in view of the difficulty experienced in meeting the program objectives by alternative available techniques, this approach appeared to offer much potential.

The ultrasonic test comprised the application of an ultrasonic wave pulse to the top end plug of a fuel rod and the monitoring of the subsequent propagation and reflection of the waves along the length of the rod. With such wave propagation, acoustic impedance along the path causes a portion of the acoustic energy to be reflected back and at the bottom end plug of the fuel rod nearly 100 percent of the energy reaching that point is reflected back. However, if water exists within the fuel rod attenuation of the ultrasonic pulse will occur as evident by the absence of a reflected signal. Thus, provided liquid water exists in a perforated fuel rod at the time of testing, identification of the failed rod should be readily apparent. In the W test equipment used, the system was set up to display the reflected ultrasonic signal on an oscilloscope screen to facilitate analysis.

First Campaign: Scope and Results

During the first campaign, Assembly D-14 contained 164 rods of the original 179 loaded into the assembly. The remaining rods were in the BCL hot cell and included the 10 candidate rods selected by the previous nondestructive examinations, and several rods that had been tested with encircling coil eddy current which had yet been returned to the assembly.

In this campaign an ultrasonic test frequency of 464 kHz was utilized. The frequency was selected during the calibration of two unirradiated full-length rods containing depleted pellets. These calibration rods were inserted into a dummy assembly to simulate the grid supports; in addition, the dummy assembly was inserted in the pool to ensure comparable environmental conditions to the irradiated fuel rods. The frequency selected was judged to be the optimum for distinguishing between one calibration rod which had been deliberately punctured to simulate a failure and the second calibration rod which was maintained intact. Examples of signal reflections from the leaking and nonleaking calibration rods are given in Figures 3.1-23 and -24.

From the testing of fuel rods by this approach and subsequent analysis of the oscilloscope displays, it was tentatively concluded that the fuel assembly could contain as many as 36 failed fuel rods. That is, 36 rods displayed dampened echo signals suggestive of internal attenuation by contained water. To confirm this interpretation, three key rods were therefore selected for puncturing and checking of backfill pressure in the hot cells. (The technique adapted for confirming rod pressure is described in Appendix D.) This work, however, indicated that all three rods were intact and consequently, a second ultrasonic campaign utilizing a revised approach was undertaken.

Second Campaign: Scope and Results

During the second campaign, fuel Assembly D-14 contained 169 rods as a result of transfers between the hot cells and the storage pool. In calibrating the equipment, the two standard rods were again utilized. To improve the approach in the second campaign, however, the standard rods were swaged at several positions along the rod length to simulate pellet/clad interaction. In this condition, the failed and nonfailed standards provided optimum ultrasonic response (for both the non-swaged and swaged conditions) at 290 kHz. This frequency was therefore used in the second campaign.

From analysis of the oscilloscope displays in the second campaign, it was tentatively concluded that even more rods in Assembly D-14 were potentially defective than was apparent from the first ultrasonic campaign. Of these rods, 13 showed consistent indications of ultrasonic dampening in both campaigns. Thus, it was considered that as a consequence of both campaigns, the selection of rods for possible characterization may have been substantially narrowed.

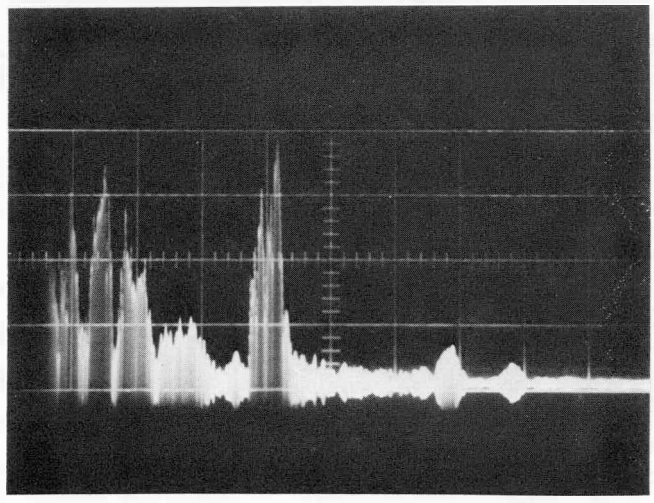

Figure 3.1-23 Nonfailed Standard Rod Ultrasonic Tested in Water (Completely Immersed). Frequency 464 KHz. Gain 50 mv/cm. Only Top Half of Signal is Displayed.

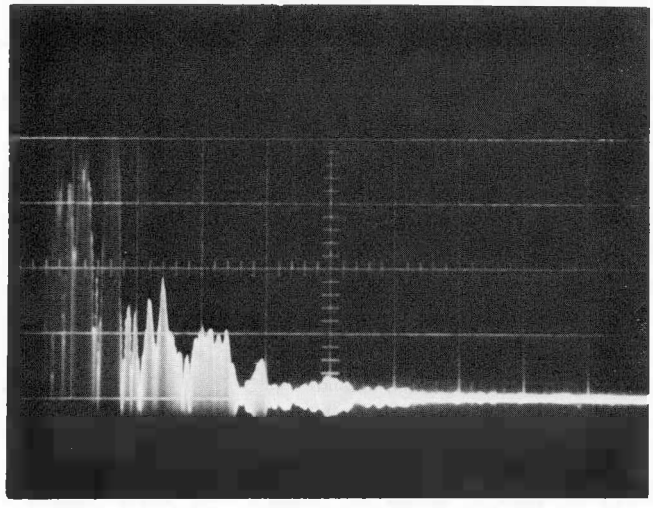

Figure 3.1-24 Punctured Standard Rod Tested Under the Same Conditions as in Figure 3.1-23

A summary of the ultrasonic test results for fuel Assembly D-14 is provided in Figure 3.1-25. In addition to indicating the ultrasonic test results, the figure illustrates the location of rods punctured prior to the ultrasonic testing and the location of rods selected for puncturing as a result of the two ultrasonic campaigns.

To test the possiblity that rods showing consistent dampened ultrasonic signals were indeed failed, 11 rods were selected and punctured for pressure checks in the hot cell. However, as for the first campaign, all rods proved to be unfailed. Thus, although a total of some 17 fuel rods had been removed from the fuel assembly and punctured/pressure checked at this stage of the program, no failed rod had been successfully identified. It was concluded that the ultrasonic system was not sufficiently well qualified to be of further use.

3.1.5.6 Additional Fuel Rod Puncture. Because of the lack of success of the nondestructive testing equipment in locating a failed fuel rod or a rod with incipient defect in Assembly D-14, it was decided to select additional rods in the assembly and ascertain their integrity through puncturing and measuring the backfill pressure. In this way, a failed fuel rod would be unambiguously identified. To provide for this effort, and in order to maintain the scrap disposal costs at a minimum, the BCL Hot Laboratory developed a technique for rewelding all punctured though nonfailed fuel rods. A procedure was carefully established by BCL to consistently produce a quality seal weld of the punctured fuel rods. This procedure was subsequently accepted by the operators of the WEPCO fuel storage facility,* thus, enabling a continuation of this phase of the program.

Rod Selection--Scope and Results

As stated in the previous section, following the two ultrasonic testing campaigns a total of 17 fuel rods had been punctured from fuel Assembly D-14 and shown to be intact. All 17 rods had been selected because prior nondestructive examinations suggested that the rods were potential candidates for subsequent destructive characterization of incipient and/or through-wall defects. Consequently, the 17 rods did not, in themselves, constitute a representative sample of rods in failed fuel Assembly D-14; therefore, an additional 29 rods were selected for puncturing and measurement of backfill pressure.

---

* G. E. Morris, Illinois. The cooperation of GE personnel in this work is hereby gratefully acknowledged.

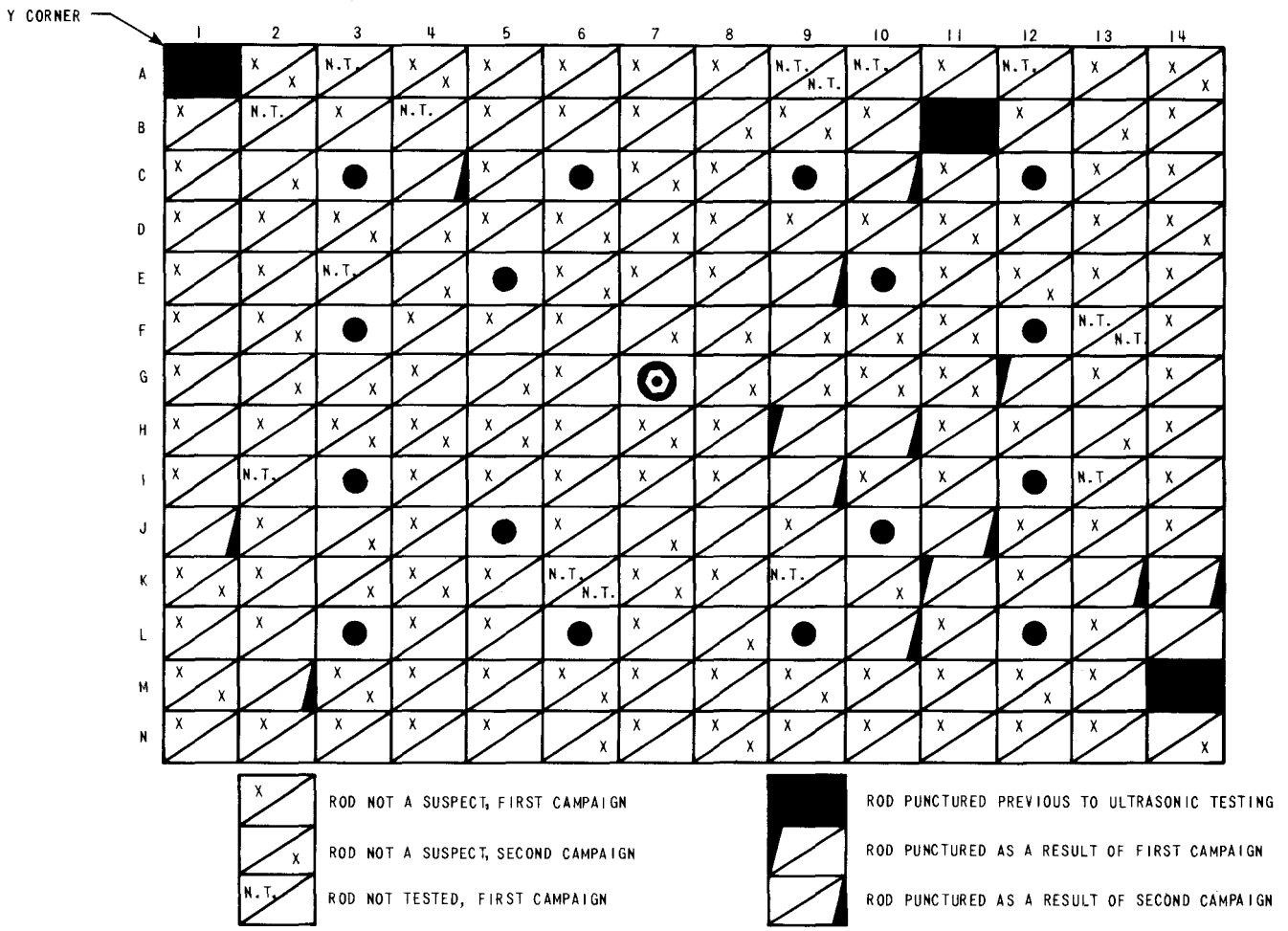

Figure 3.1-25 Ultrasonic Test Results on Point Beach Assembly D-14

The total of 46 rods thus defined to be examined through the puncturing campaign was judged to provide a representative sample from the following division or rod subgroups contained in the assembly: burnup, power level, power increase, pellet group, and cladding lot.*

The location in the fuel assembly of all 46 rods selected for puncture is provided in Figure 3.1-26. This figure shows that the selected rods provide a representative sample with respect to physical location in the assembly. Table 3.1-9 illustrates the representativeness of the selected rods for the rod subgroupings as defined above. This table shows that essentially all important groups of rods are represented in the samples. Thus, in conducting a puncture campaign on the remaining 29 rods selected, it was judged that a high probability for detecting a failed fuel rod existed. It was calculated, given that random statistics apply, that if 8 failed rods were assumed to exist in the assembly, the probability of detecting one of them out of a total of 46 rods punctured was greater than 90 percent. Figure 3.1-27 illustrates how the probability of detecting a failed rod depends upon the sample size and the number of failed rods assumed to exist in the assembly.

All 29 additional rods were therefore punctured and pressure checked following the procedure described in Appendix D. All of the rods indicated positive pressure readings, however, suggesting none was failed. The total range of all pressure measurements was only $\pm$ 14 percent of the mean value which was considered reasonable recognizing the variation in as-built void volumes and the range of clad creepdown and other dimensional changes during irradiation which influence the rod internal free volume (and hence pressure). Actual pressure readings on the 46 rods for the volumes of the Battelle fission gas puncture system are provided in Appendix Table D.

Evaluation of the Puncture Data

A breakdown of the puncture data for the five most important subgroups of fuel rods in assembly D-14 is provided in Table 3.1-10. From this table, it is evident that a substantial fraction of rods in each subgroup was tested in the puncture campaign. Many rods, of course, are common to several subgroups. In addition, it

* Only rod groups having at least four rods in the assembly were considered significant.

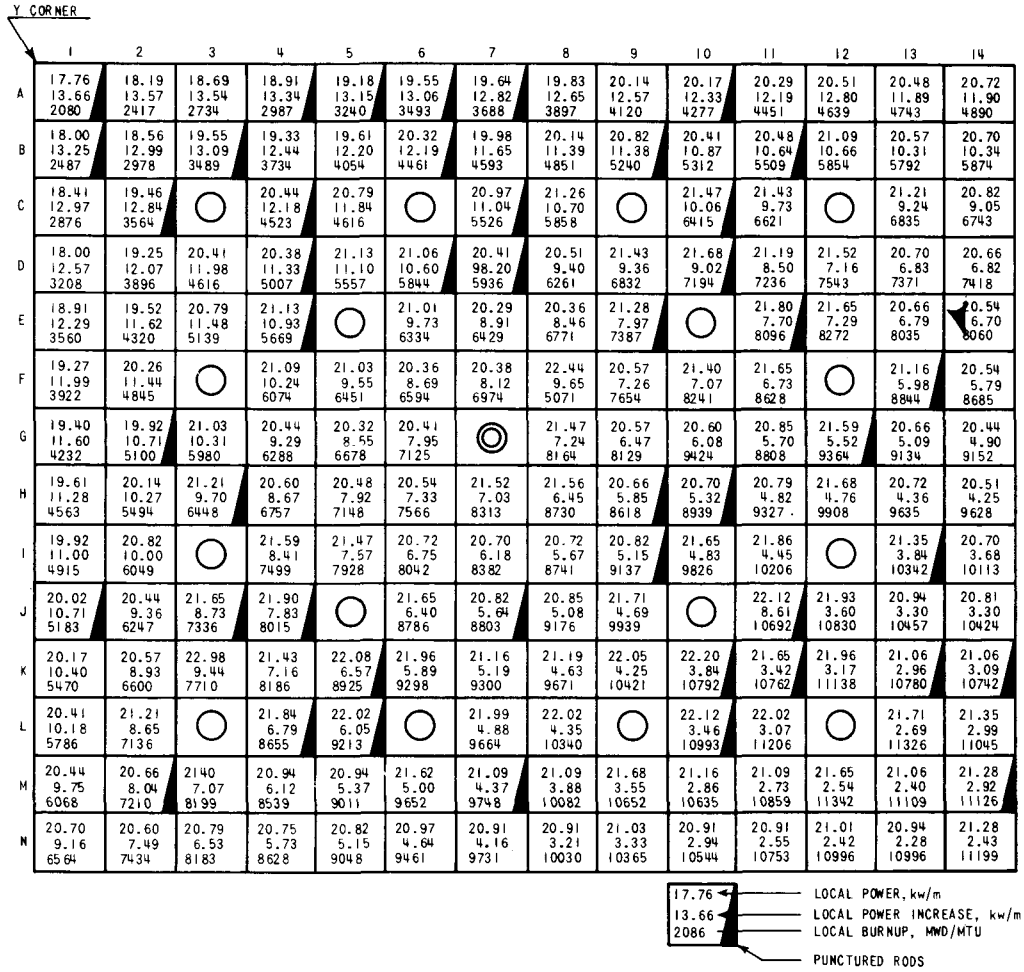

Figure 3.1-26. Location of Punctured Rods in Point Beach Assembly D-14.

Indicated Powers and Burnups are Those at Peak Power Locations (64% of the Fuel Stack Height), Just Prior to the Coolant Activity Increase (70% of Reactor Full Power).

Table 3.1-9

REPRESENTATIVENESS OF RODS SELECTED FOR PUNCTURE
IN POINT BEACH UNIT 1 FUEL ASSEMBLY D-14

Item	Number of Rod Groups in Assembly	Number of Rod Groups Examined
Cladding Lots (with more than 4 rods/lot)	7	7
Fuel Groups (with more than 4 rods/group)	13	11
Burnup Groups	5	5
Power Groups	4	4
Power Increase Groups	6	6

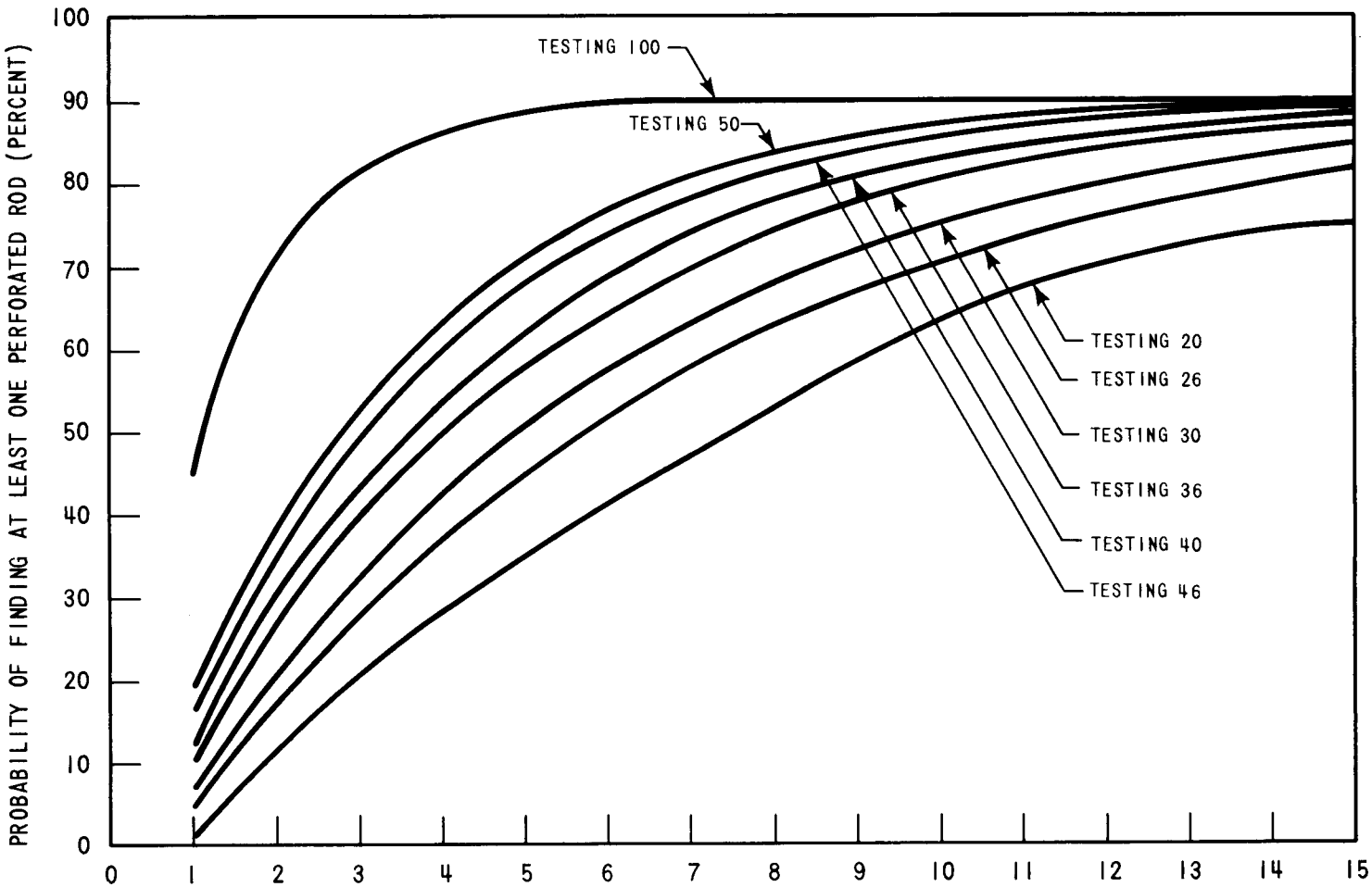

Figure 3.1-27 Probability of Finding at Least One Perforated Rod for an Assumed Number of Perforated Rods in the Assembly as a Function of the Number of Sampled Rods

Table 3.1-10

PROBABILITY OF PERFORATED RODS REMAINING IN A GIVEN SUBGROUP OF FUEL RODS IN ASSEMBLY D-14

Rod Subgroup Parameter	Parametric Range	Fuel Rods In Assembly	Fuel Rods Punctured	Fraction Punctured	Probability of Three Perforated Rods Still In This Group
Beginning of Cycle 3 B.U., GWD/MTU	2-3	7	3	0.43	0.11
	3-5	34	12	0.35	0.26
	5-7	46	10	0.22	0.47
	7-9	50	12	0.24	0.43
	9-11	42	9	0.21	0.48
Beginning of Cycle 3 Power, kW/ft	5.6-6.0	4	2	0.5	0.0
	6.0-6.4	17	6	0.35	0.24
	6.4-6.8	83	15	0.18	0.54
	6.8-7.2	82	23	0.28	0.36
Ratio of Average Power Increase, BOC-3/EOC-2	4.6-3.8	4	2	0.5	0.0
	3.8-3.0	10	6	0.6	0.03
	3.0-2.4	21	3	0.14	0.61
	2.4-2.0	24	10	0.41	0.18
	2.0-1.4	74	16	0.21	0.48
	1.4-1.0	46	9	0.19	0.51

(Continued on p 3-61)

Table 3.1-10 (Continued)

Rod Subgroup Parameter	Parametric Range	Fuel Rods In Assembly	Fuel Rods Punctured	Fraction Punctured	Probability Three Perforated Rods Still In This Group
Pellet Group	Gr. 19	18	3	0.16	0.56
	Gr. 8	15	5	0.33	0.26
	Gr. 15	15	2	0.13	0.62
	Gr. 12	14	4	0.28	0.33
	Gr. 13	13	2	0.15	0.58
	Gr. 22	13	2	0.15	0.58
	Gr. 20	12	2	0.16	0.55
	Gr. 30	9	0	0.0	--
	Gr. 42	9	2	0.22	0.42
	Gr. 14	8	3	0.37	0.18
	Gr. 17	6	3	0.50	0.05
	Gr. 31	5	2	0.40	0.1
	Gr. 34	5	0	0.0	--
	Others (less than 4/Gr.)	37	16	0.43	--
Cladding Lot	5DJ 1948	39	8	0.20	0.49
	5AX 6460	26	3	0.11	0.68
	5DR 1946	25	10	0.40	0.19
	5AZ 1773	21	4	0.19	0.51
	5EE 1946	18	3	0.16	0.56
	5BG 1816	13	2	0.15	0.58
	5BG 1802	6	3	0.5	0.50
	Others (less than 4/lot)	31	13	0.41	--

is to be noted that for the power history subgroups, very little distinction between the subgroups exists. For example, fuel rods identified as those which experienced the largest power increase during the reactor startup were the same rods as those identified in the lowest burnup category. Nonetheless, despite some overlap, it was considered that examination of the data in this manner might prove useful.

The purpose of breaking down the data as given in Table 3.1-10 was to determine if any identifiable trends of failure probability were evident for a particular subgroup of fuel rods. If no trends were evident, then the data can be reasonably assumed to be of one population and pooled. That is, failure probability can be regarded as random and independent of the subgroup attribute. The final column of the Table 3.1-10 provides the calculated probability for failure in a particular subgroup assuming a given number of failed rods exist;* three rods were assumed to be failed in each subgroup for this purpose. As an example, for the seven fuel rods constituting the burnup subgroup for the exposure range 2000-3000 MWD/MTU (at the time of failure), the probability of three failed rods existing and remaining undetected in the untested portion of the subgroup is only 0.11 (i.e., 11 percent).

Examination of the final column of Table 3.1-10 indicates that with the possible exception of burnup, no clear trend of failure probability with power history exists. For the low burnup subgroup (2000-3000 MWD/MTU), in which all four rods of the high power swing group (3.8-4.6 ratio for BOC-3:EOC-2 power level) also belong, it can be concluded that the probability of three rods remaining in the assembly undetected is essentially zero. Also for the pellet group and cladding lot subgroup of rods, no clear trends of failure probability are evident. Thus, while it is possible that several failed rods could exist in the assembly in essentially one subgroup of fuel rods, Table 3.1-10 suggests that this is not very probable. Therefore, if several failed rods are indeed present in the assembly, it is probable that their distribution is essentially random. It is concluded that with 90 percent probability, no more than eight failed fuel rods are present in the assembly and that their distribution throughout the assembly is essentially

---

* The calculations were performed utilizing standard binomial distributions modified for a finite population.

random. With 50 percent probability, the potential number of failures becomes no more than four rods. While it is not possible to correlate well the number of failed fuel rods in the core with coolant activity, this reduced number of failed fuel rods in the assembly is less than that initially supposed.

3.2 DRESDEN-3 FUEL ROD STUDIES

3.2.1 Introduction

To study the effects of fuel pellet-cladding interaction (PCI) on BWR fuel, fuel rods were selected which had been in the core of the Dresden Nuclear Power Station, Unit 3, during the first three cycles of that reactor. This fuel population was believed to be appropriate for the study of the effects of PCI in commercial BWR fuel because during Cycle 3 on October 31, 1974, some control blade adjustments were made which resulted in an inadvertent transient power increase. Immediately after those control blade movements the offgas activity at the steamjet ejector increased, indicating that fuel rod failures had indeed occurred. The reactor continued to be operated at a somewhat reduced power until the end of Cycle 3 operations (April 16, 1975). During the subsequent refueling outage "leaker bundles" were identified and were discharged from the core.

This fuel population, i.e., fuel rods in the "leaker bundles", was thought appro-iate for the present study because:

(a) This fuel had a power history and a power increase conducive to the PCI phenomenon, and

(b) Within the leaker bundles some rods had failed, but probably there were other rods which had not failed and which might contain incipient defects which extend only partially through the cladding wall and which were caused by the PCI event.

It is the objective of this project to identify such incipient PCI-induced defects with the ultimate objective of elucidating the rate-controlling fracture mechanisms.

In November, 1976, 14 of the leaker bundles which had been discharged at the end of Cycle 3 were disassembled and examined in the Dresden-3 fuel pool. The examination was by nondestructive techniques. Based on the examinations at the reactor fuel pool, 10 fuel rods were selected for further study. These 10 rods were shipped to the BCL hot-cell facility for more detailed study by both nondestructive

and destructive means. Ultimately, specimens were selected for detailed microscopic studies which were done at the GE Vallecitos Nuclear Center (GE-VNC) and at the Argonne National Laboratory (ANL).

In this Section the fuel rod selection and examinations will be described with emphasis on the microscopic studies which were done at GE-VNC and at ANL. Details of the fuel rod selection process have been previously reported (2) as have those of the hot-cell examinations which were done at BCL (4).

3.2.2 Rod Selection

In each of the bundles examined, the maximum power excess over the previous power profile established in cycle 3 (ΔP) occurred within roughly 0.8 m (2.5 ft) from the bottom of the active fuel length. Thus, it is in this lower region of the fuel rods where the maximum PCI effect was expected.

In the 14 fuel bundles which were examined at the Dresden-3 site, each rod was examined by:

1. Visual inspection by use of an underwater periscope.
2. Ultrasonic inspection seeking evidence of water in the fuel rod.
3. Encircling coil eddy current seeking cracks in the cladding wall.

Based on these examinations, 10 rods were selected for further study at BCL, GE, and ANL. The selection was intended to obtain unfailed rods with a high probability of containing one or more incipient defects. Thus, the selected rods had: (a) no evidence of liquid phase water within them as seen by the ultrasonic inspection, (b) eddy current indications in the bottom 0.8 m of the active fuel length, (c) no external cause (as seen by visual examination) for the eddy current indications, and (d) a power history conducive to PCI. To satisfy criterion (d) fuel rods which were located within their bundle in positions known to have a high failure probability were chosen. For example, if a rod had failed in the same bundle and in a symmetric rod location, we have reason to judge the PCI effect to have been strong. Power histories of the selected rods have been reported previously (2).

To guard against the possibility that the eddy current indications might be insensitive to PCI incipient cracks which are too small to measurably affect the

electromagnetic field, one rod was selected which was apparently not only unfailed, but which also contained no eddy current indications. That was KD-0451 (location A1-Assembly DD-0021) which was from a location within its bundle with a high probability of failure. Thus, 9 of the 10 candidate rods selected for further study had eddy current indications in the high ΔP region of the rods, as expected for PCI-induced defects. A summary of power history information for the 10 candidate fuel rods is given in Table 3.2-1.

3.2.3 Examinations of Candidate Fuel Rods

The 10 candidate fuel rods (Table 3.2-1) were shipped to the BCL Hot Laboratory for detailed examinations. Those examinations and their results have been reported by Pasupathi, et al, (4). Only a very brief summary will be given here.

At the BCL Hot Laboratory the 10 candidate rods were examined by the following methods: (a) visual/macrophotographic, (b) profilometry, (c) gamma scans (axial distributions of gross gamma activity and of the isotope Cs-137), and (d) eddy current (both by the encircling coil method and by a two frequency probe technique).

All the data available were evaluated in detail to obtain a basis for selecting samples for destructive evaluation.

The gross gamma scan data from the Dresden fuel rods showed no major anomalies. The gamma activity profile was similar to the calculated burnup profile suggesting that the actual power history of the rods was not much different from the calculated power history. There was no significant change in the fuel stack length.

The Cs-137 gamma scans showed some Cs activity peaks but did not suggest significant redistribution of fission products. The data on rods containing dished fuel pellets clearly showed depressions in Cs-137 activity at pellet interfaces and fuel stack gaps. The data again did not indicate any specific locations in the fuel rods which might contain incipient defects.

The profilometry data showed that most of the rods contained localized areas of diameter increases. The diameter traces in general were "noisy" with sharp local changes in average diameter and ovality probably due to the hard adherent layer of oxide or crud on the fuel rod surface. The presence and the magnitude of clad ridging was not obvious because of the irregular diameter trace. In addition, the

Table 3.2-1

SUMMARY OF INITIAL NDE DATA AND POWER HISTORIES(2)

Bundle	Rod	Rod Identification No.	Location of Transient P_{max};[a] Distance from Bottom of Fuel Column	Relevant E/C Indications	Local Maximum p[a] at Node[b] K = 2						P_{max}		Local Power Transient at Node K = 2				Local Burnup Node K = 2 (MWd/t-U)[d]		Peak Burnup (MWd/t-U	
					Cycle 1		Cycle 2		Cycle 3[c]				ΔP of Event		ΔP[a] Over Previous Maximum		At Event	EOC3	At Event	EOC3
					kW/m	(kW/ft)	kW/m	(kW/ft)	kW/m	(kW/ft)	kW/m	(kW/ft)	kW/m	(kW/ft)	kW/m	(kW/ft)				
DD0021	A1	KD-0451	15-30 cm	No	11.15	(3.40)	13.12	(4.00)	22.77	(6.94)	41.6	(12.68)	35.4	(10.79)	18.13	(5.74)	5,136	5,638	16,147	18,288
DD0191	C7	KJ-0723	15-30 cm	Yes	10.37	(3.16)	21.75	(6.63)	30.71	(9.36)	43.31	(13.20)	16.21	(4.94)	12.60	(3.84)	7,548	9,262	15,563	17,071
	G1	KC-4411	15-30 cm	Yes	10.10	(3.08)	21.95	(6.69)	30.94	(9.43)	44.16	(13.46)	16.93	(5.16)	13.22	(4.03)	7,121	8,799	15,925	17,920
DD0693	C7	KL-0633	15-30 cm	Yes	9.81	(2.99)	16.50	(5.03)	31.56	(9.62)	41.86	(12.76)	10.30	(3.14)	10.30	(3.14)	6,986	8,484	11,674	13,258
DD0706	G1	KG-2119	15-30 cm	Yes	10.14	(3.09)	18.50	(5.64)	29.50	(8.99)	43.41	(13.23)	13.91	(4.24)	13.91	(4.24)	6,841	8,162	12,012	13,314
	G6	KE-2225	15-30 cm	Yes	11.94	(3.64)	18.47	(5.63)	29.72	(9.06)	42.95	(13.09)	13.22	(4.03)	13.22	(4.03)	7,626	9,012	12,770	14,040
DD0710	A7	KG-0113	15-30 cm	Yes	14.24	(4.34)	14.34	(4.37)	25.26	(7.70)	43.57	(13.28)	26.28	(8.01)	18.31	(5.58)	6,257	7,625	15,214	16,990
	D2	KB-5249	15-30 cm	Yes	16.54	(5.04)	13.22	(4.03)	23.52	(7.17)	40.29	(12.28)	25.56	(7.79)	16.77	(5.11)	6,699	7,629	15,190	16,503
	E2	KB-5239	15-30 cm	Yes	15.85	(4.83)	13.10	(3.99)	23.33	(7.11)	39.93	(12.17)	24.15	(7.36)	16.60	(5.06)	6,759	7,745	14,954	16,168
	G6	KE-3038	15-30 cm	Yes	16.11	(4.91)	18.67	(5.69)	25.32	(7.72)	43.08	(13.13)	17.88	(5.45)	17.75	(5.41)	8,612	10,132	16,971	17,789

[a] p = Power (linear heat generation rate).

[b] Node K = 2 is centered at 22.9 cm (9 inches) from bottom of fuel column.

[c] Prior to event.

[d] MWd/t-U = megawatt-days/short ton of uranium.

length of pellets without dishing varied significantly, therefore making it difficult to clearly identify clad ridging at pellet interfaces. However, clad ridging could be discerned in the rods containing dished pellets. The extent of clad creepdown in most of the fuel rods was small but appeared to vary significantly. Again, no specific choice of samples for further studies could be made on the basis of the profilometry data alone.

The eddy current tests (both probe coil and encircling coil systems) indicated the presence of possible internal fuel rod defects in all but one of the candidate fuel rods. The larger defect indications, however, were much stronger in comparison to the indications seen in the Point Beach fuel rods. In fact, most of the Dresden fuel rods appeared to contain defect indications suggesting clad perforations. Figure 3.2-1 shows an example of probe coil indications observed in rod KB-5249. The eddy current test results used in conjunction with both the gamma scan and profilometry results became the primary basis for sample selection for destructive studies.

The profilometry and gamma scan data at the locations of eddy current indications were examined in detail. It was found that contrary to the Point Beach-1 rod data (Section 3.1) very few of the eddy current indications are associated with gaps in the fuel stacks. However, at or near the location of most of the indications fuel rod diameter increases to various extents were observed. This also indicated that the source of the eddy current indications could be incipient defects related to the PCI phenomenon. In addition, the majority of the indications were located in the bottom end of the fuel rod which had experienced high power levels during the transient power increase. Through-wall defects were observed on a number of fuel rods near the bottom end during the fuel inspection carried out in the Dresden spent fuel pool (2).

Based on the results of these nondestructive examinations, five rods were selected for puncture and fission gas analysis. These were the five with the smallest eddy current signals, including rod KD-0451, which had none. The results of the fission gas analyses are shown in Table 3.2-2. From these data rod KD-0451 was judged to be definitely unfailed and rod KE-2225 to be probably unfailed. Two metallographic samples were taken from a failed rod (KB-5249). The metallographic examination of the samples showed that a strong eddy current indication was associated with a through-wall crack which was filled with corrosion products and a weak indication

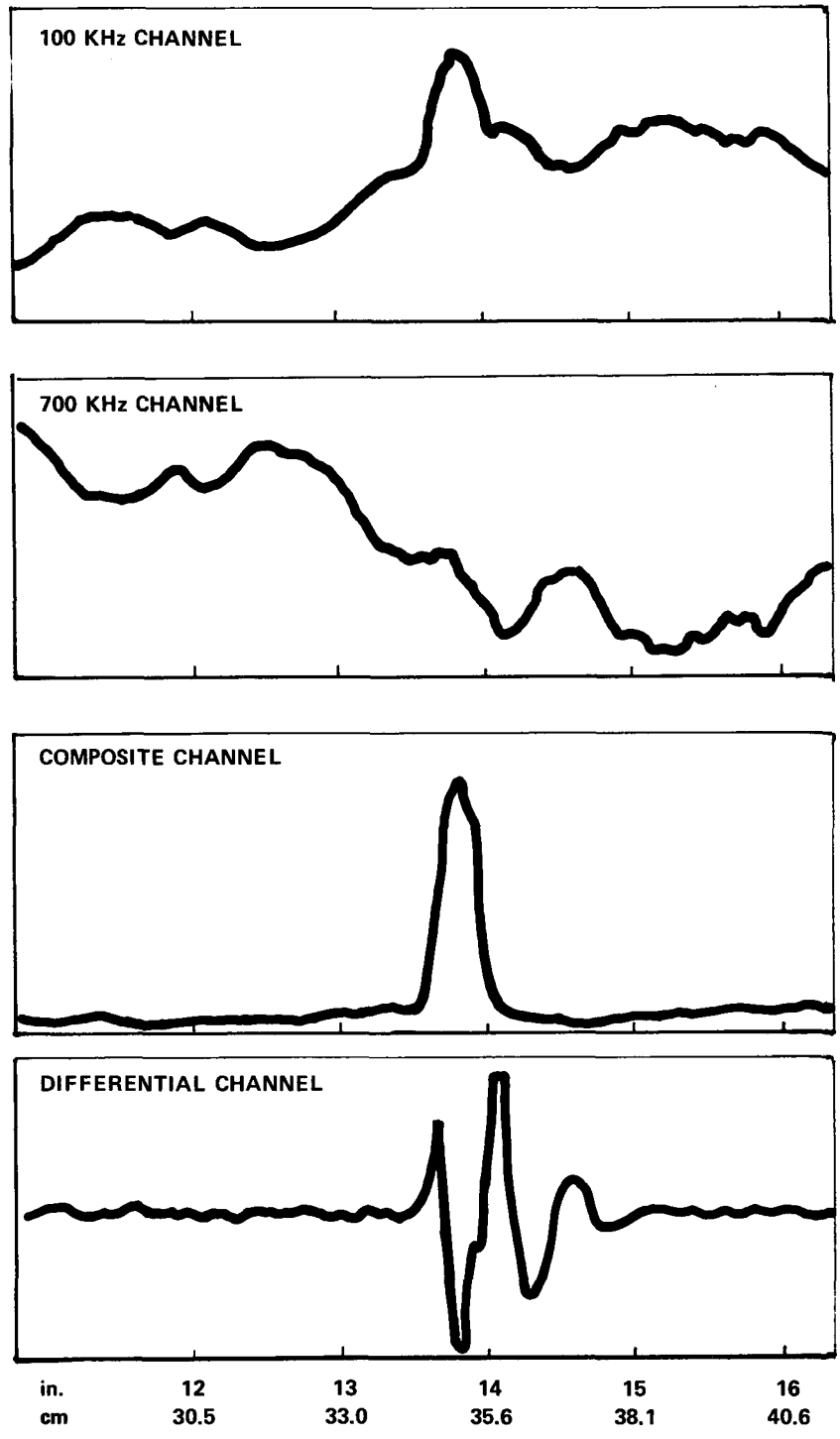

Figure 3.2-1 Probe Coil Eddy Current Chart Showing a Defect Indication on Dresden-3 Rod KB-5249 at ~ 35 cm

Table 3.2-2

FISSION GAS AND VOID VOLUME IN DRESDEN UNIT 3 FUEL RODS

Rod No.	Rod Avg. Burnup MWD/MTU	Rod Void Vol. cc	Total Gas Collected from Rod STP cc	Gas Composition Vol. Percent								Vol. of (Xe + Kr) Released STP cc	Vol. of (Xe + Kr) Generated* STP cc	Percent Fission Gas Released
				H_2	H_2O	He	H_2	O_2	A	Kr	Xe			
Kd 0451	14382	64.93	252.96	<0.01	<0.1	17.15	0.13	<0.01	<.01	8.65	73.9	208.81	1771 cc	11.8
KB 5249	11920	64.93	51.90	60.35	3.41	11.34	12.39	<.01	<01	1.36	9.88	5.83	1468	NA-Rod Failed
KB 5239	11920	67.24	132.86	10.86	<0.1	54.05	<.01	<.01	<.01	4.32	31.02	46.96	1468	NA-Rod Failed
KE 2225	11381	72.25	89.63	0.23	<0.1	87.98	<.01	<.01	<.01	1.43	10.6	10.78	1364	0.79
KG 0113	14435	Water vapor observed in the collection system - failed rod - gas not analyzed												

[a]Based on the generation of 0.30 atoms of (Xe + Kr) per fission and 4000 MWD/MTU = 1 x 10^{20} fiss/cc.

with some hydriding and a cluster of cracks in the hydrided region. Figure 3.2-2 shows the appearance of the through-wall crack at the location of the strong eddy current indications.

A detailed examination of the crack characteristics shows the following:

- The absence of any significant diameter change at this location suggests that the crack was caused by a PCI-induced stress corrosion cracking mechanism.
- The presence of corrosion products in the crack and an absence of high concentration of hydride suggests the crack to be a primary defect and not related to secondary hydriding observed in failed fuel rods.
- The presence of corrosion products in the crack suggests the rod to have sealed itself and explains the ability of the rod to sustain a vacuum and overpressure during fission gas collection and void volume measurements. This also explains why the poolside ultrasonic inspection system showed these rods to be unfailed. This system requires liquid phase water in the failed rods for an unambiguous detection of failed fuel rods.

On the basis of the examinations carried out on the sample, the axial length of the crack is estimated to be 13 mm (~ 0.5 inch).

3.2.4 Selection of Specimens for Microscopic Study

Three rods were selected for further study:

- DD-0710, A7 (KG-0113)--failed
- DD-0706, G6 (KE-2225)--probably unfailed
- DD-0021, A1 (KD-0451)--unfailed.

Power history information is shown for these rods in Figures 3.2-3--3.2-5, respectively. Rod KG-0113 was known to have failed, and this was used in this study solely to compare the eddy current methods used by BCL and by ANL. Rod KE-2225 was used extensively for the microscopic studies and was shared between ANL and GE-VNC. The distribution of specimens between ANL and GE-VNC is shown in the cutting diagrams, Figure 3.2-6. Rod KD-0451 was examined only at GE-VNC.

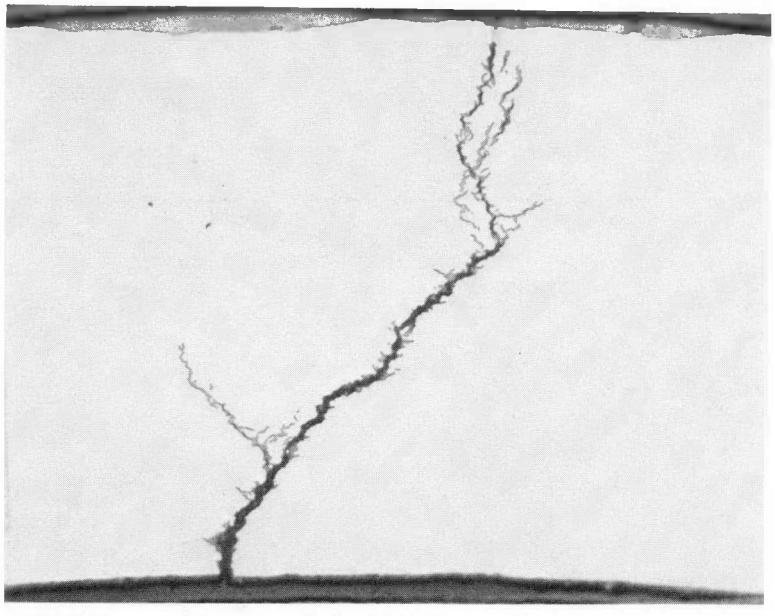

HC45610 (a) 270° 100X

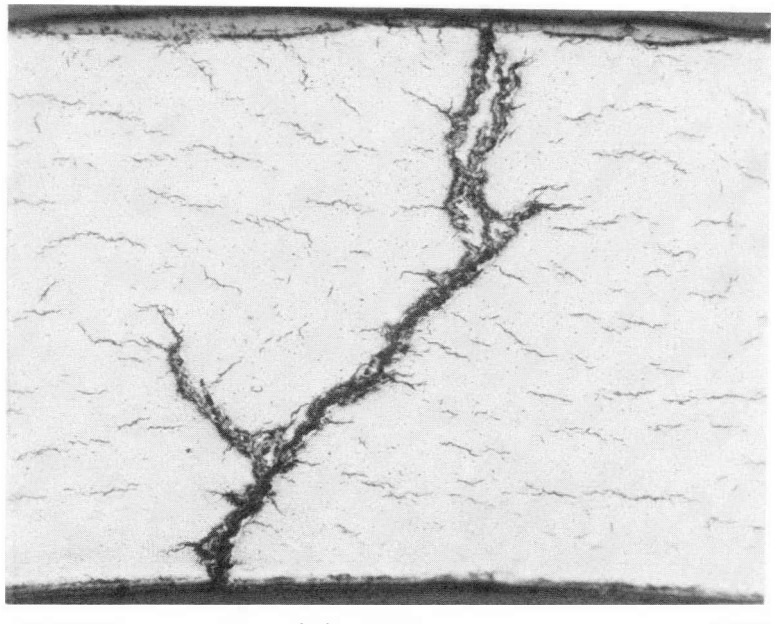

HC45611 (b) 270° 100X

Figure 3.2-2 Appearance of the Through-Wall Crack in the Specimen from Rod KB-5249 Near the Center of the Eddy Current Signal at 35.7 cm (14 in.) from Rod Bottom

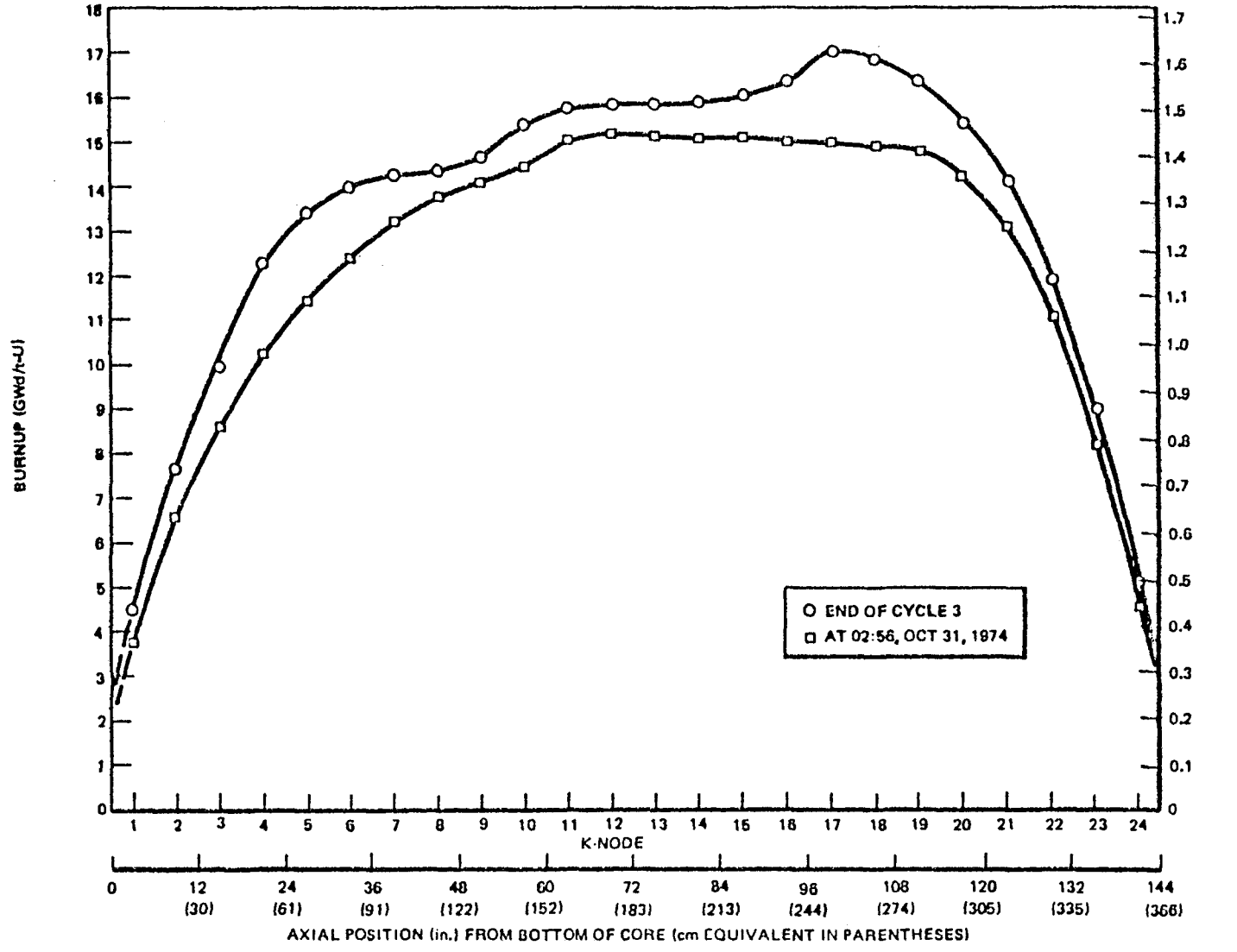

Figure 3.2-3a Axial Burnup Profile of Rod KG-0113 (DD-0710, A7)

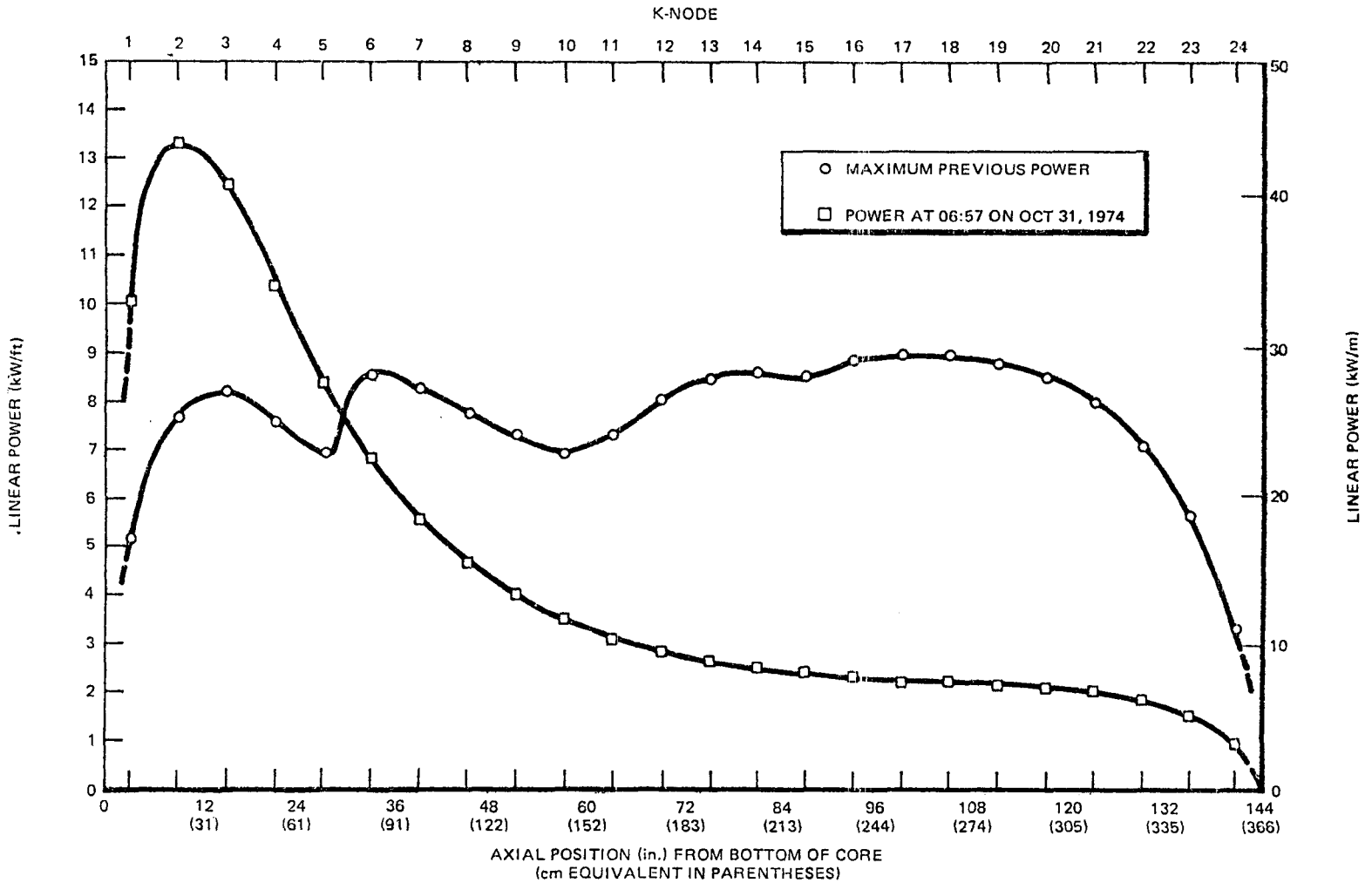

Figure 3.2-3b Axial Distribution of Transient Power and Maximum Previous Power for Rod KG-0113 (DD-0710, A7)

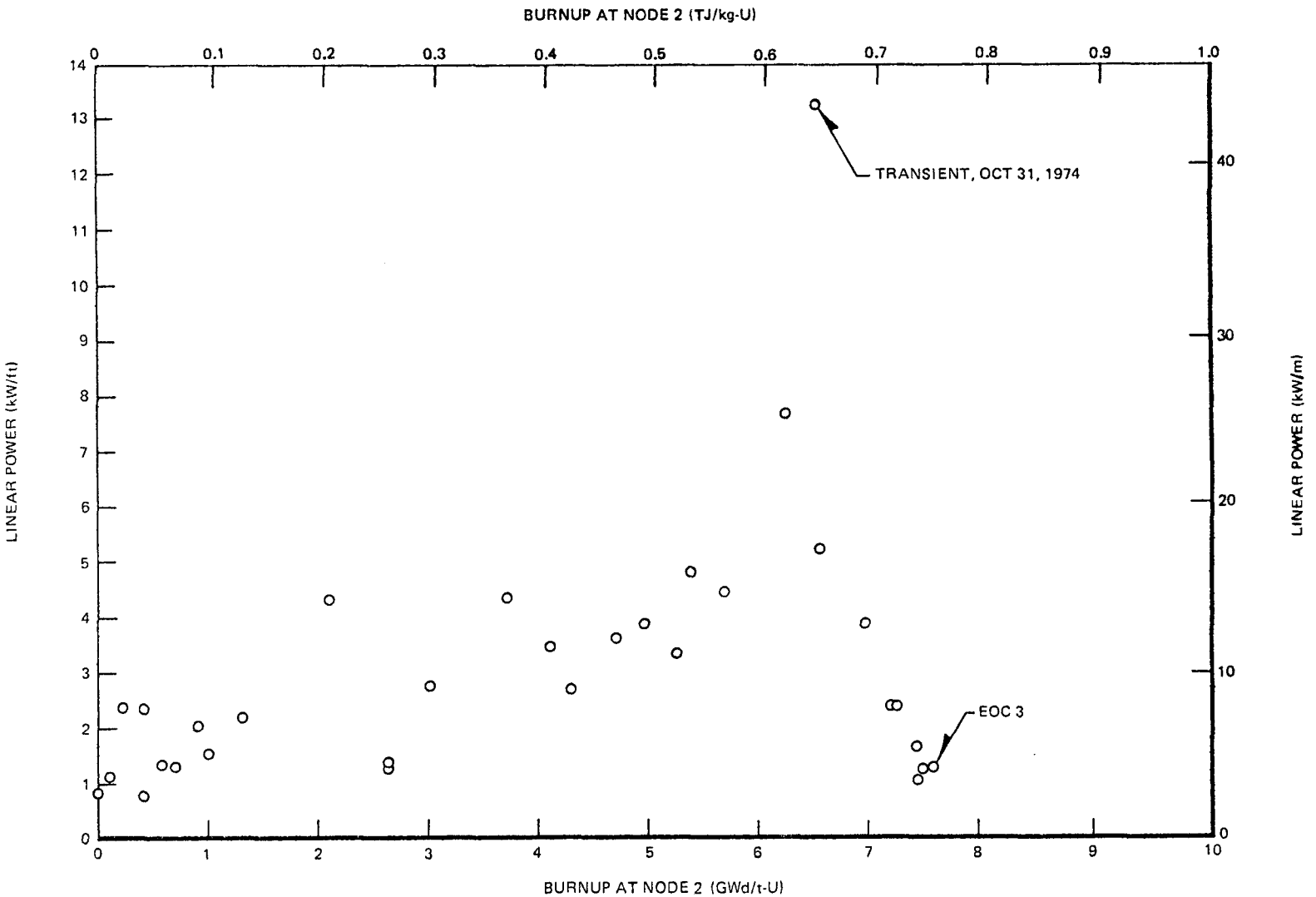

Figure 3.2-3c Power History at Node 2 for Rod KG-0113 (DD-0710, A7)

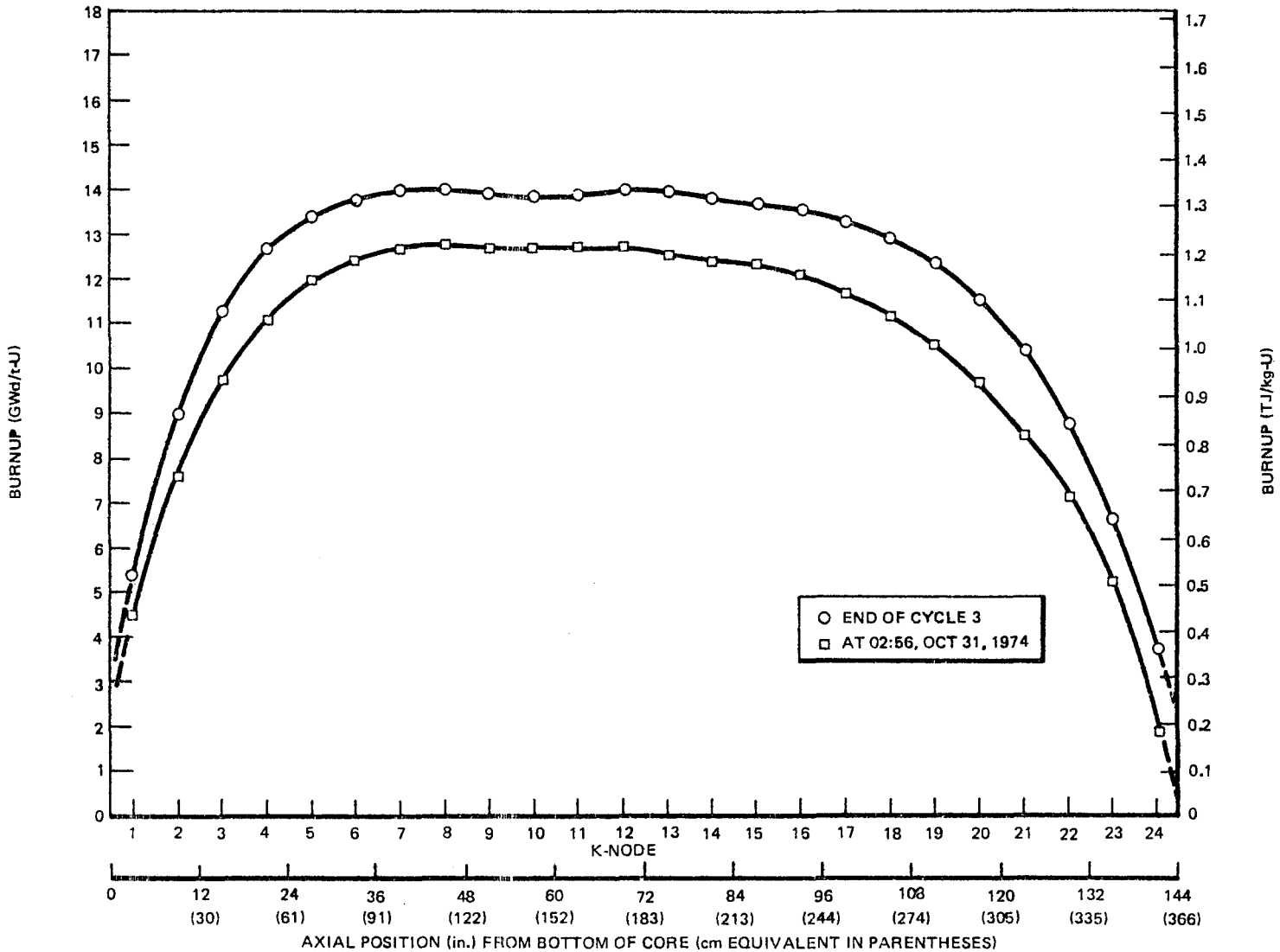

Figure 3.2-4a Axial Burnup Profile of Rod KE-2225 (DD-0706, G6)

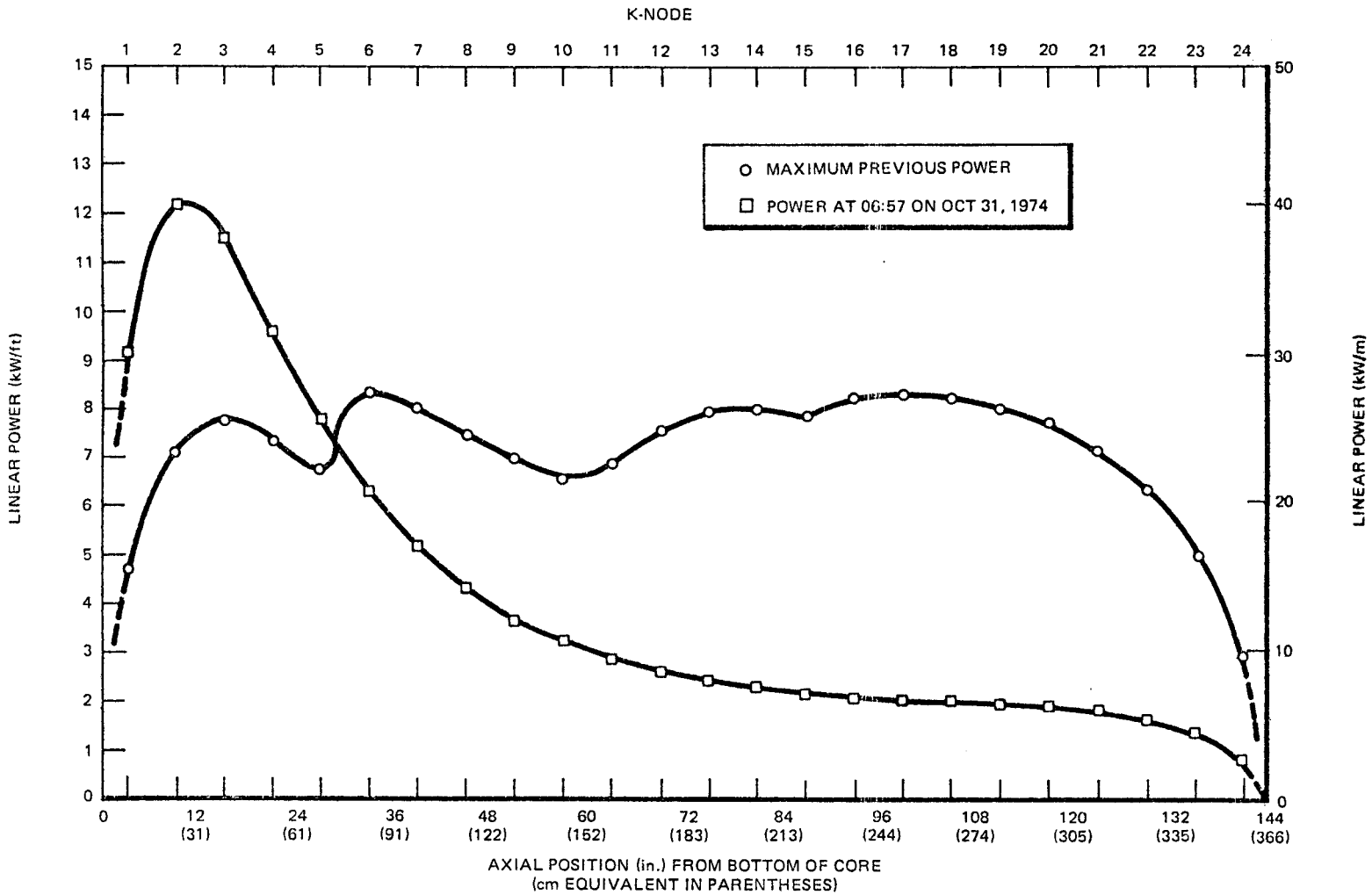

Figure 3.2-4b Axial Distribution of Transient Power and Maximum Previous Power for Rod KE-2225 (DD-0706, G6)

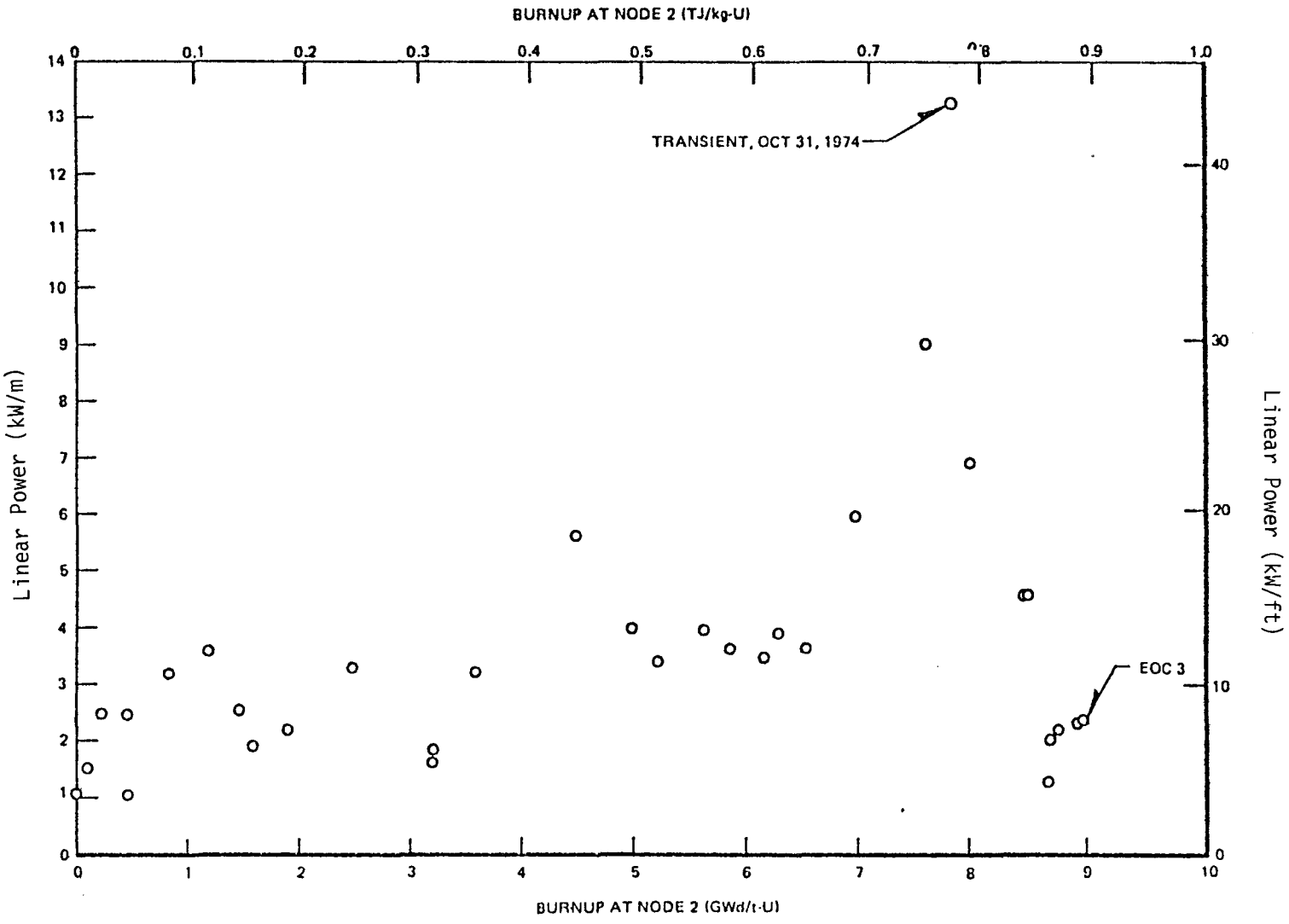

Figure 3.2-4c Power History at Node 2 for Rod KE-2225 (DD-0706, G6)

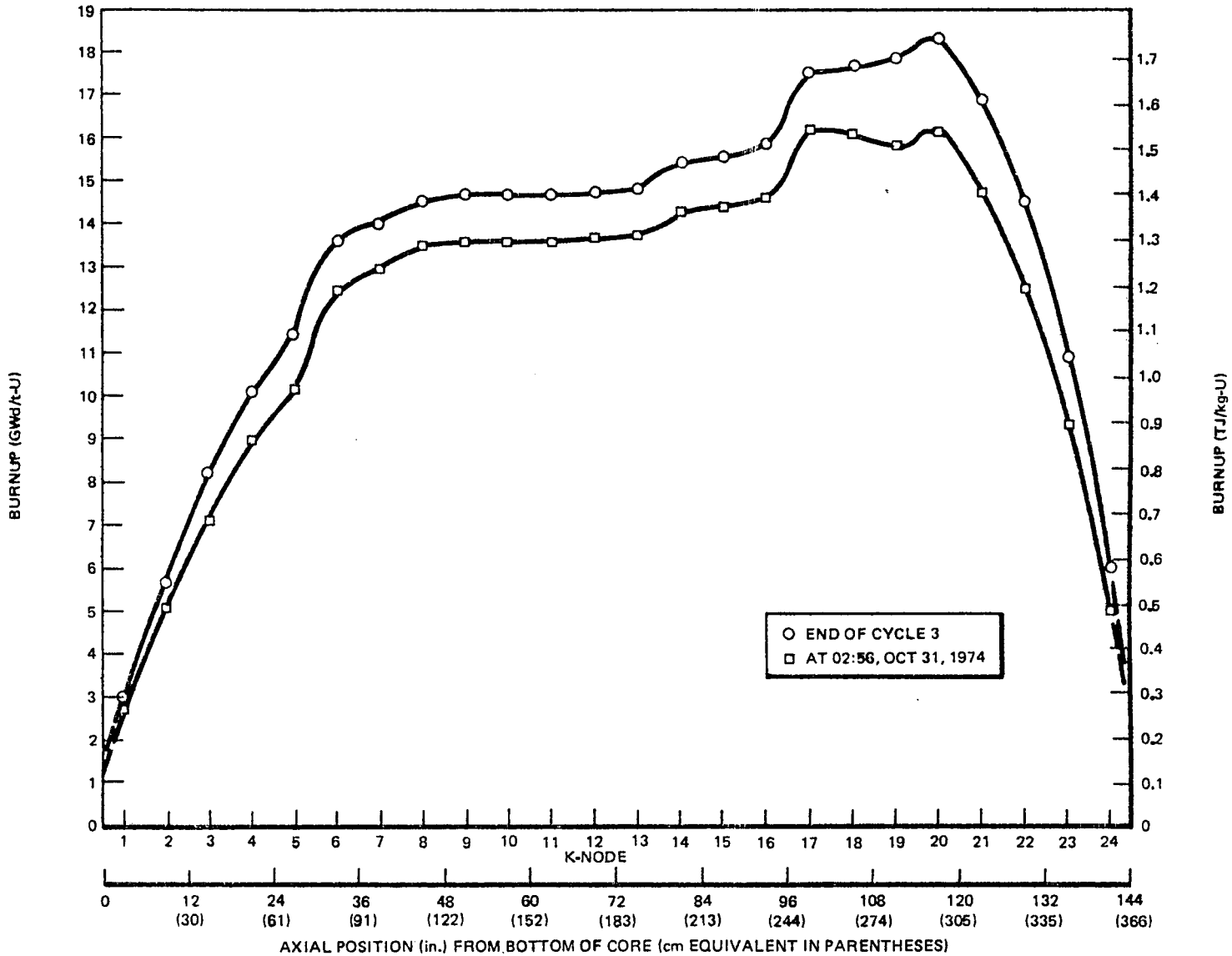

Figure 3.2-5a Axial Burnup Profile of Rod KD-0451 (DD-0021, A1)

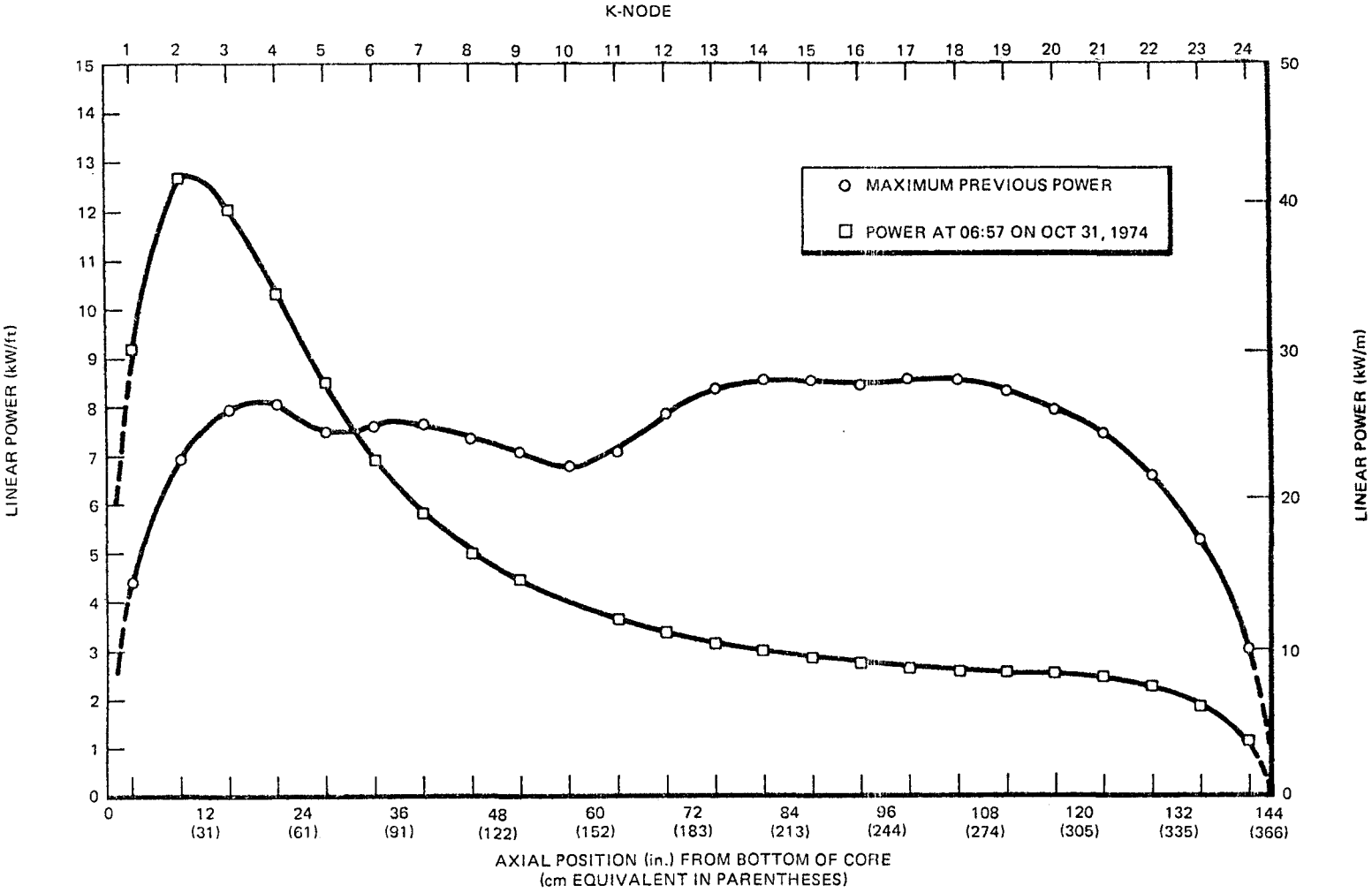

Figure 3.2-5b Axial Distribution of Transient Power and Maximum Previous Power for Rod KD-0451 (DD-0021, A1)

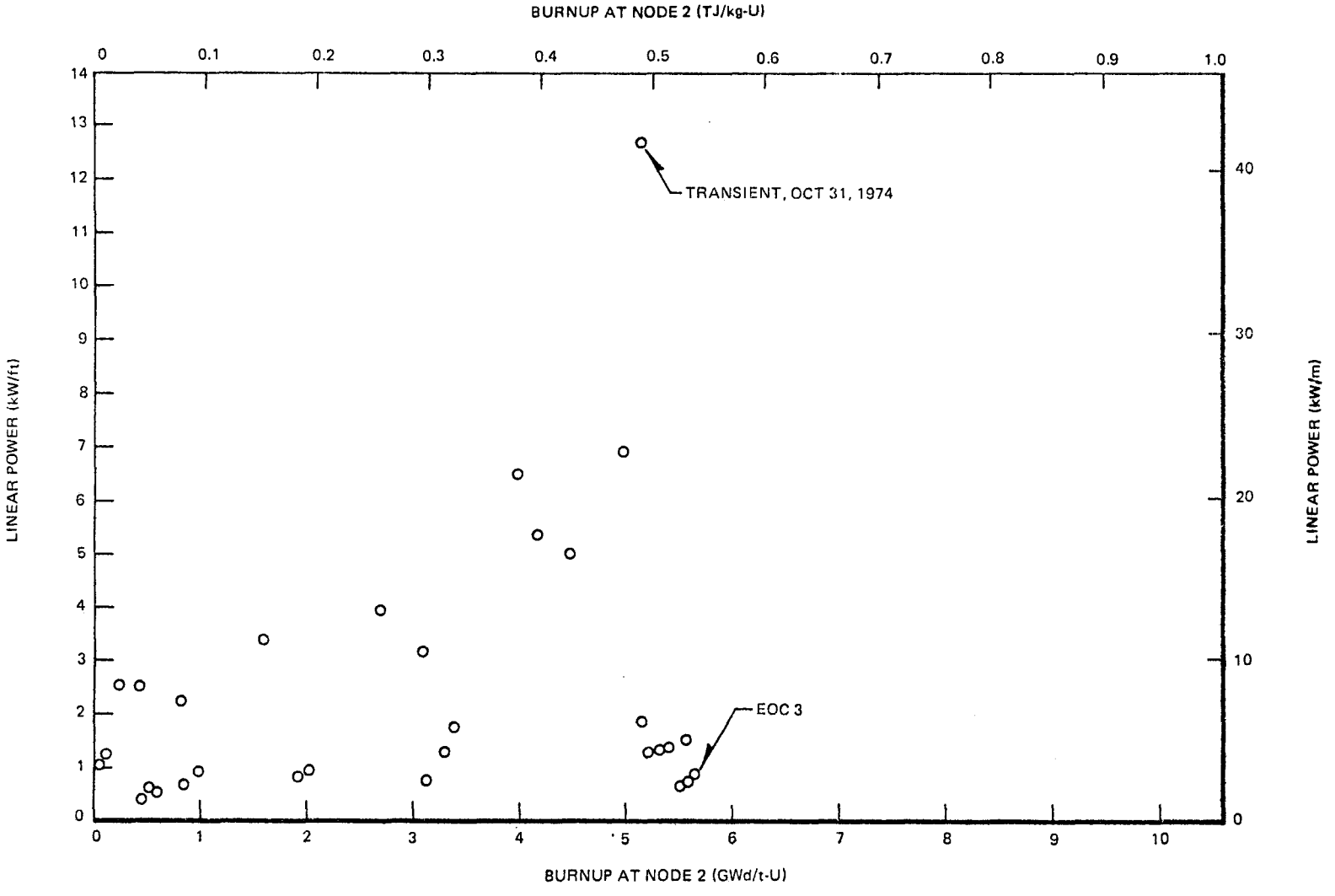

Figure 3.2-5c Power History at Node 2 of Rod KD-0451 (DD-0021, A1)

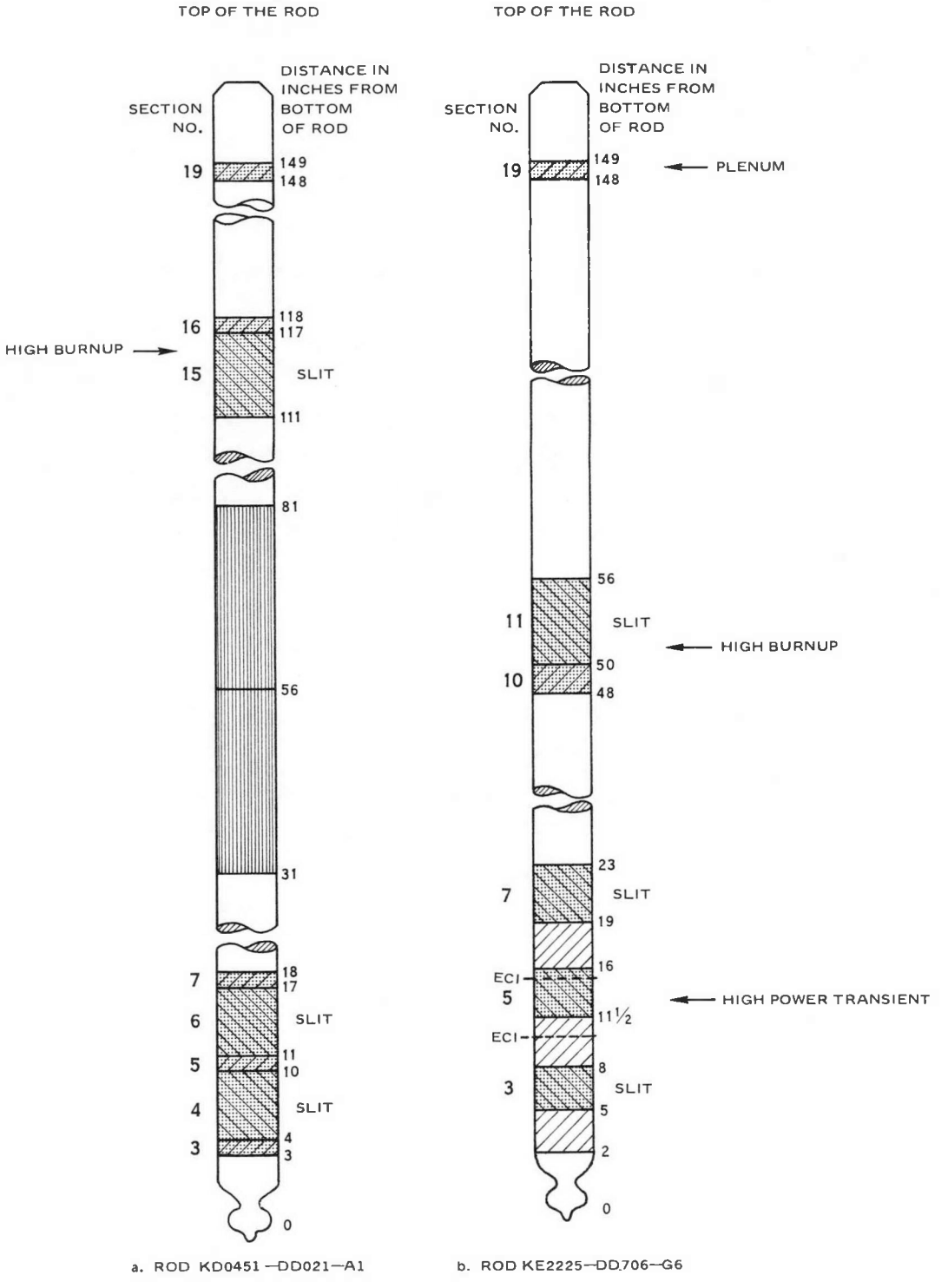

Figure 3.2-6. Cutting Diagrams

3.2.5 Eddy Current Inspection (ANL)

The section of rod KG 0113 tested on the ANL pulsed eddy current system came from an elevation between 25.4 cm (10 inches) and 88.9 cm (35 inches) from the bottom of the rod.* This region had produced several eddy current indications, ranging from weak to very strong, on the BCL probe eddy current system. To directly compare the results of the two systems, the ANL eddy current measurements were made with the fuel still contained in the cladding.

The ANL pulsed eddy current system produces a train of current pulses, at a rate of 1 kHz, that flow into a field coil which induces currents in the cladding (15). The total pulsed magnetic field produced by all currents flowing in the coil and the specimen produces a train of voltage pulses at a pickup coil in a "point" probe adjacent to the cladding. The point probe interrogates approximately 15 degrees of arc on the cladding circumference. The voltage pulses are then filtered, amplified, and recorded for analysis. Any defect which alters the electrical or magnetic characteristics of the cladding will alter the induced voltage wave form. The voltage, which is recorded, can be taken from any point on the wave form. This ability to sample the voltages of the wave form allows the operator to tune the instrument for the maximum sensitivity of a particular defect. In actual practice, two sampling points are chosen for maximum sensitivity to defects at the outer and inner surfaces of the cladding. For this examination, the sampling points on the inner and the outer surfaces were set by testing a section of sound, unirradiated Zircaloy tubing (15). The voltage transducer used on the ANL system is specifically designed to detect tubing defects that are predominantly longitudinal in character. Large circumferential defects that cover more than 15 degrees of the circumference will be detected with reduced sensitivity with respect to the same defect oriented in the longitudinal direction. The normal scanning rate is 6.0 cm/s.

The section of rod KG-0113 was scanned every 15 degrees around the circumference maintaining the same orientation used at BCL. The bottom 52.7 cm (20.75 inches) of the section was scanned, the remaining 10.8 cm being held in the chuck of the device. A comparison of weak and strong eddy current signals recorded at ANL is

---

* Note that the axial scale used in Figures 3.2.3-3.2-5 were measured from the bottom of the fuel column and not from the bottom of the rod. The measurements quoted in the present context and those used henceforth include the bottom end plug which extends 1.25 inches (3.18 cm) beyond the bottom of the fuel column.

shown in Figure 3.2-7, and a summary of the eddy current indications produced by this piece of cladding is presented in Table 3.2-3. Most of the signals were observed in the range from 48.3 to 60.9 cm from the bottom of the rod. Four strong signals were observed in this area, two of which occurred over a range of angular orientation. A number of weak signals were also identified, although some were marginal. In Table 3.2-3 also shown are the eddy current results obtained at BCL for a direct comparison of the two techniques. Whereas the ANL technique is that of a pulsed eddy current with a probe-type coil, the BCL system is not pulsed; it uses a two-frequency method.

3.2.6 Metallurgical, Fractographic, and Chemical Studies--(GE-VNC)

Figure 3.2-6 shows the cutting diagrams for the two rods. General Electric-VNC received eight sections of rod KD-0451 and six sections of rod KE-2225. The numbers to the right of the drawings give the distance in inches from the bottom of the rod. The numbers to the left are the identification numbers assigned at GE-VNC. All sections received by GE had been defueled prior to shipment and some had been slit longitudinally in half, as indicated in the diagrams.

3.2.6.1 Macroexamination of Clad Surfaces. All accessible surfaces of the as-received sections were examined in the hot cell with a periscope at a magnification of ~ 4X.

Rod KD-0451

The outside cladding surfaces of the ring sections, Nos. 3, 5, and 7, looked quite clean and had numerous straight axial scratches or grooves (Figure 3.2-8a) which apparently were shallow. They might have been produced during withdrawal of the fuel rods. The outside surface of the slit section, No.15, had only a few shallow grooves. The outside surfaces of the ring sections, Nos. 16 and 19 were black and had no visible grooves. The inside of the slit cladding section, No. 4, is shown in Figure 3.3-8b. Part of the surface is shiny with some markings indicating the location of a fuel pellet-to-pellet interface and of fuel cracks. The other half of the surface is dark, consisting of a rather thick layer (probably an oxide) which possibly constitutes the fuel-cladding interaction layer, and which is partially spalled (see arrow). To this layer numerous fuel particles are bonded. The location of fuel cracks and pellet-pellet interfaces are visible. The inner surfaces of the slit sections, No. 6 (Figure 3.2-8c) and No. 15, are

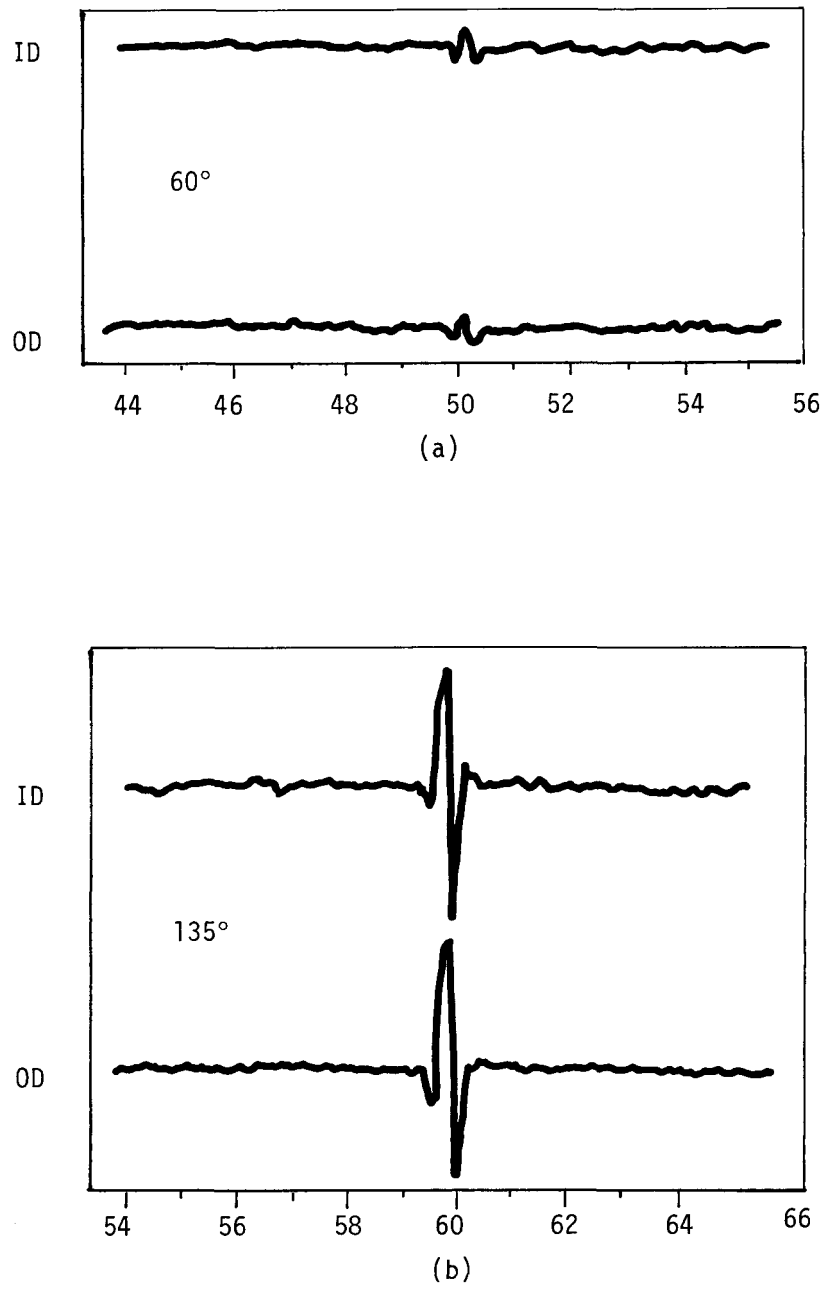

Figure 3.2-7. Comparison of (a) Weak and (b) Strong Eddy Current Indications--ANL

Table 3.2-3

EDDY CURRENT DATA SUMMARY FROM ROD KG-0113

BCL Probe Eddy Current			ANL Pulsed Eddy Current		
Axial Location (cm)	Strength	Orientation	Axial Location (cm)	Strength	Orientation
33.02	W	45-225°			
38.1	W	135°			
39.62	W	225°			
			41.9	W	285-315°
48.26	VW	45°			
	VS	90-135°	48.3	S	90-120°
			49.3	M	165-180°
			50.2	W	30-60°
57.4	VS	0°	57.5	S	75°
	W	45°	57.8	S	345°
	S	90°	58.4	M	315-345°
59.94	S	90°	59.7	S	120-150°
	VS	135°	69.53	W	90°

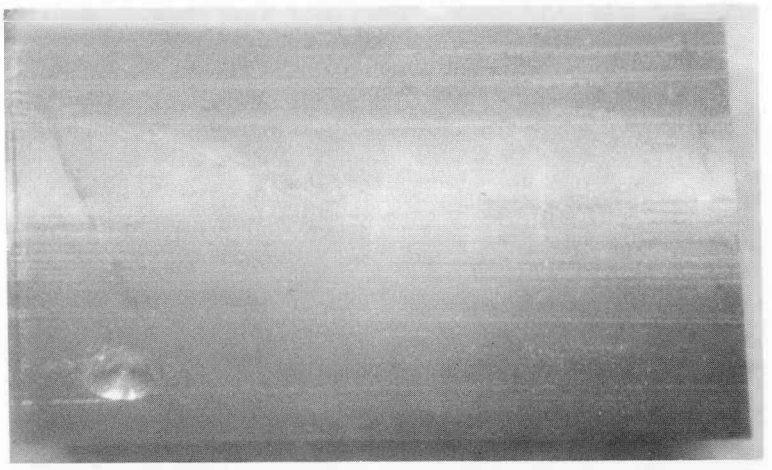

a. SECTION 3, OUTSIDE SURFACE

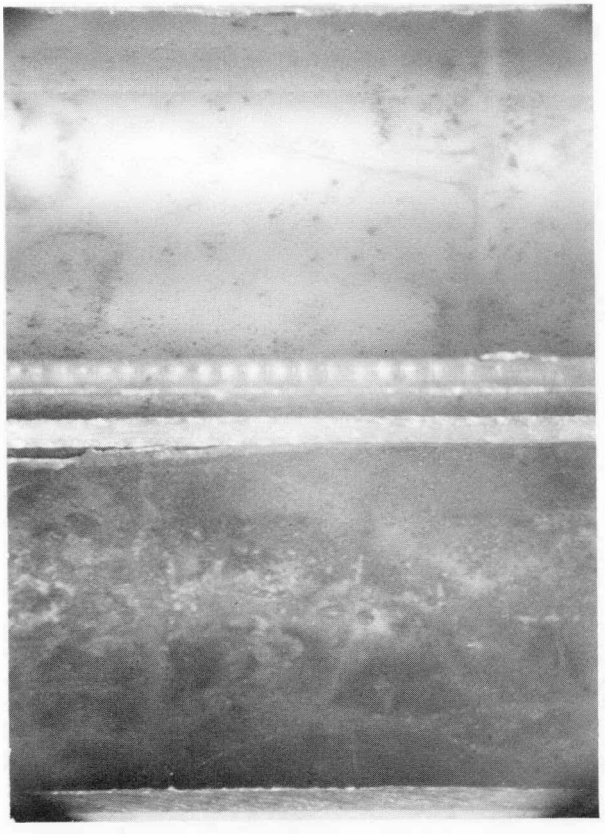

b. SECTION 4, INSIDE SURFACE

c. SECTION 6, INSIDE SURFACE

Figure 3.2-8 Macrophotographs of Cladding Sections From Rod KD-0451 ~ 3.5X

completely covered with the dark interaction layer. However, here the layer appears to be tightly adherent to the Zircaloy. No spalling was observed in these sections. A considerable amount of fuel is bonded to this layer.

Rod KE-2225

The outside surfaces of most of the sections were defect-free. Only the top-most section, No. 19, (from the plenum) had several sharp longitudinal grooves or scratches (Figure 3.2-9).

The inside surfaces of sections, Nos. 3, 7, and 11, (Figures 3.2-10 and -11) were rather clean except for a few fuel particles and surface markings originating from deposits at fuel cracks and pellet-pellet interfaces. The heavy interaction layer observed in rod KD-0451 was absent in this rod (possibly completely spalled off during sample cutting).

3.2.6.2 Sampling and Experimental Procedures

Fractography

An expanding mandrel was used in an effort to fracture a cladding ring at the location of an incipient crack, without damage to the crack. To test the procedure several 1.3 cm (1/2 inch) long rings of unirradiated Zircaloy-2 tubing were used. These were tested with an expanding split mandrel whose outside diameter matched the inside diameter of the tubing. Some tests were made with an artificial defect [a 1.9 mm (0.073 inch) or 1.6 mm (0.062 inch) hole drilled in the side of the tube], others were made without a defect but at liquid nitrogen temperature. In all cases, the ring split in the shear mode (Figure 3.2-12). The drilled hole was not a severe enough defect to reliably cause fracture at that location.

For testing the irradiated cladding, a ring 1.3 cm (1/2 inch) long was cut from rod KE-2225, at the location of the suspected incipient defect, i.e., 36.8 to 38.1 cm (14.5 to 15 inches) from the bottom of the fuel rod. The ring was placed over the mandrel with the 0-degree position of the rod over the mandrel split. (The major eddy current defect indication was located at 0 degree.) The mandrel with the sample was immersed in liquid nitrogen for approximately 5 minutes. Then the mandrel was expanded until the ring split. The ring, after the experiment, is shown in Figure 3.2-13. A piece of the ring was missing* and two incipient

* The missing piece could not be located in the hot cell.

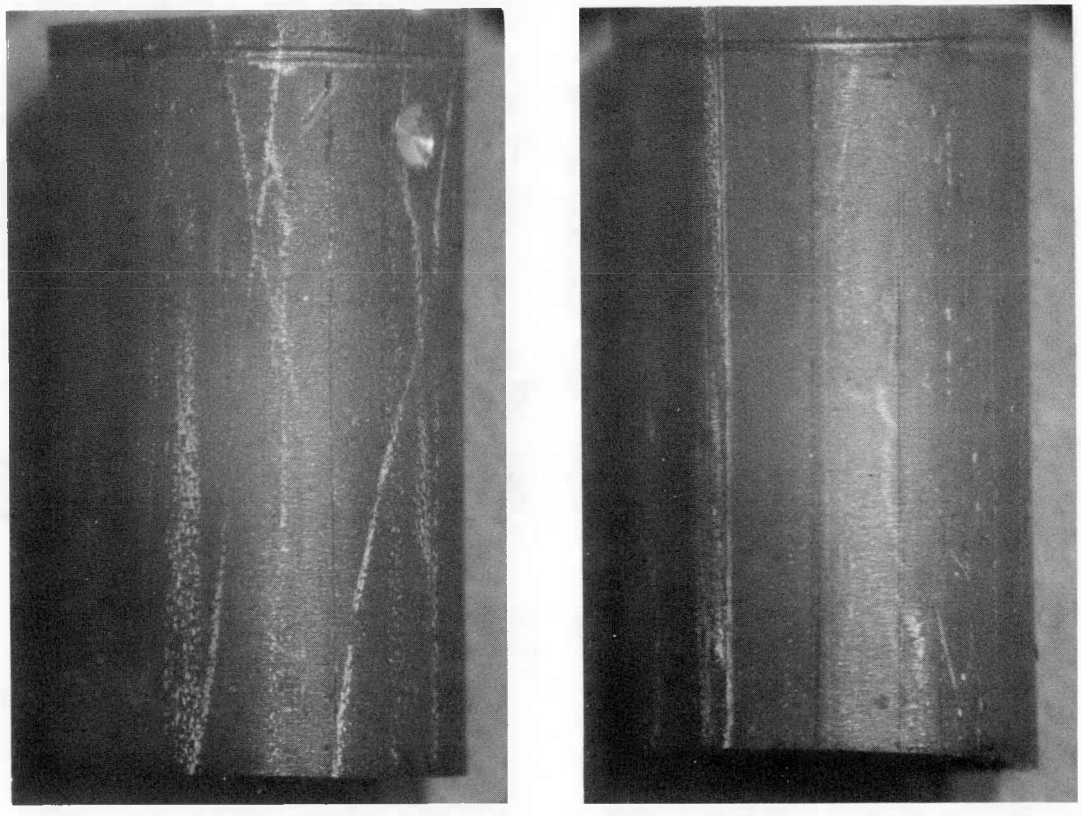

(a)

(b) ROTATED ABOUT 180° AGAINST (a)

Figure 3.2-9 Macrophotographs Of Outside Surface of Cladding Section 19 From Rod KE-2225 ~ 3.5X

Figure 3.2-10 Macrophotographs Of One-Half Of Inside Surface Of Cladding Section 3 From Rod KE-2225 ~ 3.5X

a. SECTION 7

b. SECTION 11

Figure 3.2-11. Macrophotographs of Inside Surface of Cladding Sections from Rod KE-2225 ~ 3.5X

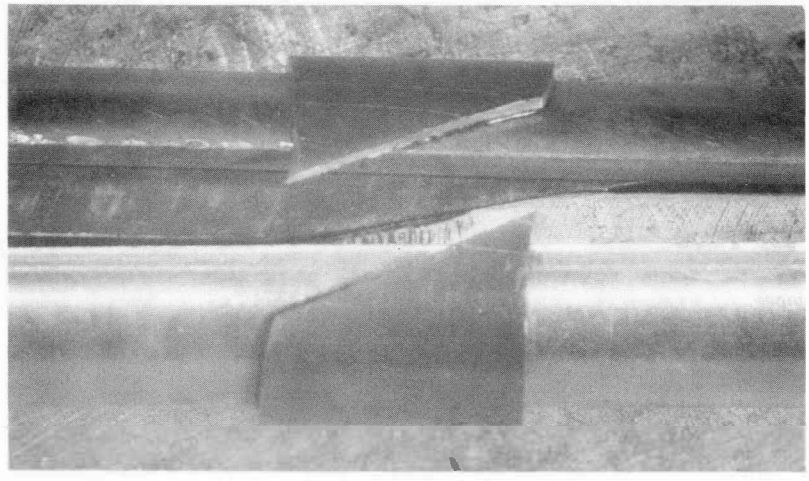

Figure 3.2-12 Unirradiated Zircaloy-2 Tube Section Tested With Expanding Mandrel ~ 3X

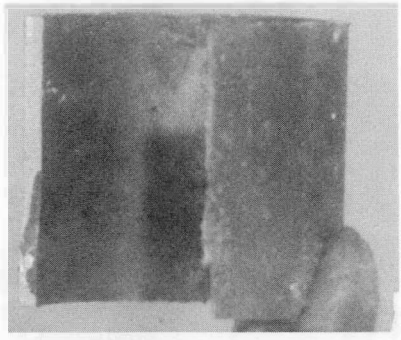

a. CRACK A AT 0° AZIMUTH ~3X

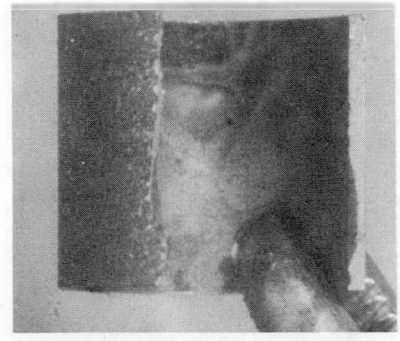

b. CRACK B AT 105° AZIMUTH ~3X

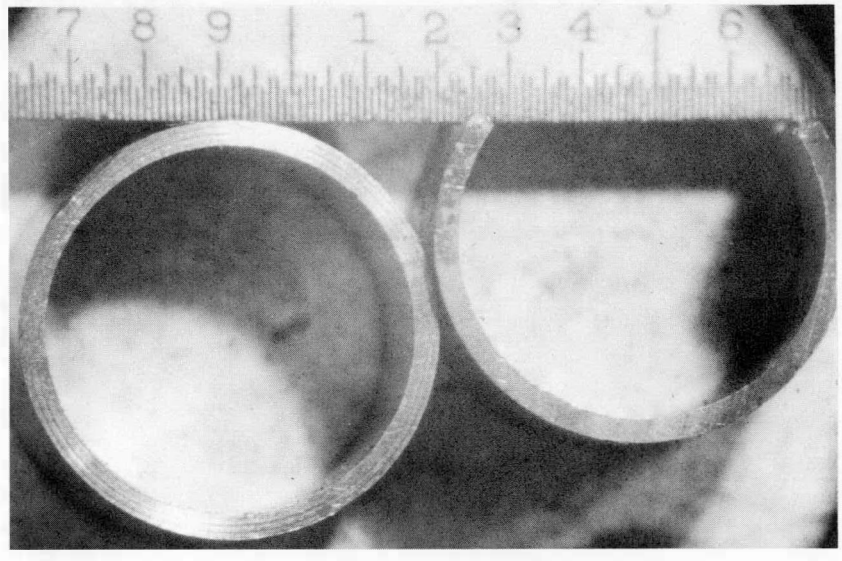

c. COMPARISON OF CRACKED SAMPLE WITH FULL CROSS SECTION ~ 3.75X

Figure 3.2-13 Section 5, 14.5 to 15 Inches from Bottom of Rod KE-2225, after Expanding Mandrel Test

fractures were present, both at a distance of 36.8 to 37.3 cm (14.5 to 14.7 inches) from the bottom of the rod. One fracture was located at approximately 0 degrees at azimuth, the other approximately 105 degrees from the first (measured counter-clockwise when viewed from the top of the rod).

Surface Analysis by Scanning Electron Microscopy (SEM)

Cutting of cladding samples was done with a low-speed diamond saw (~ 250 rpm). Samples for SEM analysis of the interior clad surface were cut from the following locations (see Figure 3.2-6).

Rod KD-0451, Section No. 5

This ring, 25.4 to 27.9 cm (10 to 11 inches) from the bottom of the rod, was slit longitudinally in thirds. One of the thirds (Figure 3.2-14a) was further cut to produce three pieces, each about 0.8 cm (1/3 inch) long and 0.8 cm (1/3 inch) wide. The two lower of these three pieces were flattened and used for SEM (Figures 12b and c).

Sections Nos. 6 and 15

Two samples of the same size were cut and flattened, one from Section No. 6, 27.9 to 29.2 cm (11 to 11-1/2 inches) from the bottom of the rod (i.e., at the location of the high power transient), the other from Section No. 15, 295.9 to 297.2 cm (116-1/2 to 117 inches) from the bottom (i.e., at the location of high burnup; see Figure 3.2-5a). No water or alcohol was used for the preparation of these samples in order to preserve soluble fission products.

Rod KE-2225, Section 5

A 2.5 cm (1 inch) long ring was cut from the lower end of Section No. 5, i.e., 29.2 to 31.8 cm (11-1/2 to 12-1/2 inches) from the bottom of the rod. This ring was slit longitudinally in thirds. As can be seen in Figure 3.2-15b a small saw-cut was inadvertently placed near one end of the section.

During flattening, the cladding cracked along this cut (Figure 3.2-15c). Two SEM samples were cut from the section, one of them containing the crack, as seen in Figures 3.2-15d and e.

All SEM samples were mounted on SEM sample holders with silver-containing conducting epoxy. A shielded, wave-length dispersive spectrometer, which is part of the SEM system, was used for the chemical studies.

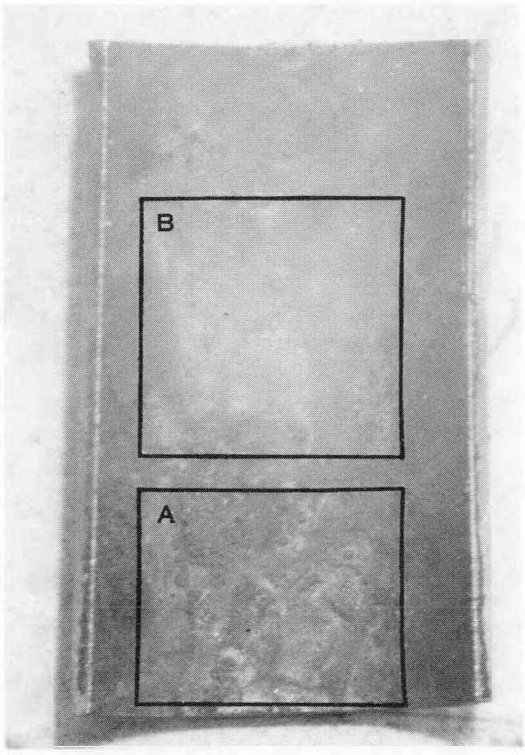

a. INSIDE SURFACE OF WHOLE SECTION

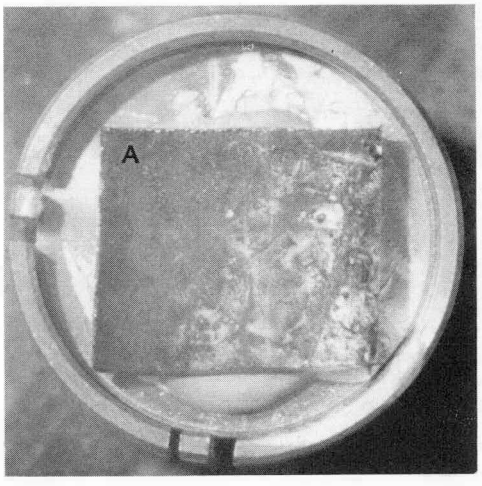

b. SAMPLE A ON SEM MOUNT

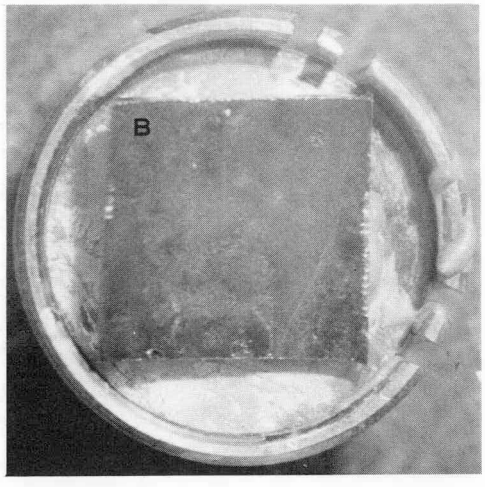

c. SAMPLE B ON SEM MOUNT

Figure 3.2-14 Section 5, 10 To 11 Inches from Bottom of Rod KD-0451, Flattened ~ 3.5X

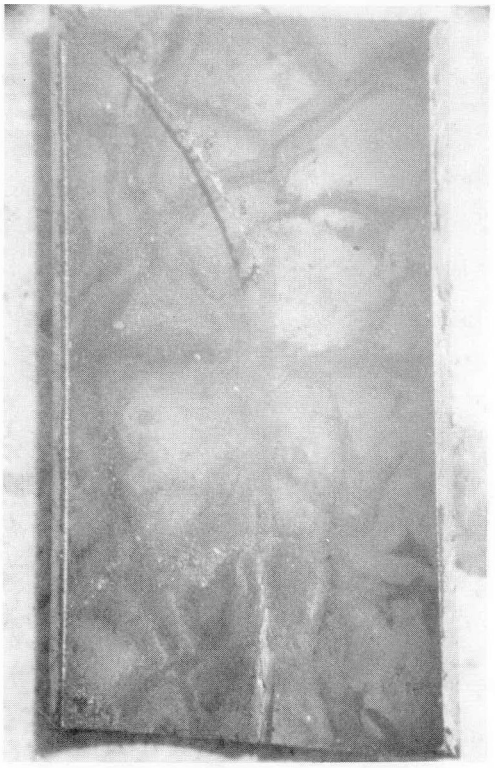

b. INSIDE SURFACE OF WHOLE SECTION

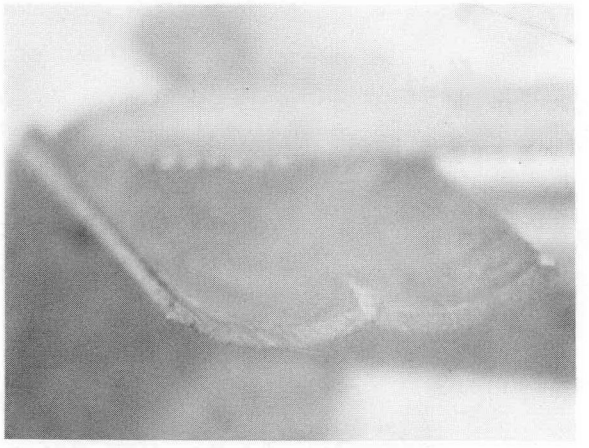

c. LOWER HALF OF SECTION WITH CRACK CAUSED BY CUT

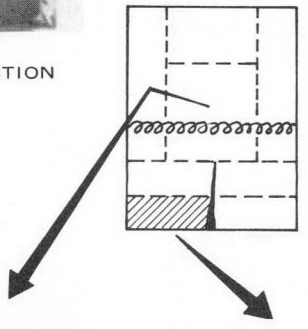

a. CUTTING DIAGRAM FOR SEM SAMPLES

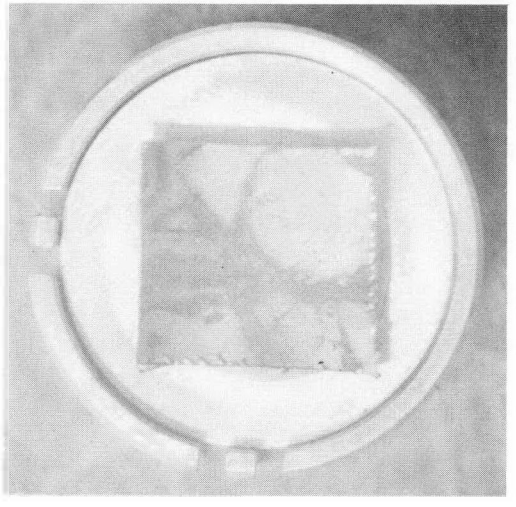

e. SAMPLE D ON SEM MOUNT

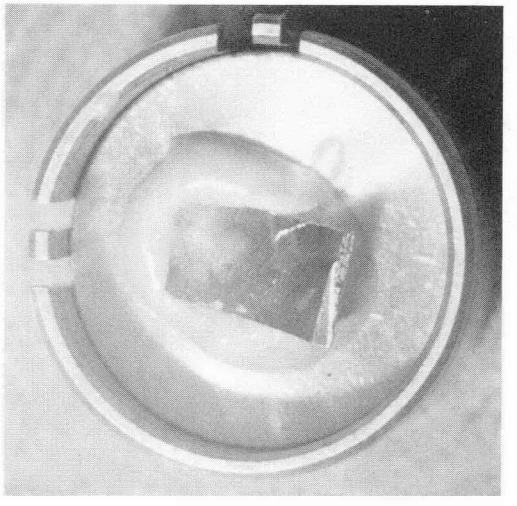

d. SAMPLE C WITH CRACK ON SEM MOUNT

Figure 3.2-15 Section 5, 11-1/2 To 12-1/2 Inches From Bottom Of Rod KE-2225, Flattened ~ 3.5X

Metallography

Adjacent to the fractography sample of rod KE-2225, a 0.5 cm (0.2 inch) long ring was cut (36.3 to 36.8 cm from the bottom of the rod) and mounted in cross section for hot cell metallography. After the fractographic examination was completed a cross section through the 0-degree fracture (A) was prepared at a location of part-through cracking.

Sectioning for metallography was done with a low-speed diamond saw (~ 250 rpm) with water lubricant (except where cutting was specified to be dry). The specimens were ultrasonically cleaned in isopropyl alcohol and then mounted in epoxy resin. Grinding was done with SiC abrasive papers through 600 grit and then polished with 6 μm and 1/2 μm diamond paste using kerosene as a lubricant. The sections were chemically polished and etched. The chemical polish solution was:

17 ml HNO_3 (70 percent)
23 ml H_2O
5 ml glycolic acid (70 percent)
3 g NH_4F .

The etchant was:
45 ml HNO_3
45 ml H_2O_2 (30 percent)
1-4 ml HF (48 percent).

Four additional sections were prepared from the following locations:

1. Rod KD-0451, ring sections Nos. 5 and 16, 25.4 to 27.9 cm (10 to 11 inches) and 297.2 to 299.7 cm (117 to 118 inches) from the bottom of the rod, respectively.

2. Rod KE-2225, ring section No. 5, 29.2 to 31.8 cm (11-1/2 to 12-1/2 inches) from the bottom of the rod, one cross section and one longitudinal section.

Transmission Electron Microscopy (TEM)

Samples for microstructural analysis by TEM were taken from the following locations (see Figure 3.2-6):

1. Rod KD-0451, ring sections No. 3, 5, 7, 16, and 19

2. Rod KE-2225, ring section No. 5.

The ring sections were cut with a low-speed (~ 170 rpm) diamond saw (Isomet) to obtain much smaller sections with faces parallel to the axial direction,

approximately 6 mm (1/4 inch) long and 3 mm (1/8 inch) thick. Strips were then cut from these sections with a special (~ 800 rpm) saw with counter weight feed and equipped with an annular diamond saw (Microslice). A water-base lubricant was used (Glenoil). The thin strips 0.25 mm to 0.38 mm (0.010 to 0.015 inch) were then spark cut to yield lengths suitable for use as electron microscopy specimens.

Prior to electropolishing, the edges of the strips were coated with opaque lacquer to protect the exposed edges and to prevent light leakage about the sides. Specimens were twin-jet electropolished in a solution of 10 percent perchloric acid in ethanol at about -40 C. When perforated, the viewing directions for the specimens in the electron microscope were approximately along the tangential direction of the cladding. This choice of viewing direction allowed the basal planes to be used for imaging in many of the grains observed.

3.2.6.3 Results. A. Fractography of Incipient Cracks on Rod KE-2225. Macrophotographs (Figures 3.2-13a and b) (see also Figures 3.3-17a and 3.2-24a) of the two cracks exposed by the expanding mandrel test show dark portions with a shape roughly like the cross section through a plane-convex lens. These areas are oxidized or corroded and are apparently in-service parts of the crack. The more penetrating of the two cracks located at 0-degree azimuth was called A, the other B.

Crack A

All SEM micrographs taken on fracture A and their relation to each other are shown in Figure 3.2-16. A composite of low-magnification SEM micrographs (Figure 3.2-17b) shows the whole incipient crack. By comparing this composite with the corresponding macrograph (Figure 3.2-17a), the outline of the incipient crack portion can easily be traced. Some areas apparently have been damaged, but all important features are visible. The incipient crack on the inner surface is ~ 5.7 mm long, and near the middle of its length it appears to penetrate the whole wall thickness. In a few places the crack has branched, and especially near its penetration it has two main branches.

The region of through-wall penetration is shown at higher magnifications and in stereo in Figures 3.2-18 to 20. Close inspection of these micrographs reveals that through-wall penetration has occurred along a length of approximately 0.4 mm,

Blank Page

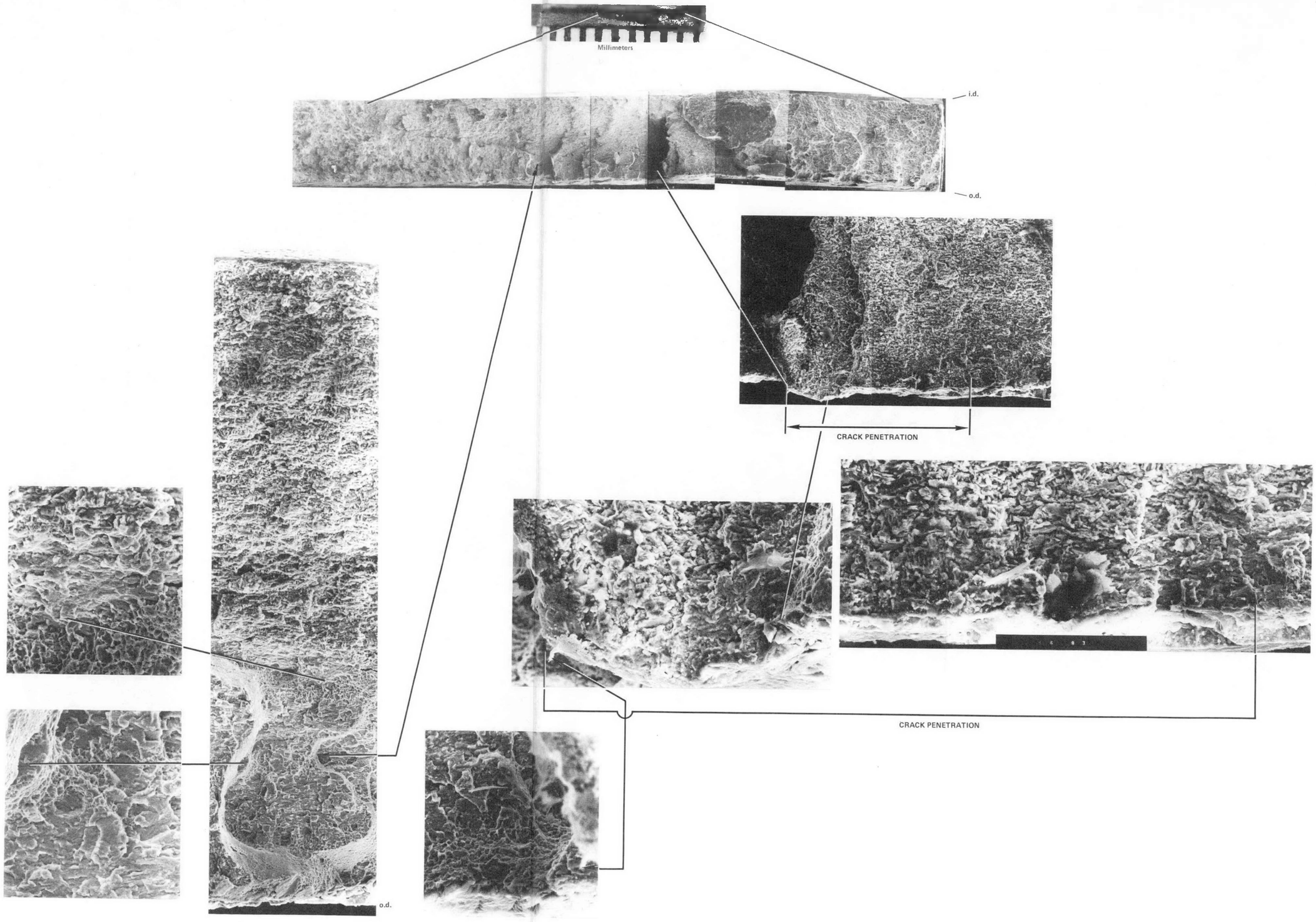

FIGURE 3.2-16. ROD KE–2225, CRACK A; OVERVIEW OF ALL SEM MICROGRAPHS

Blank Page

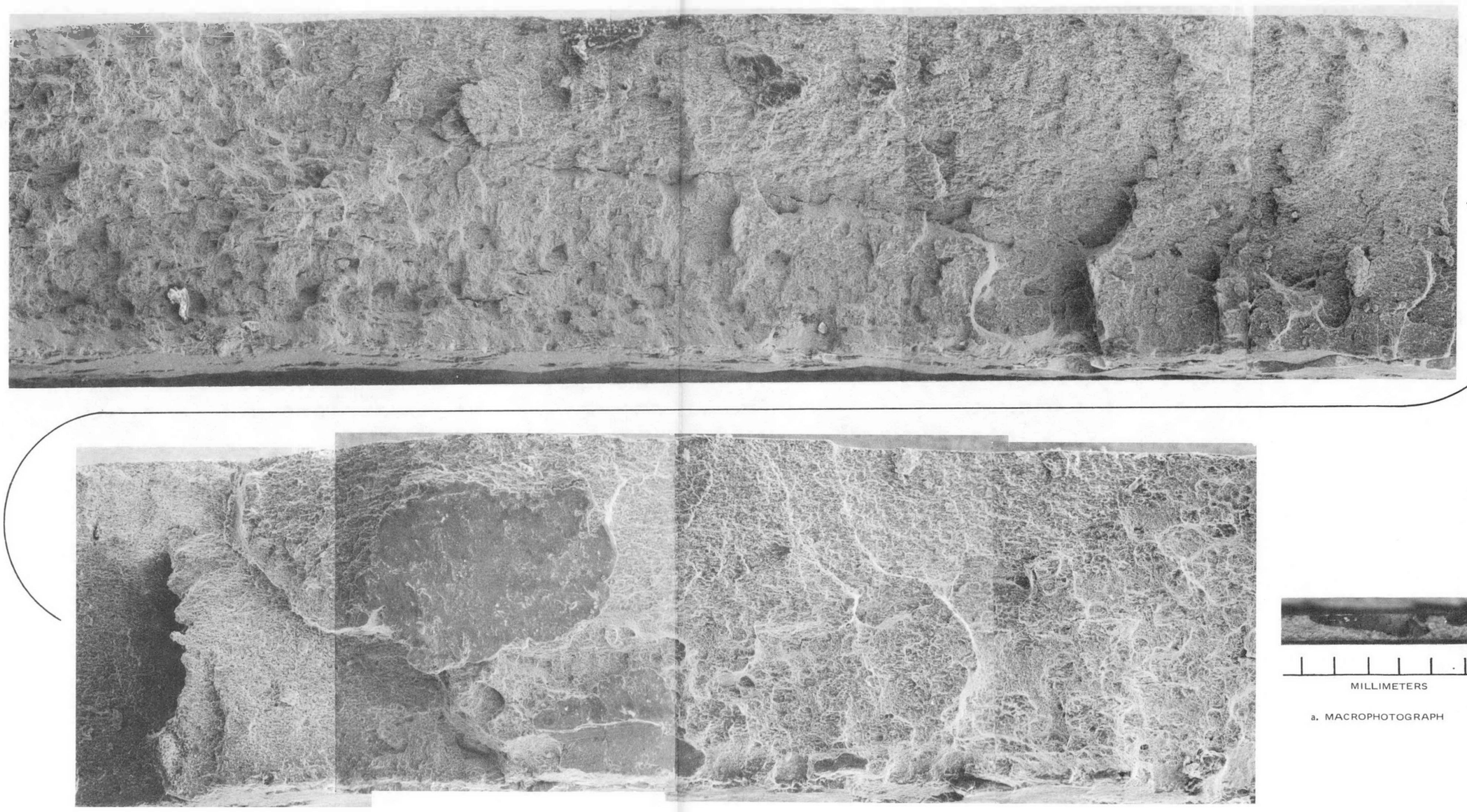

a. MACROPHOTOGRAPH

b. COMPOSITE SEM MICROGRAPHS 100X

Figure 3.2-17. Rod KE-2225, Whole Fracture Surface of Crack A

Blank Page

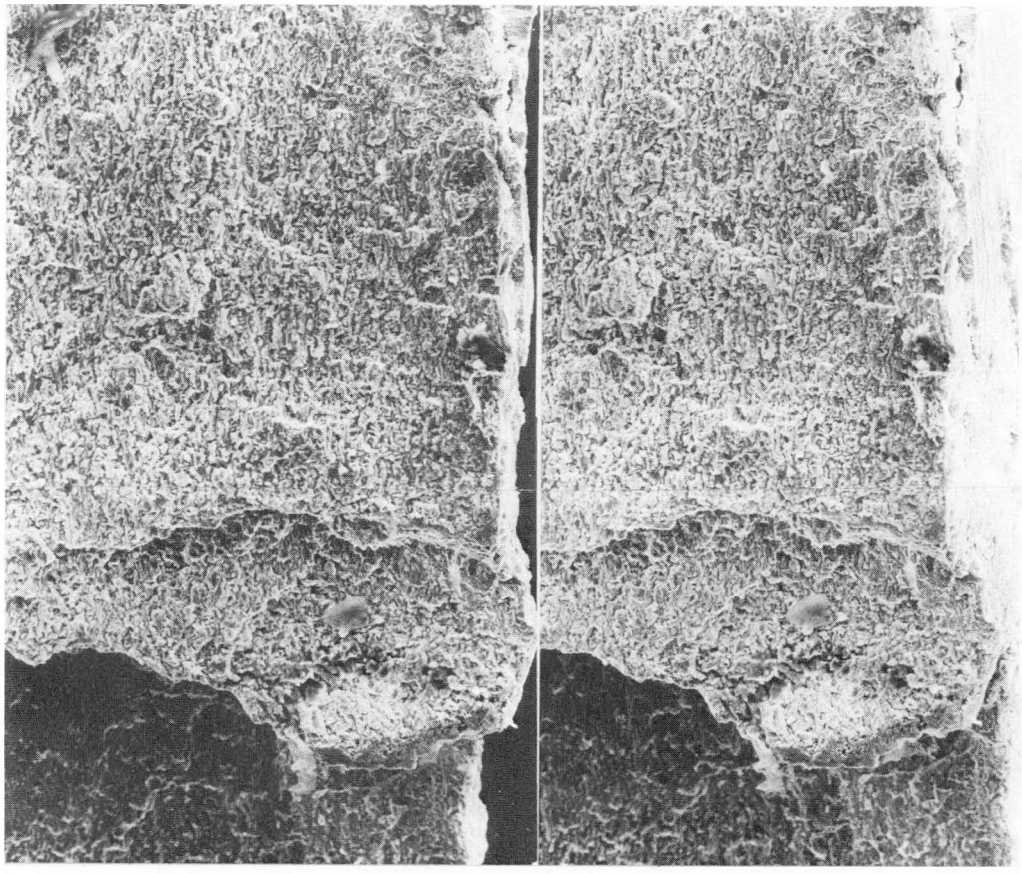

Figure 3.2-18. Rod KE-2225, Crack A; Area of Crack Penetration (Stereo Pair) 200X

a. UPPER CRACK BRANCH, STRESS CORROSION FRACTURE

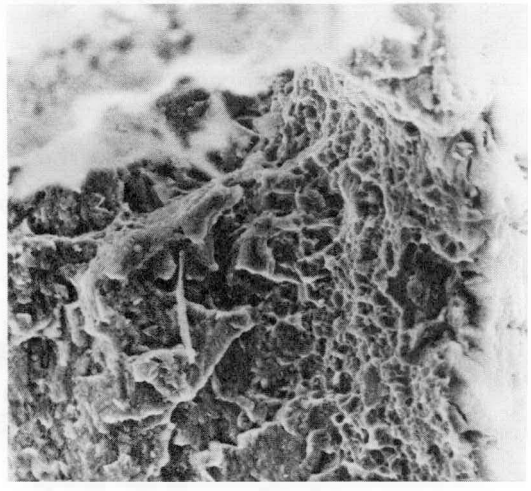

b. LOWER CRACK BRANCH WITH DUCTILE FRACTURE LIP

Figure 3.2-19. Rod KE-2225, Crack A; Lower Part of Figure 3.2-18
800X

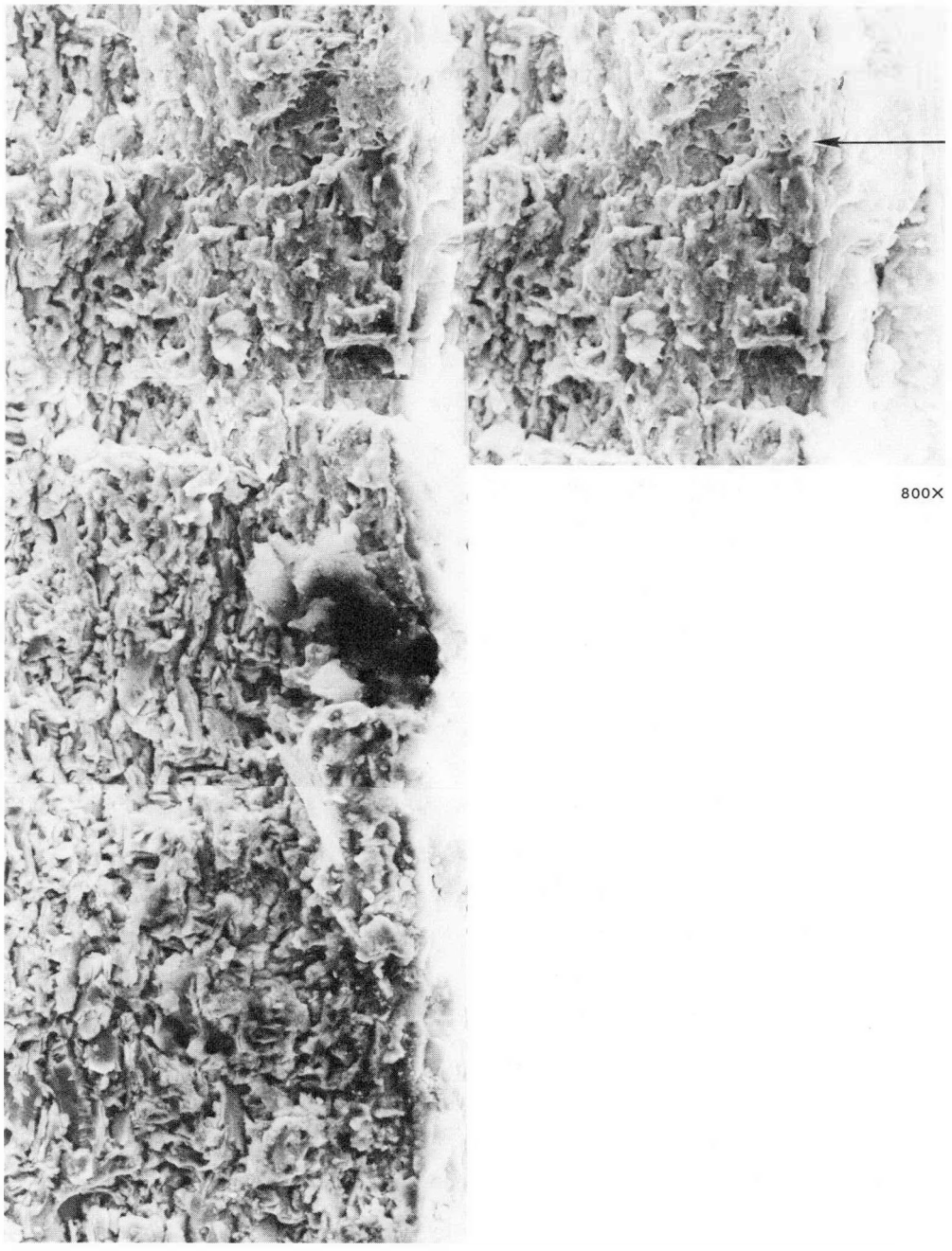

Figure 3.2-20. Rod KE-2225, Crack A; Upper Part of Figure 3.2-18 (Stereo Pair)
Arrow Points to End of Penetration of Original Crack

from the edge of the upper crack branch (Figure 3.2-19) to the arrow (Figure 3.2-20). Beyond the location of the arrow the fracture surface shows ductile dimples near the outer cladding surface, a sign that this portion of the crack was produced during the expanding mandrel procedure. The lower branches of the crack did not reach the outer surface of the cladding wall; Figure 3.2-19b shows ductile dimples at the outer surface.

An area of part-through crack penetration is shown in Figure 3.2-21, and in the higher magnification stereo pairs, Figure 3.2-22. Near the cladding inner surface, i.e., near the start of the crack, the crack surface is heavily oxidized. The crack tip is marked by the abrupt end of oxidation (Figure 3.2-22a) and by a change in crack direction. The final ductile portion of the crack has strong shear components. As seen in Figures 3.2-21 and -22b, the final fracture contains large areas with a flaky quasi-cleavage surface morphology, possibly associated with hydrides.

Crack B

Figure 3.2-23 gives an overview of all SEM micrographs of fracture B. This crack (Figure 3.2-24) at the cladding inner surface is ~ 5.0 mm long, i.e., nearly as long as crack A; however, it penetrates only about half the wall thickness. It has two branches near one end (the loose chunk is bordered by the two branches). Higher magnifications of the fracture surface (Figures 3.2-25 to 30) show the different fractographic features in more detail. Near the inner cladding surface, i.e., at the crack origin, the crack surface is oxidized (Figure 3.2-26) but not enough to obscure the cleavage and fluting features characteristic of stress corrosion cracking (16). Figure 3.2-30 shows an area less oxidized near the crack tip, where cleavage and fluting can be recognized (Figure 3.2-30c). The crack tip (Figures 3.2-25 and 3.2-27) is recognizable by the first appearance of ductile dimples. The fresh fracture (i.e., the fracture produced by the expanding mandrel) again is characterized by islands of quasi-cleavage (Figures 3.2-27 to 30) possibly associated with hydrides. Also in the fresh fracture, cracks are observed lying in a circumferential plane (Figures 3.2-27, 30, and 31; also see Figure 3.2-33). Such cracks may also be associated with hydrides. More definitive evidence of the presence of hydrides will be presented later in this Section.

Inner Surface of Cladding

Rod KE-2225

The fracture originating at the inadvertent cut (Figure 3.2-15b and c) (Section 5C)

Figure 3.2-21. Rod KE-2225, Crack A; Area of Part-Through Crack Penetration (See Figure 3.2-16 for Location) ~ 400X

Blank Page

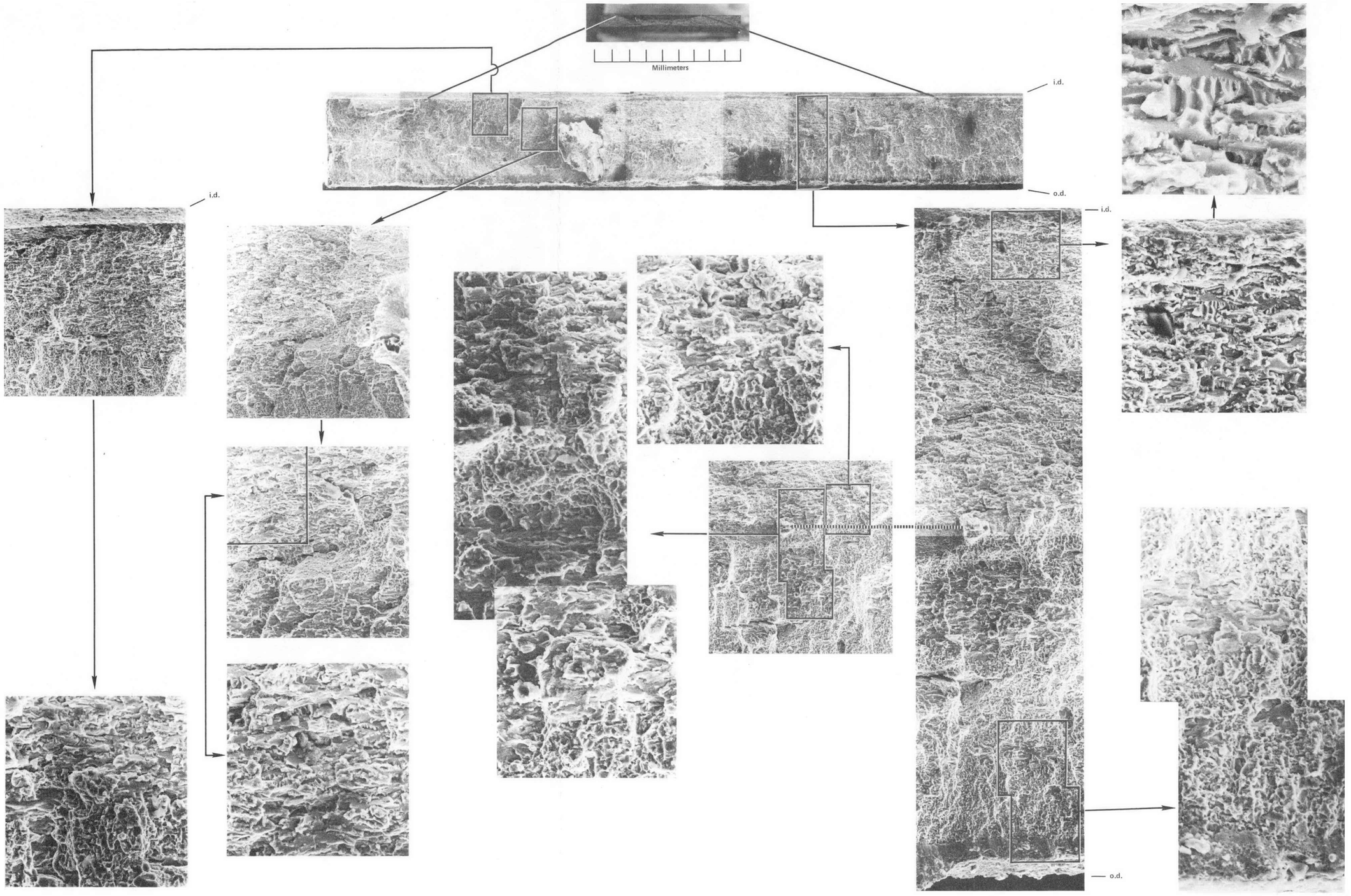

FIGURE 3.2-23. ROD KE—2225, CRACK B; OVERVIEW OF ALL SEM MICROGRAPHS

Blank Page

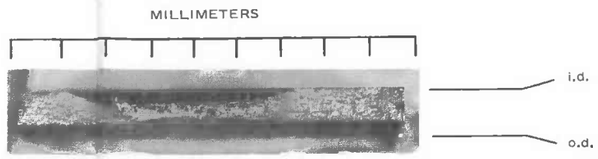

a. MACROPHOTOGRAPH

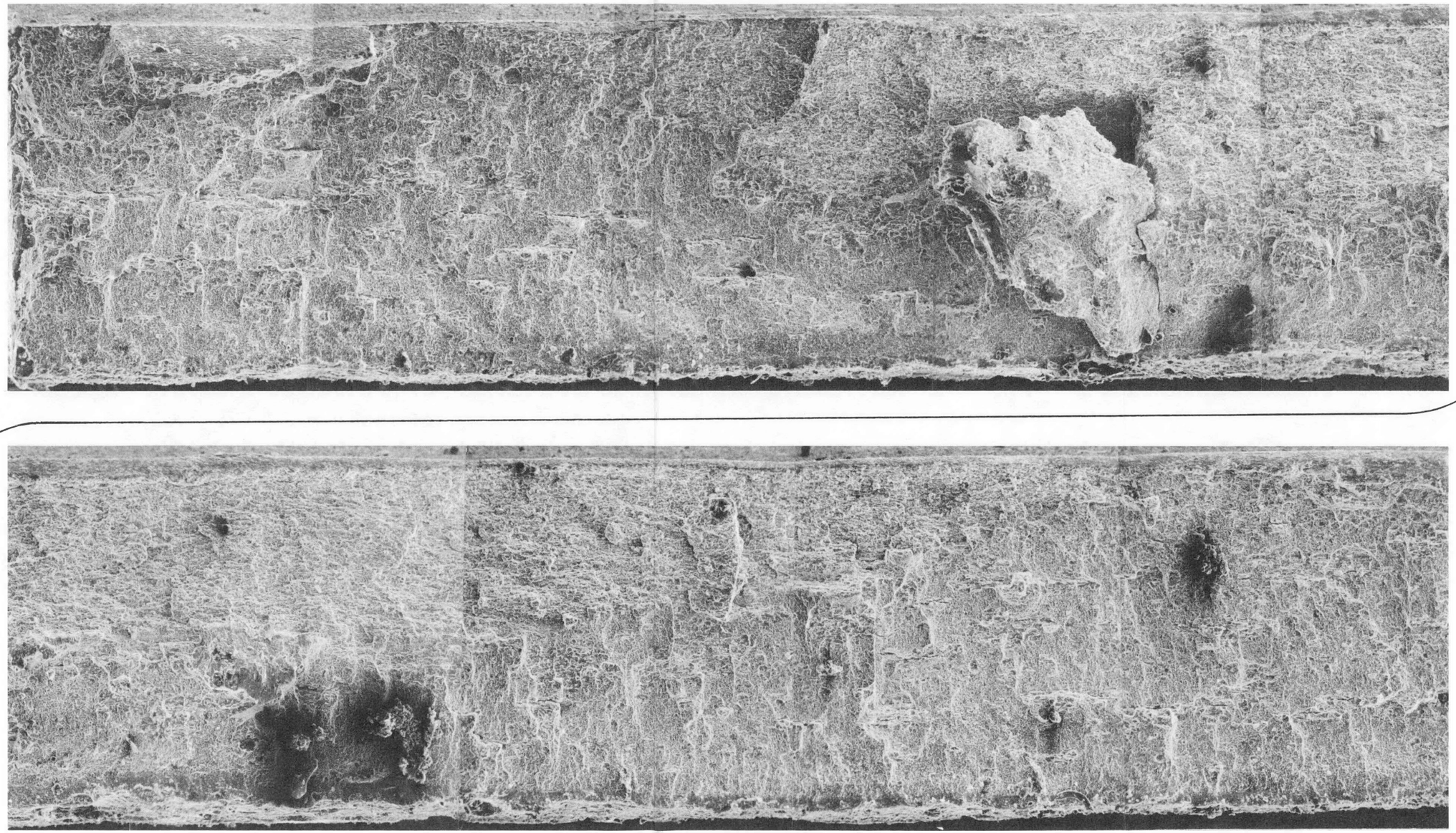

b. COMPOSITE SEM MICROGRAPHS 100X

Figure 3.2-24. Rod KE-2225, Whole Fracture Surface of Crack B

Blank Page

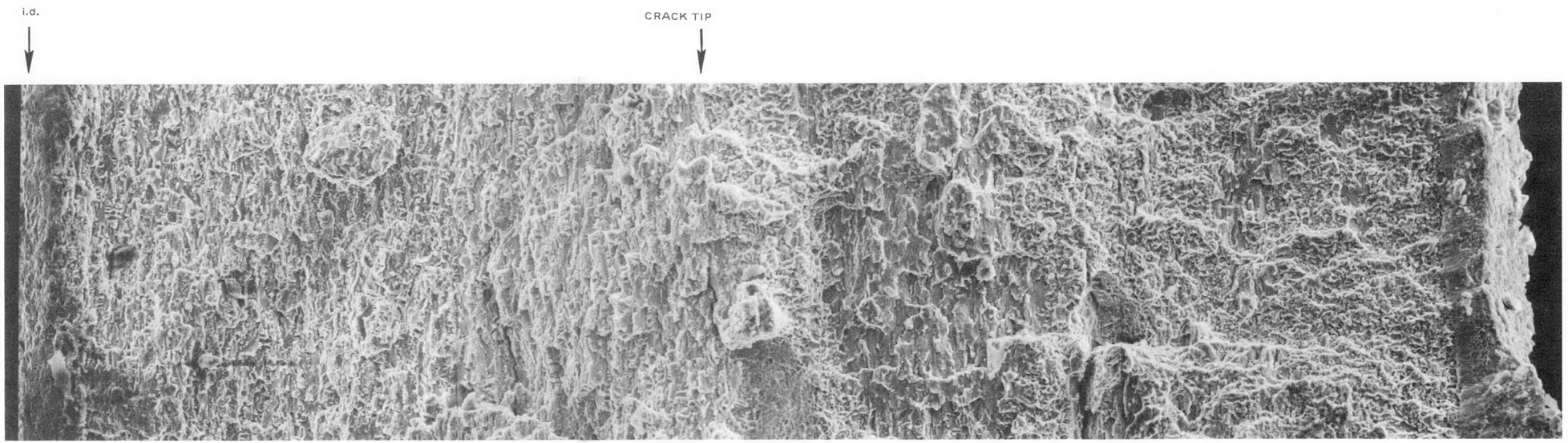

Figure 3.2-25. Rod KE-2225, Crack B (See Figure 3.2-23 for Location) 400X

Blank Page

a. STEREO PAIR 1000X

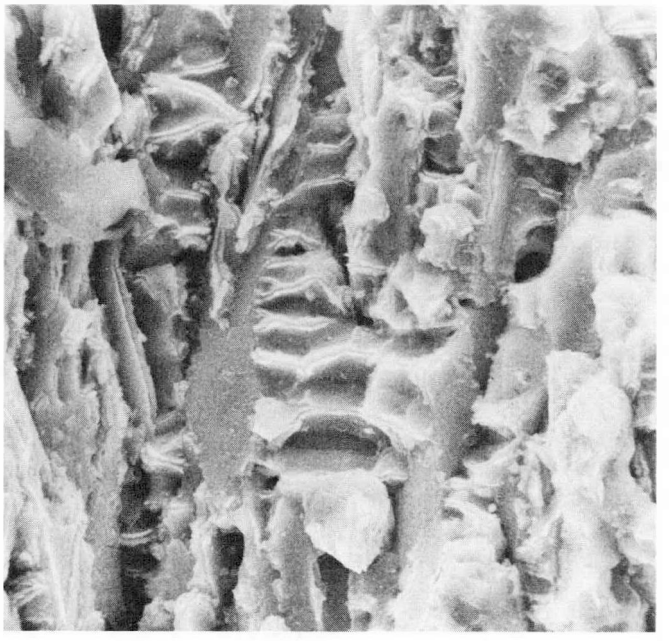

b. PART OF (a), CLEAVAGE AND FLUTING FEATURES 3000X

Figure 3.2-26. Rod KE-2225, Crack B; Part of Figure 3.2-21 Near Inside Cladding Surface, Stress Corrosion Fracture

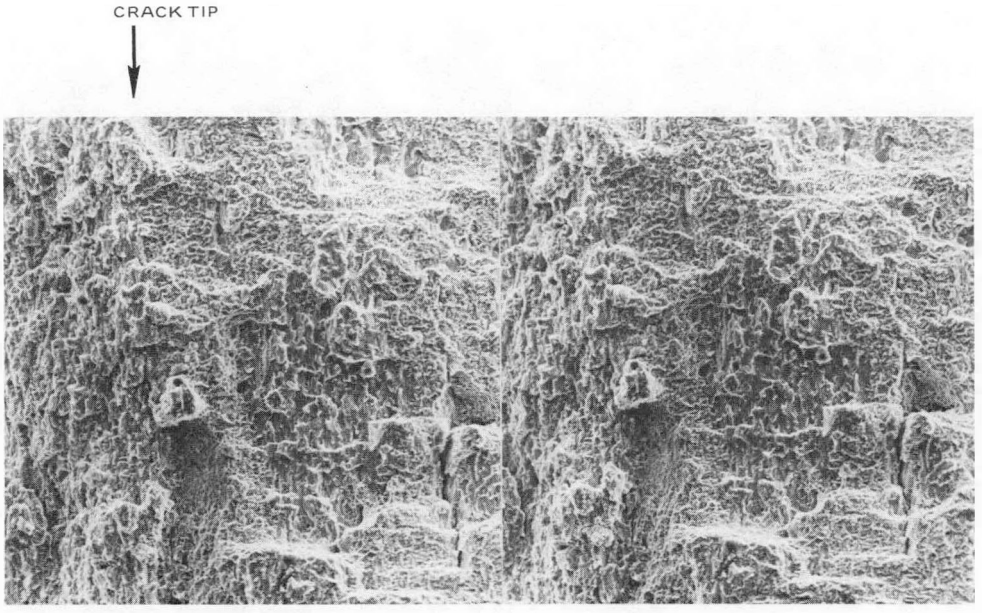

a. 200X

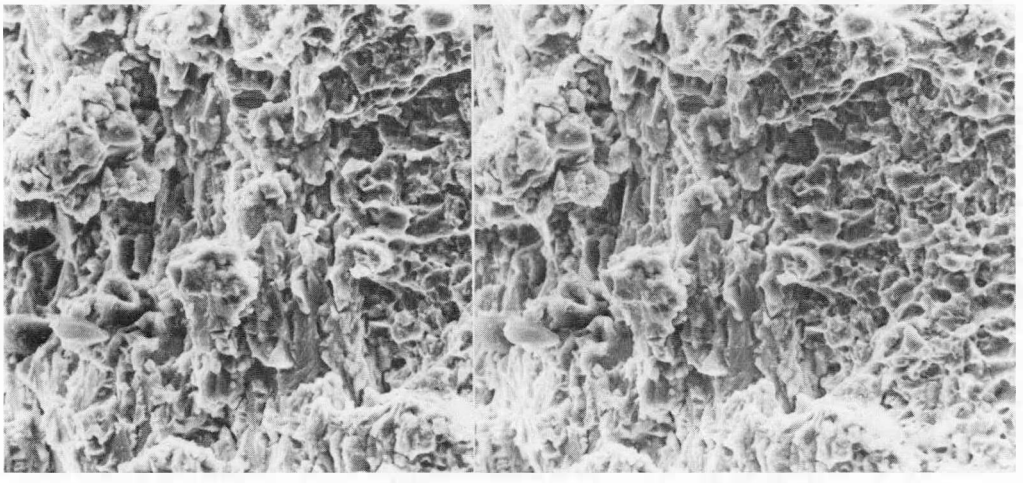

b. 800X

Figure 3.2-27. Rod KE-2225, Crack B; Part of Figure 3.2-21 at Crack Tip (Stereo Pairs)

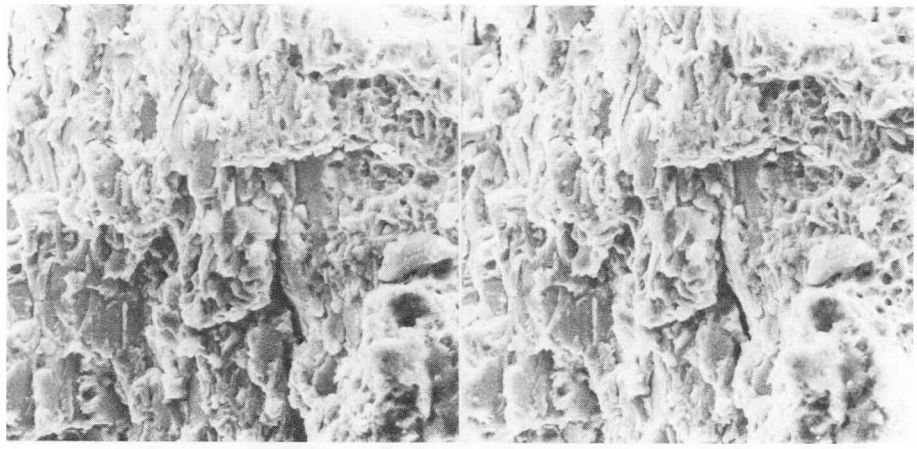

a. STRESS CORROSION CRACK TIP — TRANSITION TO DUCTILE DIMPLES

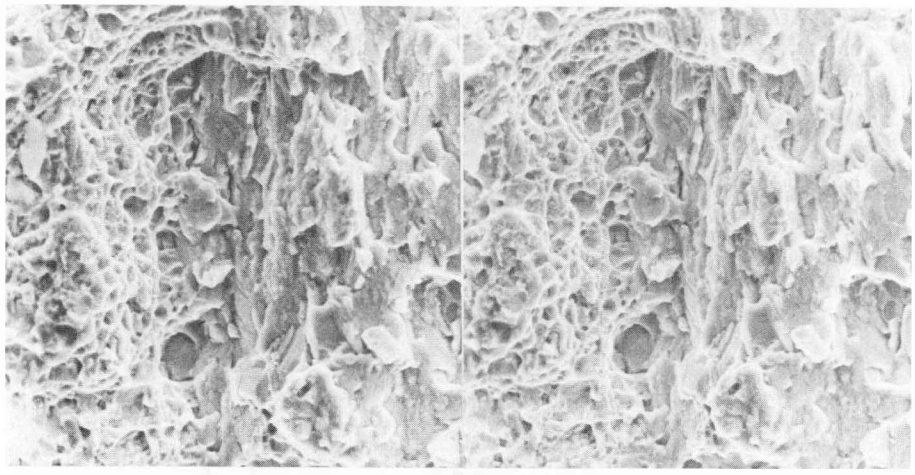

b. QUASI—CLEAVAGE AND DIMPLES

c. QUASI—CLEAVAGE AND DIMPLES

800X

Figure 3.2-28. Rod KE-2225, Crack B; Part of Figure 3.2-27 at Crack Tip (Stereo Pairs)

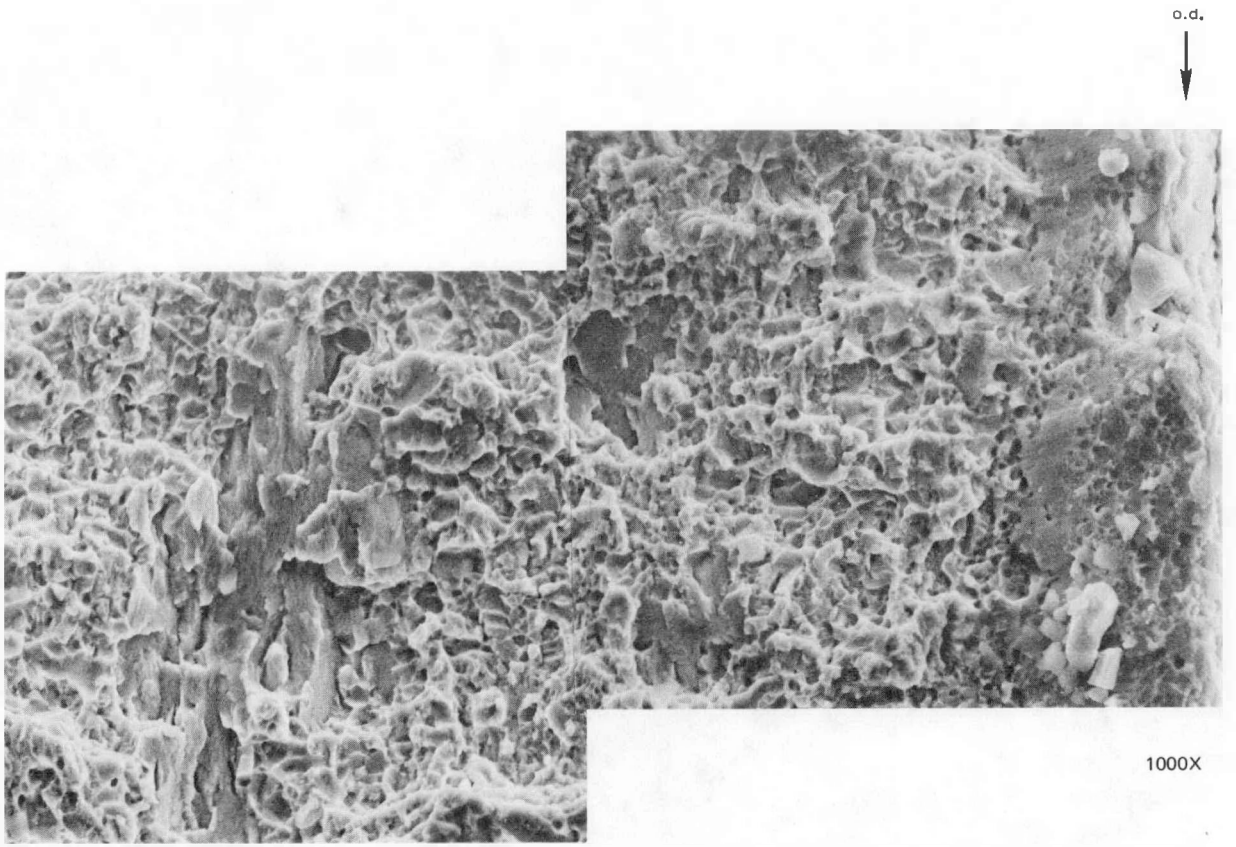

Figure 3.2-29. Rod KE-2225, Crack B; Part of Figure 3.2-21, Near Outside Surface of Cladding, Quasi-Cleavage and Ductile Dimples

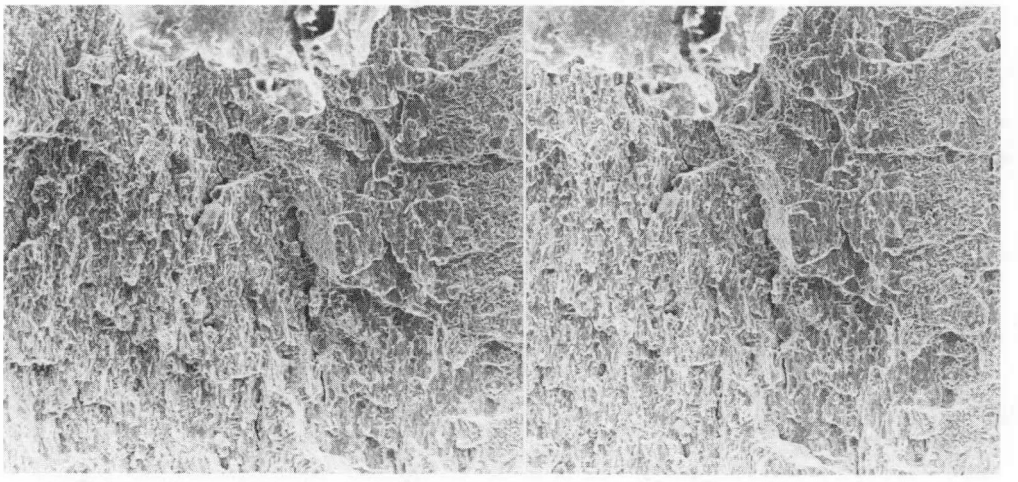

a. STEREO PAIR 200X

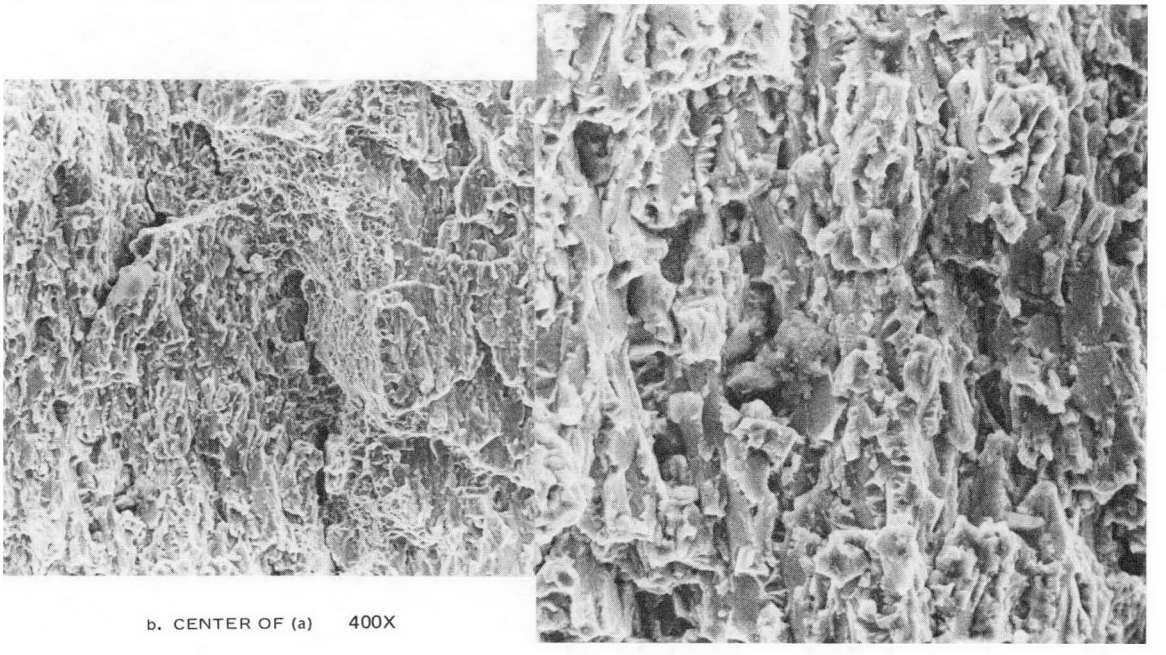

b. CENTER OF (a) 400X

c. LOWER LEFT QUADRANT OF (b), CLEAVAGE AND FLUTING FEATURES 1000X

Figure 3.2-30. Rod KE-2225, Crack B; Area Near Crack Tip (See Figure 3.2-23 for Location)

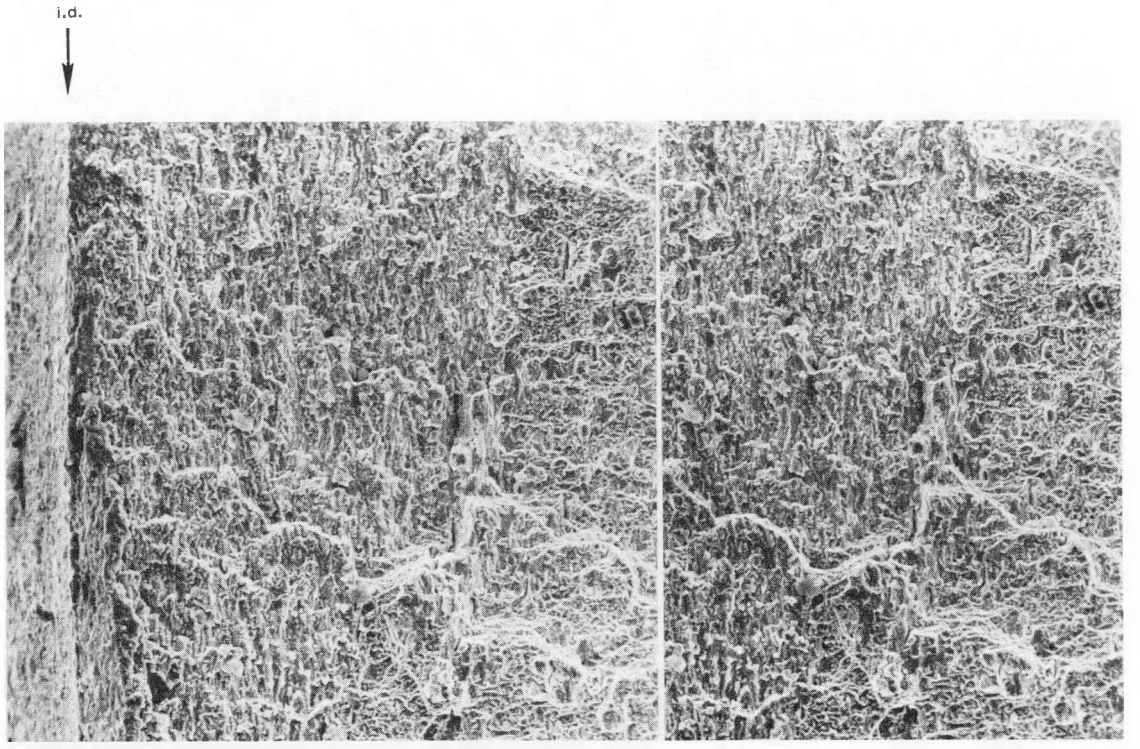

a. STEREO PAIR 250X

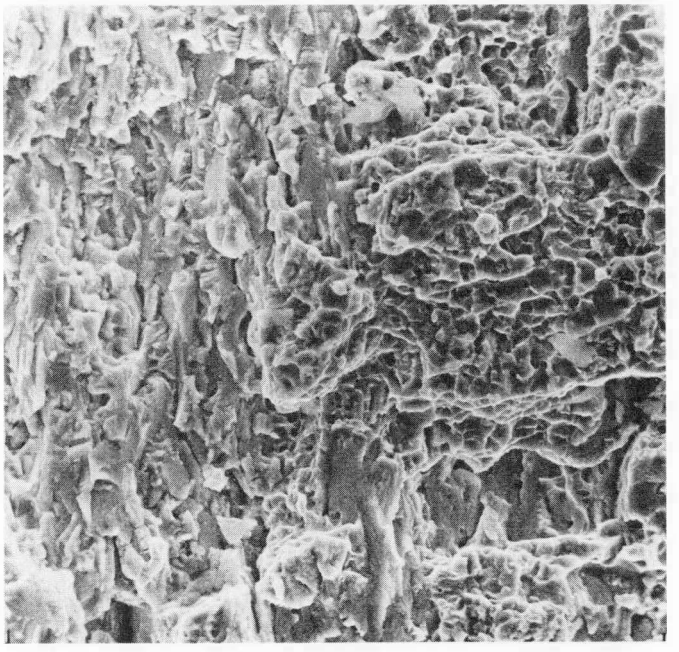

b. UPPER RIGHT CORNER OF (a) 1000X

Figure 3.2-31. Rod KE-2225, Crack B; Near End of Incipient Crack (See Figure 3.2-23 for Location)

is shown in Figures 3.2-32a and 33. The fracture mode is completely ductile signifying that no incipient crack was present at this location. The flattening has caused numerous longitudinal cracks (Figure 3.2-32), but these cracks apparently penetrate only the UO_2-ZrO_2 interaction layer and possibly the ZrO_2.

The uncracked section (5D) has similar surface cracks (Figures 3.2-34, 35a, and 36a). UO_2 pieces are bonded to the surface and an interaction layer of varying morphology has formed. This layer has a beaded surface (Figure 3.2-37, also Figure 3.2-32b) with the bead size possibly dependent on the local temperature and/or on the proximity of the UO_2 pellet surface. The bead size changes at the location of a pellet-pellet interface (Figure 3.2-37). The beads, or small nodules, contain uranium (Figures 3.2-38 and 39). Cracking of the interaction layer has occurred only during flattening of the cladding. This can be seen in Figure 3.2-40 taken near the incipient Crack A exposed by the expanding mandrel test (but not flattened). Here the layer has occasional holes but no cracks. Its surface is relatively smooth giving the impression that beads might have coalesced. The layer contains both uranium and zirconium as seen in the X-ray maps, Figures 3.2-35 and 36. Since fission products are also expected in the interaction layer, X-rays of cesium and tellurium were made to pinpoint the location of these elements (Figures 3.2-38 and 39). Cesium is mainly associated with UO_2 particles. The tellurium signal is barely above background; no particular spatial tellurium concentrations was found.

Rod KD-0451

The inside surface of this unfailed rod (Figures 3.2-41 to 48) also contains longitudinal surface cracks involving only the interaction layer and the ZrO_2 as was the case in rod KE-2225. However, the interaction layer looks different from that in the failed rod.

In Section 5 (Figures 3.2-41 to 43a) the surface is not beaded. In certain regions, apparently related to fuel cracks and interfaces, the layer has holes and discontinuities (Figures 3.2-42 and 43b, and c). X-ray maps show that numerous small UO_2 particles (Figures 40c and 42a) are bonded to the cladding surface. Considerable amounts of Te and smaller amounts of Cs are associated with UO_2 particles (Figure 3.2-44c and d).

In Section 6 (where the high power transient occurred) the inside cladding surface is covered with a network of rope-like features (Figure 3.2-45) which appear to be

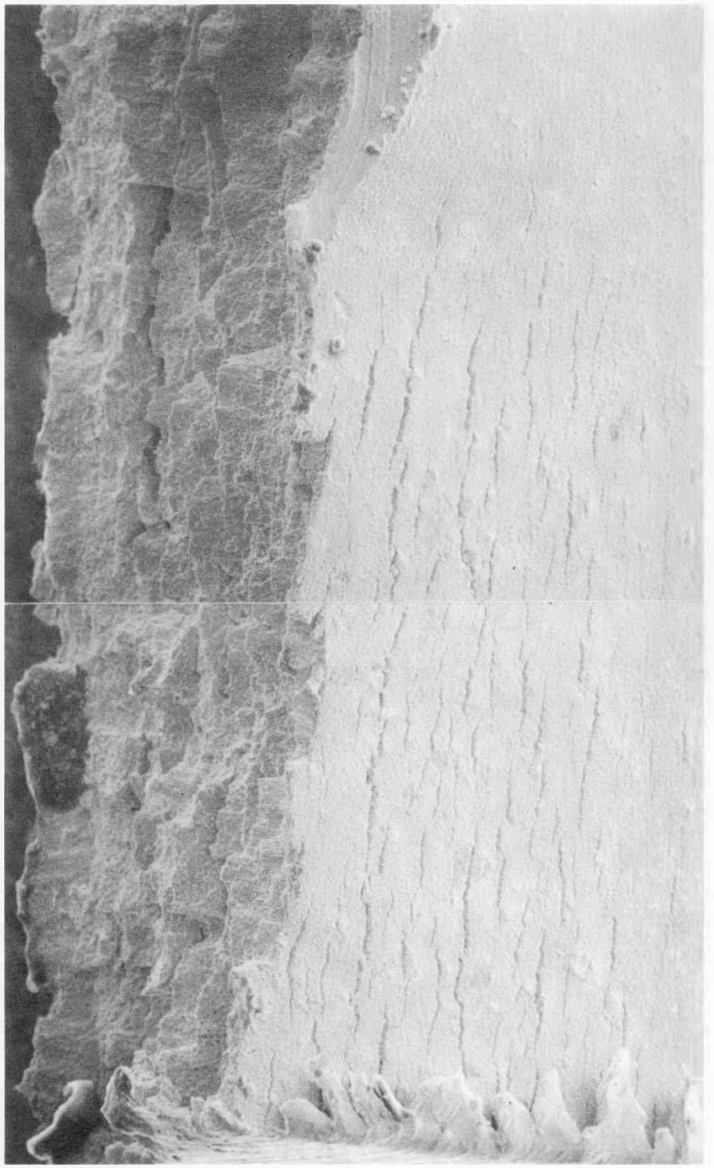

a. CRACK SURFACE AND INSIDE CLADDING SURFACE 100X

b. INSIDE CLADDING SURFACE WITH BEADED INTERACTION LAYER 500X

Figure 3.2-32. Rod KE-2225, Section 5C, Flattened

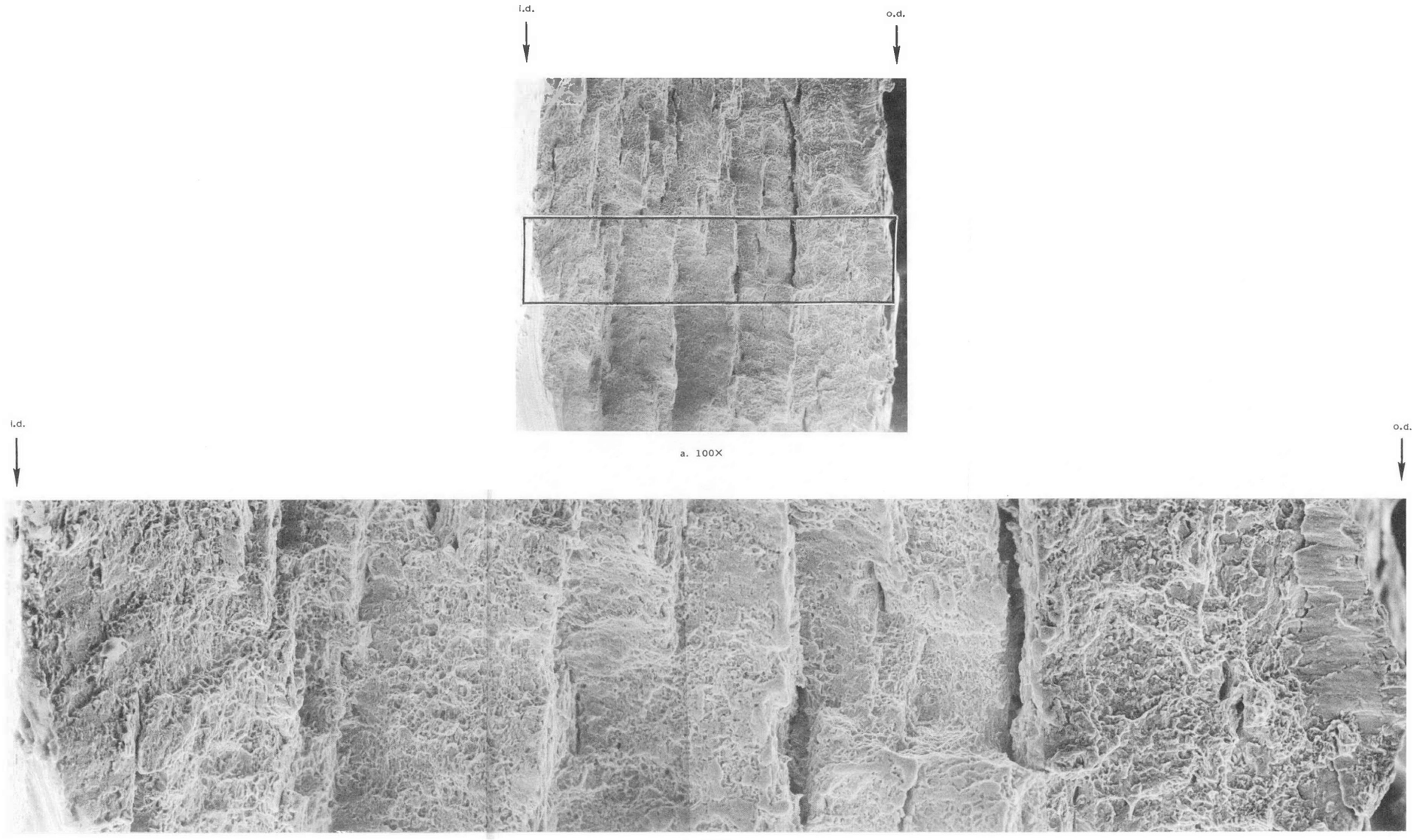

Figure 3.2-33. Rod KE-2225, Section 5C; Ductile Fracture Surface

Blank Page

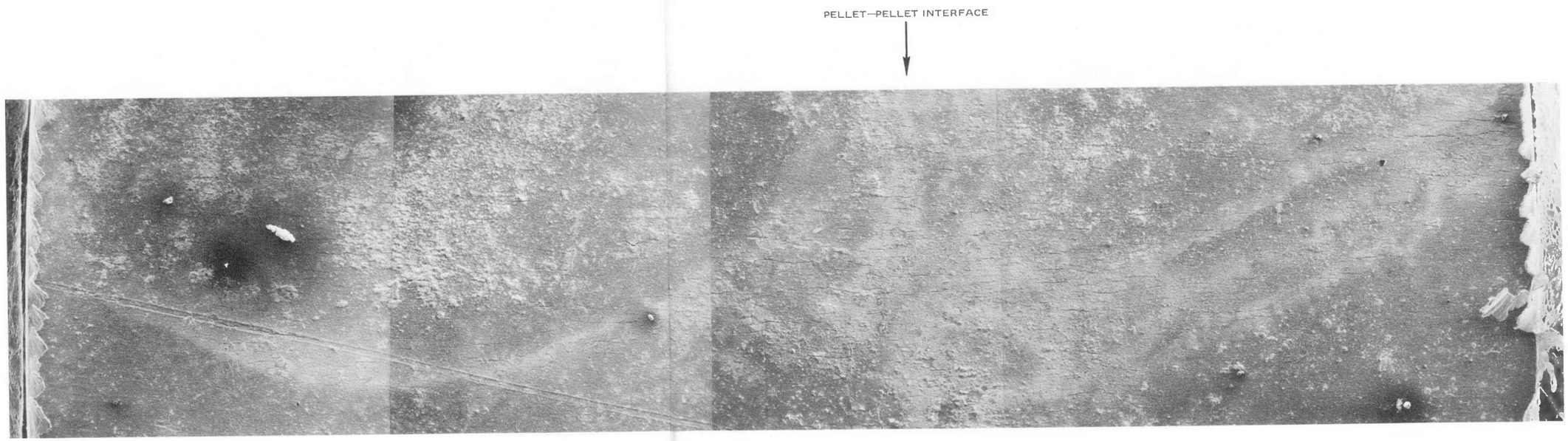

Figure 3.2-34. Rod KE-2225, Section 5D, Flattened 40X

Blank Page

a. SECONDARY ELECTRON IMAGE

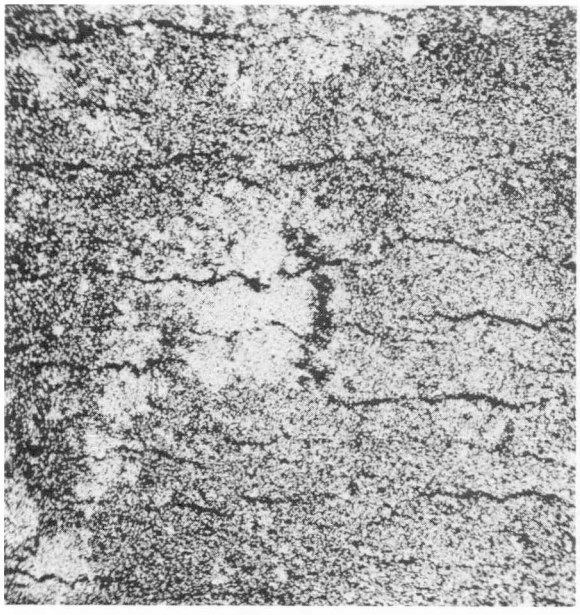

b. UM_{β} X—RAY MAP

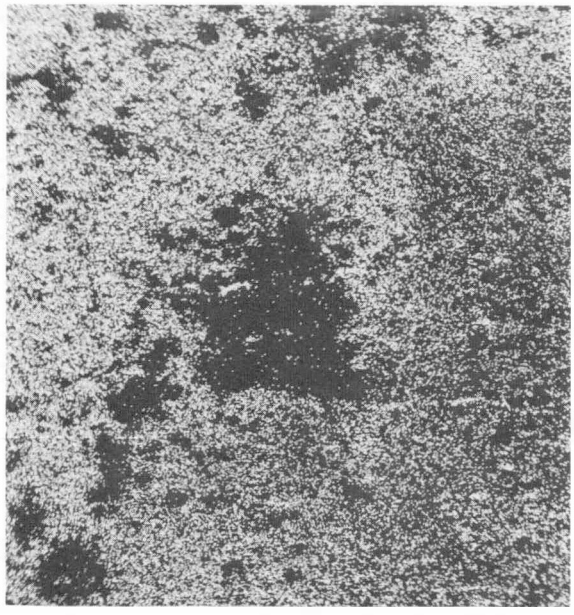

c. Zr L_{α} X—RAY MAP

Figure 3.2-35. Rod KE-2225, Section 5D, Flattened; Area Near Center of Figure 3.2-34 200X

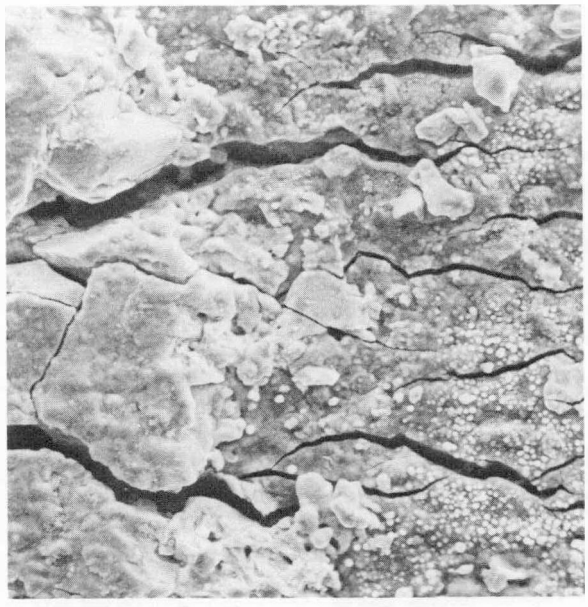

a. SECONDARY ELECTRON IMAGE

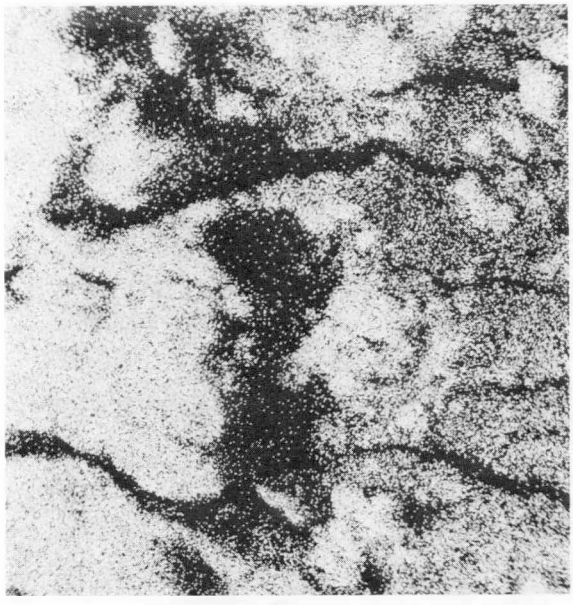

b. UM β X-RAY MAP

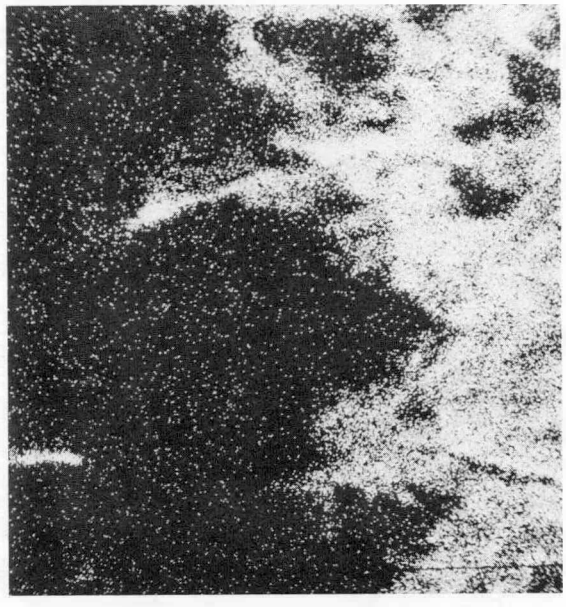

c. Zr L_{α} X-RAY MAP

Figure 3.2-36. Rod KE-2225, Section 5D, Flattened; Area in Center of Figure 3.2-35 1000X

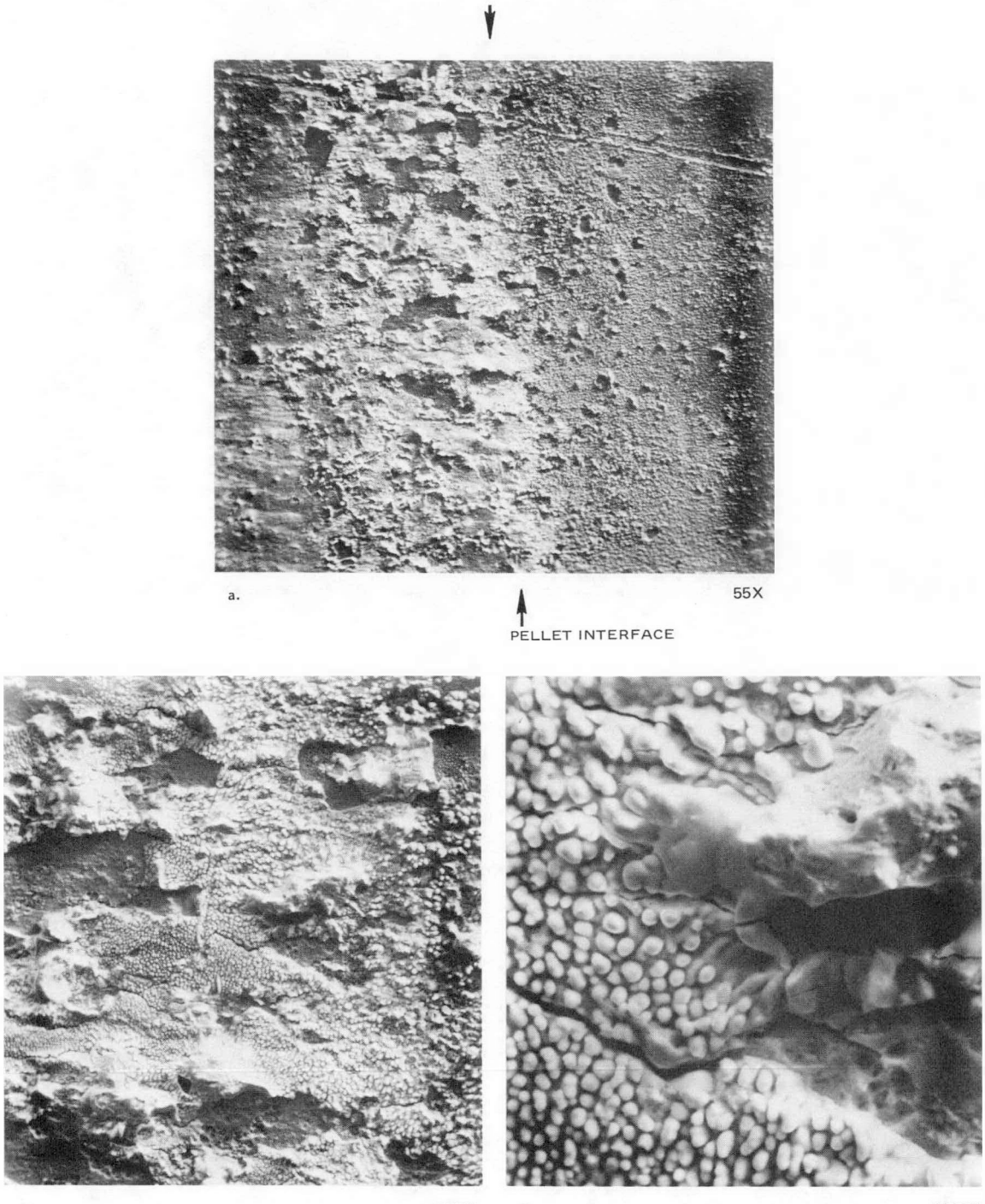

Figure 3.2-37. Rod KE-2225, Section 5D, Flattened; Area Including Location of Fuel Pellet-To-Pellet Interface

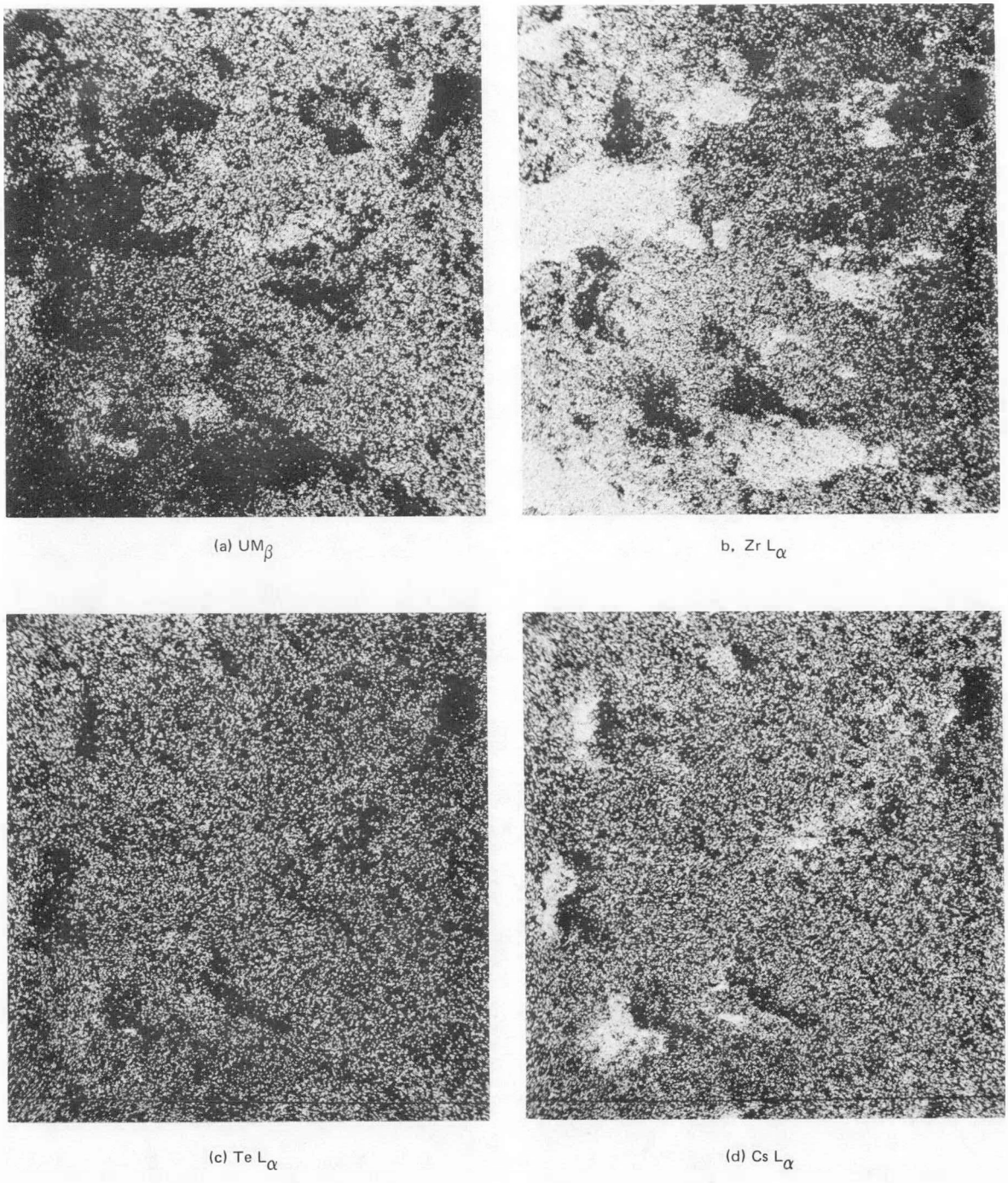

(a) UM_{β}

b. $Zr\ L_{\alpha}$

(c) $Te\ L_{\alpha}$

(d) $Cs\ L_{\alpha}$

Figure 3.2-38. Rod KE-2225, Section 5D; Area of Figure 3.2-37b; X-Ray Maps 200X

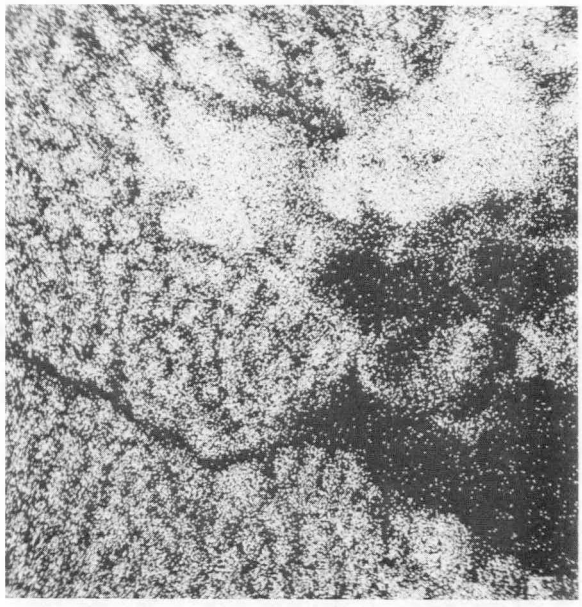

(a) UM_{β}

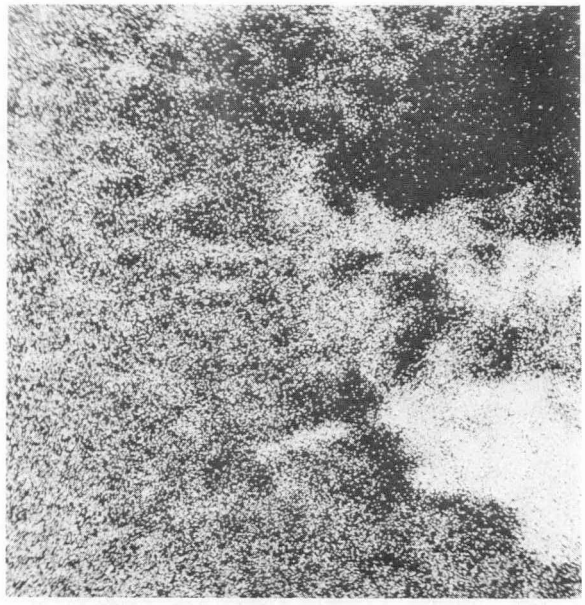

(b) Zr L_{α}

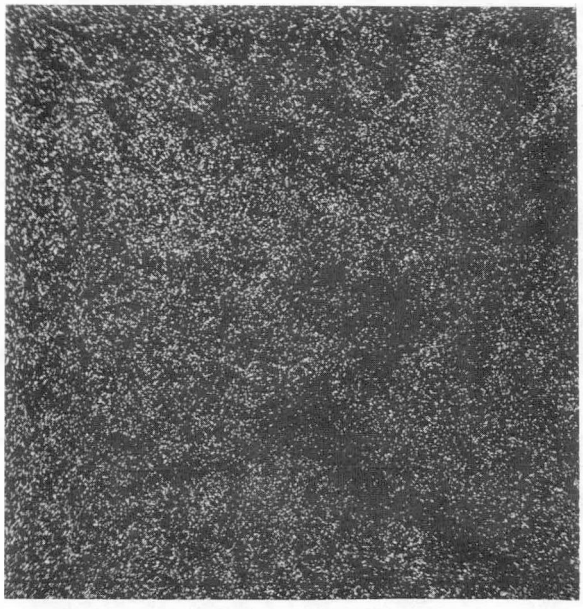

(c) Te L_{α}

(d) Cs L_{α}

Figure 3.2-39. Rod KE-2225, Section 5D; Area of Figure 3.2-37c; X-Ray Maps 1000X

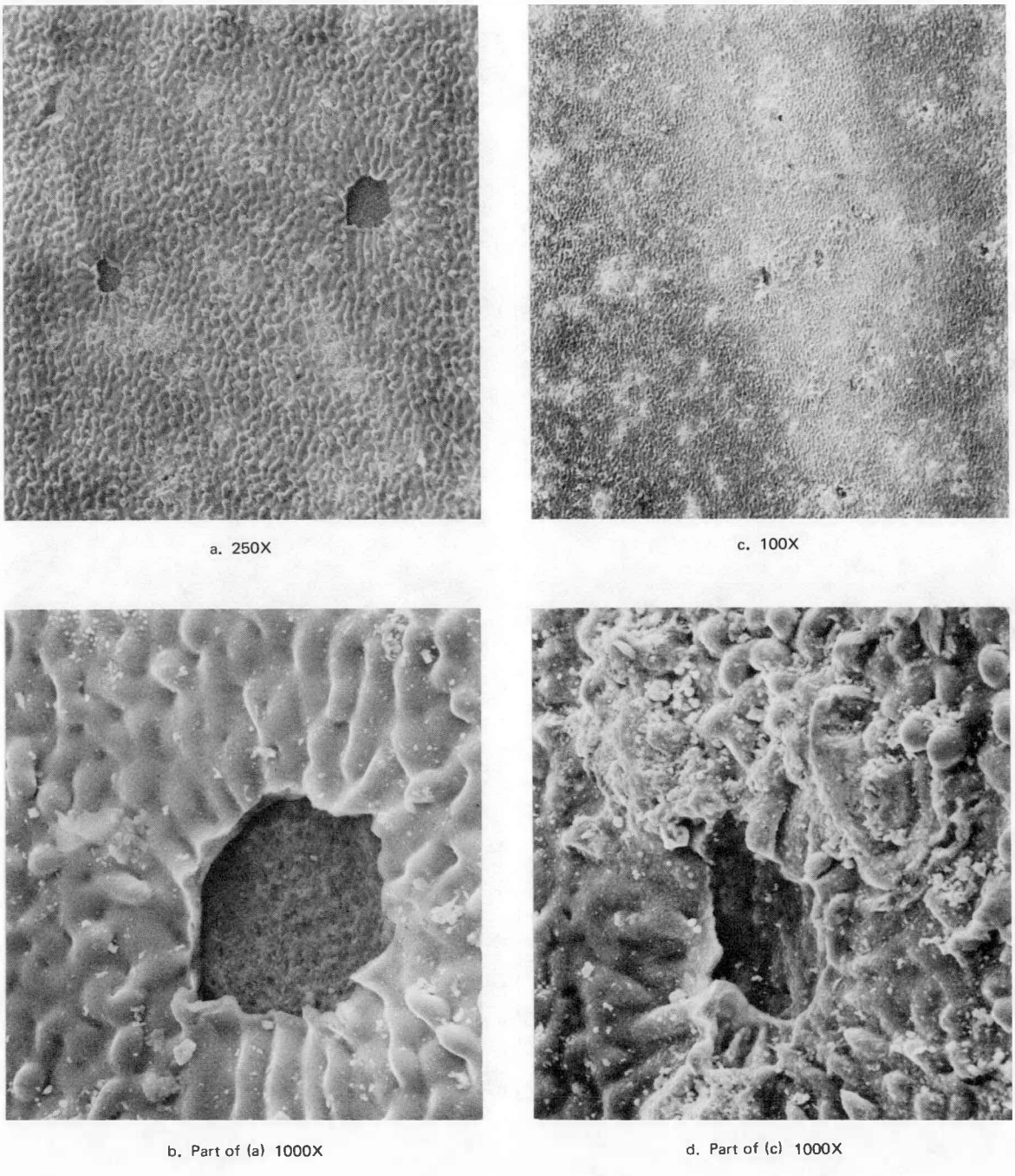

a. 250X

c. 100X

b. Part of (a) 1000X

d. Part of (c) 1000X

Figure 3.2-40. Rod KE-2225, Section 5A; Interaction Layer on Inside Cladding Surface

PELLET INTERFACE

b. NEAR CENTER OF (a), WITH PELLET–PELLET INTERFACE MARKINGS

PELLET INTERFACE

200X

c. CENTER OF (b) 1000X

a. 40X

Figure 3.2-41. Rod KD-0451, Section 5A, Flattened

Blank Page

a. 200X

b. CENTER OF (a) 1000X

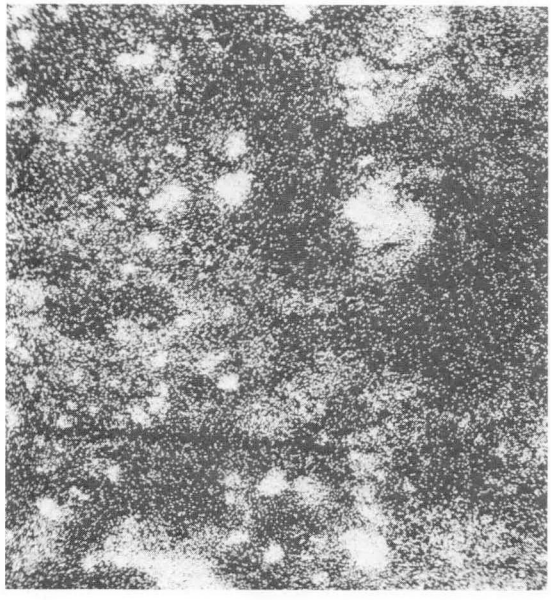

c. UM_{β} X—RAY MAP OF AREA (b) 1000X

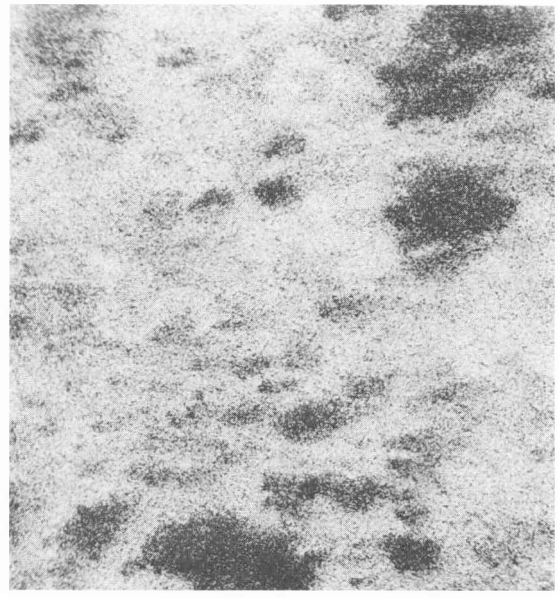

d. Zr L_{α} X—RAY MAP OF AREA (b) 1000X

Figure 3.2-42. Rod KD-0451, Section 5A, Flattened; Area Marked in Figure 3.2-41

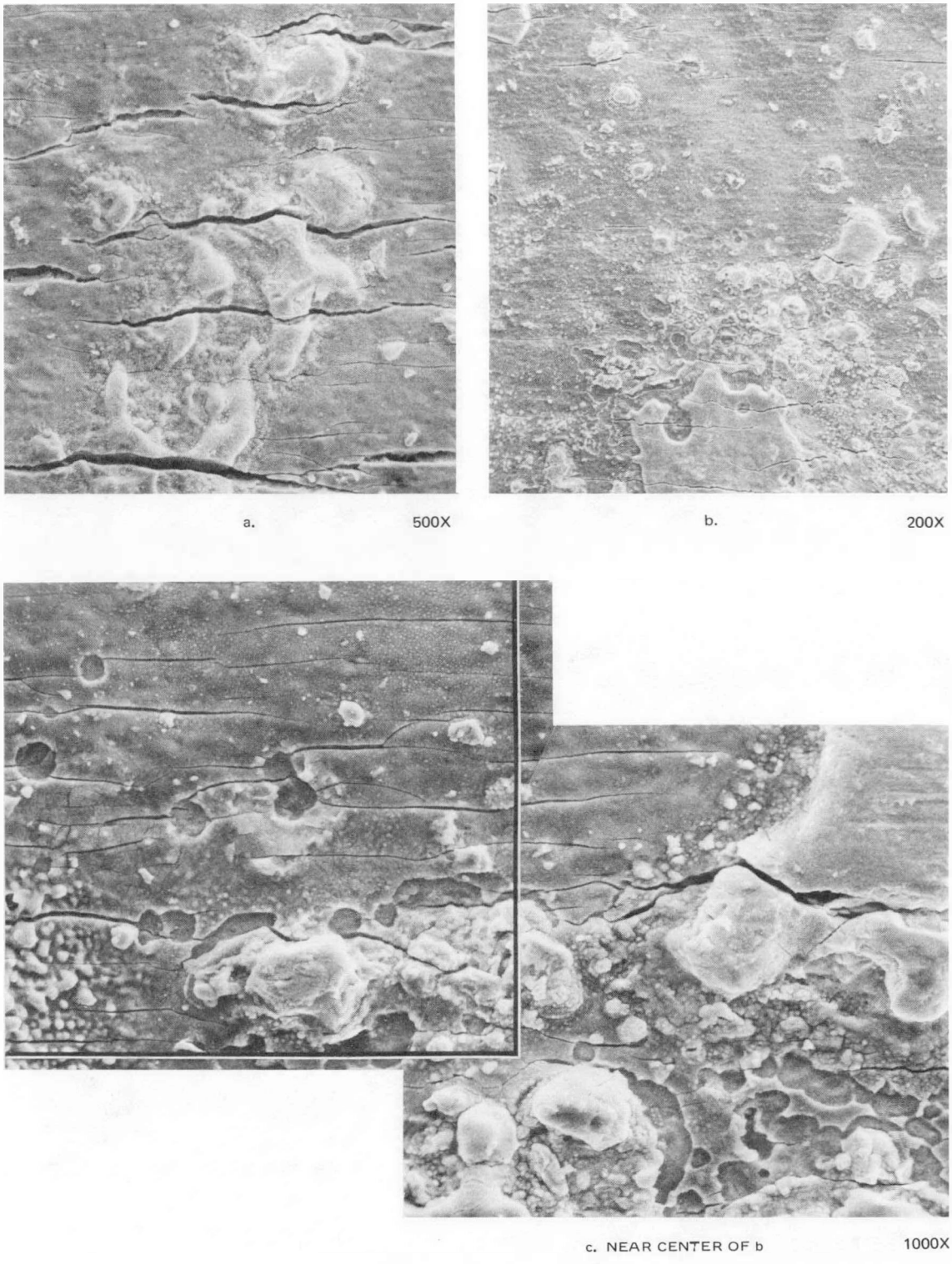

Figure 3.2-43. Rod KD-0451, Section 5B, Flattened

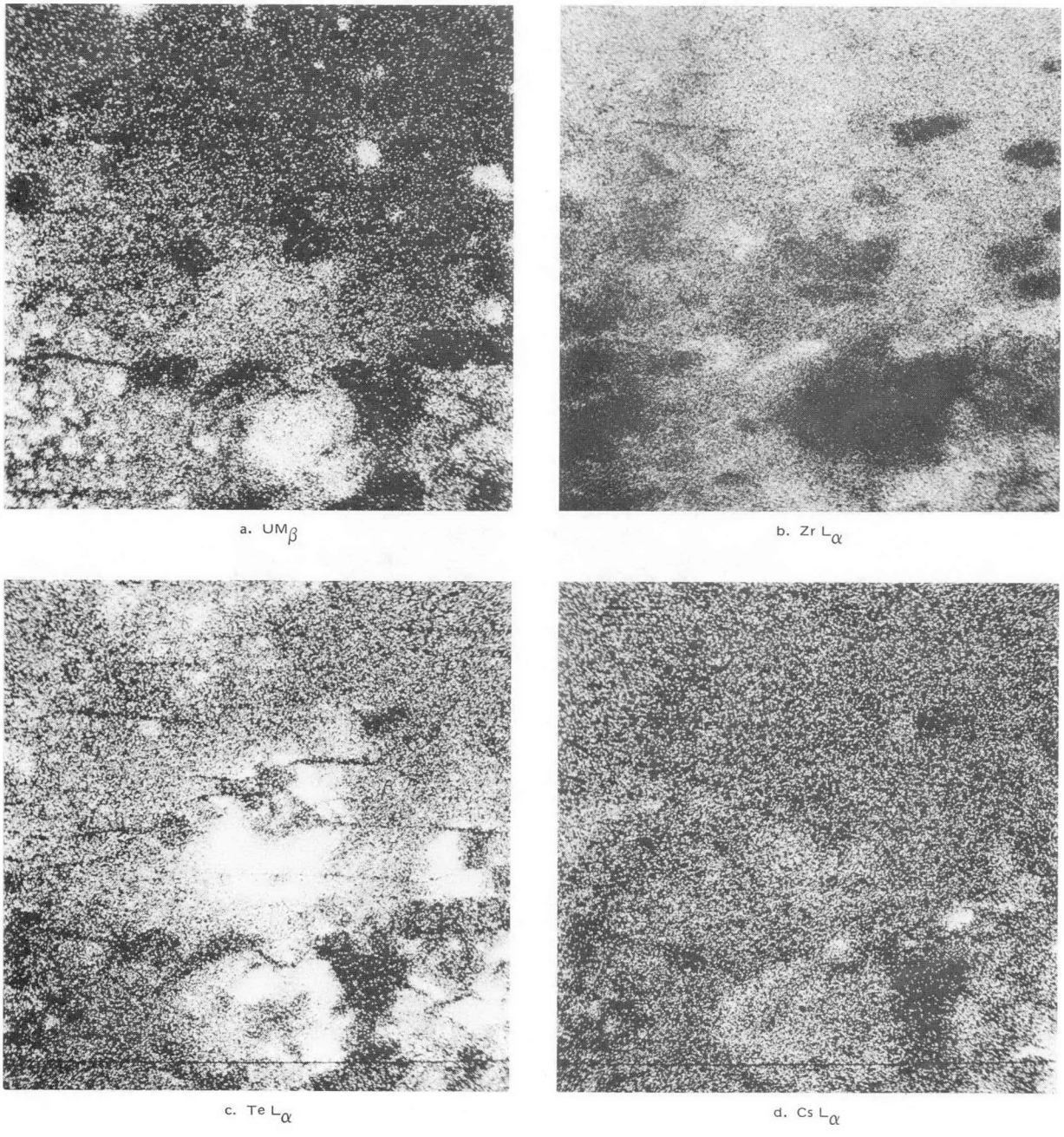

Figure 3.2-44. Rod KD-0451, Section 5B, Left Half of Area in Figure 3.2-43c; X-Ray Maps 1000X

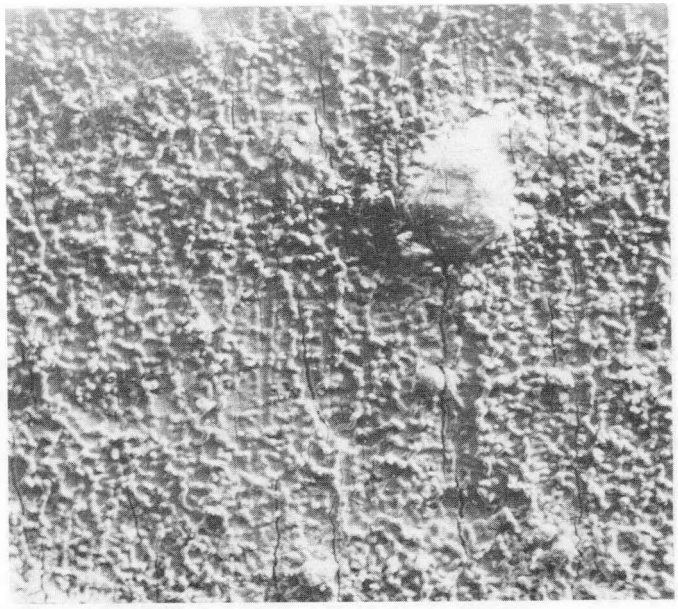

a. 200X

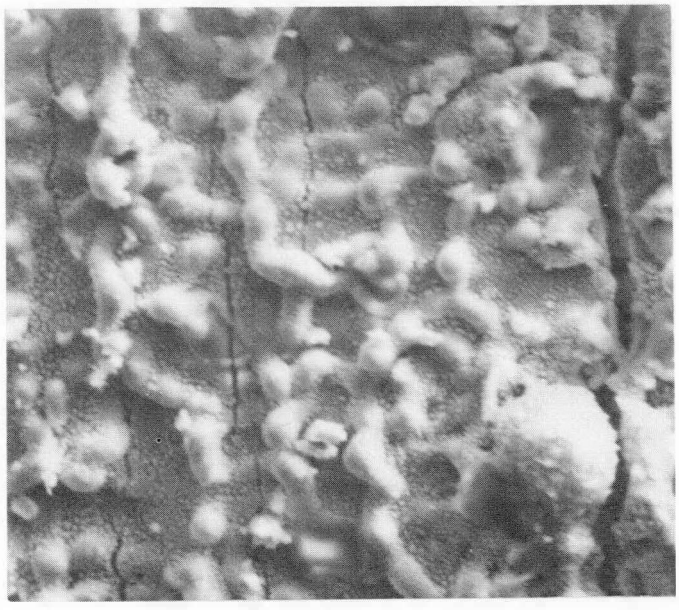

b. CENTER OF (a) 1000X

Figure 3.2-45. Rod KD-0451, Section 6, Flattened

on the verge of coalescing into beads. However, these "ropes" are rich in Zr (see Figure 3.2-46b) while the "beads" in rod KE-2225 were rich in U (compare with Figures 3.2-37c and 39a). Numerous small UO_2 particles are bonded to the cladding. Small amounts of Te (Figure 3.2-46c are uniformly distributed; Te is associated with the ropes as well as with UO_2. Cesium is located in concentrated pools in pockets formed by the ropes or by UO_2 particles (Figures 3.2-46d and 45b). The absence of water in sample preparation probably has preserved this Cs.

In Section 15 at the high burnup end of the rod (but no power transient) the features on the cladding inner surface are much smaller (Figure 3.2-47) than in the other sections. Many UO_2 particles of various sizes are bonded to the cladding. The interaction layer is bumpy and undulating but apparently of rather uniform composition (within the spatial resolution of the X-ray mapping technique--Figure 3.2-48). Small amounts of Cs are associated with UO_2 and the amount of Te is hardly above background.

Metallography

Rod KE-2225

The sample cut next to the flattened piece [29.2 to 31.8 cm (11-1/2 to 12-1/2 inches) from the bottom of the rod] shows a few small fuel particles bonded to the cladding (Figure 3.2-49b). An occasional pit (Figure 3.2-49a) appears to be insignificant; it has not served for crack initiation. The ring cut next to the incipient cracks [36.3 to 36.8 cm (14.3 to 14.5 inches) from the bottom] does not contain any cracks. It shows the same features as the other sample, e.g., occasional fuel particles bonded to the cladding (Figure 3.2-50a). The hydride distribution is uniform and the amount of hydrides appears small (Figure 3.2-50b). In the sample cut through fracture A the amount of hydrides is slightly larger (Figure 3.2-51) and apparently their orientation has been modified by the stress pattern at the tip of the incipient crack. The hydrides are oriented predominantly circumferentially out to the crack tip; beyond that, near the outside surface of the cladding, the orientation is predominatly radial Figures 3.2-52). These results tend to confirm the interpretation given the flaky or quasi-cleavage fractographic features (see above Section a). The longitudinal section [29.2 to 31.8 cm (11-1/2 to 12-1/2 inches) from the bottom] has long hydride stringers (Figure 3.2-53). From Figures 3.2-50 to 53 it is concluded that the hydrides form long ribbons or bands in axial direction with a length many times their width.

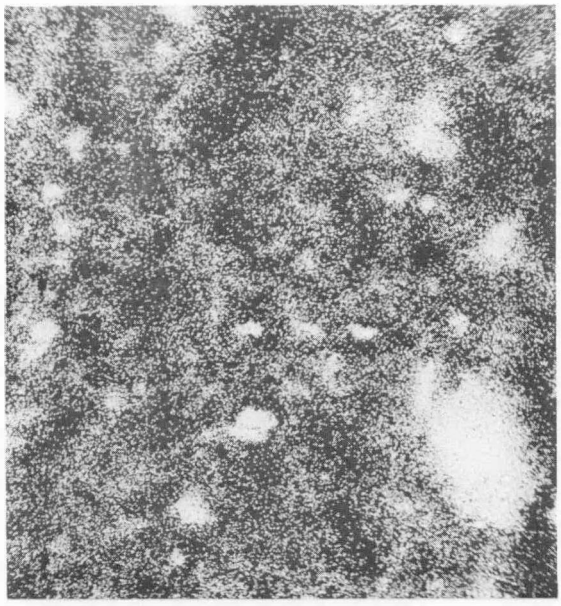

(a) UM_{β}

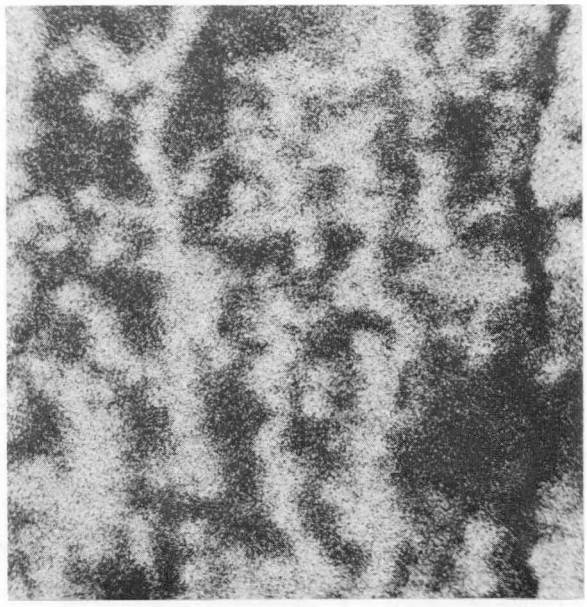

(b) ZrL_{α}

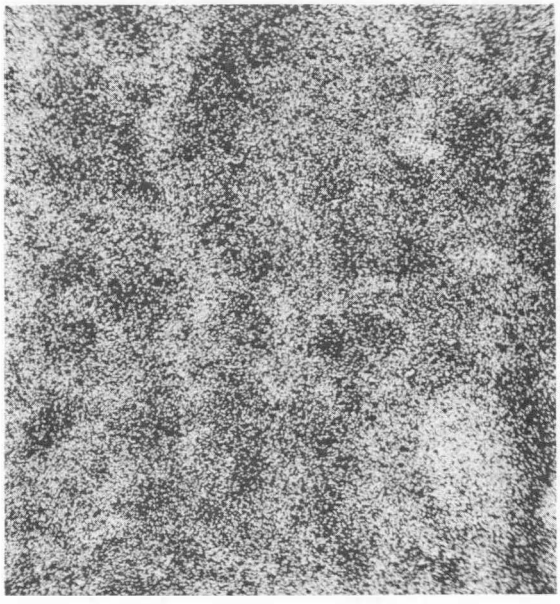

(c) TeL_{α}

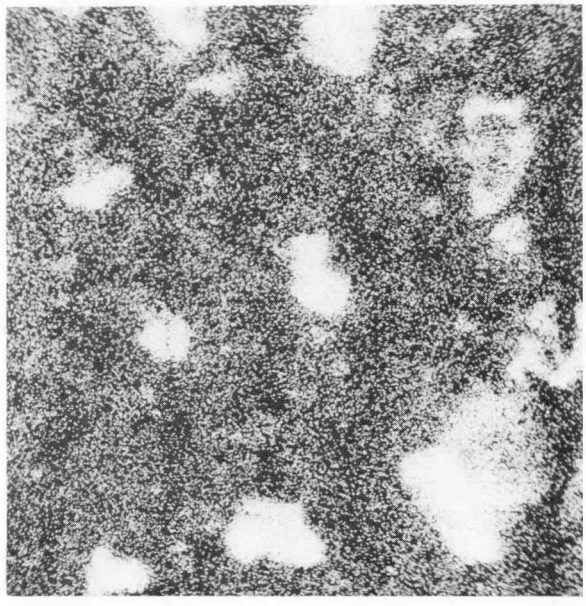

(d) CsL_{α}

Figure 3.2-46. Rod KD-0451, Section 6, Area of Figure 3.2-45b; X-Ray Maps 1000X

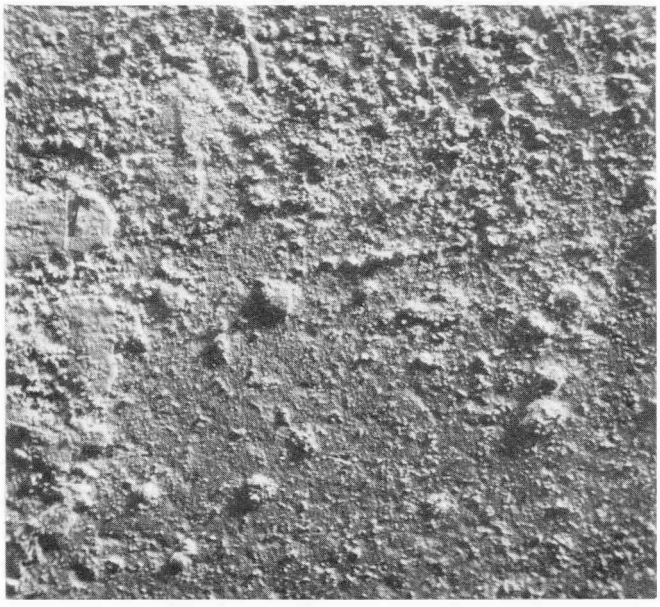

a. 55X

b. CENTER OF (a) 200X

c. CENTER OF b, 1000X

Figure 3.2-47. Rod KD-0451, Section 15, Flattened

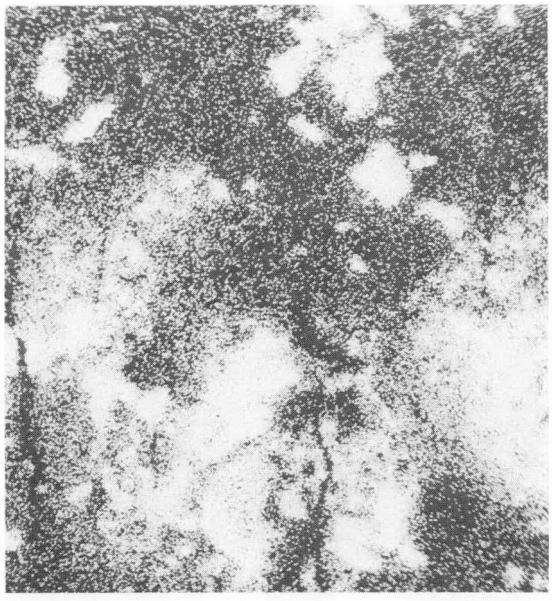

(a) UM_{β}

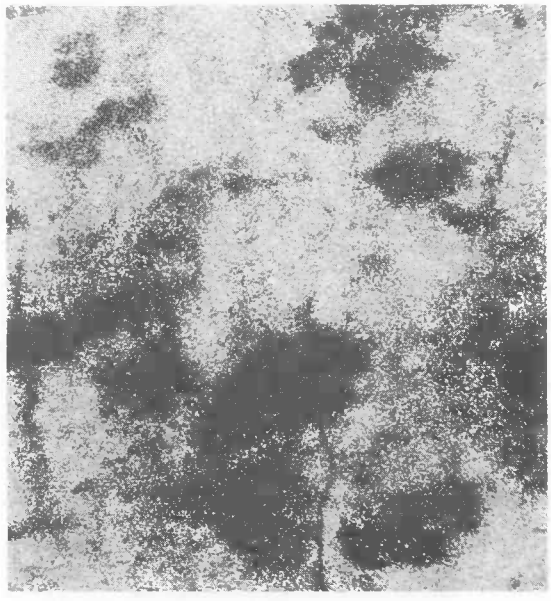

(b) ZrL_{α}

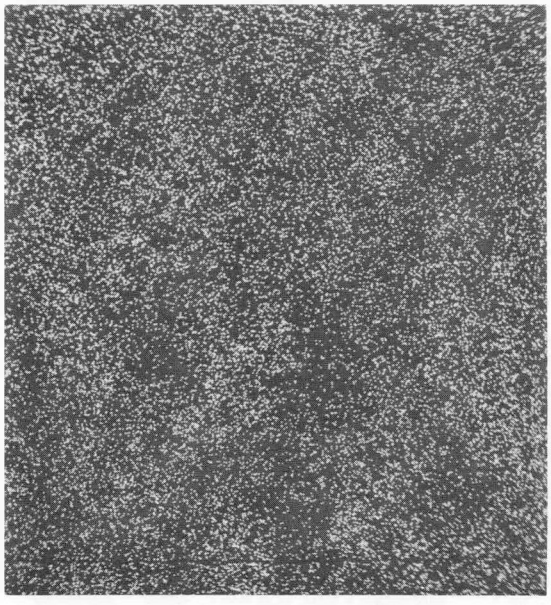

(c) TeL_{α}

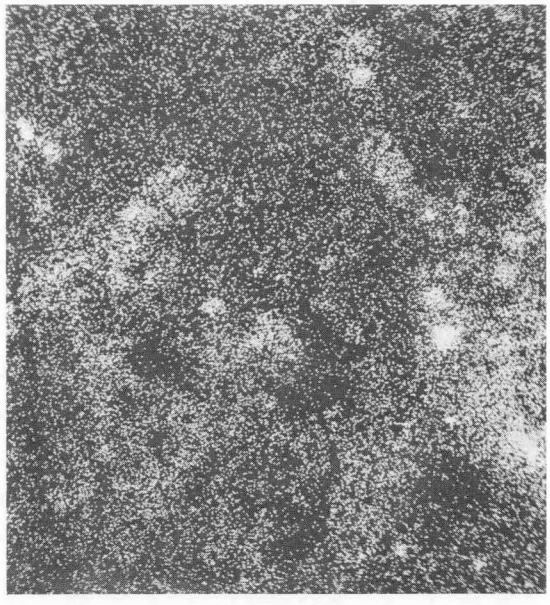

(d) CsL_{α}

Figure 3.2-48 Rod KD-0451, Section 15, Area of Figure 3.2-47c; X-Ray Maps

a. SMALL PIT ON INSIDE CLADDING SURFACE

b. FUEL BONDED TO CLADDING IN PIT

Figure 3.2-49. Rod KE-2225, Section 5, Metallographic Cross Section 11.5 to 12.5 Inches from Bottom of Rod, Unetched 500X

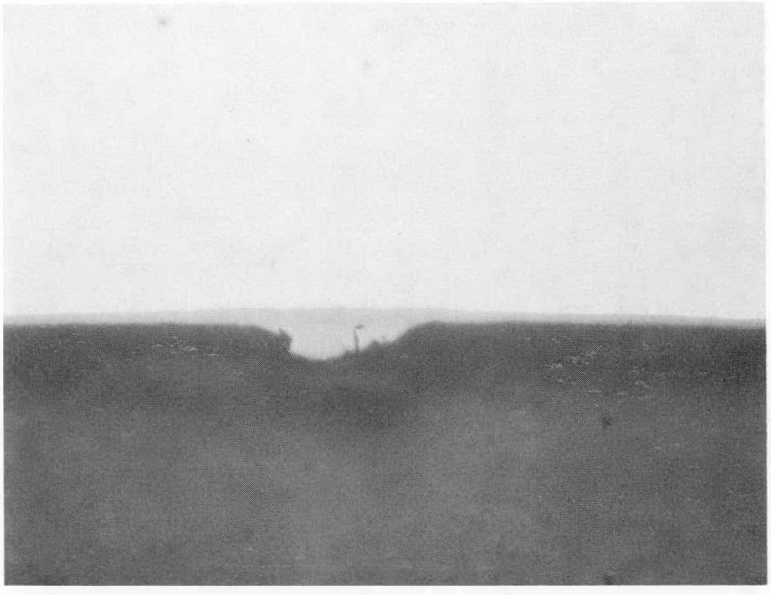

a. UNETCHED, FUEL BONDED TO CLAD, 500X

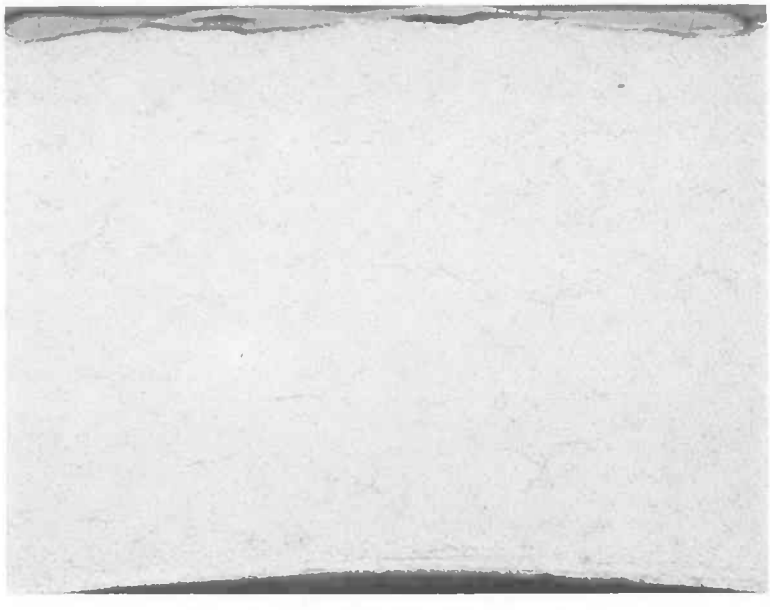

b. ETCHED, SMALL AMOUNT OF HYDRIDES, 100X

Figure 3.2-50. Rod KE-2225, Section 5, Metallographic Cross Section 14.3 to 14.5 Inch from Bottom of Rod

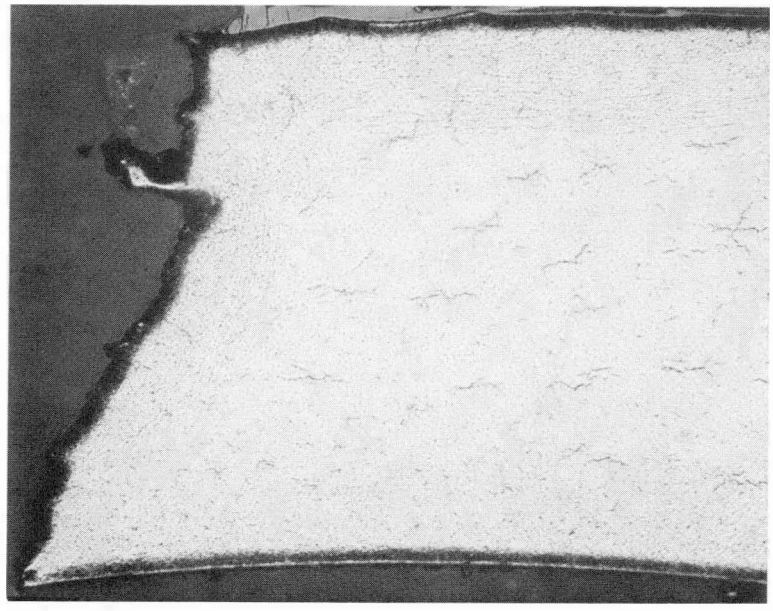

Figure 3.2-51. Rod KE-2225, Section 5, Metallographic Cross Section Through Crack A, Etched 100X

a. BRIGHT FIELD

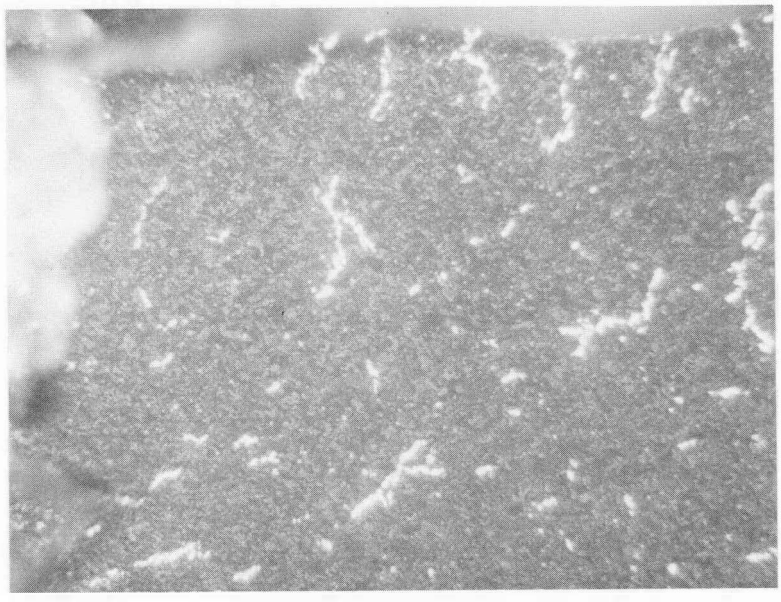

b. POLARIZED LIGHT

Figure 3.2-52. Rod KE-2225, Section 5, Metallographic Cross Section Through Crack A, at Outside Cladding Surface, Etched 250X

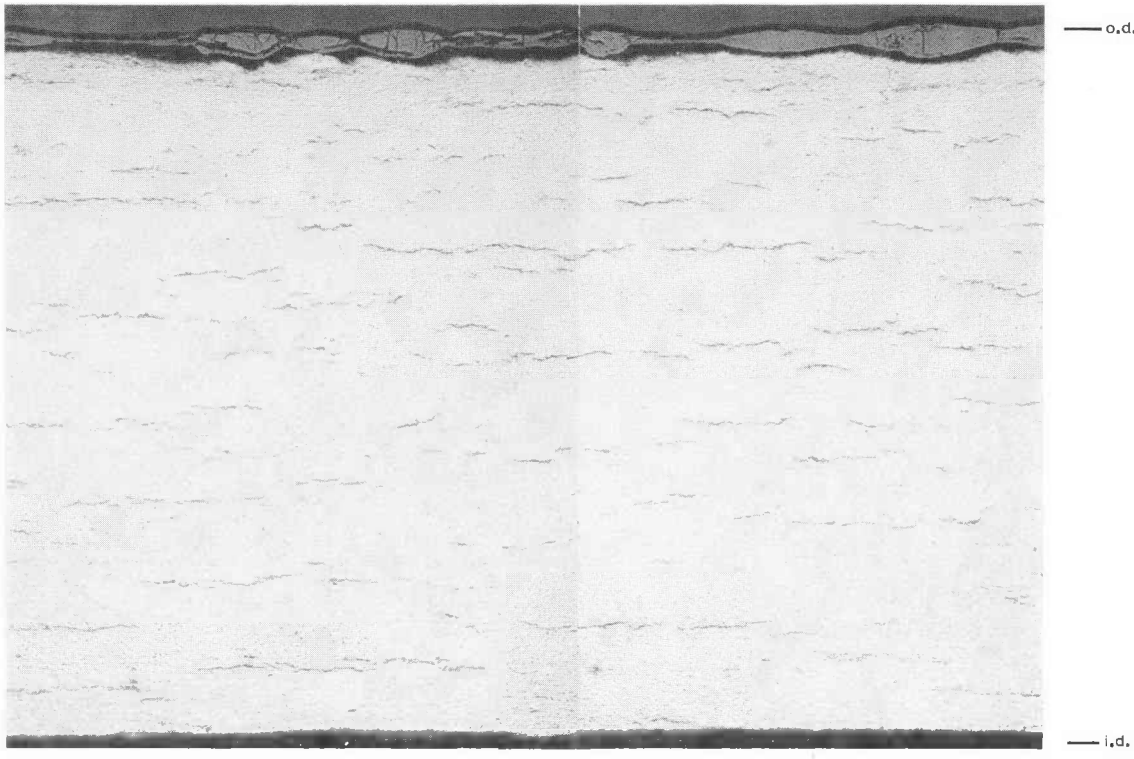

100X

250X

Figure 3.2-53. Rod KE-2225, Section 5, 11-1/2 to 12-1/2 Inches from Bottom of Rod, Longitudinal Metallographic Section, Etched

Rod KD-0451

In the section at the 25.4 to 27.9 cm (10 to 11 inches) axial location no defects were found. Occasionally, fuel particles are bonded to the cladding (Figure 3.2-54). The section 297.2 to 299.7 cm (117 to 118 inches) from the bottom has a few oxide-filled pits on the cladding outer surface (Figure 53a). On the cladding inner surface shallow pits (Figure 3.2-55a and bonded fuel (Figure 3.2-55c) are seen. The bonding layer between ZrO_2 and UO_2 in Figure 3.2-55c contains round features corresponding in size to the beaded surfaces seen in SEM micrographs of the cladding inner surface (e.g., Figure 3.2-32b). In one place a shallow spalling crack parallel to the surface was observed (Figure 3.2-55d). However, this crack did not propagate into the cladding.

Transmission Electron Microscopy

Rod KD-0451

The microstructures of all ring sections of this rod consist of partially recrystallized material characteristic of the post-forming stress relief anneal and examples are shown in Figure 3.2-56. In the recrystallized grains, corduroyed images, Figure 3.2-57, were often observed and were consistent with such features generally observed in irradiated Zircaloy (17). In the unrecrystallized regions $\vec{c} + \vec{a}$ dislocations introduced during the forming process could be observed when the basal planes were diffracting as shown in Figure 3.2-58. The Burgers vectors of these dislocations have a $\vec{c}$-axis component; purely $\vec{a}$-type dislocations are out of contrast here. The inference that they are $\vec{c} + \vec{a}$ is based on the crystallographic constraints (18) and on experience (19). The radiation damage observable in recrystallized material consists of small black dots, illustrated in Figure 3.2-59 which are characteristic of unresolvable dislocation loops.

In the two outermost sections of this rod, the low power bottom section (No. 3) and also the plenum section (No. 19), no unusual features were observed which could be related to in-service deformation. However, in the intermediate cladding sections, various features were observed that may be related to such deformation. The most common observations consist of defected recrystallized grains with features shown in Figure 3.2-60. From the diffracted spots generated by these features, they could be analyzed as hydrides although it was difficult to distinguish them from twins in some cases.

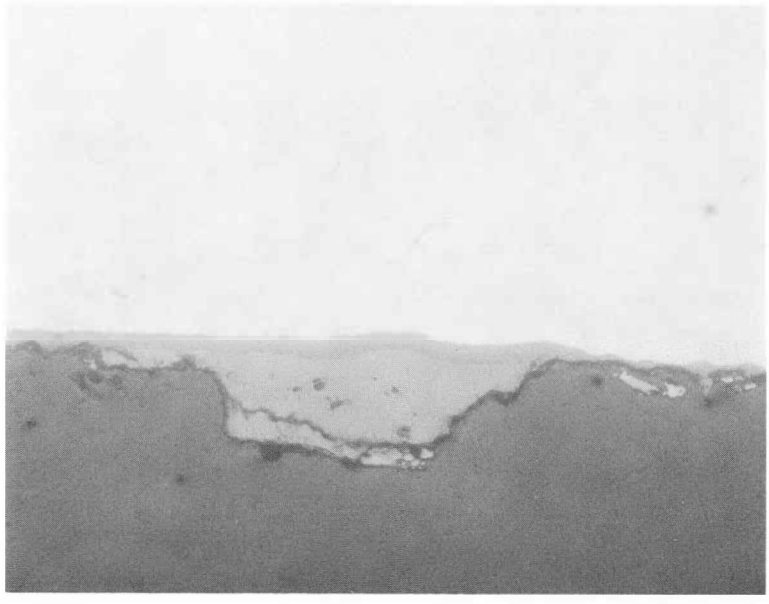

Figure 3.2-54. Rod KD-0451, Section 5, Metallographic Cross Section 10 to 11 Inches from Bottom of Rod, Unetched; Fuel Bonded to Cladding with Smooth Interaction Layer

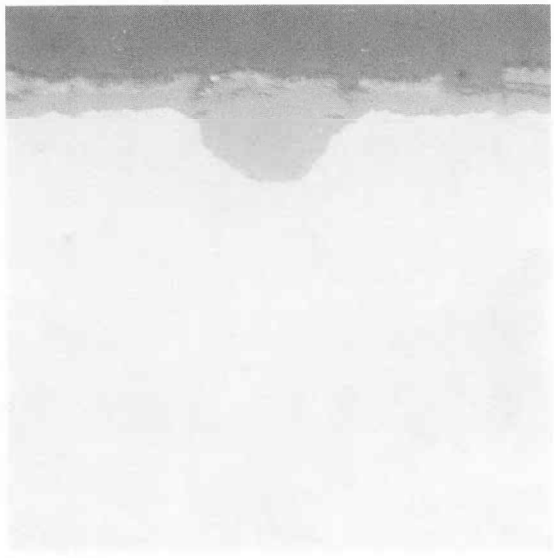

a. OXIDE—FILLED PIT ON OUTSIDE OF CLADDING

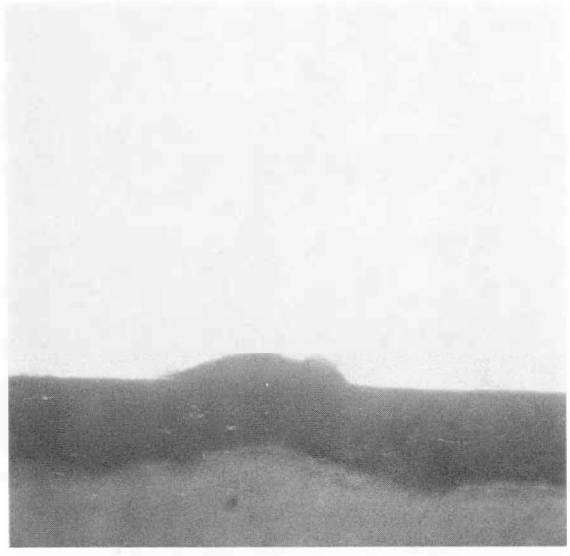

b. SHALLOW PIT ON INSIDE OF CLADDING

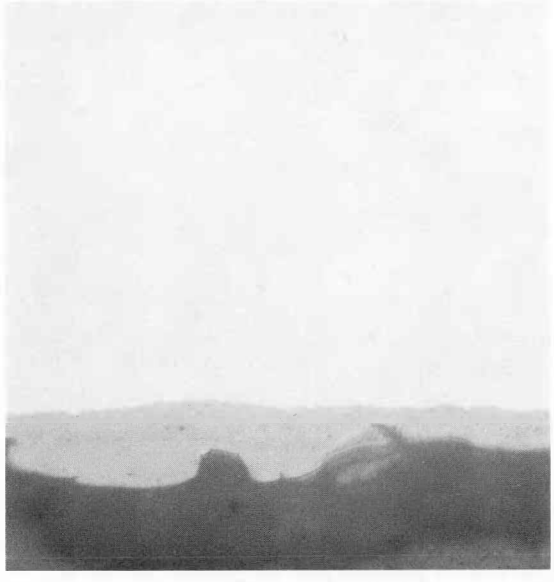

c. FUEL BONDED TO CLADDING WITH BEADED INTERACTION LAYER

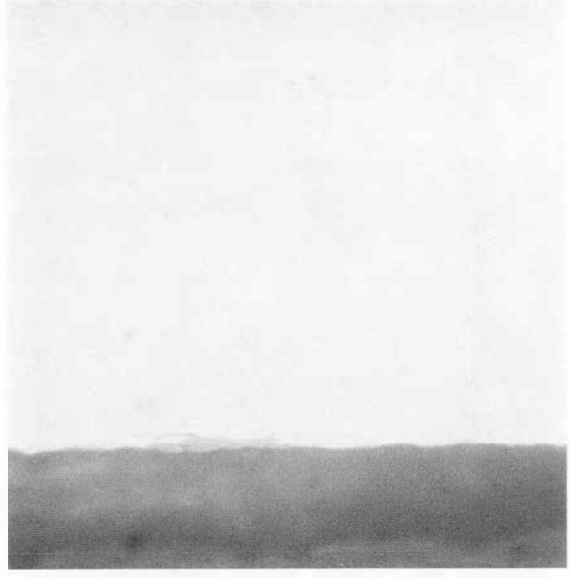

d. SHALLOW SPALLING CRACK ON INSIDE OF CLADDING

Figure 3.2-55. Rod KD-0451 Section 16, Metallographic Cross Section 117 to 118 Inches from Bottom of Rod, Unetched 500X

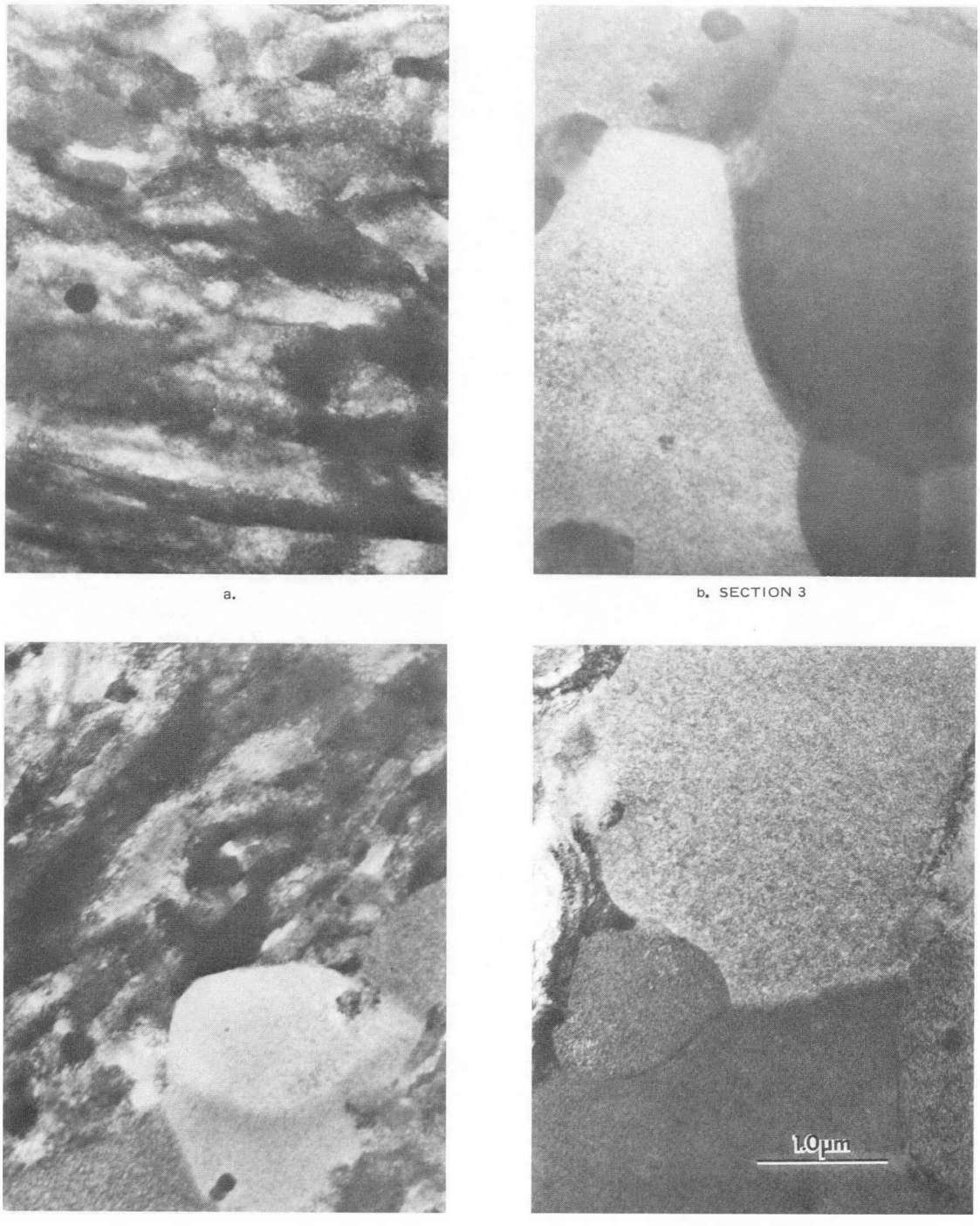

a.

b. SECTION 3

c.

d. SECTION 19

Figure 3.2-56. Microstructures of Fuel Rod KD-0451 Showing Mixed Unrecrystallized and Recrystallized Portions

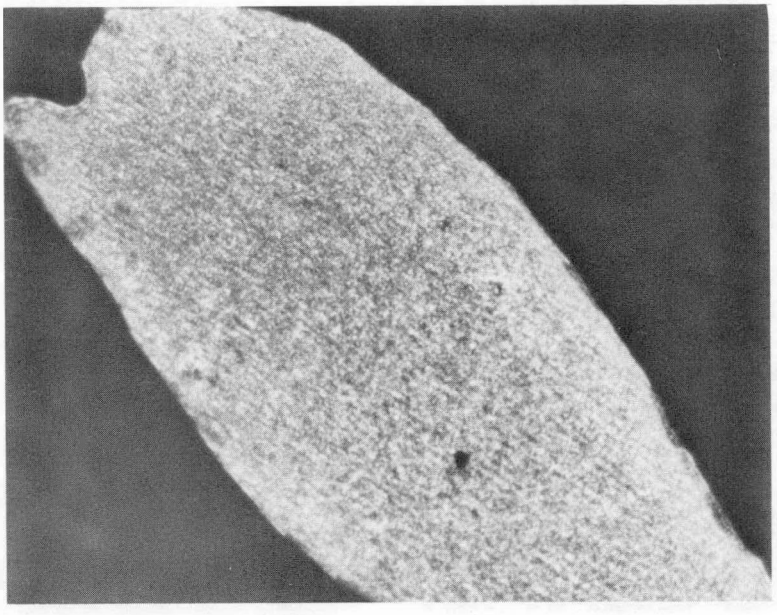

a. SECTION 19

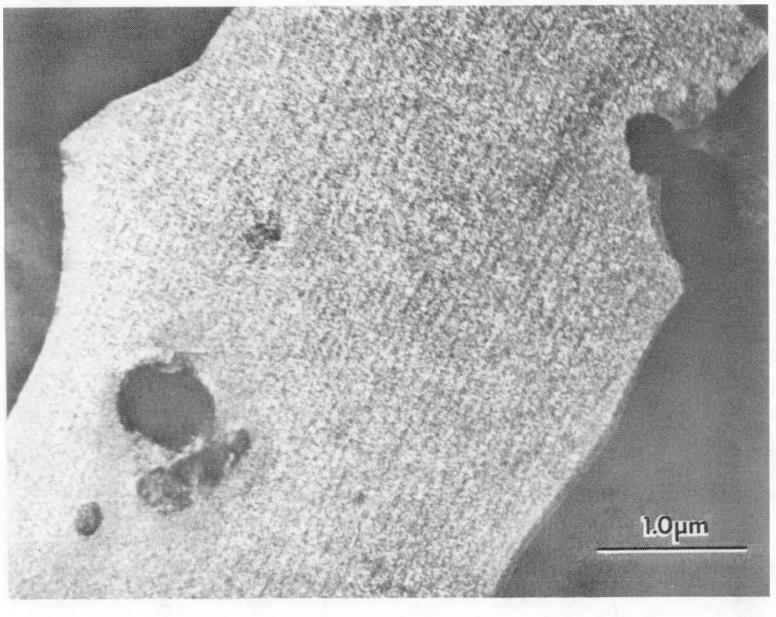

b. SECTION 7

Figure 3.2-57. Corduroy Image Effects in Fuel Rod KD-0451

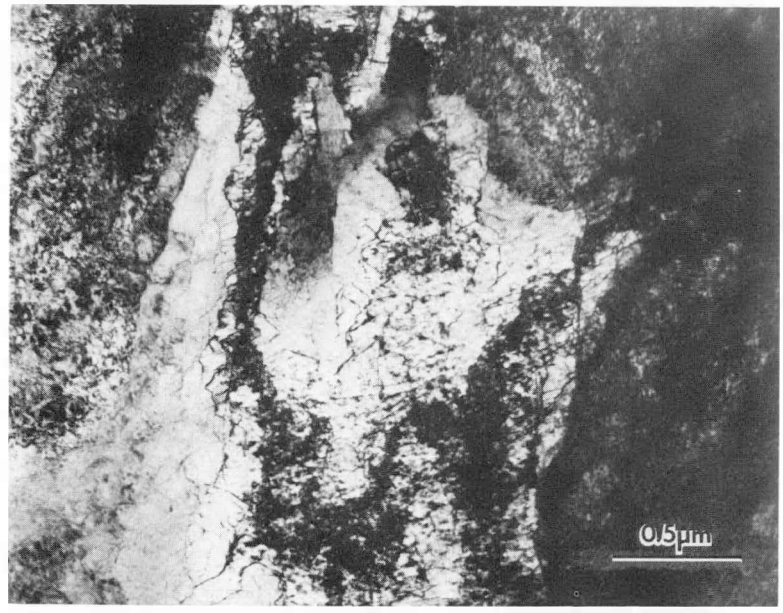

a. SECTION 3, BRIGHT—FIELD IMAGE

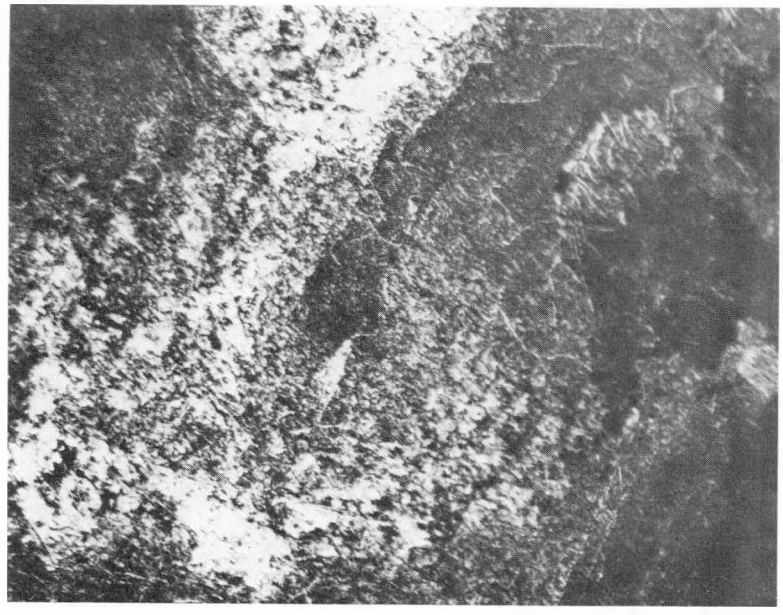

b. SECTION 16, DARK—FIELD IMAGE

Figure 3.2-58. $\bar{c} + \bar{a}$ Dislocations in Unrecrystallized Areas of Fuel Rod KD-0451 Observed with Basal Planes Diffracting

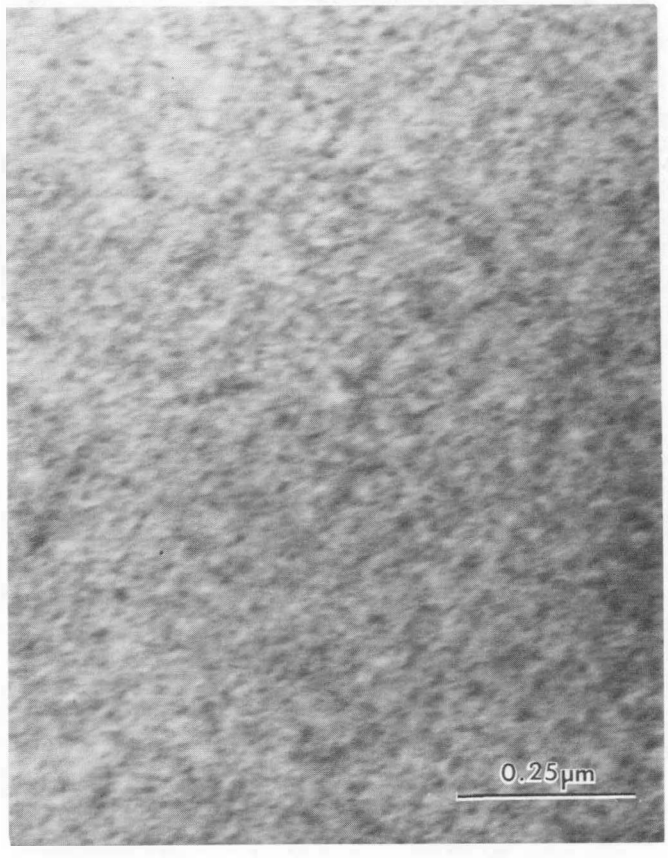

Figure 3.2-59. "Black Spot" Radiation Damage in Recrystallized Portion of Fuel Rod KD-0451, Section 7

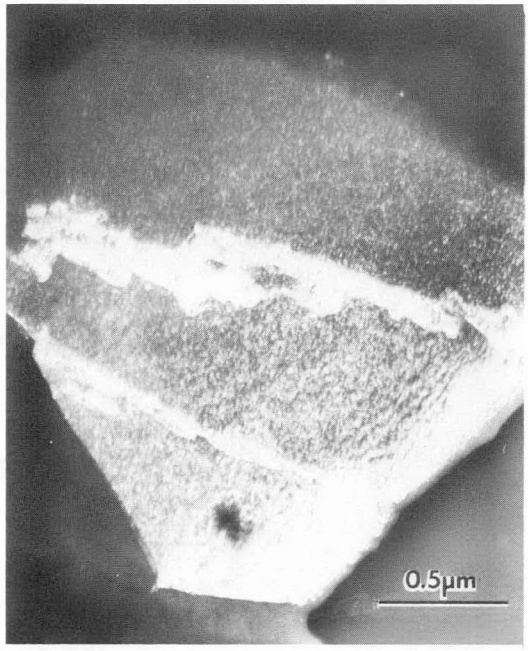

a. SECTION 5, DARK—FIELD IMAGE

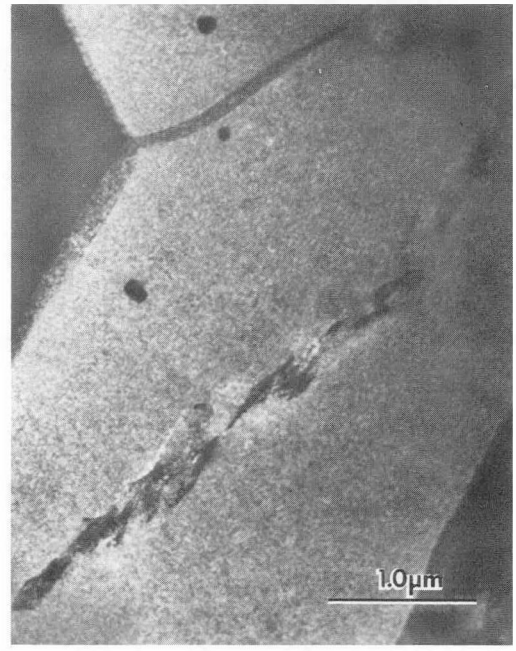

b. SECTION 5, BRIGHT—FIELD IMAGE

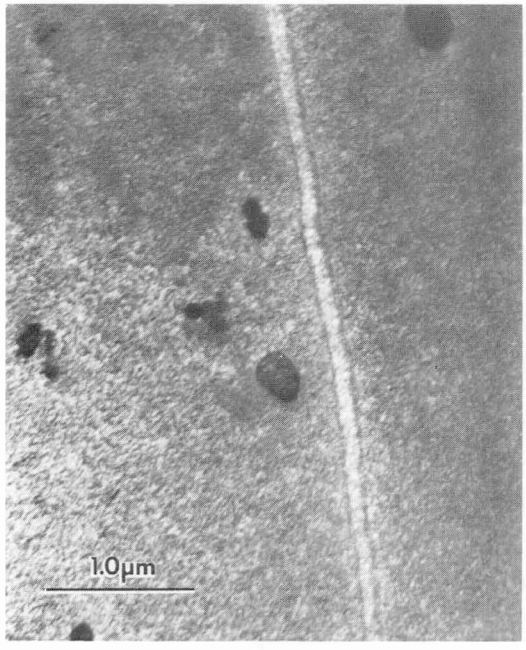

c. SECTION 7, BRIGHT—FIELD IMAGE

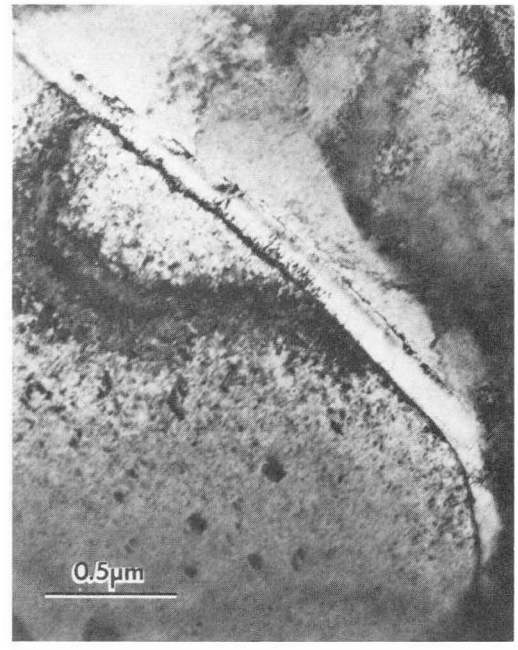

d. SECTION 16, BRIGHT—FIELD IMAGE

Figure 3.2-60. Hydrides in High Power and High Burnup Regions of Fuel Rod KD-0451

In the power transient region, a number of very weak features could be found which were in appearance like dislocation channels, although much healed by further irradiation. These features are illustrated in Figure 3.2-61. The contrast from these channels was such that they were entirely unnoticeable unless diffracting conditions were carefully adjusted (compare Figure 3.2-60c and Figure 3.2-61c obtained from the same grain). They did, however, extend from grain to grain and were parallel with traces of $\{10\bar{1}1\}$, $\{10\bar{1}2\}$, and $\{10\bar{1}3\}$ planes.

Hydrides were associated with features that could usually be traced from grain to grain, through both recrystallized and unrecrystallized material. The general direction of such features in the plane of the thin foil was along the axial direction of the cladding, that is, roughly parallel with the elongated unrecrystallized grains. When traced into the thicker foil regions, the features exhibited notable transparency compared to the surrounding material as illustrated in the composites of Figures 3.2-62a and b).

When the polished areas of the electron microscopy specimens were viewed optically, they appeared to be smooth and shiny, but striations could be observed when reflecting conditions were adjusted. It is important to note that these striations were observed on almost all the specimens, even that obtained from the plenum region as shown in Figure 3.2-63 and are generally along the axial direction of the cladding. The electropolished dish of a TEM specimen is approximately 0.13 mm (0.005 inch) deep, and the striations appear to be relatively straight on the steeply inclined edges of the dish indicating that the normal to the planar defect involved is in the radial direction of the tubing. It will be shown shortly that these features are hydride stringers.

Rod KE-2225

The one ring specimen for this rod was located approximately in the high transient power region and microstructural features were essentially the same as was observed in rod KD-0451. Figure 3.2-64 shows that a mixture of unrecrystallized and recrystallized material is present. Figure 3.2-65 illustrates some of the defected recrystallized grains including hydride plates and twinned material (Figure 3.2-65a) of sufficient volume to give an unmistakable α-zirconium diffraction pattern.

The composite of Figure 3.2-66 illustrates that the features which exhibit anomalous electron transmission are also present in the very thick regions of this

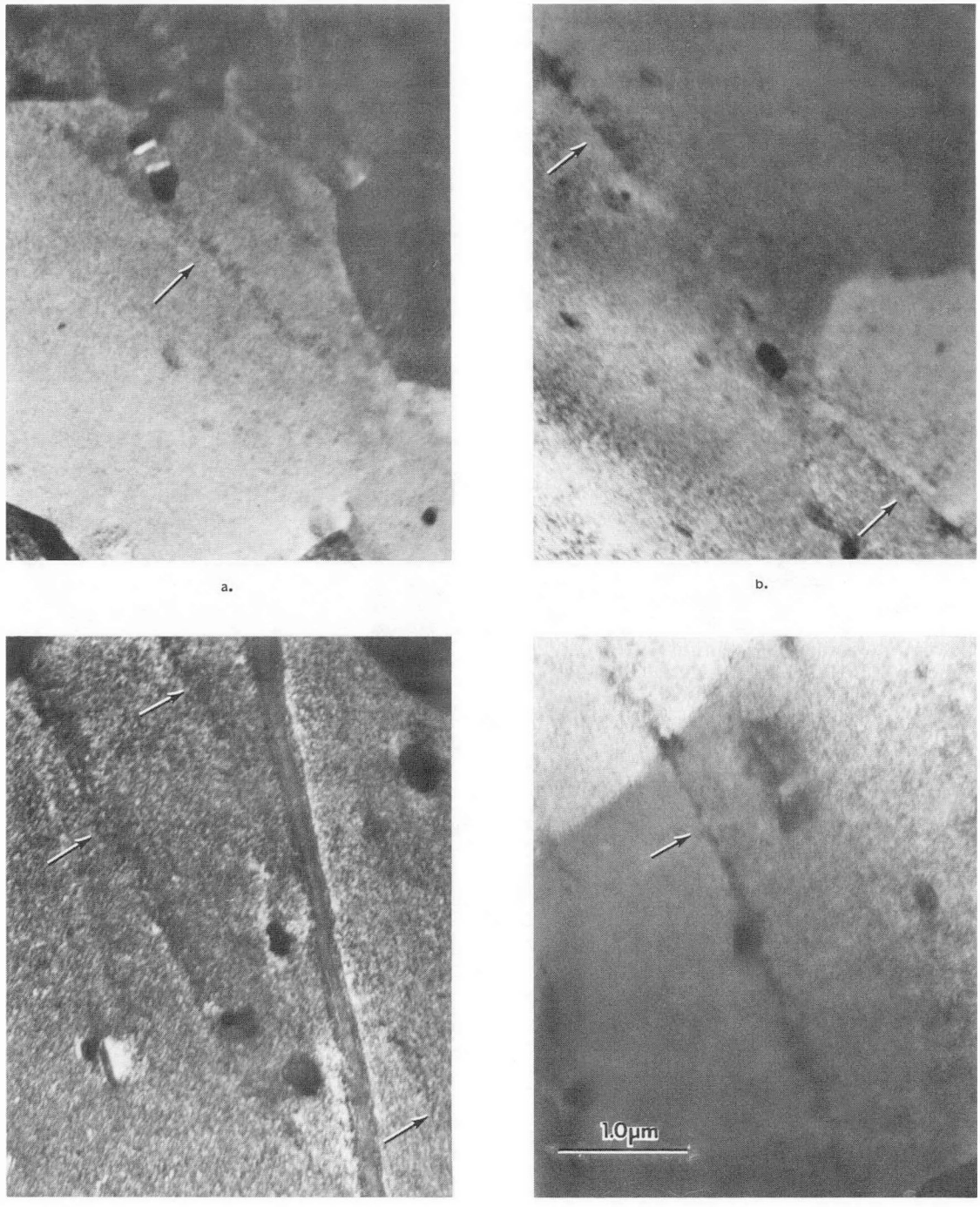

Figure 3.2-61. Faint Dislocation Channels in Fuel Rod KD-0451, Section 7

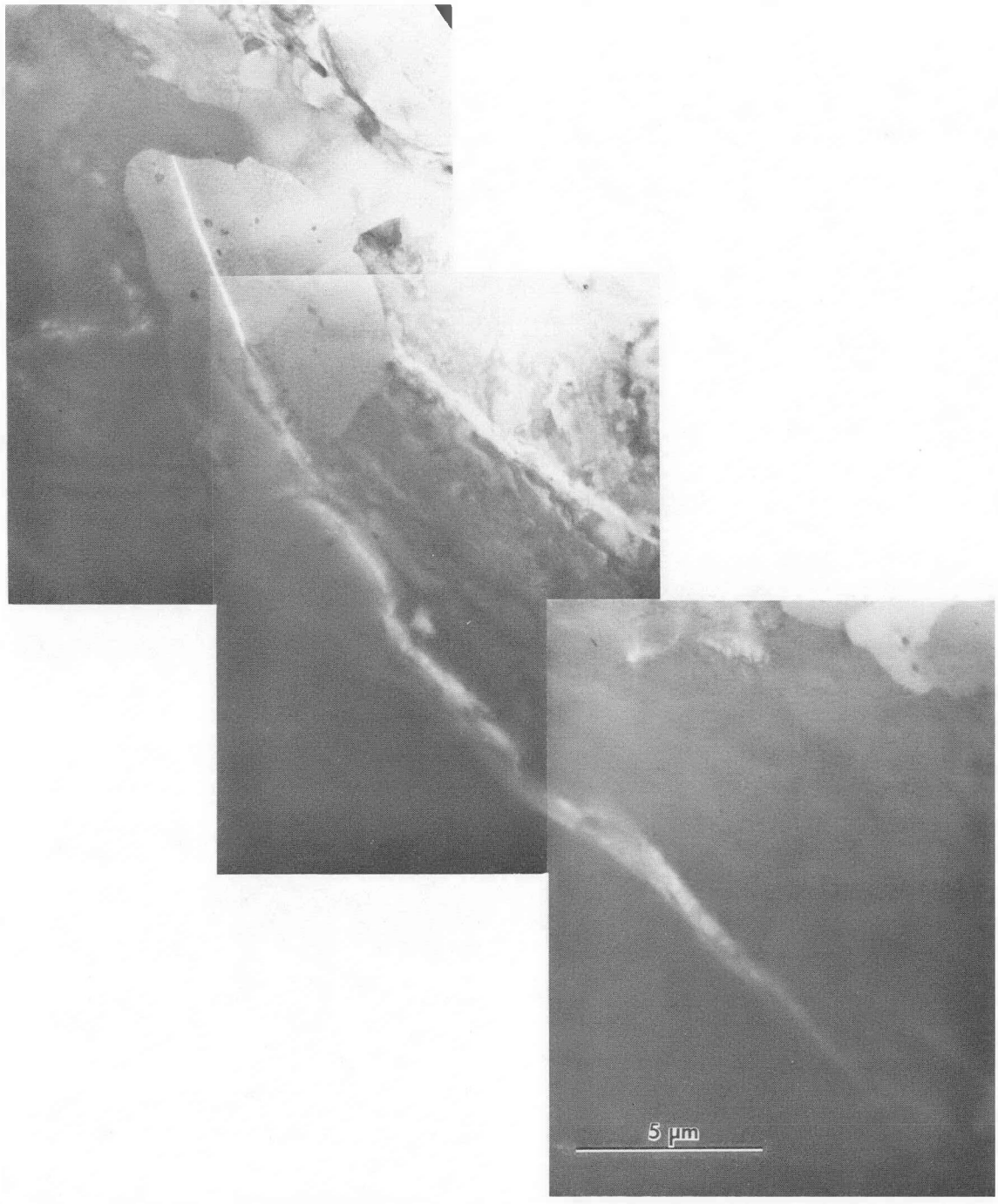

Figure 3.2-62a. Continuous Grain-to-Grain Features Exhibiting Anomalous Electron Transparency in Thick Foil Regions of Fuel Rod KD-0451, Section 7

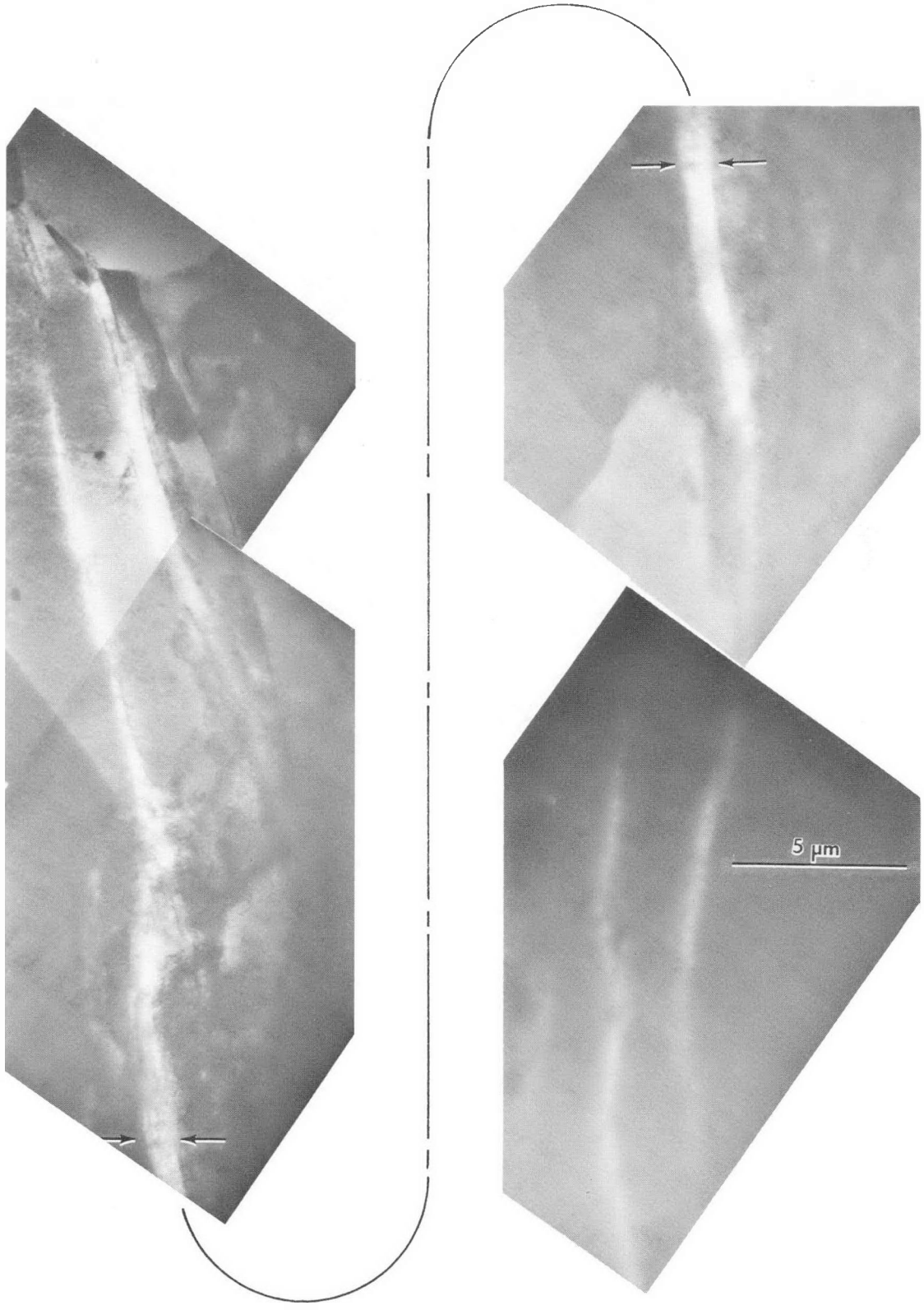

Figure 3.2-62b. Similar to Figure 3.2-62a, Arrows Indicate Continuation

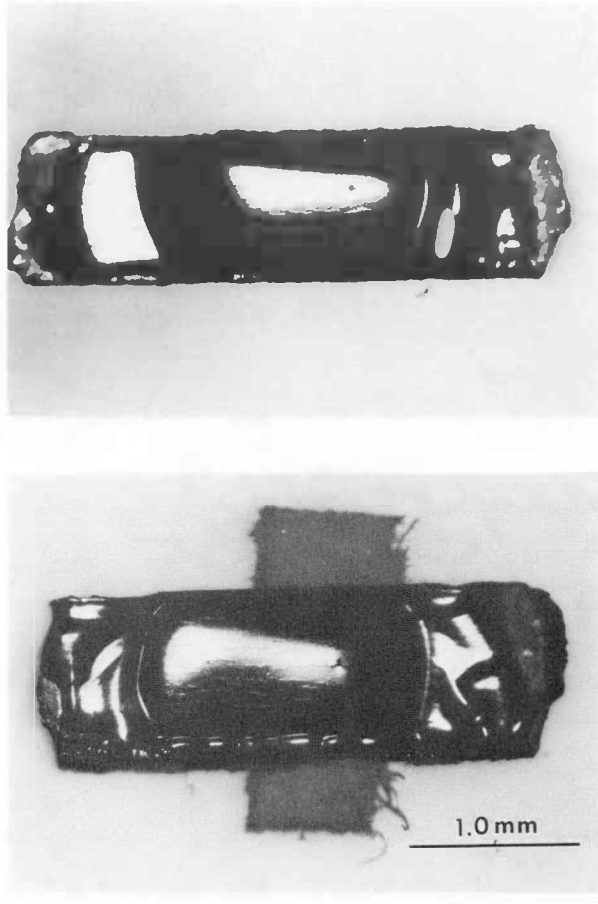

Figure 3.2-63. Optical Images of Transmission Electron Microscopy Specimens from Fuel Rod KD-0451 Showing Stringerlike Features in the Axial Direction of the Cladding

a.

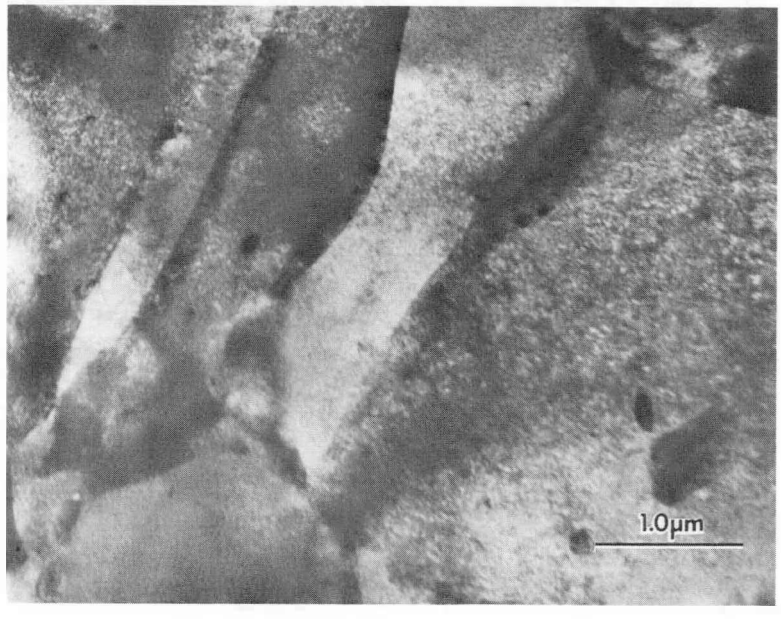

b.

Figure 3.2-64. a. Unrecrystallized, b. Recrystallized Regions of Fuel Rod KE-2225

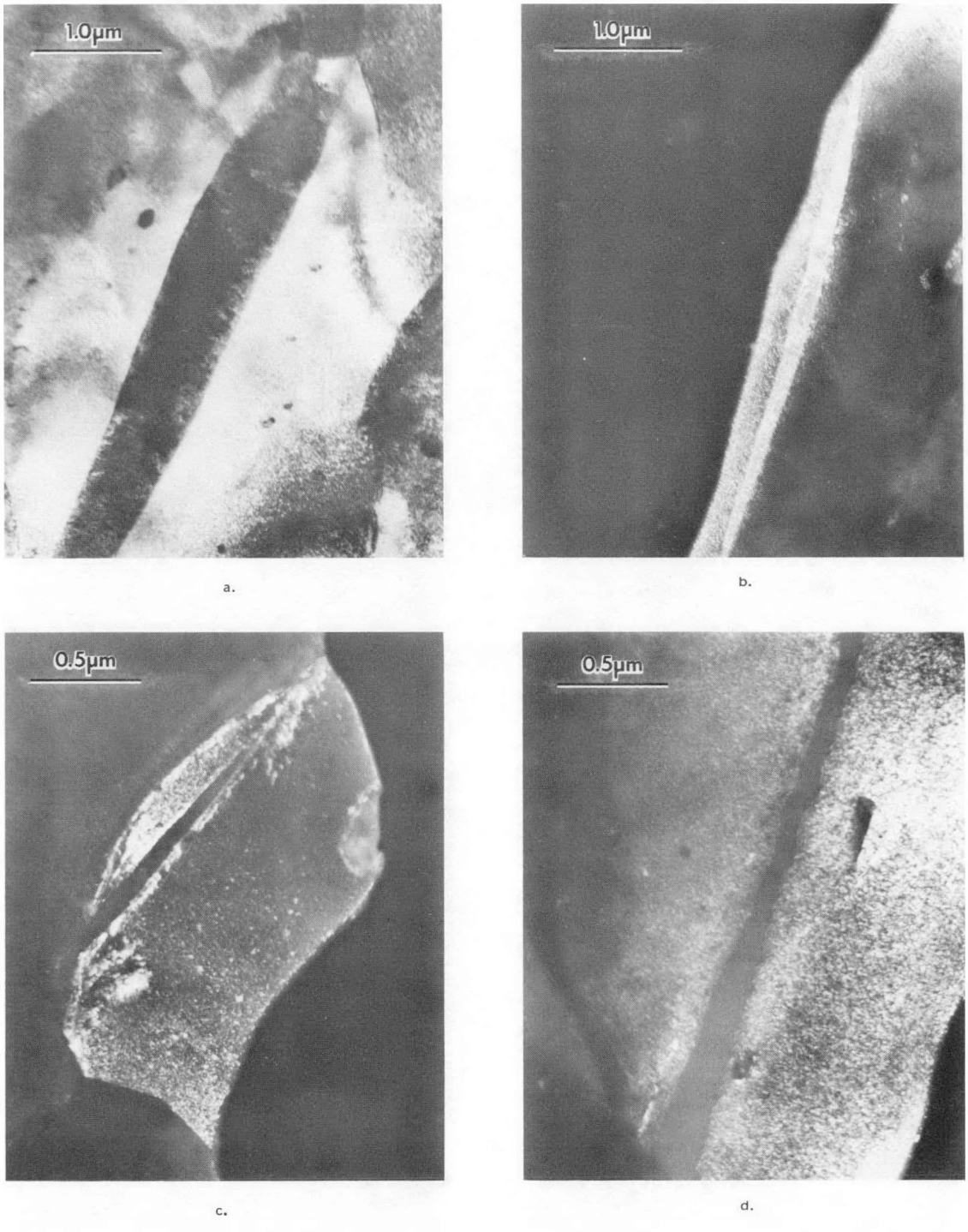

Figure 3.2-65. Twins and Hydrides in Ramp Region of Fuel Rod KE-2225

Figure 3.2-66. Continuous Grain-to-Grain Features in Fuel Rod KE-2225

specimen. This same area is shown as it appears optically in Figure 3.2-67 and shows that the electron transparent features are of the same nature as the stringerlike features observed in both rods. Backscattered electron images obtained in the scanning electron microscope with a solid state detector pair are shown in Figure 3.2-68 where it can be seen that the features differ from the surrounding material in composition and are not topographical features, that is, the surfaces of the electropolished foils are smooth and image contrast is obtained from compositional changes. A discussion of this technique for use of backscattered electron images in a SEM to detect hydrides in Zircaloy has been written by Wolff, and that discussion appears in Appendix E. The image contrast in Figure 3.2-68 shows that the string-like features are hydrides. The anomalous transmission of electrons in the TEM images of these defects is consistent with the decreased density, on the order of 13 percent, associated with zirconium hydride (20). The presence of such long and numerous hydrides was also seen in the longitudinal metallography sample (Figure 3.2-53).

3.2-7 Fractographic and Chemical Studies--(ANL)

The Dresden-3 cladding section which were sent to ANL came from fuel rods KG-0113 and KE-2225. Rod KG-0113, which had failed in reactor, contained a number of eddy current signals indicative of defects, and the section sent to ANL was to be examined on the ANL pulsed eddy current system for comparison purposes. One section received from rod KE-2225 contained an eddy current signal believed to be indicative of a cladding defect. This defect was to be characterized on the cladding inner surface and opened for fractographic examination. Two other sections from this rod were received for additional cladding characterization of the inner surface and ceramographic examination of two pellet-pellet interfaces. Figure 3.2-69 shows the segment of interest of rod KE-2225 and identifies the locations of the ANL specimens and their intended purpose (also see Figure 3.2-6b). All of the cladding sections were cut dry at BCL with the fuel inside. The ends of the segments were impregnated with epoxy resin to prevent the fuel from falling out during shipment to ANL.

Special emphasis was placed on the segment which produced the eddy current defect signal. Following the characterization of the inner surface of this segment, cracks which were observed on the inner surfaces were opened by flattening the curved cladding piece. The fracture surfaces were then examined in detail in the SEM.

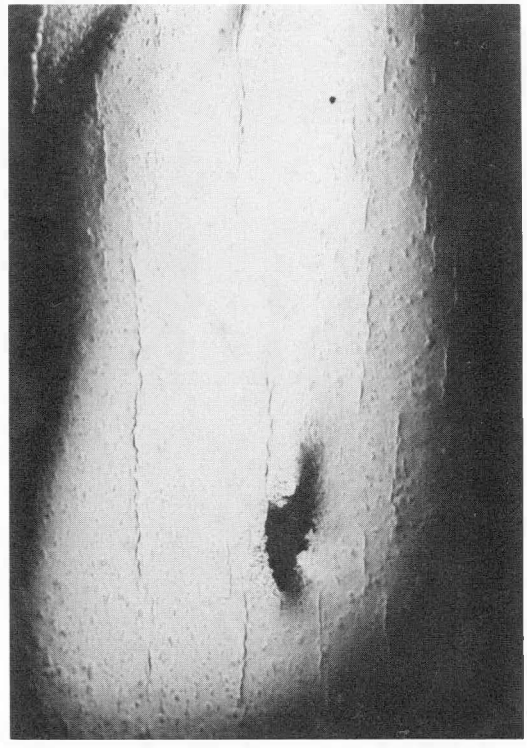

a. 140X

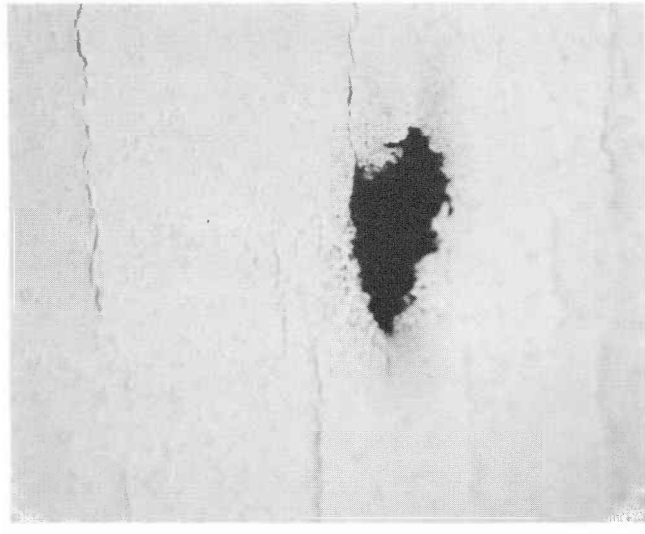

b. 250X

Figure 3.2-67. Optical Images of Same Features of Fuel Rod KE-2225 As Shown in Figure 3.2-63

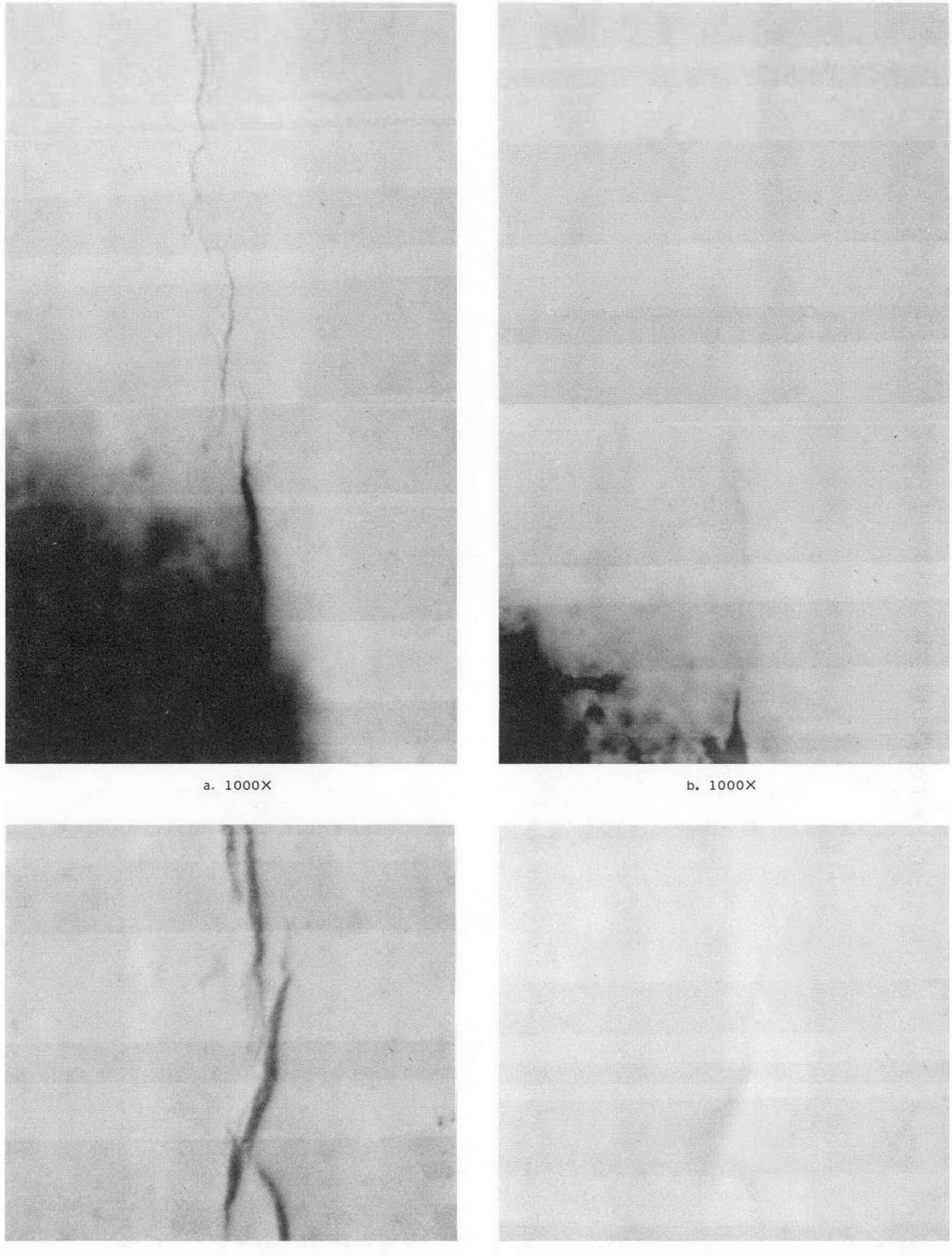

a. 1000X

b. 1000X

c. 3000X COMPOSITION IMAGES

d. 3000X TOPOGRAPHY IMAGES

Figure 3.2-68. SEM Backscattered Electron Images of Stringerlike Features of Fuel Rod KE-2225

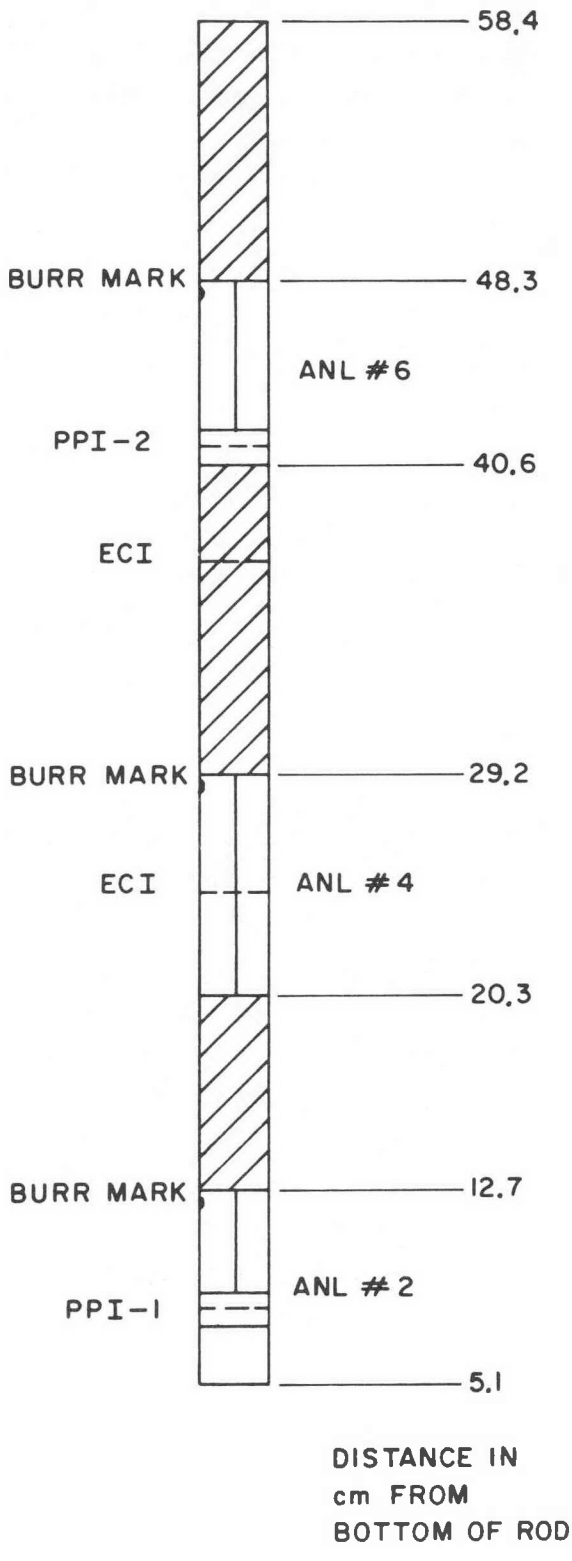

Figure 3.2-69. Cutting Diagram for ANL Dresden-3 Specimens from Rod KE-2225(DD706-G6)

Figure 3.2-69 also shows the manner of subsequent cutting operations after the KE-2225 sections were received at ANL. The initial clamshell and transverse cuts were performed dry with a high speed (~ 1000 rpm) Al_2O_3 cut-off wheel. After the pellet-pellet interface (PPI) specimens were cut, the remaining cladding sections, containing fuel, were secured in an aluminum block for clamshell sectioning. The aluminum block functioned as a chill block and prevented the fuel from dislodging during the cutting operation. The clamshell cuts were all made at 90 degrees to the burr marks located at the top end of each section. Further sectioning prior to SEM examination was performed dry with a slow-speed (~ 100 rpm) SiC cutoff wheel.

3.2.7.1 Characterization of Cladding Inner Surface. The three pieces of cladding from rod KE-2225 were cut into clamshell sections. The examination results that will be presented are primarily those from specimen ANL#4 which produced the weak eddy current indication. With the exception of the defects observed, the physical and chemical appearance of this piece of cladding is similar to the other pieces.

The two halves of specimen ANL#4 are shown in Figure 3.2-70. The burr mark, which identifies the end of the specimen towards the top of the rod as well as the 0-degree orientation, is located at the right end of the photograph at 90 degrees to the clamshell cut of the cladding without fuel. The location of the eddy current signal is at the 24.3 cm level and at the 15 degree orientation. The inner surface was a light brown metallic color and was relatively free of heavy deposits. The dark lines that meander over the inner surface correspond to cracks in the fuel pellets. In several areas, large fuel particles (~ 1 mm in diameter), including one at the location of the eddy current indication (ECI) can be seen adhering to the inner surface. The inner surfaces of all three pieces of cladding are compared in Figure 3.2-71. Specimens ANL#4 and ANL#6 had very similar appearances. Specimen ANL#2, from the bottom of the rod, had a slightly darker inner surface, and the lines corresponding to fuel cracks and pellet-pellet interfaces were lighter than those seen on the other two samples.

SEM examinations were made of the dark lines, pellet-pellet interfaces, fuel particles and clean inner surface areas. Typical examples of these features along with the chemical analysis are illustrated in Figures 3.2-72-75. The examples shown are taken from specimen ANL#4 which exhibited all of the features of

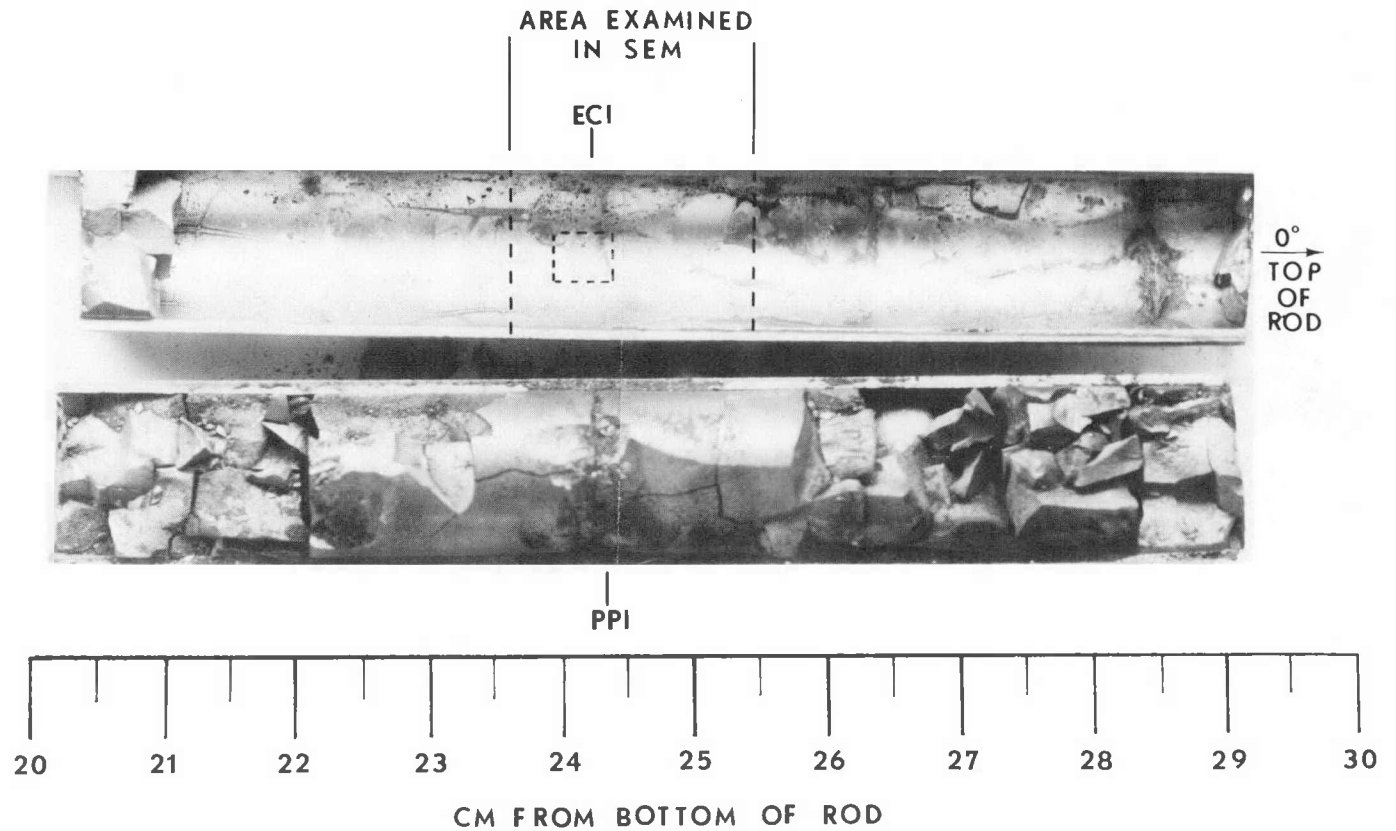

Figure 3.2-70. Clam Shell Sections of Specimen ANL #4 Showing Location of ECI

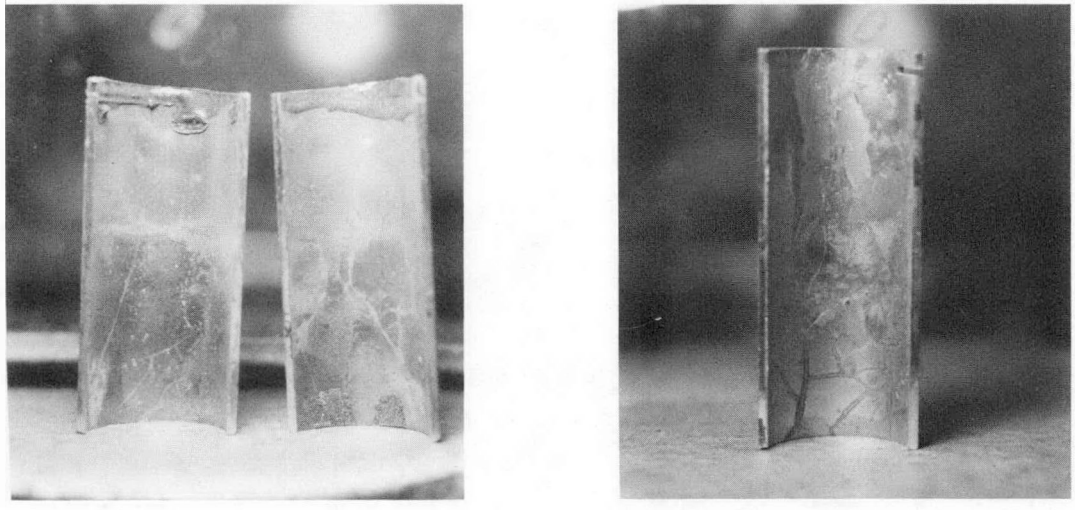

(a) (b)

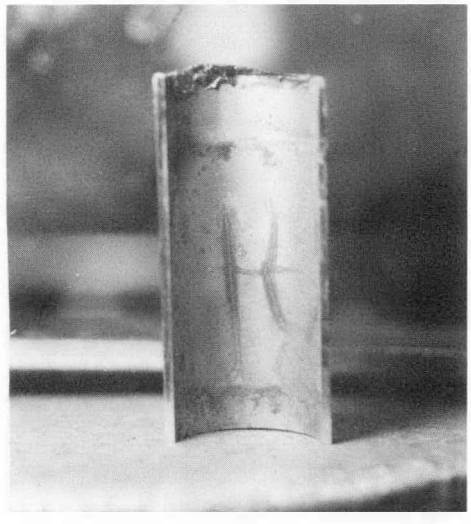

(c)

Figure 3.2-71. Inner Surface of Specimens (a) ANL #2, (b) ANL #4, and (c) ANL #6 2X

interest. A composite corresponds to the section of specimen ANL#4 which includes the ECI as shown in Figure 3.2-70. Located on the composite are the different features shown at high magnification in the following figures. The features that visually appear darker than the cladding, appear lighter than the cladding in the SEM.

The structure associated with the lines which were opposite fuel cracks is shown in Figure 3.2-73 (Area A, Figure 3.2-72). There are no heavy deposits in the area, but a higher magnification micrograph, Figure 3.2-73b, reveals that the surface is covered with light hemispherical nodules or beads. The diameters of the nodules range from 0.5 to 1.0 μm. In this particular case, shown in Figure 3.2-73, a preexisting scratch has also been covered with the nodules. The inner surface adjacent to the line shows a complete absence of nodules (Figure 3.2-73c). The surface, which is composed of hills and valleys approximately 5 μm across, is typical of the clean surface areas observed on these specimens. X-ray analysis of the area covered with nodules indicates a high concentration of uranium in addition to zirconium. No fission products were detected with the SEM X-ray system (a collimated energy dispersive X-ray spectrometer). However, electron microprobe measurements of a similar area from this piece of cladding revealed the presence of trace amounts of cesium. [Other work at ANL has shown similar nodules to contain uranium, cesium and tellurium (6).] In the area without nodular growths, the X-ray measurements showed a high zirconium concentration with a low concentration of uranium. Again, no fission products were detected on the SEM X-ray system.

A portion of a PPI (Area B, Figure 3.2-72) is shown in Figure 3.2-74. There are several areas where heavy deposits were observed, as is illustrated in Figure 3.2-74c. The deposits appear to be either adhering pieces of fuel (Area 1) or nodular growths (Area 2) similar to those previously discussed. The zirconium oxide layer adjacent to some of the deposits shows cracking (Area 3), and the original oxide layer in some areas is absent (Area 4). Figure 3.2-74c shows the formation of submicron size nodular growths in the PPI region (Area B, Figure 3.2-74a). The fuel deposits and nodular growths show a high concentration of uranium, but fission products were not detected.

An example of fuel adhering to the inner surface is shown in Figure 3.2-75 (Area C, Figure 3.2-72). Such deposits are randomly distributed over the specimen inner

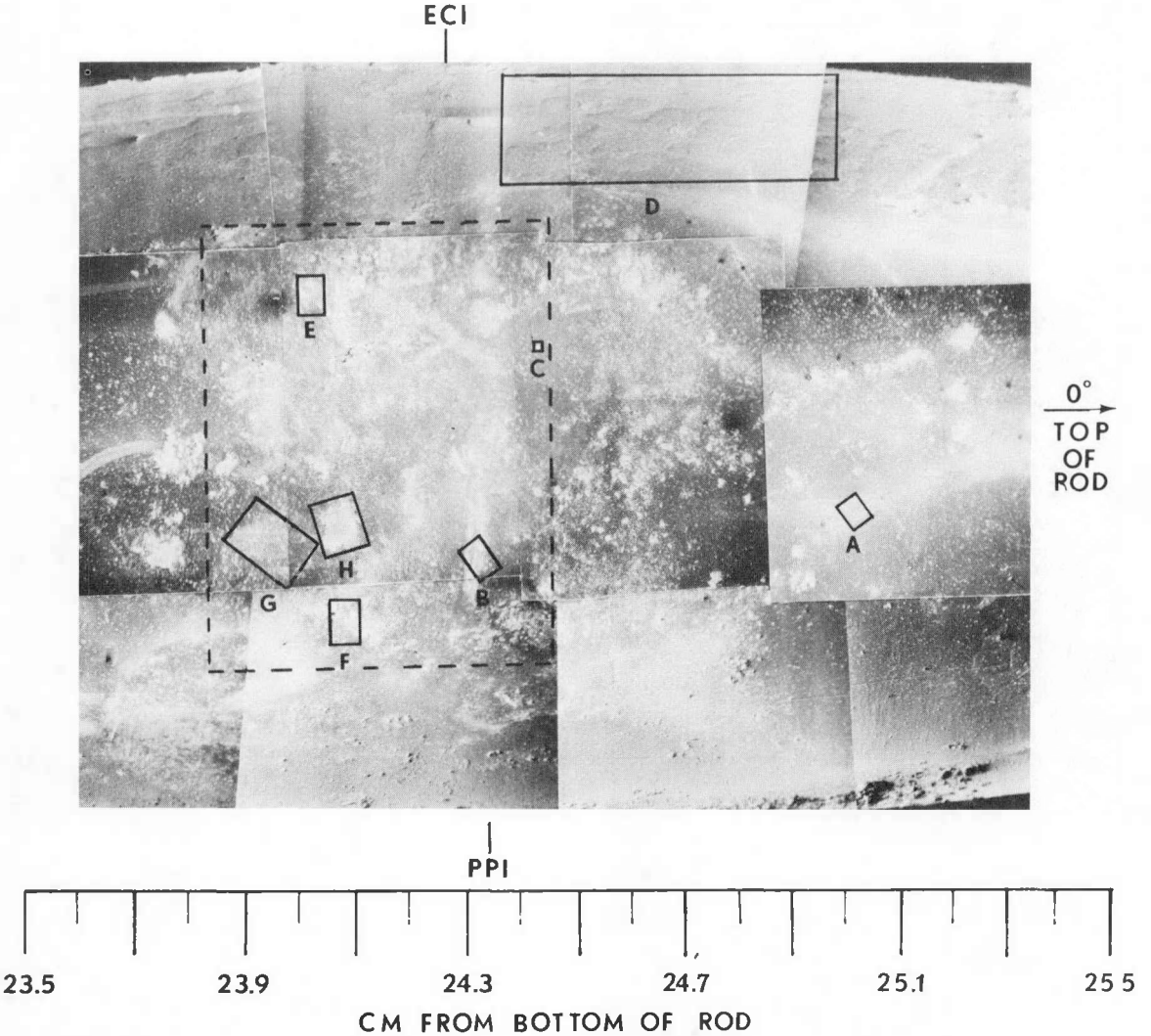

Figure 3.2-72. SEM Composite of Specimen ANL #4 Showing Location of ECI

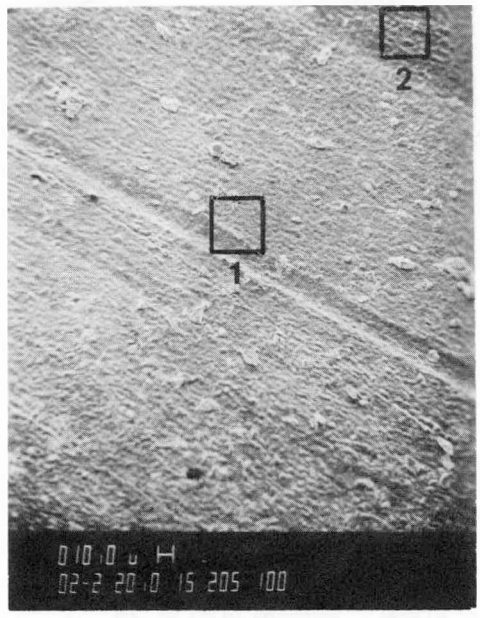

(a)

(b)

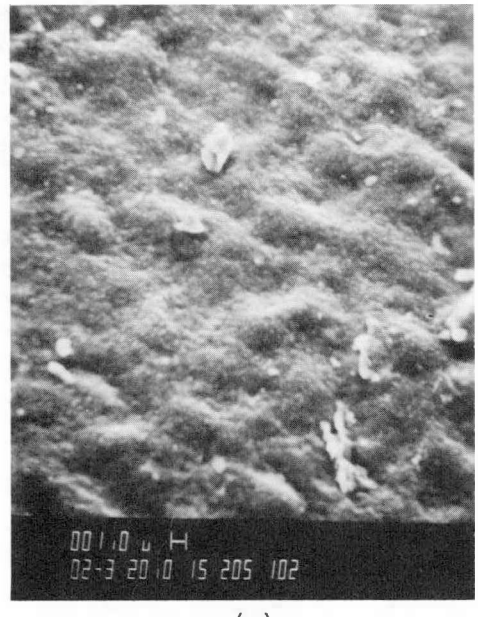

(c)

Figure 3.2-73. Dark Line Corresponding to Fuel Cracks
(a) Close-up of Area A, Figure 3.2-72
(b) Nodules from Area 1
(c) Smooth Surface from Area 2

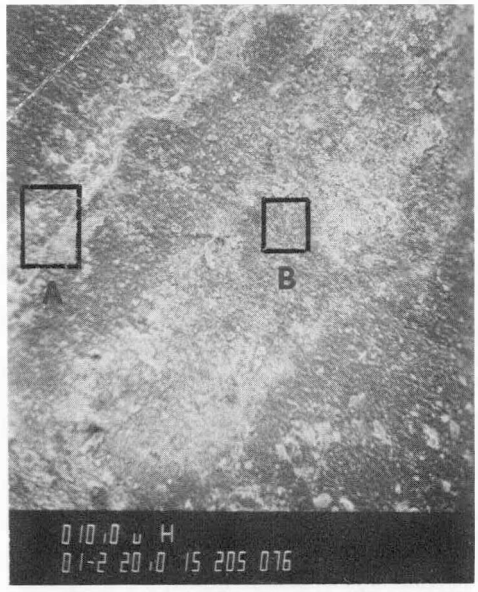

(a)

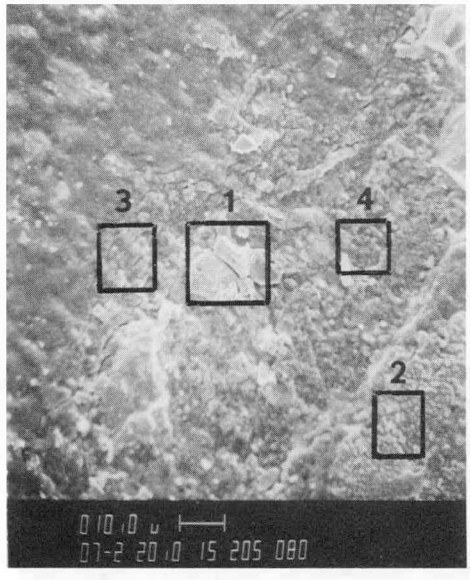

(b)

(c)

Figure 3.2-74. Pellet-Pellet Interface
(a) Area B, Figure 3.2-72 are Detailed in Text
(b) Area A--Areas 1 to 4 are Detailed in Text
(c) Area B

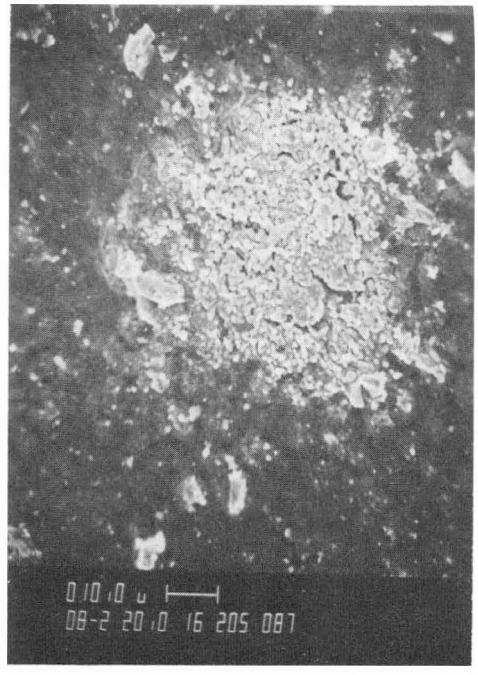

Figure 3.2-75. Fuel Particle Adhering to Inner Surface. Area C, Fig. 3.2-72

surface. A few of the deposits are associated with oxide surface cracking and possible substrate cracking as will be discussed later in this section.

The area of the eddy current indication in specimen ANL#4 was examined in detail in order to characterize the defect site. The inner surface was scanned at high magnification in the SEM to search for the presence of cladding defects. Several unique surface structures were found in this area, but a single large defect could not be identified as the cause of the ECI. Instead, features such as oxide cracking, small cladding defects, fuel adhering to the cladding, and hydride-like structures were observed in several places. The montage of the inner surface shown in Figure 3.2-72 maps the locations of the structures shown in this section. X-ray analysis of the ECI area showed only the presence of uranium and zirconium; any fission products that were present were below the level of detectability of the system.

A significant feature on the inner surface shown in Area D of Figure 3.2-72, is the extensive surface mounding. Closer examination of this area indicated the presence of cladding defects shown in Figure 3.2-76 which generally had no particular orientation. Stereomicrographs of the defects showed that they were present only in the mounded areas. Cladding defects were also observed in several other areas. These defects were usually in the vicinity of both large adherent fuel particles and extensive cracking of the surface oxide. Examples of such defects from areas E, F, G, and H, of Figure 3.2-72 are illustrated in Figure 3.2-77. The oxide cracking often forms a circular pattern on the inner surface with the cladding defects located near the center of the pattern with no particular orientation. Figure 3.2-78 shows closeups of the main defect and the edge of the area of surface cracking from Areas 1 and 2 of Figure 3.2-77a.

Areas G and H of Figure 3.2-72 (Figures 3.2-77c and d) combine to form the largest defect area in the vicinity of the ECI with a total length of oxide cracking plus fuel particle of ~ 2.5 mm. This area was examined in detail, ultrasonically cleaned in ethanol, and reexamined. The surface of the extensive area of oxide cracking is shown in Figure 3.2-79a (Area A, Figure 3.2-77c). In addition to the oxide cracks, there is an area approximately 50 μm in diameter where the oxide is absent. The surface of the underlying Zircaloy is shown in Figure 3.2-79b. In order to examine the substrate, the oxide was removed by ultrasonic cleaning. The mounted piece of cladding was cleaned by placing it in a beaker filled with ethanol into which the tip of the ultrasonic unit was lowered to a point just

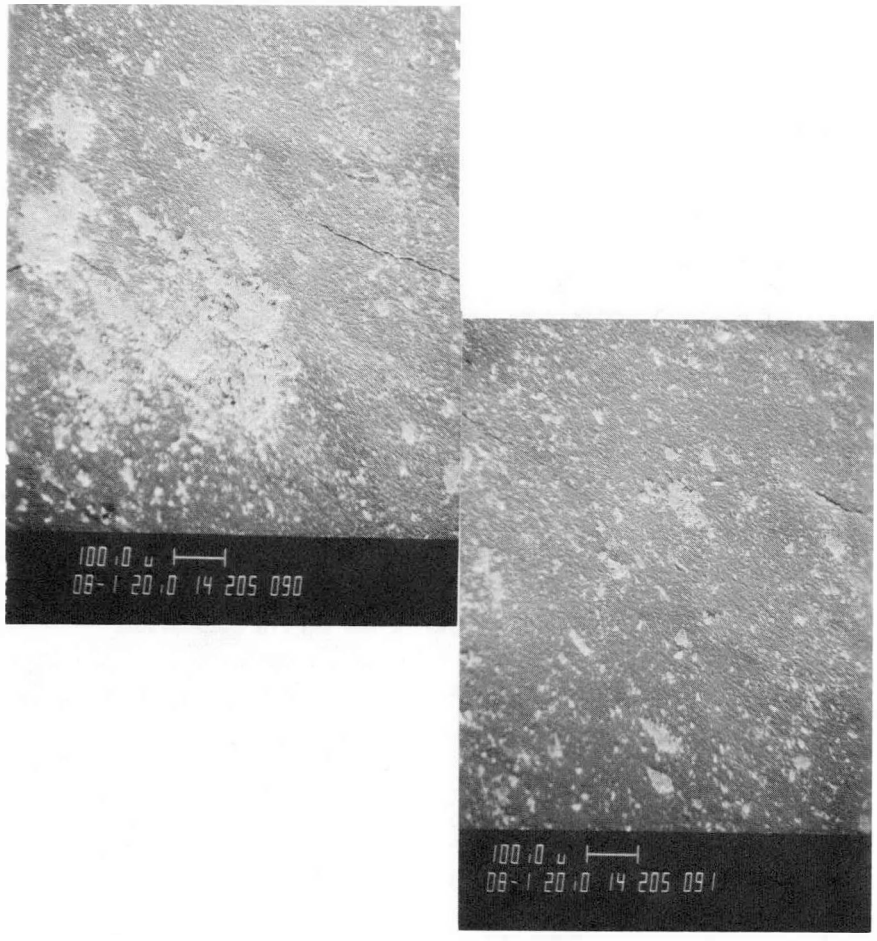

Figure 3.2-76. Cracks Located at Sites of Surface Mounting, Area D, Figure 3.2-72

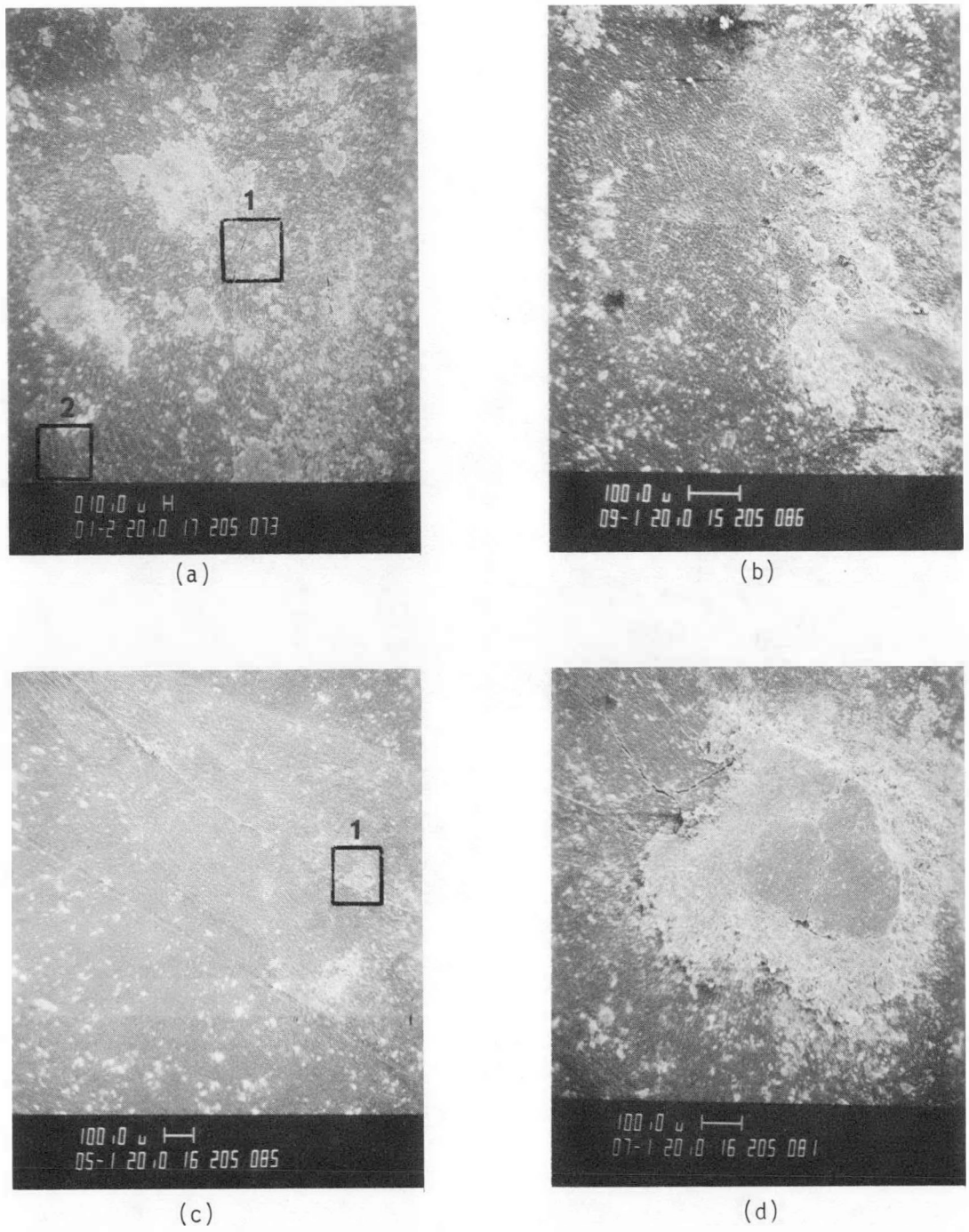

Figure 3.2-77. Defect Structures Observed in Area of ECI (a) Area E, Figure 3.2-72, (b) Area F, Figure 3.2-72, (c) Area G, Figure 3.2-72, (d) Area H, Figure 3.2-72

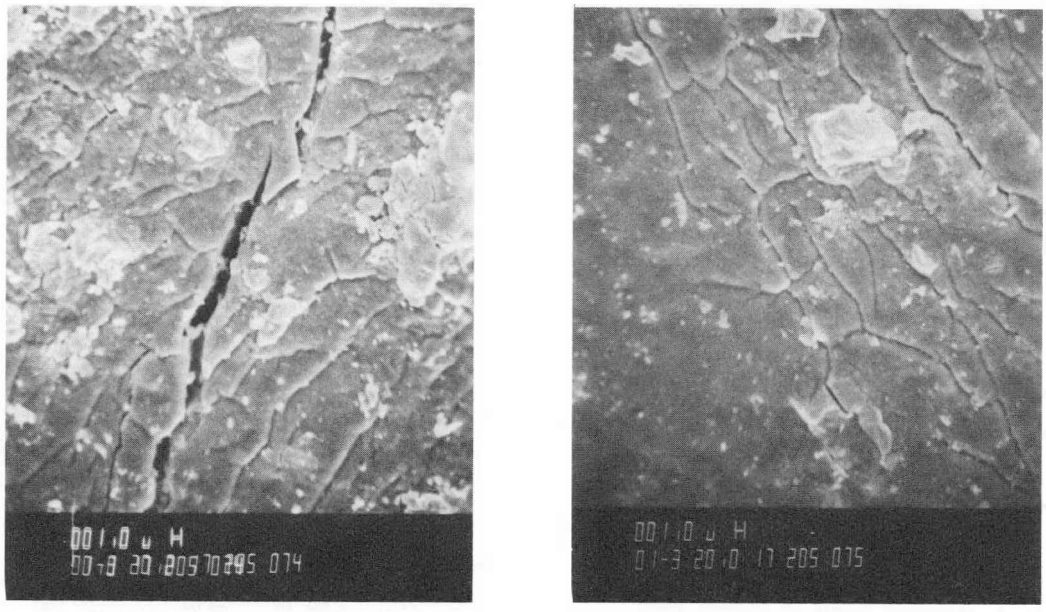

(a) (b)

Figure 3.2-78. Close-Ups of (a) Area 1, Figure 3.2-77a and (b) Area 2, Figure 3.2-77a

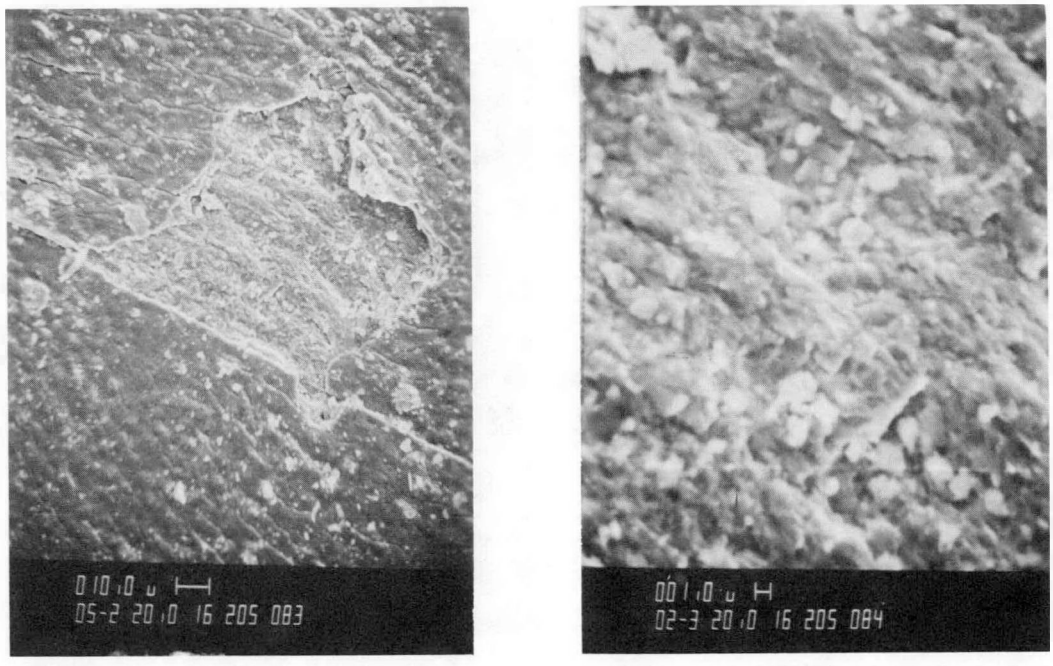

(a) (b)

Figure 3.2-79. Close-Ups of Area of Oxide Surface Cracking (a) Area 1, Figure 3.2-77c, (b) Middle of (a)

above the cladding inner surface. A 1 to 3 minute cleaning was usually sufficient to remove deposits and portions of the zirconium oxide. The ultrasonic cleaning removed the fuel particle and a significant amount of oxide from the cracked area as shown in Figure 3.2-80. The pit which remained at the site of the fuel particle is estimated to penetrate ~ 50 μm into the cladding. The base of the pit is shown in Figure 3.2-80d. The particles in the pit are composed primarily of uranium, but zirconium is also present. The Zircaloy surface where the oxide layer was removed from the area of surface cracking is shown in Figure 3.2-80c. The surface resembles that shown in Figure 3.2-79a without the debris particles.

3.2.7.2 Defect Fractography. After the characterization of the cladding inner surface was completed, several of the defects from the general area of the ECI were exposed by three-point bending. Prior to bending, the cladding was positioned in the bending apparatus such that the maximum stress was applied to the area of the defect. Several fractures were required before one could be generated through a preexisting cladding defect. In all cases, the last bend was made 90 degrees to the long axis of the cladding. The fractographic examination concentrated on the defects associated with Areas G and H of Figure 3.2-72. The overall appearance of this area following three-point bending is shown in Figure 3.2-81. Several additional cracks have developed in the area of the original defects, and these cracks begin and end at the boundaries of the original surface oxide cracks. A close-up of the end of one of the new cracks is shown in Figure 3.2-81c. The fracture adjacent to the pit, where the fuel particle had been (Figure 3.2-81b) showed two distinct modes of fracture. The fracture mode near the inner surface penetrated ~ 100 μm into the cladding and corresponded in width to the area of inner surface cracking (~ 500 μm).

A fracture surface emanating from a preexisting defect is mapped in Figure 3.2-82. This defect was in the region of oxide cracking shown in Figure 3.2-81. Three modes of fracture are apparent at higher magnification: an undistinguished area within 50 μm of the inner surface, a brittle fracture which penetrates ~ 150 μm, and a ductile fracture elsewhere. The line between the brittle and ductile fracture roughly follows a circular arc. The arc crosses the inner surface at the boundaries of the inner surface cracking. The microstructure of the fracture surface from the inner surface towards the outer surface is shown in Figure 3.2-83 where the three fracture modes can be seen clearly. Area A, adjacent to the inner surface has a more rounded appearance than the brittle fracture below it

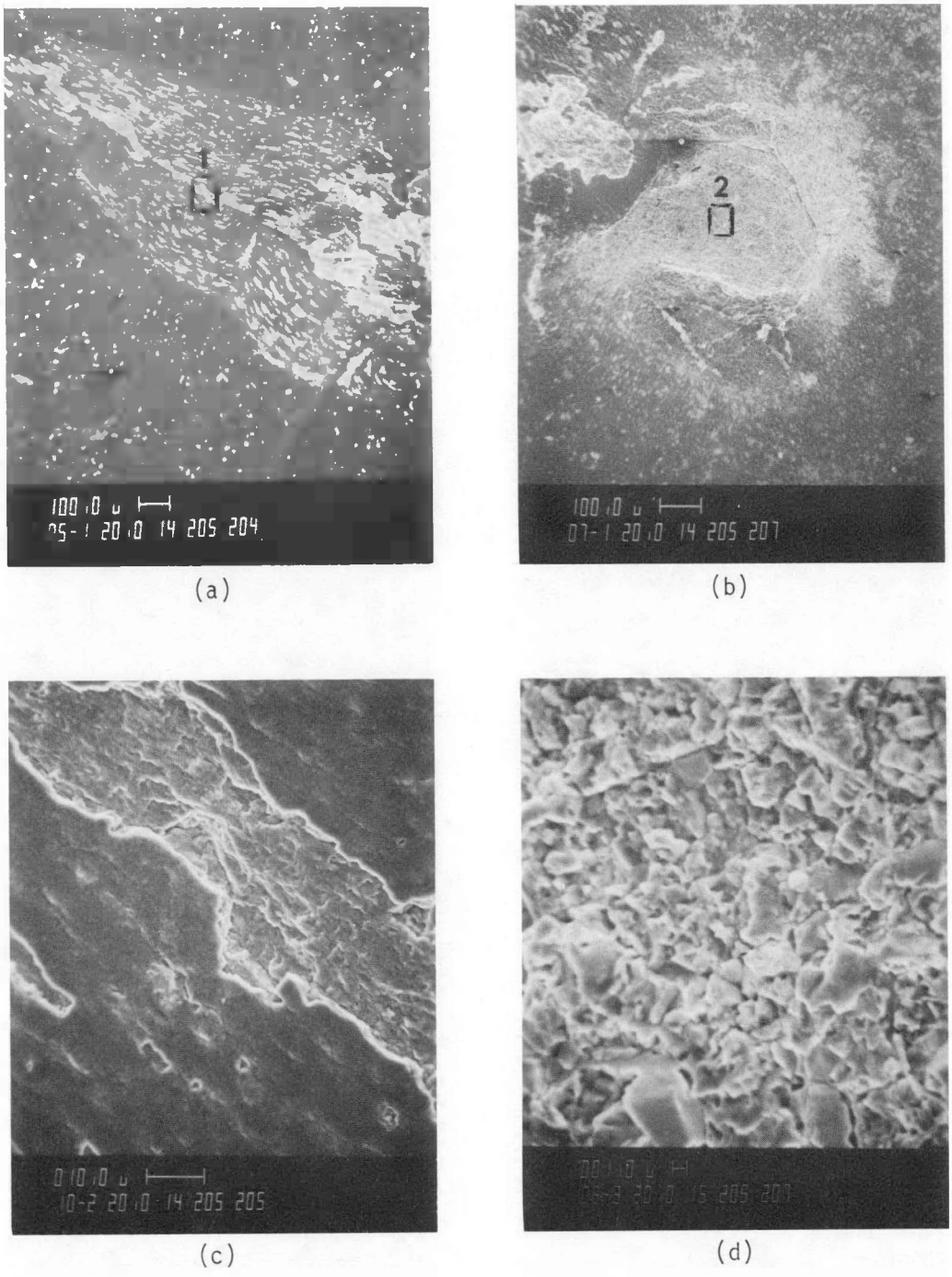

(a) (b) (c) (d)

Figure 3.2-80 (a) Area G, Figure 3.2-72 after Ultrasonic Cleaning
(b) Area H, Figure 3.2-72 after Ultrasonic Cleaning
(c) Area 1 in (a), (d) Area 2 in (b)

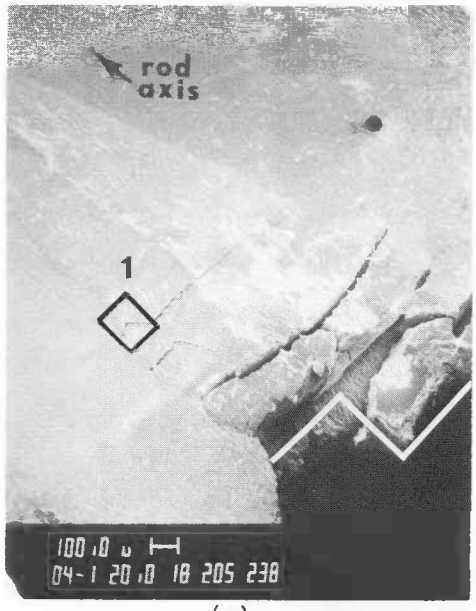

(a)

(b)

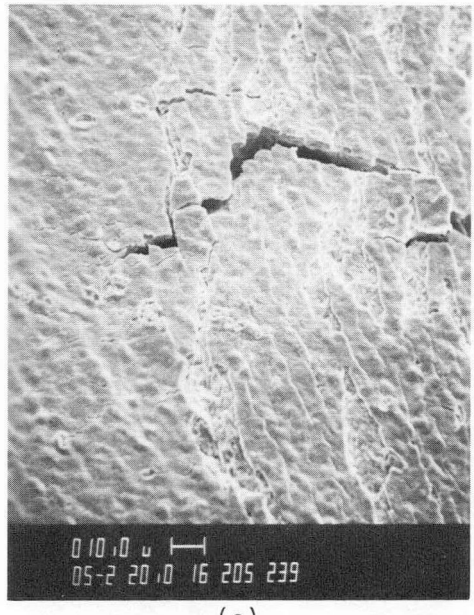

(c)

Figure 3.2-81 (a) Area G, Figure 3.2-72 after 3-Point Bending,
(b) Area H, Figure 3.2-72 after 3-Point Bending,
(c) Area 1 in (a)

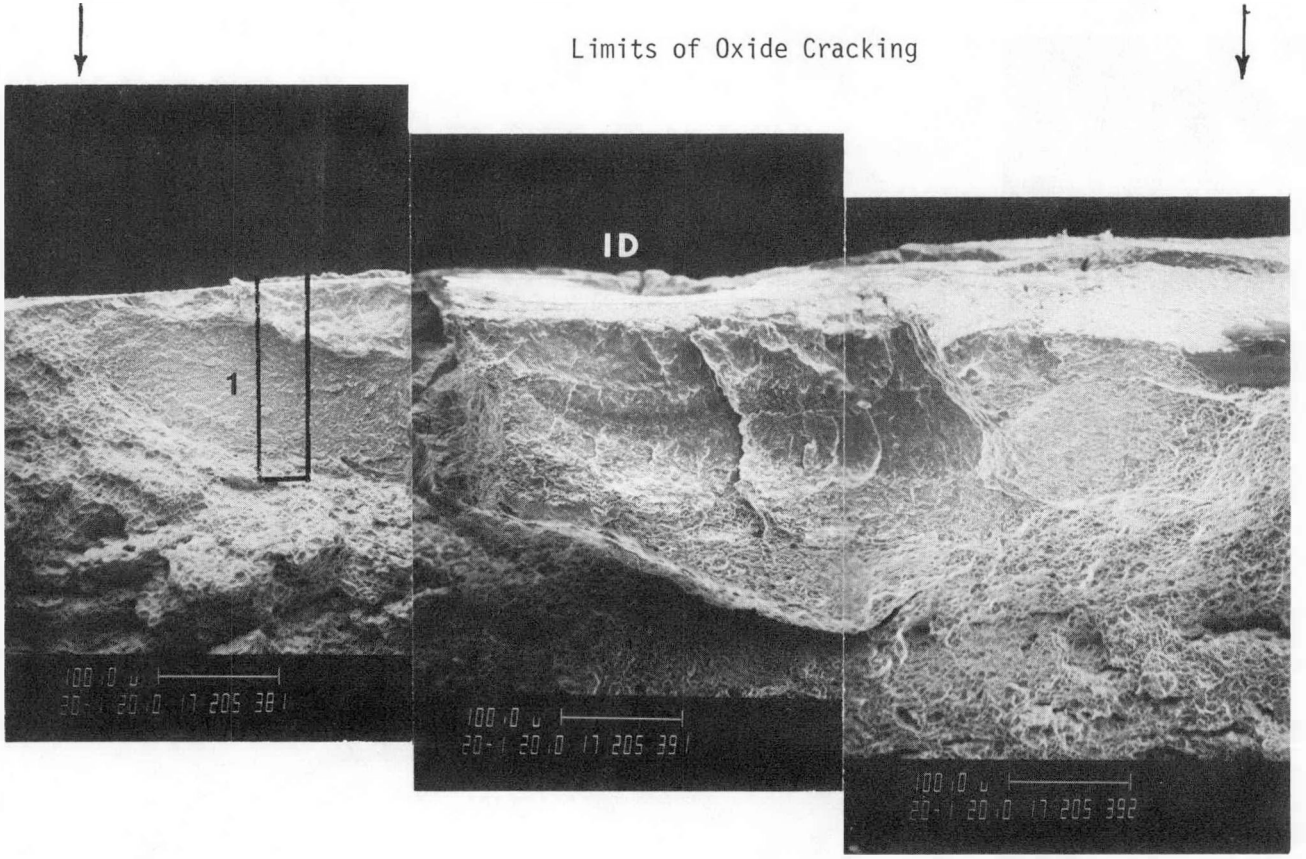

Figure 3.2-82 Map of Fracture Surface Exposed by 3-Point Bending Between Areas G and H of Figure 3.2-72. The extent of the Map is Shown by the White Line in Figure 3.2-81a.

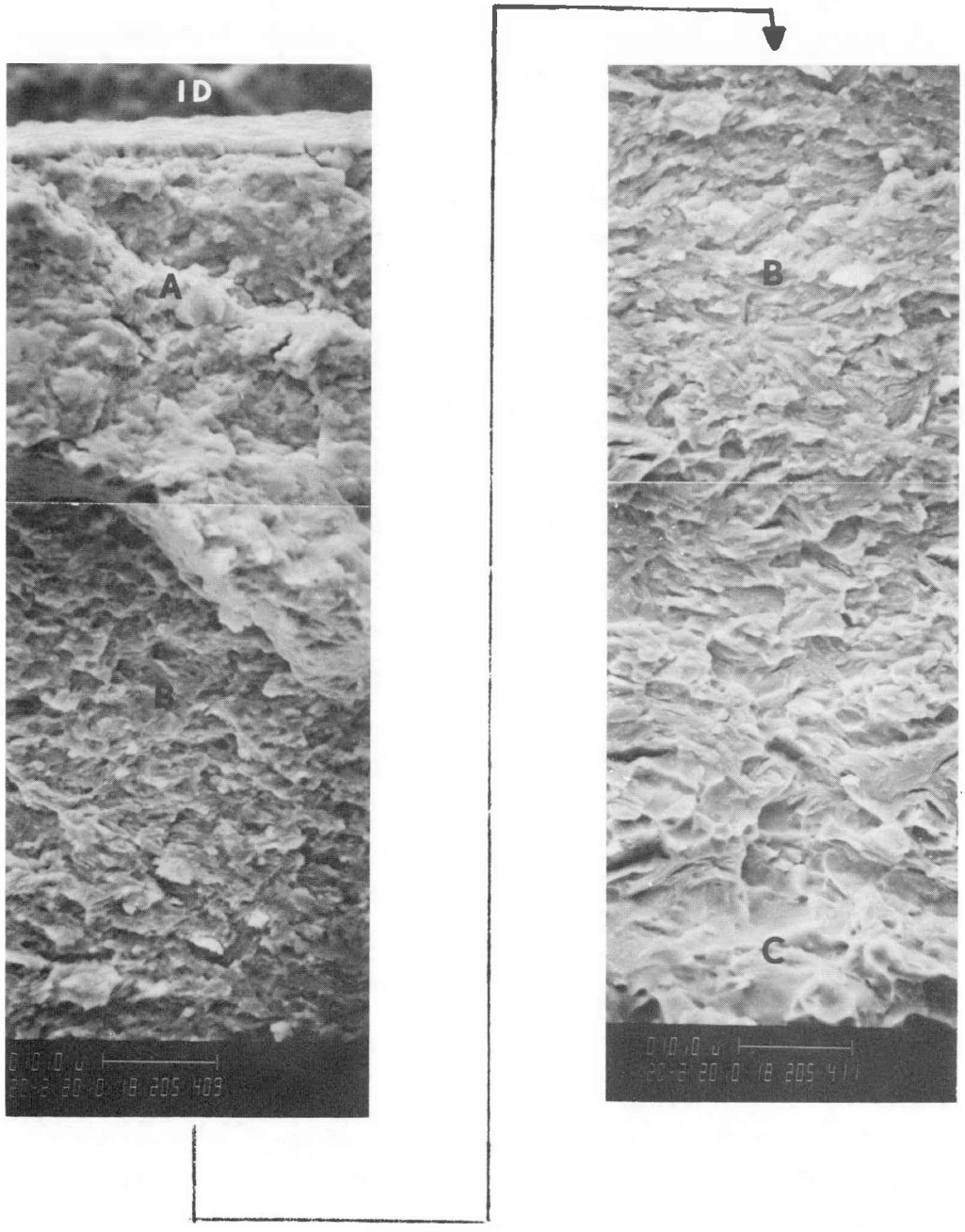

Figure 3.2-83 Map of Area 1 of Fracture Map of Figure 3.2-82 Undistinguished Area (A), Brittle Area (B), and Ductile Area (C)

(Area B). Neither fracture surface showed any evidence of cleavage and fluting which is typical of SCC fractures in Zircaloy. The remaining fracture surface is composed of the dimpled features typical of ductile fracture. The brittle fracture surface of Area B and the ductile fracture surface of Area C were observed on other surfaces produced by three-point bending in areas where oxide cracking existed on the inner surface, but the fracture surface of Area A was observed only on surfaces that were produced from pre-existing defects.

3.2.7.3 Pellet-Pellet Interface (Fuel Microstructure). The pellet-pellet interface (PPI) specimens were located at the 8.9 cm (3.5 inch) and 41.3 cm (16.25 inch) elevations of rod KE-2225. Each specimen was placed longitudinally in a metallographic mount composed of an electrically conductive thermosetting epoxy, and then was vacuum impregnated with cold-setting epoxy to keep the fuel in place during grinding and polishing. Grinding was performed with 600 SiC paper, and polishing was performed using 3 μm and 1 μm diamond paste. A kerosene-base lubricant was used to minimize the loss of fission products from the specimens during metallographic preparation.

Composite photographs of the two PPI's that were examined are shown in Figures 3.2-84 and 85. Figure 3.2-84 of Specimen PPI-1 (from the 8.9 cm level) clearly shows the dished ends of the fuel pellets. The volume between the pellet ends has been partially filled by fuel particles which apparently broke away from the upper pellet. The fuel-cladding gap appears to be free of any fission or reaction products, even at the location of the PPI. The second PPI, from the 41.3 level, is shown in Figure 3.2-85. Fuel has moved axially into the dishes from both pellets and extensive separation of grain boundaries is evident, but there is no indication of fission or reaction products in the fuel-cladding gap. The axial movement of fuel is symmetric within the dishes and it appears that the pellets were once in contact at the center of the dishes. Figure 3.2-86 shows selected areas of the two specimens at higher magnifications. Figures 3.2-86c and 86d compare the fuel microstructures from Area 1 in Figures 3.2-84 and 85. Figures 3.2-86c and 86d which represent Area 2 from Figures 3.2-84 and 85, show the only particles found in the fuel-cladding gap. The microstructure of the two particles is similar, and they have penetrated 10 to 15 μm into the cladding.

Specimen PPI-2 was analyzed in a shielded electron microprobe. Areas 1, 2, 3, 4, and 5 from Figure 3.2-85 were given complete mass scans to identify the elements that were present. Cesium was not detected at any position on this specimen;

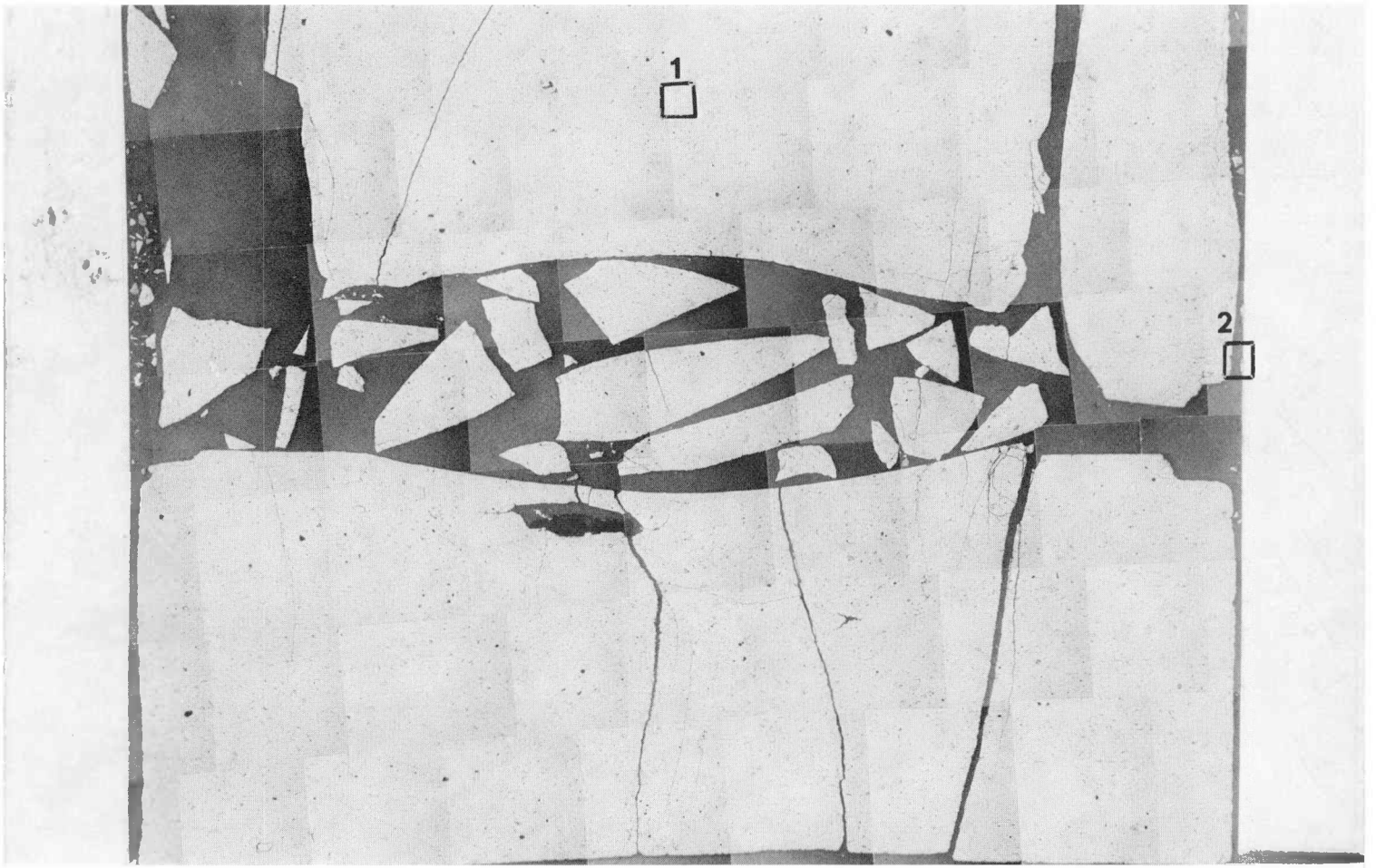

Figure 3.2-84 Composite Photograph of Specimen PPI-1. (15X)

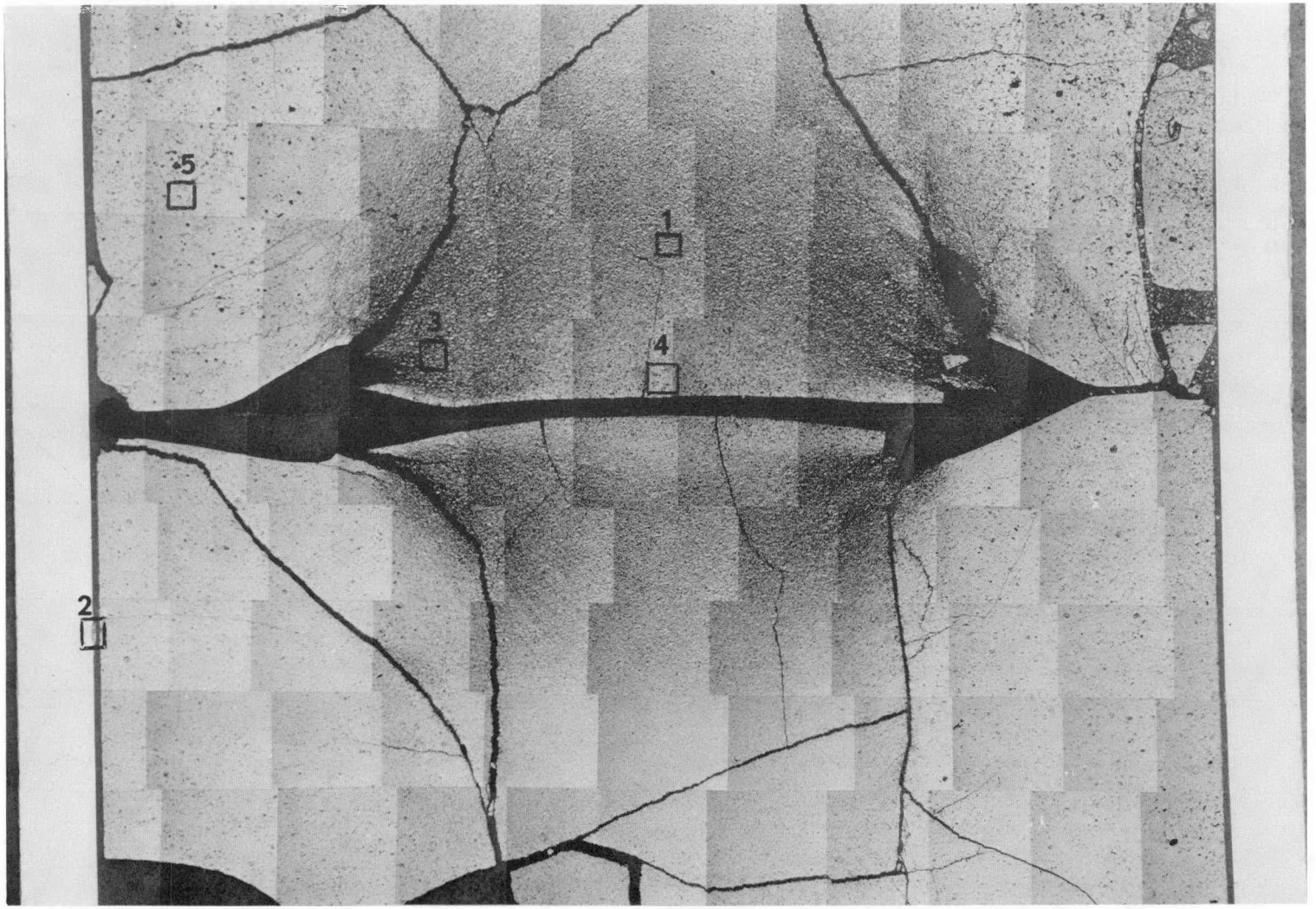

Figure 3.2-85 Composite Photograph of Specimen PPI-2. (15X)

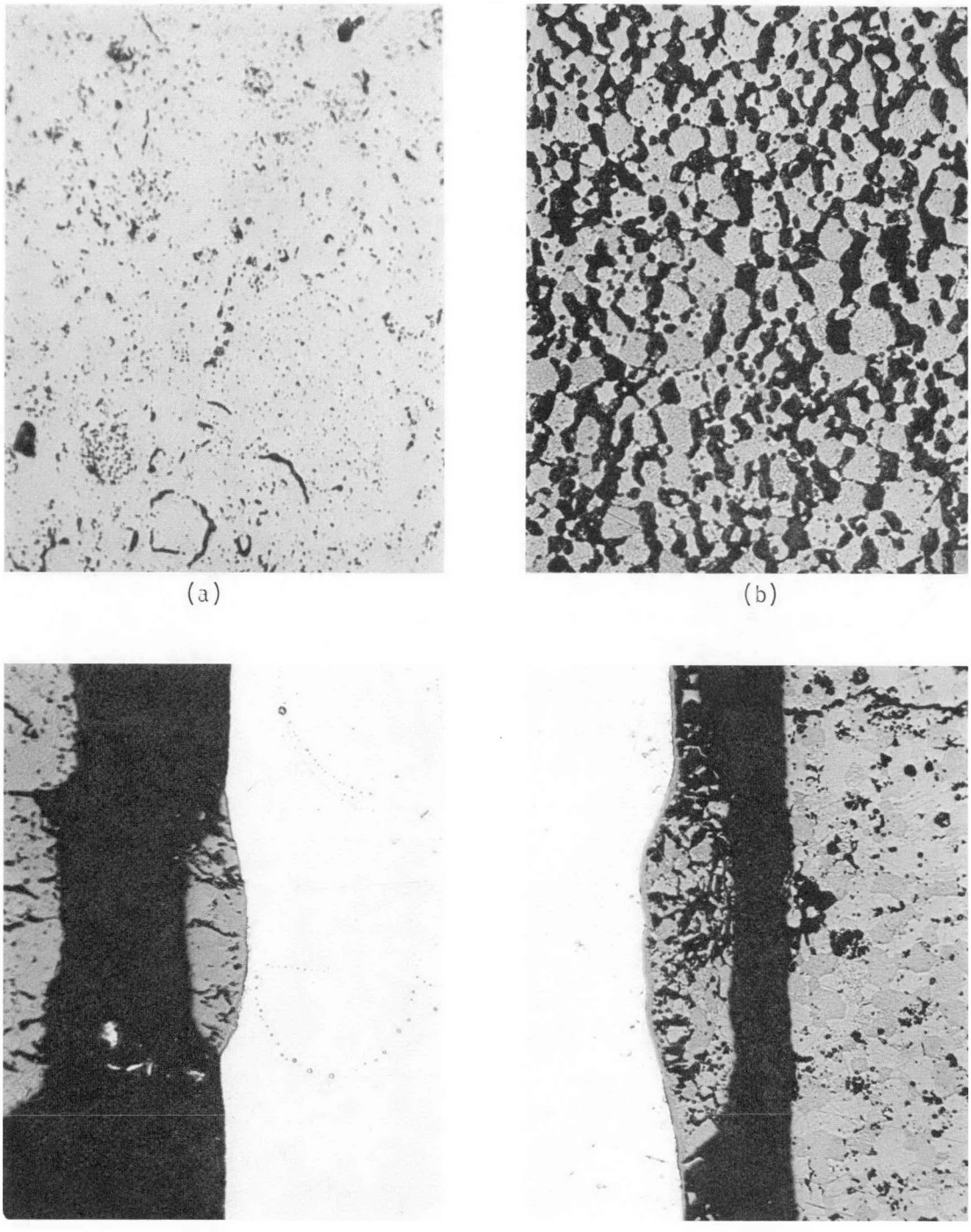

Figure 3.2-86 Microstructure of Fuel from Figures 3.2-84 and 3.2-85: (a) Area 1, Figure 3.2-84, (b) Area 1, Figure 3.2-85, (c) Area 2, Figure 3.2-84, (d) Area 2, Figure 3.2-85. All As-polished. 250X

the level of detectability is approximately 1 percent. The particle adhering to the inner surface (Area 2) was composed primarily of uranium, with a trace amount of zirconium uniformly distributed in the particle. The bonding of this particle to the cladding apparently did not involve cesium, but was probably effected by urania-zirconia solid solution formation.

In summary, neither specimen exhibited any cesium-uranium compounds, either metallographically or by microprobe analysis, that would be associated with localized stress concentrations in the cladding at pellet-pellet interfaces.

3.2.8 Data Correlations

3.2.8.1 Nondestructive and Destructive Tests. The results of the microscopic studies clearly showed that of the 10 candidate fuel rods, only KD-0451 was unfailed, and no incipient defects were discovered in it. Thus, a meaningful correlation of nondestructive test data from this study with the occurrence of incipient PCI defects in unfailed fuel rods is not possible. On rod KE-2225 the defect at the 37.1 $\pm$ 0.5 cm (14.6 $\pm$ 0.2 inch) location was detected by the encircling coil eddy current technique both at the reactor site (2) and at BCL (4). The two-frequency probe eddy current technique used at BCL also detected this defect and located not only its axial position but its azimuthal (circumferential) orientation as well. This defect location had been noted also in the profilometry data (4) as a discernable diameter increase. From the microscopic studies this defect was found to be two separate cracks: a through-wall crack at the 0 degree azimuthal orientation and an incipient crack (i.e., a crack in the cladding wall which failed to penetrate the entire wall thickness) at 105 degrees. Both of these cracks have oxidation/corrosion products on their fracture surfaces, which might have affected the eddy current signal. The two-frequency probe eddy current technique successfully located a small incipient defect located at 24.1 cm (9.5 inches) over an azimuthal range of 45 to 180 degrees. From the fractographic appearance (Figure 3.2-83) of a defect in that region of the cladding, it is likely that hydriding played a role in the fracture and perhaps hydriding contributed to the eddy current signal.

The metallographic work at BCL (4) demonstrated that the eddy current data could be correlated with regions of the cladding that had cracks and extensive hydriding.

3.2.8.2 Defects and Fuel Power History. Since the only defects found in this study were in fuel rods which had failed, it is difficult to discern which were caused by the primary PCI event and which ones were produced by the secondary effects of water which entered the fuel rod. In rod KG-0113 several defects were found by eddy current tests at both BCL (4) and subsequently at ANL (Table 3.2-3); but since that rod had not been examined destructively, the direct PCI effects cannot be distinguished from the possible secondary effects of a breach in the cladding. Nonetheless, the defects are located mainly in the region of the power transient (Nodes 1 to 4 in Figure 3.2-3). The strongest eddy current signals occurred where the fuel had burnup in the range 7.2 to 11.3 GWd/te-U (6.5 to 10.3 GWd/t-U) and a power transient, ΔP, ranging up to 26 kW/m (8 kW/ft) to peak power of ~ 43 kW/m (~ 13.3 kw/ft).

In rod KE-2225 defects were found at two axial locations corresponding approximately to Nodes 2 and 3 in Figure 3.2-4. This region had a fuel burnup of 8.4 to 10.7 GWd/te-U (7.6 to 9.7 GWd/t-U) and a transient ΔP ranging up to 13 kW/m (4 kW/ft) to peak power of 43.0 kW/m (13.1 kW/ft).

In rod KD-0451 no defects were found although it suffered a power transient ranging up to 35.4 kW/m (10.79 kW/ft) and at the time of the event the average burnup in the rod was 13.3 GWd/te-U (12.1 GWd/t-U) and the peak burnup was 17.7 GWd/te-U (16.1 GWd/t-U) (see Figure 3.2-5 and Table 3.2-1). However, locally at Node 2, where the power transient was greatest, the burnup was quite low, only 5.6 GWd/te-U (5.1 GWd/t-U). It appears that the ability of the fuel to withstand the large power transient can be directly correlated to the low burnup at that axial location.

3.3 EXAMINATION OF CLADDING FROM THE OSKARSHAMN-1 POWER RAMP EXPERIMENT

3.3.1 Introduction

In the summer of 1975, an experiment was conducted in the Oskarshamn-1 BWR to investigate the PCI susceptibility of standard ASEA 8 x 8 fuel assemblies then in the core (8). The experiment, conducted just prior to a regular shutdown, consisted of a series of power changes initiated by the withdrawal of a single control rod in 10 percent increments from 53 percent to 83 percent withdrawal from the core over a period of approximately 2 hours. The control rod positions and the off-gas acitivity during this period are shown in Figure 3.3-1. After the

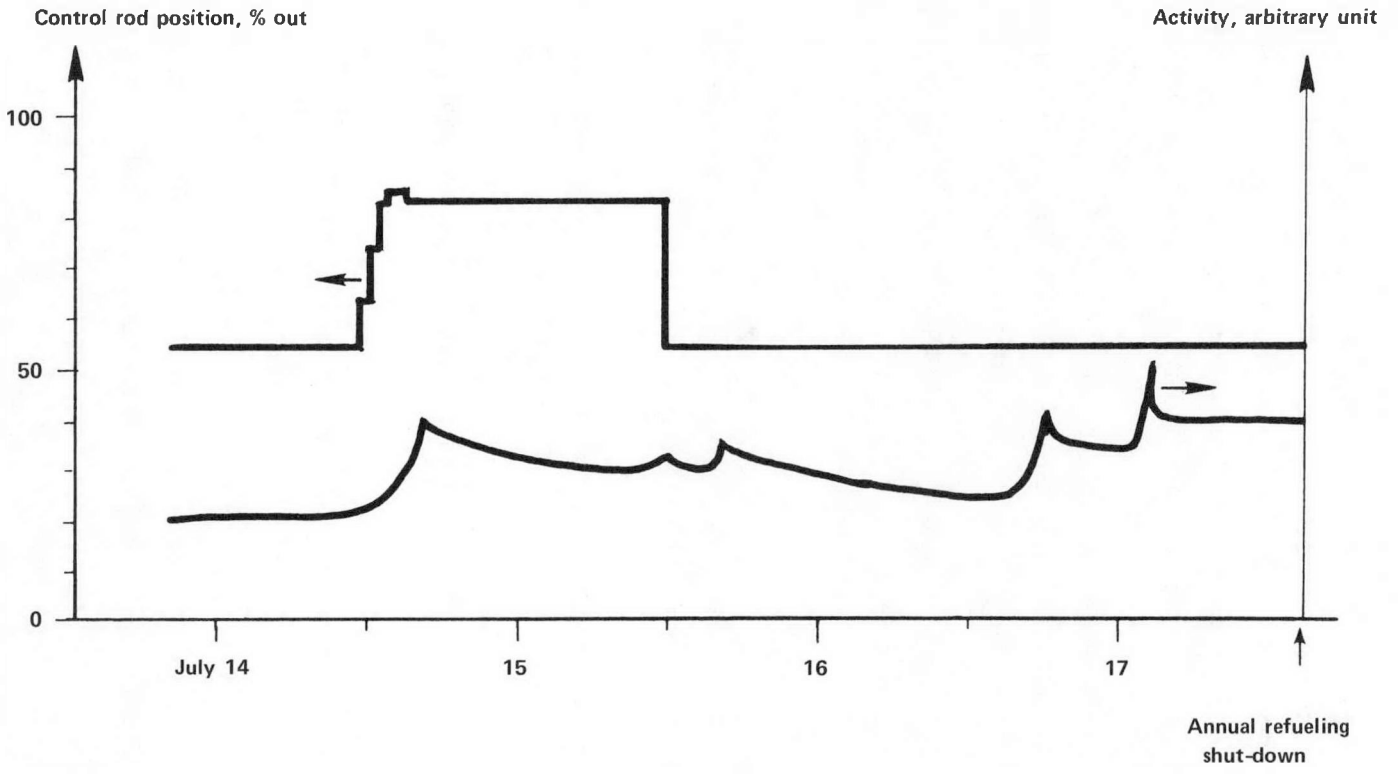

Figure 3.3-1. Control Rod Position and Turbine Condensor Off-Gas Activity During the Ramp Experiment in Oskarshamn-1

reactor shut down, it was determined by sipping that 14 assemblies in the vicinity of the control rod had failed during the experiment. The locations of the failed assemblies are shown in Figure 3.3-2. At the time of the power ramp, the average burnup of the affected assemblies was 10 to 12 GWd/MTU .

The power distribution in the core before and during the rod withdrawal was determined very carefully. Core physics calculations including xenon effects were performed. Traveling In-core Probe (TIP) measurements were done before, during, and after the experiment. Finally, individual fuel rods were gamma scanned during the reactor shut-down. Figure 3.3-3 shows the axial power distribution for one rod in one fuel assembly during the control rod withdrawal maneuvering. The maximum LHGR planned for and reached by the fuel was 38 kW/m. However, in all the assemblies exposed to this experiment there was a large spectrum of power increases leading to this maximum value in the worst case. It should be noted that the control rod withdrawal scheme exercised in this test far exceeds what would be required during normal reactor operation even without any PCI limitations. It resulted in a power distribution which was strongly skewed towards the bottom of the core. The failed fuel assemblies were removed from the core and subjected to detailed investigations by eddy current and ultrasonic testing and visual inspection of the individual rods. In the 14 assemblies failed in the ramp experiment, a total of 45 rods were deemed as failed or suspect (8). Figure 3.3-4 shows the axial distribution of the eddy current failure indications. It is seen that this distribution agrees well with the power distribution on Figure 3.3-3. The indications in the upper third of the rods were visually correlated with hydride damage, presumed to be secondary in nature, following water penetration through a primary crack.

A total of 13 suspect ramp failed rods were brought to the Studsvik hot cells and subjected to detailed investigation. In most of the cases, the failures were not detected by visual inspection and the location had to be determined from eddy current testing. Eddy current indications of cladding cracks were only recorded on rods that had defected. In defected rods, eddy current technique could locate both through-wall and incipient defects. No such indications were obtained in nonfailed rods perhaps indicating that crack contamination (e.g., oxidation etc.) is necessary to produce an eddy current signal. In a number of cases it was found that the rods were intact, showing that the reactor pool inspection had been too conservative and that the number of ramp test failed rods is probably less than 40.

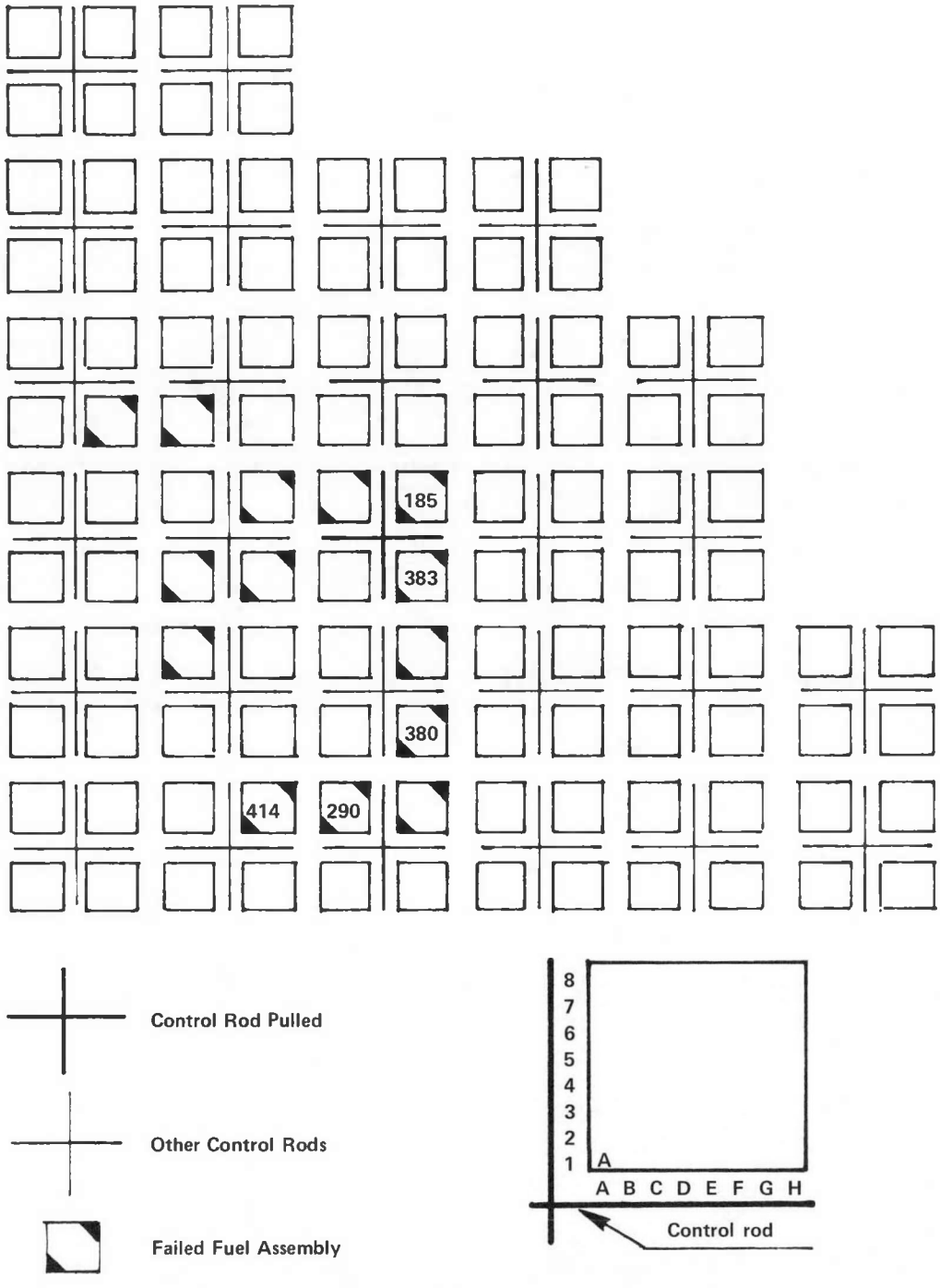

Figure 3.3-2. Location of Failed Fuel Assemblies in Oskarshamn-1 Core After the Ramp Experiment

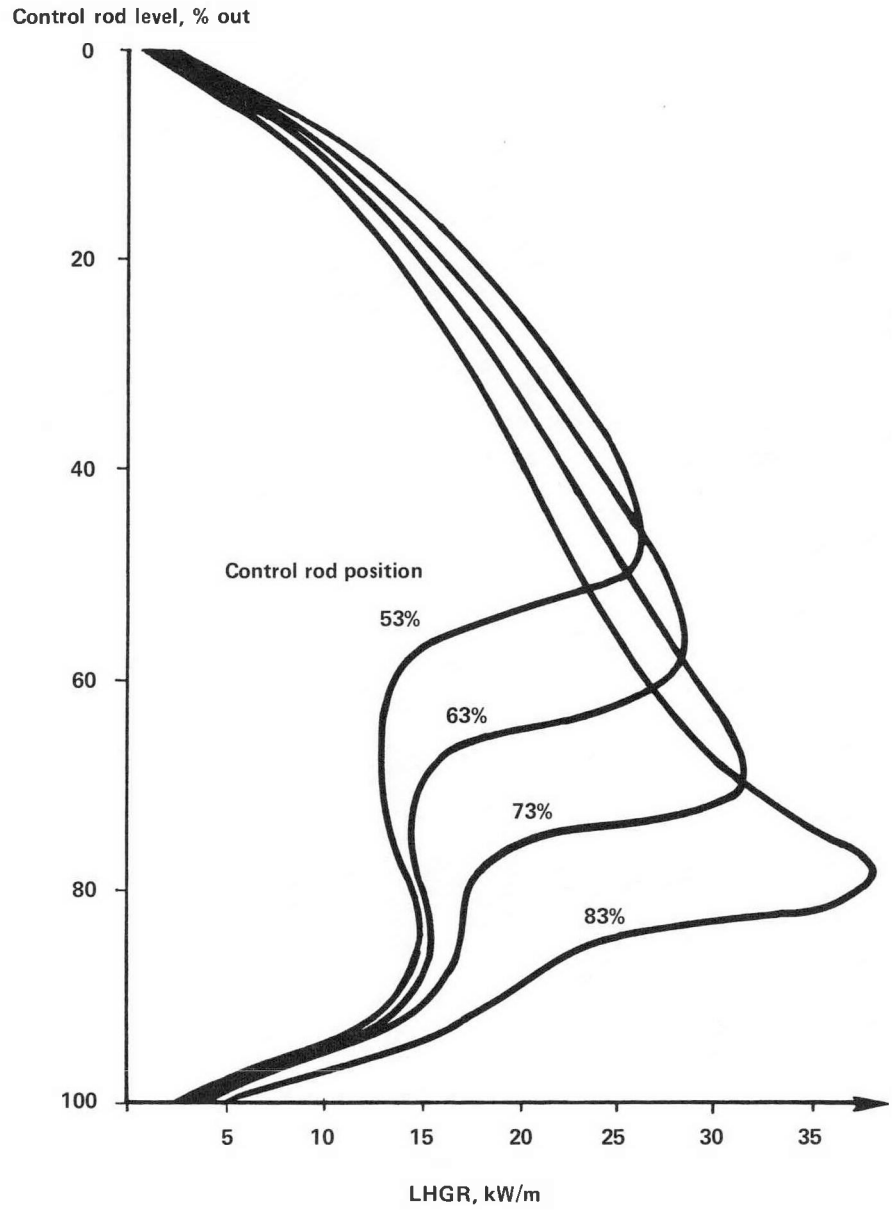

Figure 3.3-3. Axial Power Profile as a Function of Control Rod Position

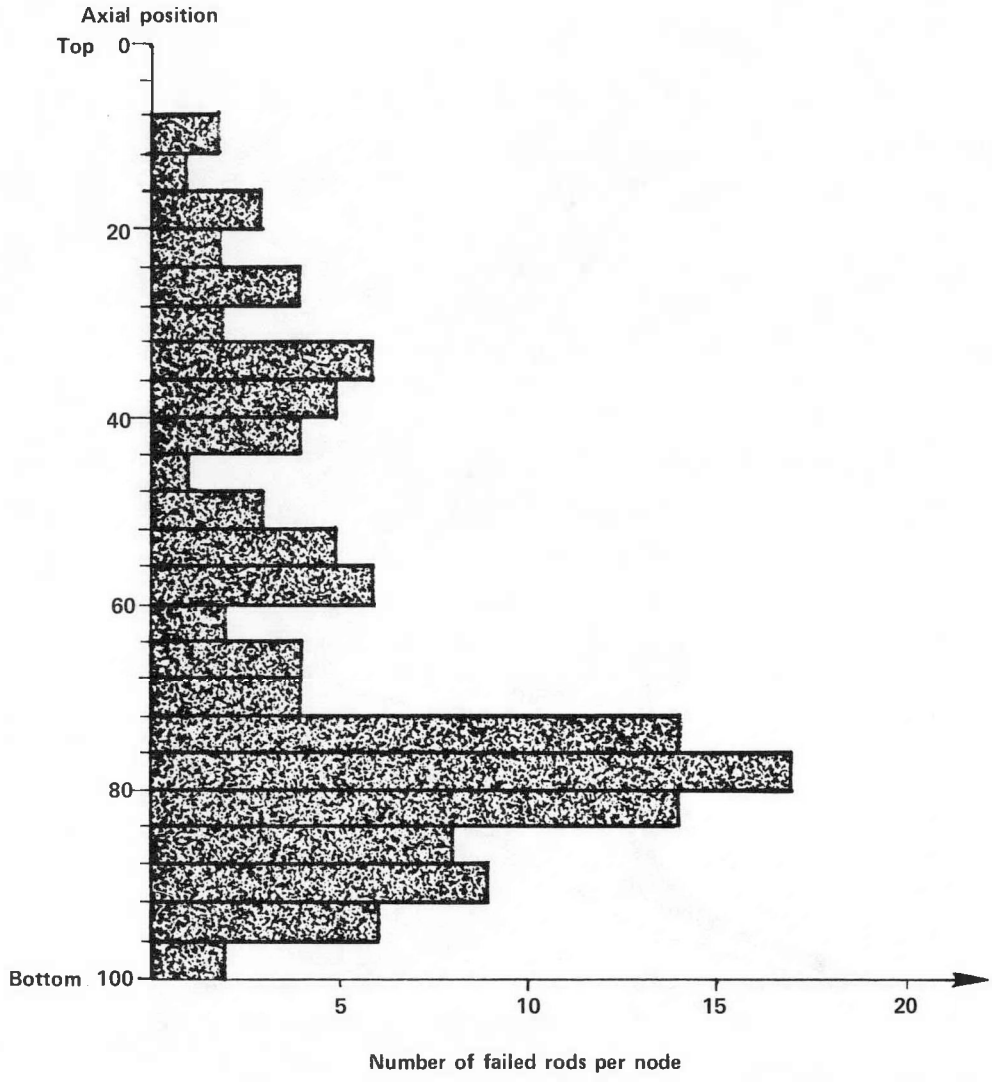

Figure 3.3-4. Number of Failed Rods Per Axial Node (Based on Eddy Current Examination) in the Group of 45 Rods Which May Have Failed Due to the Ramp Experiment

On some of these rods, the hot cell examination revealed small white deposits at positions that were in good agreement with eddy current indications. From earlier examinations it was known that the deposits contain cesium, which is forced out through small cracks in the cladding tube. These cracks, hidden under the cesium deposits, were quite small. In one instance, the cesium was wiped off with a damp rag , and afterwards it was impossible to find the crack.

It was considered that 10 of the rods might have failed due to the ramp experiment and that the cracks located by cesium extrusion were primary PCI cracks. In four cases metallographic evidence of SCC was found. The cracks exhibited the narrow, branched morphology, oriented at 90 degrees to the inside surface (Figure 3.3-5) and there was more than one crack in each sample. In the vicinity of the likely SCC cracks, there were pits on the inner surface, some were empty, while others were filled with debris. The cracks originated both between and in the pits.

To complement the extensive examinations of the Oskarshamn fuel rods performed at Studsvik (8), six rods from five assemblies were retrieved from the reactor for further defect examinations under RP829. Nondestructive and destructive examinations of the rods were conducted at Studsvik before cladding segments were shipped to ANL for detailed scanning electron microscopic (SEM) examination and mechanical property testing. Only the SEM examinations will be reported here. The purpose of these examinations was to characterize the physical and chemical nature of the cladding inner surface and cladding defect sites in an attempt to elucidate the specific chemical-mechanical relationship in the SCC process of PCI failure.

3.3.2 Selection of Specimens

The six rods selected for inclusion in RP829 represented the extremes in operating conditions during the Oskarshamn experiment. They were selected on the basis of poolside eddy current inspection and nodal power calculations. The rods selected are listed in Table 3.3-1. The rod identification contains first the assembly number and then the rod location in the assembly as shown by the key in Fig. 3.3-2. Rods 185/C1, 185/A7, and 383/A1 had undergone severe local power increases but only rod 383/A1 had failed. Rods 290/D4 and 414/A4 underwent only minor changes in power but both failed. The identification of failure was by poolside nondestructive (eddy current and ultrasonic) techniques.

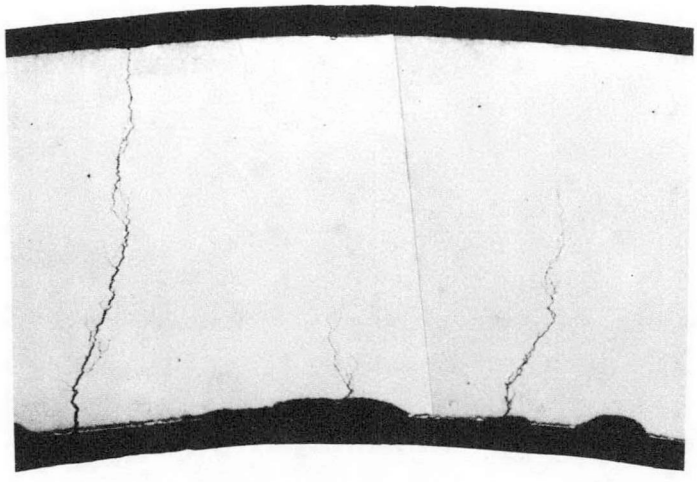

(a) 70X

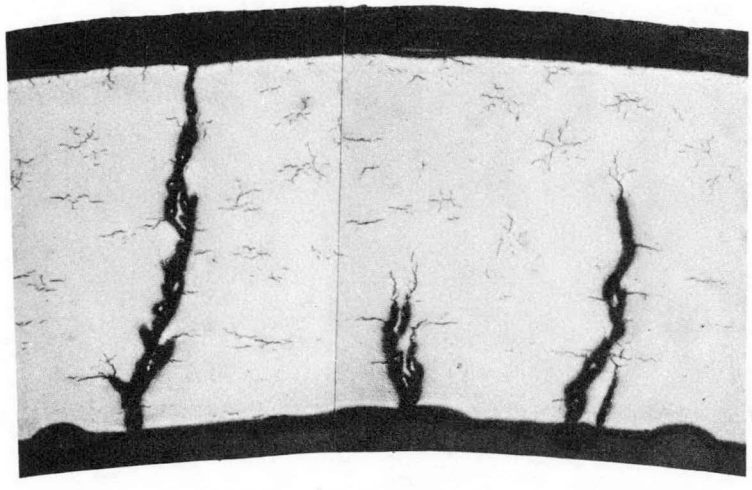

(b) 70X

Figure 3.3-5 Primary PCI Cracks Observed in Oskarshamn-1 Fuel Rods (a) As-polished (b) Etched

Table 3.3-1

DATA ON FUEL RODS IN RP829-5

Assembly Rod	Rod Average Burnup (MWd/kg U)	Initial Enrichment, % U-235	Diameter (mm)	Failure
414/A4	9.06	2.90	12.25	Yes
383/A1	11.5	1.40	11.75	Yes
380/B7	14.16	2.90	12.25	Yes
290/D4	11.48	2.55	12.25	Yes
185/C1	11.65	1.70	12.25	No
185/A7	12.21	2.05	11.75	No

Fission-gas analysis, profilometry, cesium gamma scanning, and eddy current inspection of the rods were performed at the Studsvik hot cell facility (3). The xenon release from 185/C1 and 185/A7 was 0.08 percent, and krypton gas release was 0.12 percent and 0.13 percent, respectively. Profilometry measurements on most of the rods indicated that no change, or a slight increase in the cladding diameter, occurred during reactor operation. In a few areas, ovality developed. Cesium gamma scanning showed that virtually no migration of cesium occurred. Depressions formed in the gamma scanning curves could be explained by axial gaps in the fuel column. Eddy current inspection was performed using a single encircling coil operating at 50 kHz. A number of eddy current signals were found in the failed rods, but none were found in the unfailed rods.

Two types of cladding specimens were sent to ANL: ten 2.5 cm long segments (K specimens) for inner surface characterization; and ten 15 cm long segments (L specimens) for mechanical testing. The locations of these specimens on the rods and their relationship to eddy-current defect signals is shown in Figure 3.3-6. The segments were cut dry with a diamond wheel in order to preserve the existing chemistry on the cladding. All cladding sections received at ANL were tubular with the fuel removed.

Table 3.3-2 lists the operating history of each K specimen. Three specimens, 10K, 11K, and 14K, came from the two unfailed rods; four specimens, 15K, 16K, 19K, and 20K, came from the failed rods but were not expected to contain defects based upon eddy current tests; and three specimens, 2K, 4K, and 8K, came from the failed rods and were expected to contain defects based upon eddy current measurements. Since unfailed rods did not exhibit eddy current indications, no specimens were received which contained eddy current signals from unfailed rods. Thus, the probability of examining a true incipient defect from the Oskarshamn experiment was extremely low.

3.3.3 Examinations and Results

The examinations of the Oskarshamn cladding sections were performed in a number of steps, each of which involved greater specimen segmentation. First, the outer surface of each sample was examined visually and photographed. Each sample was then cut into clamshell sections with a low speed cut-off wheel, and the surfaces were visually examined and photographed. After the major features of interest for SEM examinations were identified, further sectioning was performed in order

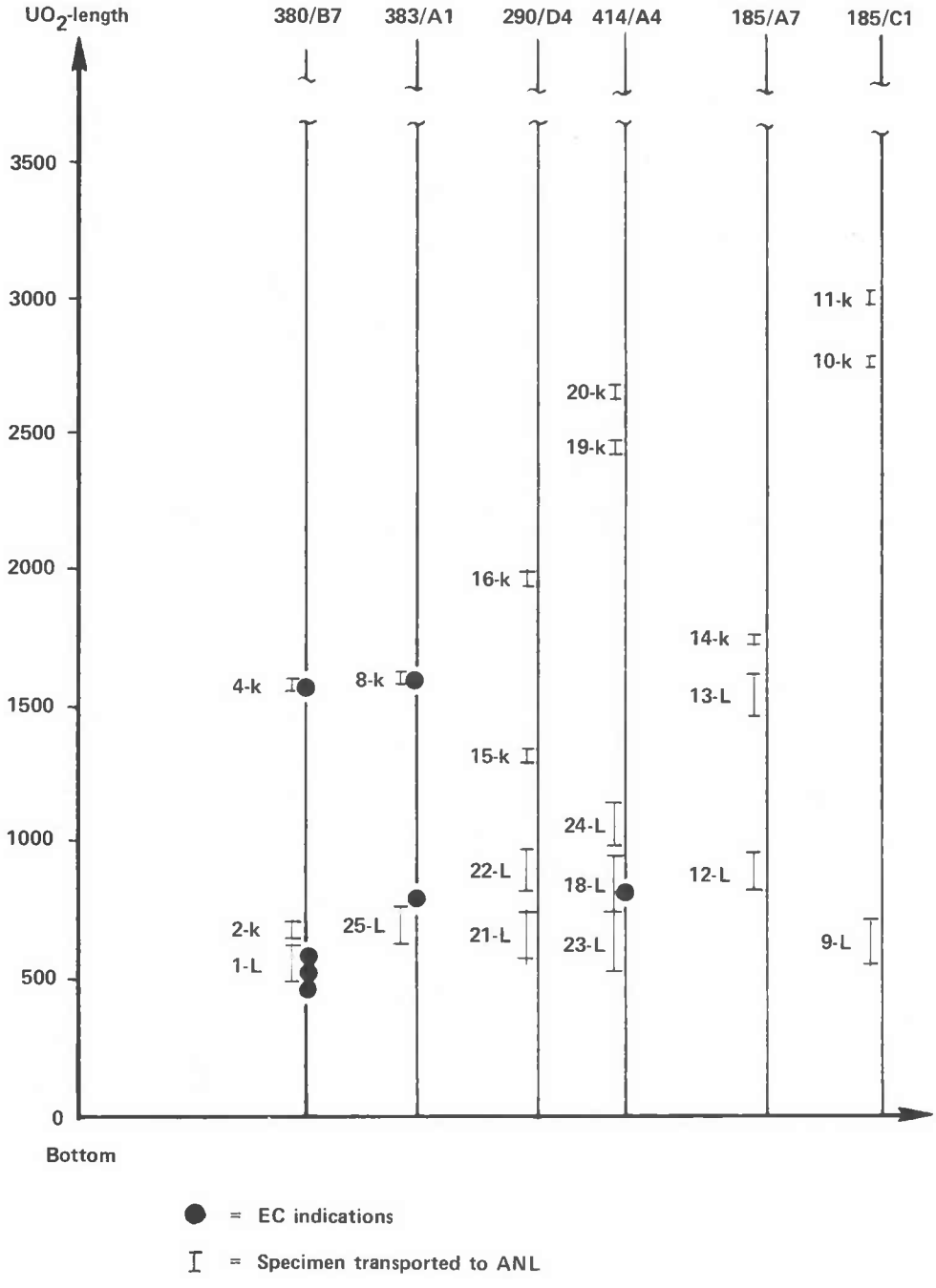

Figure 3.3-6. Locations of Eddy Current Indications and the Specimens Selected for Examination at ANL

Table 3.3-2

OPERATING HISTORY OF OSKARSHAMN SPECIMENS EXAMINED AT ANL

Specimen Number	Assembly/ Rod	Condition	Axial Position (mm)	ECI	Burnup, MWD/kg	q_L^1-max[a]	q_L^2-max[b]	Δ^1_{qL}[c]	Δ^2_{qL}[d]
2K	380/B7	F	670-695	Yes	13.4	27.6	33.2	+ 5.7	+ 5.6
4K	380/B7	F	1590-1615	Yes	13.8	28.4	24.7	+ 1.2	- 3.7
8K	383/A1	F	1600-1625	Yes	13.1	20.0	16.6	- 3.4	- 3.4
10K	185/C1	NF	2800-2825	No	13.3	21.6	14.1	- 3.2	- 7.5
11K	185/C1	NF	3040-3065	No	12.9	20.6	13.0	- 3.0	- 7.6
14K	185/A7	NF	1750-1775	No	12.3	23.5	22.4	- 1.1	- 1.1
15K	290/D4	F	1320-1345	No	13.9	20.9	18.2	+ 0.3	- 2.7
16K	290/D4	F	1930-1955	No	13.7	20.6	17.7	- 1.2	- 2.9
19K	414/A4	F	2470-2495	No	10.3	23.2	20.3	- 2.2	- 2.9
20K	414/A4	F	2650-2675	No	10.1	22.7	19.3	- 2.2	- 3.4

[a] q_L^1-max = maximum local LHGR during the 1974-75 operation, in kW/m.

[b] q_L^2-max = maximum local LHGR during the ramp in kW/m.

[c] Δ^1_{qL} = power increase during the ramp in kW/m.

[d] $\Delta^2_{qL} = {}^1_{qL} - {}^2_{qL}$

to reduce the gamma activity level in the SEM. The SEM examination consisted first of topographical mapping of the specimen surface at low magnification. The locations of features taken at high magnification could then be pinpointed on these maps. Individual features were recorded photographically and then chemically analyzed using energy dispersive X-ray analysis. Where necessary, stereophotos were taken to better determine the surface topography. The X-ray analyzer was used to take overall and spot scans of the surface. If high concentrations of particular elements were found, elemental maps of those areas were made.

3.3.3.1 Surface Characterization.

3.3.3.1.1 Specimens from unfailed rods. Specimens 10K, 11K, and 14K came from unfailed rods and did not exhibit eddy current indications. The inner surfaces of these specimens were a light metallic brown color with occasional dark deposits of fuel in the form of lines and spots as shown by specimen 11K, Figure 3.3-7. A low magnification SEM composite photograph of Specimen 11K is also shown in Figure 3.3-7. None of the specimens exhibited linear deposits of fission products that are found adjacent to fuel cracks and pellet-pellet interfaces such as were observed on the Maine Yankee (6) and Dresden-3 specimens. (Section 3.2)

Most of the features observed in the SEM occurred in varying degrees over the entire inner surface of the three specimens. The principal features were fuel deposits, wormlike and nodular growths on the Zircaloy surface, and occasional oxide surface cracking that is believed to be artifactual. The fuel deposits exhibited a blocky appearance in the SEM as shown in Figure 3.3-8. The particles varied in size from 30 μm down to submicron size. No indication of any interaction between the Zircaloy surface and the fuel particles could be detected. The particles tended to be concentrated as line or individual deposits, but small particles were scattered over most of the surface. In areas that were relatively free of fuel, two types of Zircaloy surfaces were found. These two surface types or combinations of them in many degrees of development comprised the entire Zircaloy surface. The surface that occurred with the greatest regularity were the wormlike growths shown in Figure 3.3-9. The growths were hemispherical or cylindrical in shape and were 3 to 5 μm in diameter. At higher magnification (Figure 3.3-9b), a secondary nodular-like structure was observed covering the entire surface including the wormlike growths. In other areas, a surface with a more nodular

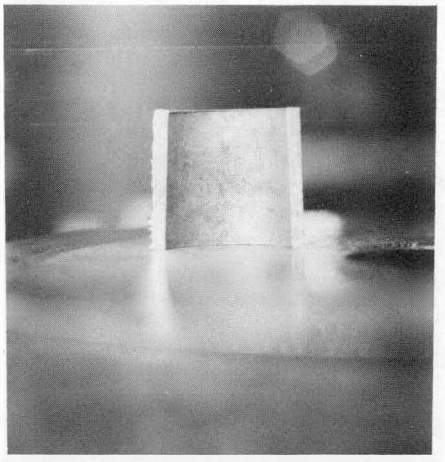

(a) Negative Number MSD-190500

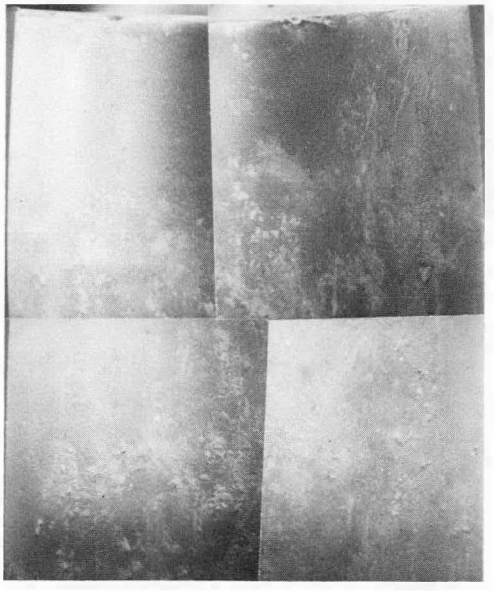

(b)

Figure 3.3-7 (a) Inner Surface of Specimen 11K (~ 1.5X)
(b) Inner Surface of Specimen 11K taken in SEM

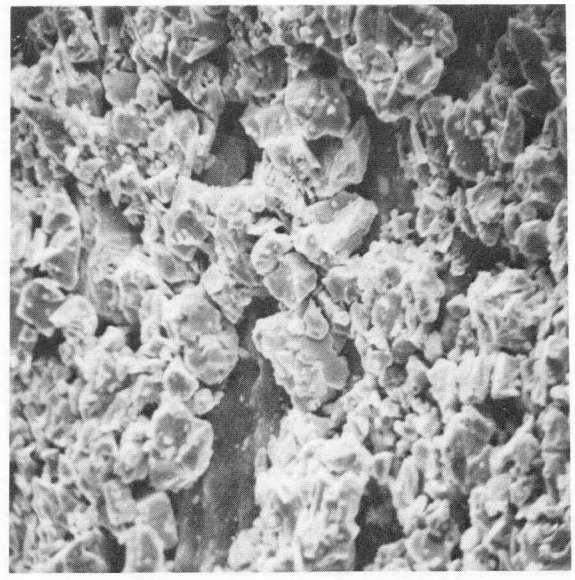

Figure 3.3-8. Fuel Particles on Inner Surface of Specimen 11K (1000X) Neg. No. MSD-203825

(a) Neg. No. MSD-203788

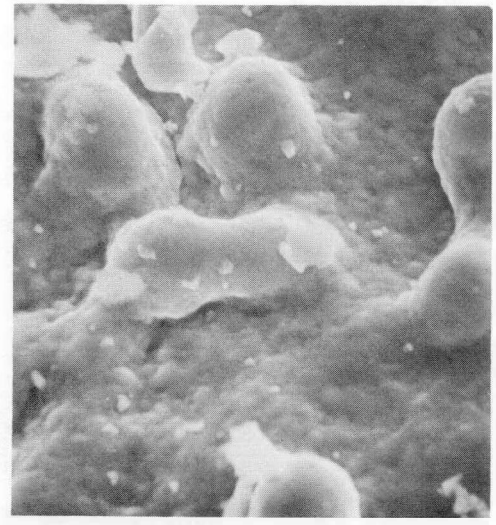

(b) Neg. No. MSD-204557

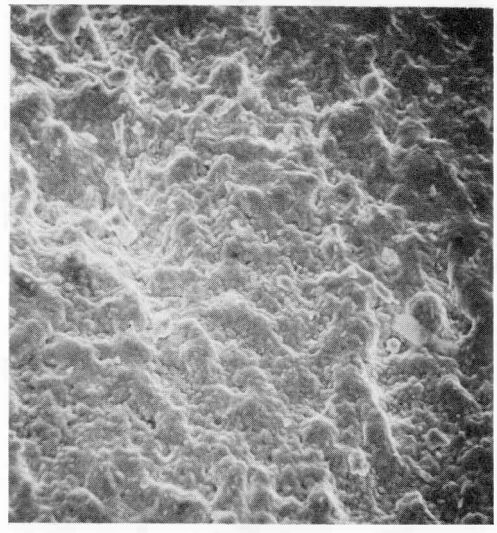

(c) Neg. No. MSD-203873

Figure 3.3-9 (a) Wormlike Growths on Specimen 10K (1000X)
(b) Close-Up of Wormlike Growths (4000X)
(c) Nodular Surface on Specimen 10K (1000X)

appearance was observed (Figure 3.3-9c). The small nodules were roughly hemispherical in shape and were less than a micron in diameter. Longer nodules were also observed in the area, and their size was approximately the same as the wormlike growths. Only uranium and zirconium were detected in the wormlike and nodular growths.

Longitudinal surface cracks were observed on the inner surfaces of Specimens 11K and 14K (see Figures 3.3-10a and b). They occurred in isolated areas and were quite narrow, ~ 0.25 μm wide, and sharp in appearance. The crack paths usually did not follow any surface features. It is believed that these cracks could have been produced during specimen preparation. To test this hypothesis, Specimen 14K was flattened to produce additional cracking. The cracks produced were uniformly distributed over the inner surface and were similar in appearance to the cracks previously observed (see Figure 3.3-10c). The fractures produced were ductile in character and it is assumed that the surface cracks initially observed, if they penetrated the substrate, would not have shown SCC characteristics.

Chemical elements which were identified on the inner surfaces are Ni, Cr, Zn, Cu, Cl, Ca, Ba, and Cs. These elements, with the exception of Cs, were always observed in individual particles and were not distributed in a uniform manner on the surface. The source of these elements is not definitely known, but it is likely that the presence of some of these elements is due to contamination from the outer surfaces or from contamination during specimen preparation and shipment. It is also possible that some of these elements were produced during irradiation or are impurities in the fuel or cladding.

3.3.3.1.2 Specimens without defect indications from failed rods. Specimens 15K, 16K, 19K, and 20K were sectioned from failed rods and gave no eddy current indications of defects being present. The inner surfaces were dark blue or black, in contrast to the light appearance of the unfailed rods, and fuel particles were observed adhering to the surfaces. These specimens had a relatively clean appearance, and there were no visible cracks or deformed areas. There were also no linear fission-product deposits from duel cracks or pellet-pellet interfaces, similar to the surfaces of the unfailed rods. Figure 3.3-11 shows both the optical and secondary electron image of Specimen 15K, which was typical of all four specimens.

(a) Negative Number MSD-204000

(b) Negative Number MSD-203956

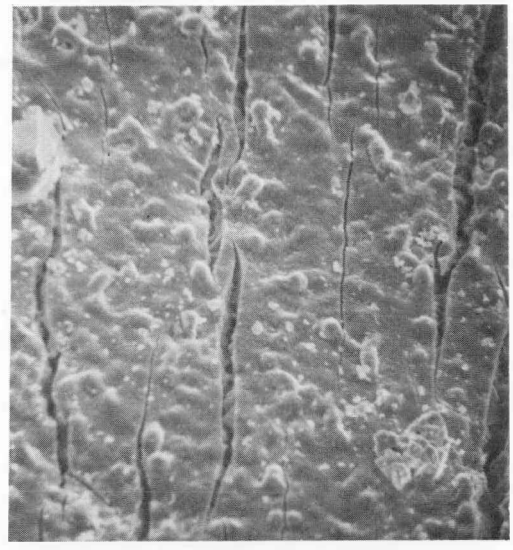

(c) Negative Number MSD-204077

Figure 3.3-10 (a) Cracks on Inner Surface of Specimen 11K (2000X)
(b) Cracks on Inner Surface of Specimen 14K (1000X)
(c) Cracks Produced by Flattening Specimen 14K (700X)

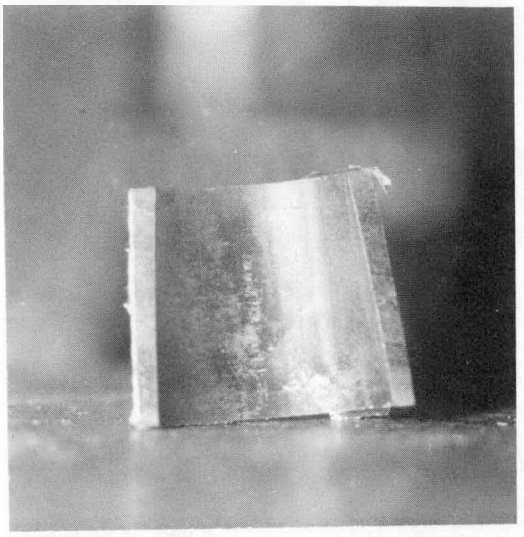

(a) Negative Number MSD-190908

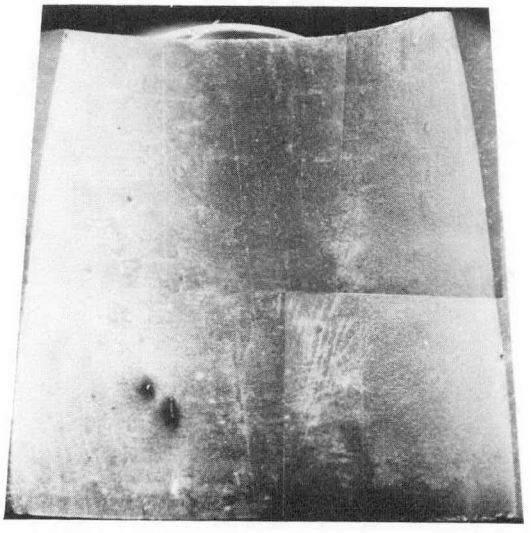

(b) Negative Number MSD-193791

Figure 3.3-11. (a) Inner Surface of Specimen 15K (~ 3X)
(b) Inner Surface of Specimen 15K taken in SEM

Although the optical appearance of these specimens was different from the specimens from unfailed rods, the surface features observed in the SEM were very similar. The wormlike and nodular Zircaloy structures were again present over a large portion of the inner surfaces and the fuel particles were of a similar nature. The size and surface distribution of the particles appeared to vary from specimen to specimen. Specimen 15K exhibited numerous line deposits of U_2 (Figure 3.3-12a) while Specimen 19K was relatively clean with only small UO_2 particles scattered on the surface. Large (20-30 μm) U_2 particles were observed on the inner surface of Specimen 16K (Figure 3.3-12b). No surface cracks were observed on any of the specimens.

The results of X-ray analysis of the specimen surfaces were similar to those from Specimens 10K, 11K, and 14K. In addition to uranium and zirconium, iron, calcium, chlorine, copper, and nickel were found on the inner surfaces.

3.3.3.1.3 Specimens with defect indications from failed rods. Specimens 2K, 4K, and 8K were sectioned from failed rods and exhibited eddy current signals. The presence of defects was confirmed during SEM examination in all three specimens. Before clamshell cuts were made, the outer surfaces of these specimens were thoroughly scanned in a stereo viewer in an attempt to locate the defect sites. In all cases, there were no indications on the outer surface at the defect locations. Since the axial and angular locations of the defects were not known, the positions of the initial clamshell cuts were selected at random.

The initial sectioning of Specimen 4K consisted of cutting a 3 mm thick ring from one end to shorten the piece so that it would fit in the longitudinal sectioning fixture, and then making the longitudinal clamshell cut. As shown in Figure 3.3-13, most of the inner surface was black with deposits of fuel and was similar in appearance to Specimens 15K, 16K, 19K, and 20K. A few thin (< 0.5 mm) white lines were observed in the longitudinal direction. The most important feature on the inner surface was a 4 μm diameter circular pit found visually near the end of the specimen through which the initial ring cut had passed. The pit, shown in Figure 3.3-13, was a metallic purple color and had penetrated the cladding to a substantial degree.

(a) Negative Number MSD-203937

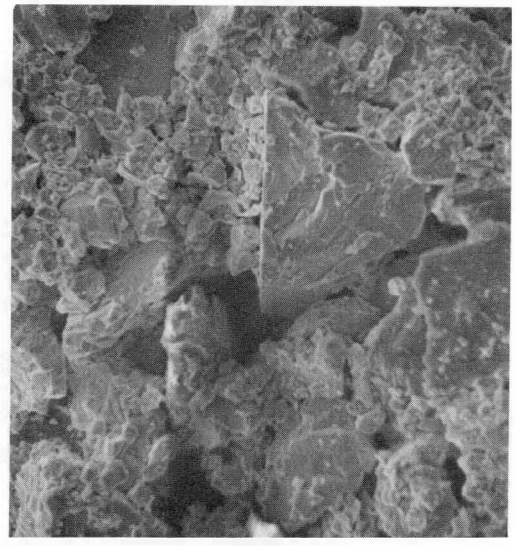

(b) Negative Number MSD-203953

Figure 3.3-12 (a) UO_2 Line Deposits on Specimen 15K (60X)
(b) UO_2 Particles on Specimen 16K (700X)

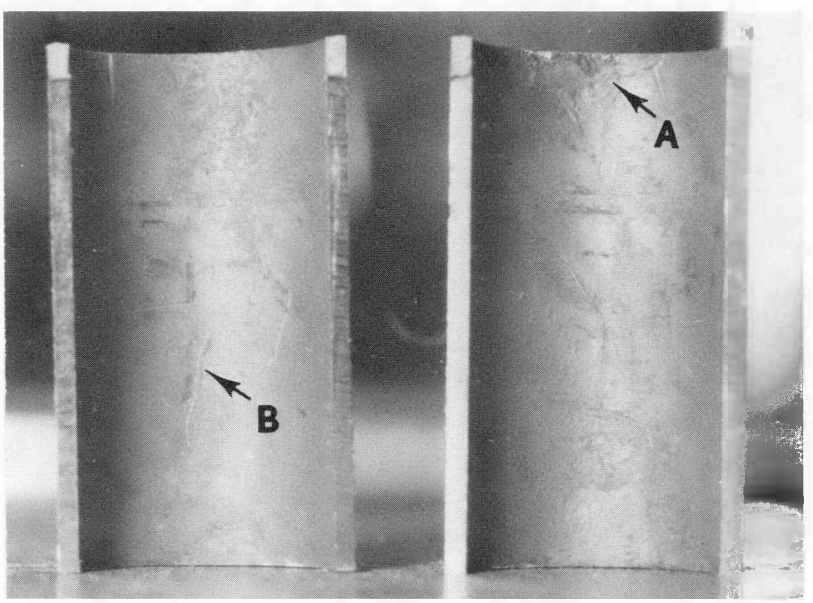

Neg. No. MSD-192103

Figure 3.3-13. Inner Surface of Specimen 4K
Defect is Located at Area A (2.5X)

The same features observed in the specimens which did not exhibit eddy current indications were seen on the inner surface of Specimen 4K. Uranium was detected over the entire inner surface, and cesium was detected in several areas in low concentrations. A close-up of the white line deposits (Area B, Figure 3.3-12) is shown in Figure 3.3-14. The deposits were composed primarily of uranium, but cesium and zirconium were also detected.

Close examination of the surface pit shown in Figure 3.3-13 indicated there was a through-wall crack associated with it as shown in Figure 3.3-15. It is not known if the crack was present before sectioning or if the crack was created during sectioning. The pit surface indicates a nonductile fracture (Figure 3.3-16), but the cleavage and fluting which are typical of SCC failures are not present. Only zirconium was detected on this surface. Another circular defect, which was very similar in appearance to this one, was located on the 3 mm thick ring, is shown in Figure 3.3-17. Figure 3.3-17 also shows a longitudinal crack associated with the defect. Closer examination of the crack near the defect showed that a surface layer had been removed from the vicinity of the crack (Figure 3.3-18a). This surface layer proved to be rich in uranium (Figure 3.3-18b).

The inner surface of Specimen 8K, shown in Figure 3.3-19, was optically similar in appearance to specimens which did not exhibit eddy current indications from failed rods. A circumferential line, possibly the location of a pellet-pellet interface, was observed in the middle of the specimen (Area A, Figure 3.3-19). No defects or cracks were found during visual examination.

The surface features of Specimen 8K observed in the SEM were similar to those previously discussed, with two exceptions. First, white nodular growths were found in areas along the circumferential line and also along some longitudinal lines. These growths, shown in Figure 3.3-10, were ~ 1 μm in diameter and contained a high uranium concentration and a low concentration of cesium. Second, the circumferential line contained numerous small, circumferentially oriented cracks that were determined from stereo photos to be associated with a surface depression. The total length of the cracks in the circumferential direction was ~ 3 mm. A portion of the cracked area is shown in Figure 3.3-21. There are many hairline cracks in the area, but the larger cracks tend to follow the ridge of the deformation area. This depression and

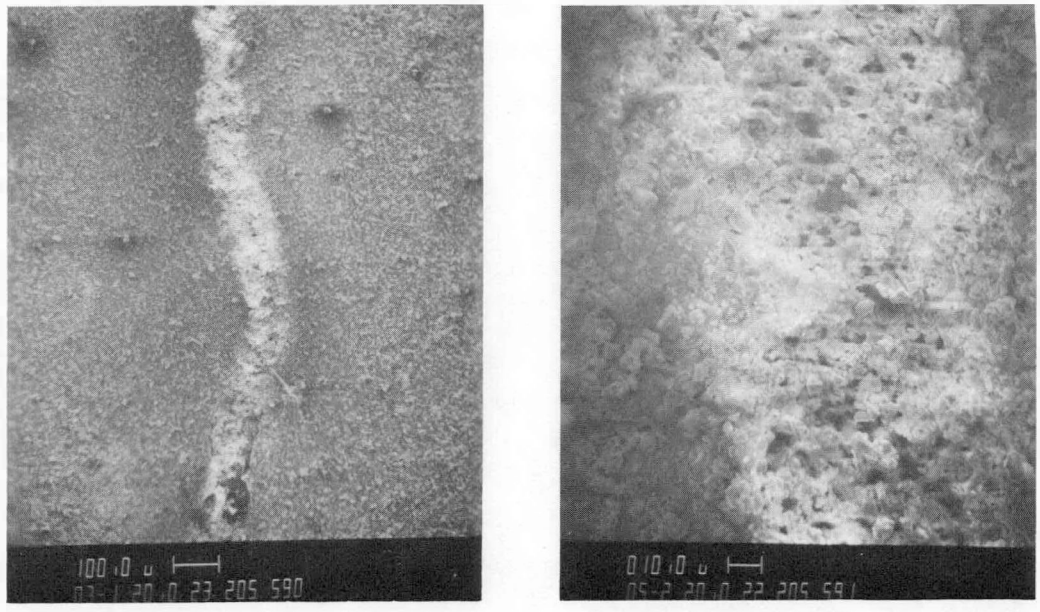

(a) (b)

Figure 3.3-14. (a) White Line Deposit from Specimen 4K (Area B, Figure 3.3-13;
(b) Close-Up of (a)

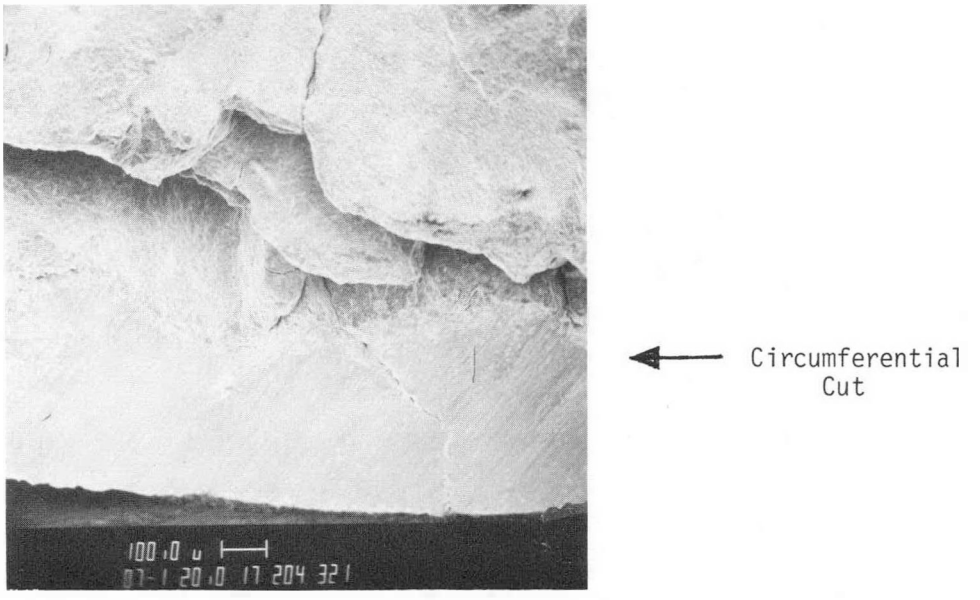

Figure 3.3-15 Through-Wall Crack Associated With Defect, (Area A, Figure 3.3-13) in Specimen 4K

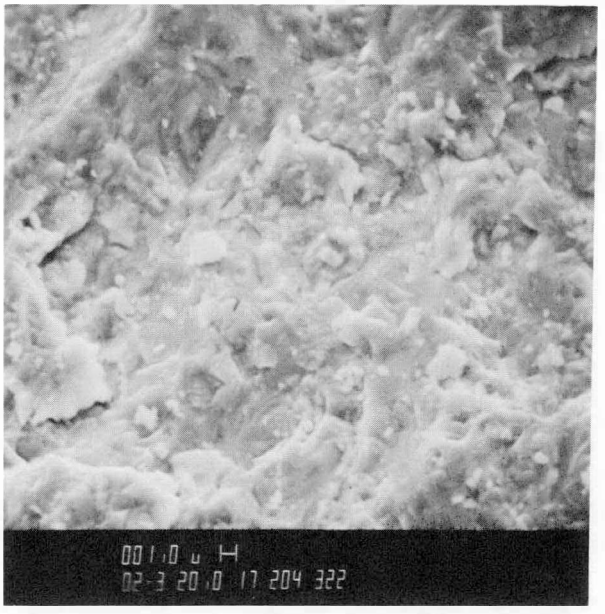

Figure 3.3-16. Fracture Surface of Defect on Inner Surface of Specimen 4K (Area A, Fig. 3.3-13)

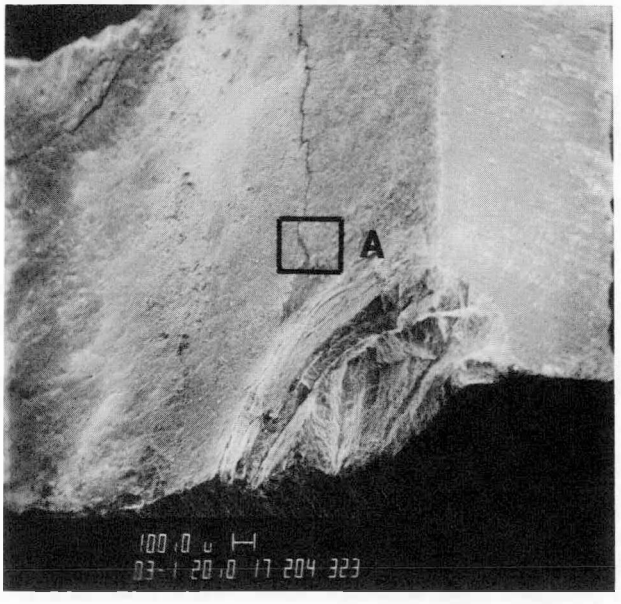

Figure 3.3-17. Second Defect on Inner Surface of Specimen 4K
Note Longitudinal Crack

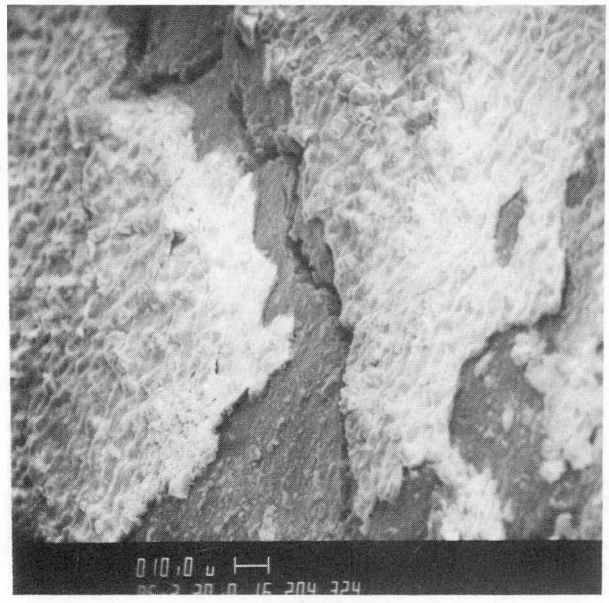

(a)

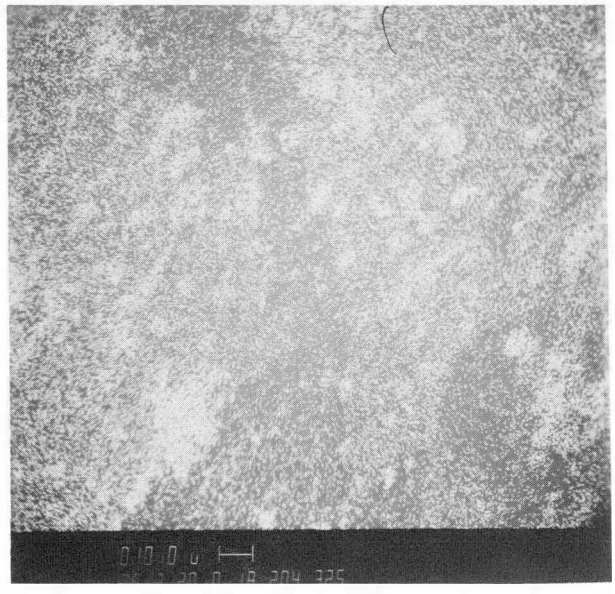

(b)

Figure 3.3-18 (a) Crack Associated With Defect Shown in Area A, Figure 3.3-17, and (b) Uranium Map of (a)

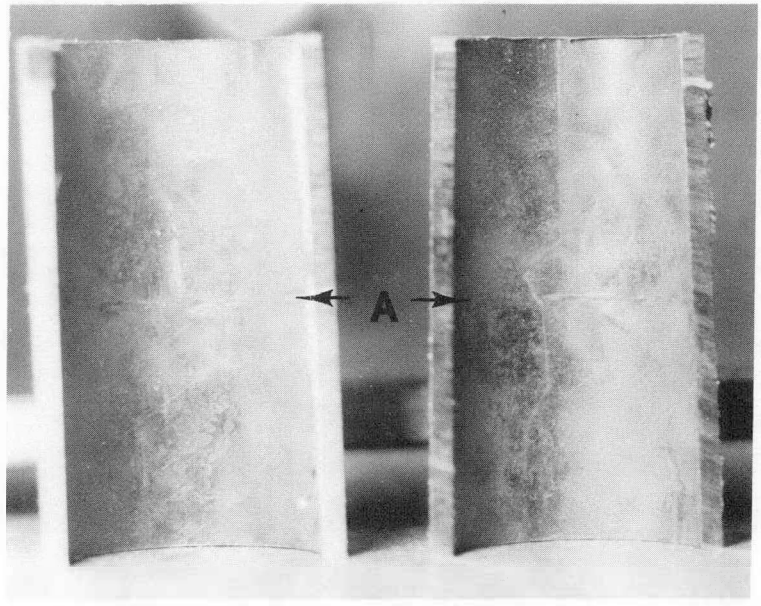

Figure 3.3-19. Inner Surface of Specimen 8K (~ 2.5X)
Neg. No. MSD-192105

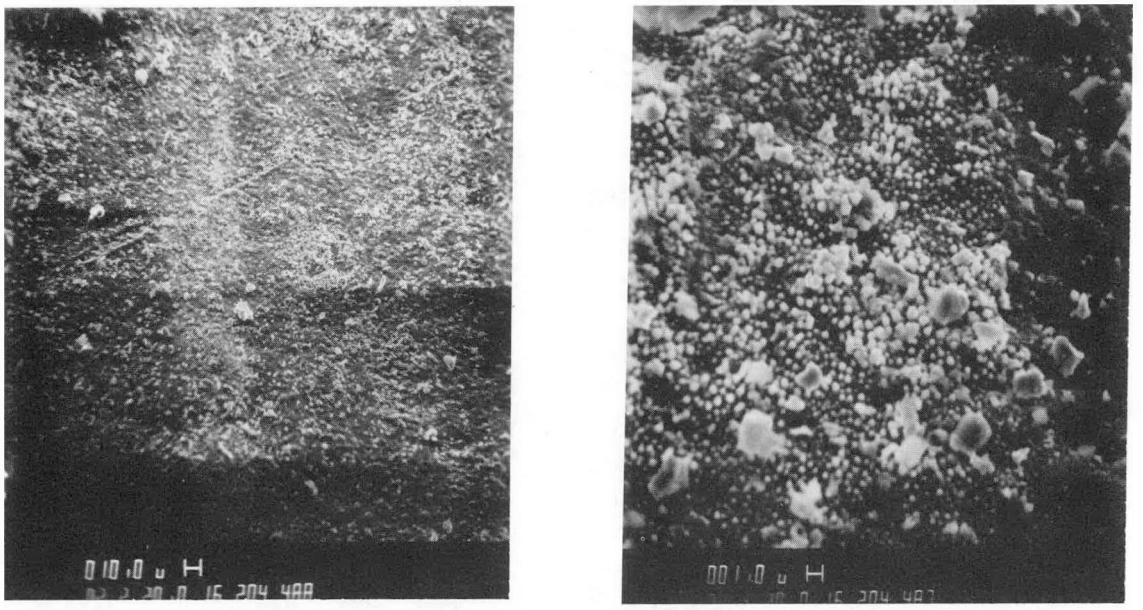

(a) (b)

Figure 3.3-20 (a) Light Strip on Inner Surface of Specimen 8K (200X), and (b) Close-Up of (a) (2000X)

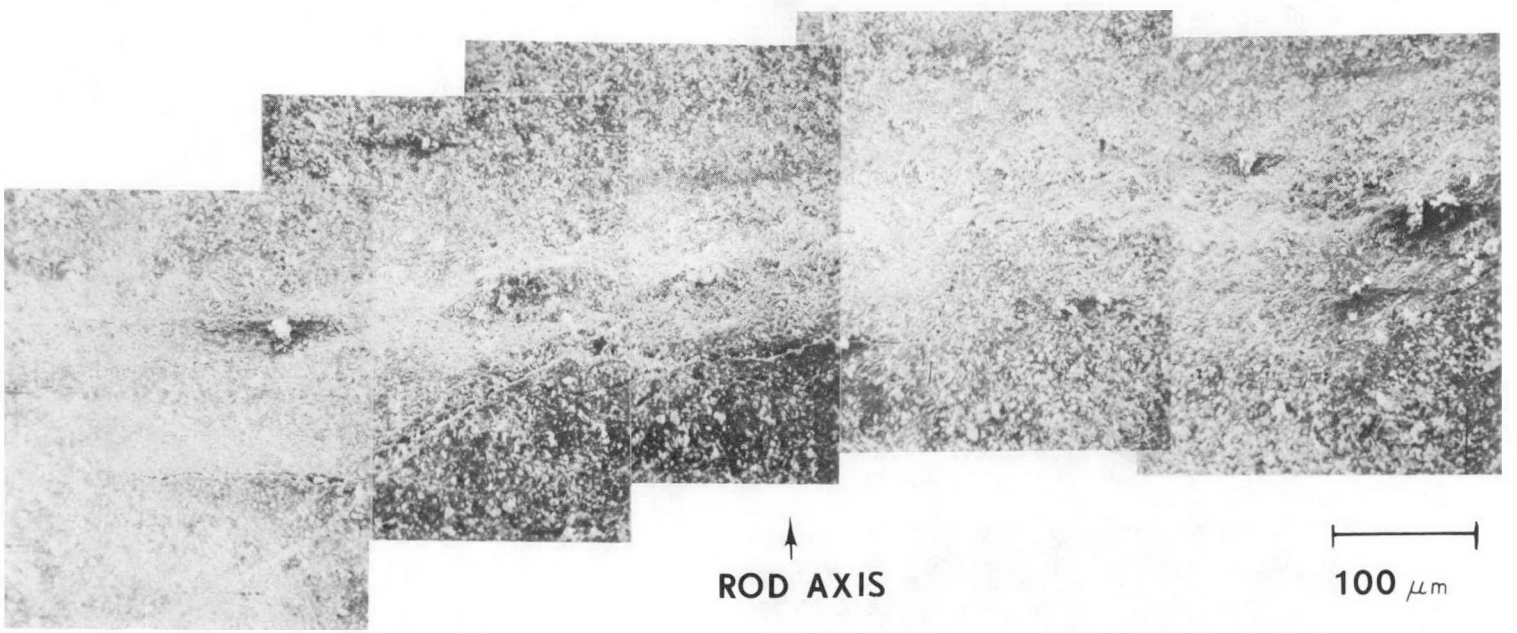

Figure 3.3-21 Cracks Located Along PPI of Specimen 8K

the resulting circumferential cracks were possibly caused by pellet hourglassing and pellet-cladding mechanical interaction. The cracks in this area, which are the probable cause of the eddy current signal in this specimen, were opened by 3 point bending and examined as described in the next section.

The inner surface of Specimen 2K, shown in Figure 3.3-22, was partially covered by heavy white deposits. The initial longitudinal cut passed through a major defect (Point A), which resulted in the removal of the white deposit in that area. The size of the exposed area was approximately 6.5 x 6.5 mm. Other white deposits on the surface were linear or circular. The linear deposits on the surface were linear or circular. The linear deposits varied in width from 0.5 to 2 mm, while two large circular deposits were approximately 5 mm in diameter. Darker deposits were also observed on the surface. Although they did not appear visually to be fuel deposits, X-ray analysis indicated they were high in uranium content with a small quantity of cesium. The SEM examination indicated that the presence of these large deposits over most of the surface resulted in a charge buildup of the specimen from the electron beam. The charge buildup, which indicates the nonconducting nature of the deposits, was not observed in any of the other specimens. Such a charge buildup from deposits containing uranium could be due to a higher oxide of uranium than UO_2. A higher oxide would result from water ingress to the rod and subsequent fuel oxidation. A low magnification SEM map of the 2K surface indicating significant features is shown in Figure 3.3-23.

In several areas on 2K, the uranium-containing deposits appeared to be the result of liquid flow in channels between the fuel and cladding, as shown in Figure 3.3-24 (Area A, Figure 3.3-23). Surface cracking of the heaviest uranium containing deposits was observed, while in areas where the deposits were absent, the wormlike growths seen in previous samples were observed. Two areas showed circular cracking of the Zircaloy over a width of 2-3 mm in the vicinity of heavy uranium-containing deposits (Areas B and C, Figure 3.3-23). A close-up of Area B, Figure 3.3-23 is shown in Figure 3.3-25. This area is raised on the periphery, depressed around the center, and again raised in the center. A typical example of a fuel deposit is shown in Figure 3.3--26a (Area D, Figure 3.3-23). The fuel had a rounded appearance, rather than the blocky appearance seen in previous samples, and the deposit was surrounded

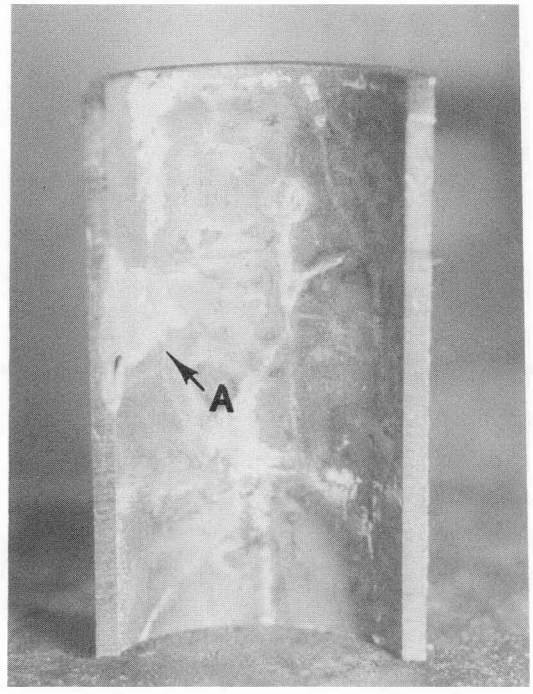

Figure 3.3-22 Inner Surface of Specimen 2K (~ 2.5X) Defect is Located at Area A. Negative Number MSD-191632

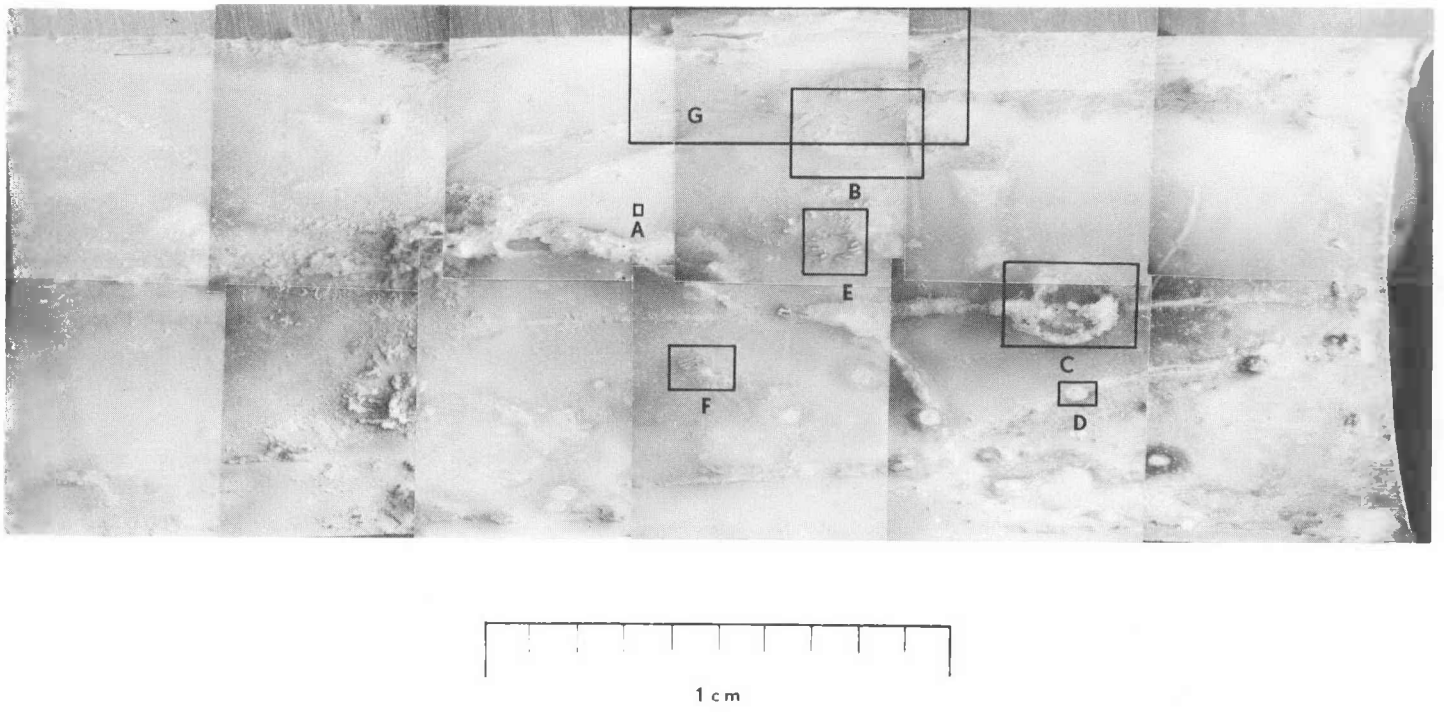

Figure 3.3-23 SEM Composite of Specimen 2K

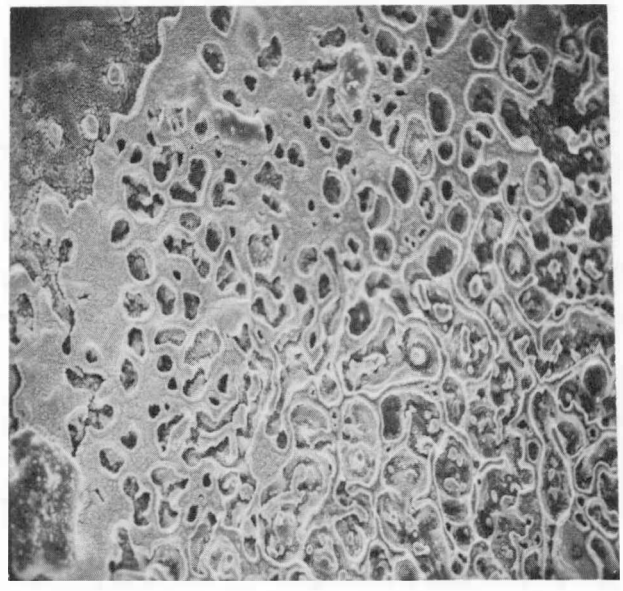

Figure 3.3-24 Uranium Containing Deposit on Inner Surface of Specimen 2K (Area A, Fig. 3.3-23) 400X
Neg. No. MSD-204133

Figure 3.3-25 Circular Cracks Near Large Uranium Containing Deposit on Inner Surface of Specimen 2K (Area B, Fig. 3.3-23) 30X
Neg. No. MSD-204129

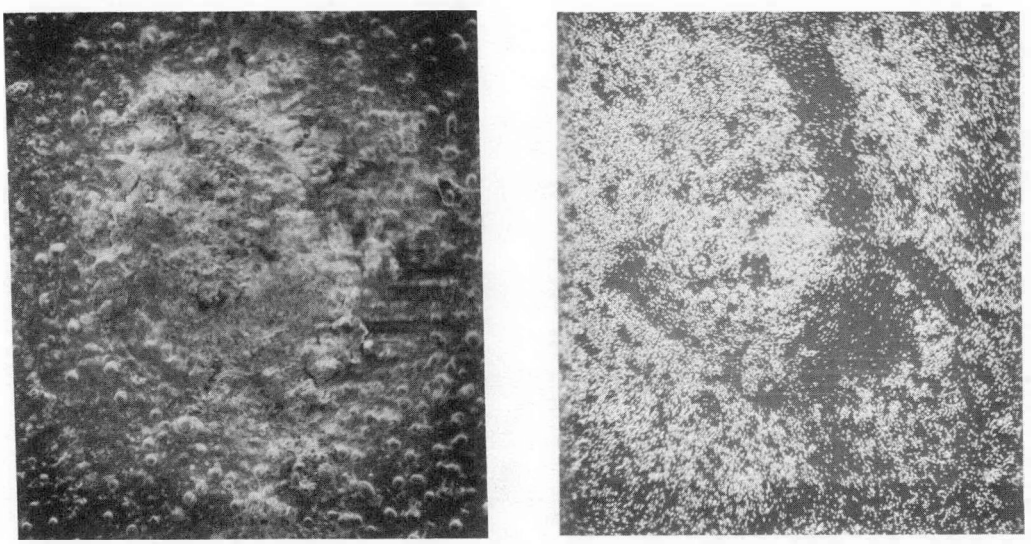

(a) (b)

Figure 3.3-26 (a) Circular Deposit Containing a High Uranium Concentration (Area D, Figure 20), 200X, Negative Number MSD-204285. (b) Uranium Map of (a) Negative Number MSD-204286

by a halo that had a high uranium concentration (Figure 3.3-26b). Surface oxide flaking was observed in two areas (Areas E and F, Figure 3.3-23). Figure 3.3-27 (Area E, Figure 3.3-23) shows a uranium-containing particle, possibly a deformed piece of fuel, surrounded by surface flaking. The light areas of the flakes are the result of electron charge buildup.

The defect which was exposed by the sectioning of 2K is shown in Figure 3.3-28 (Area G, Figure 3.3-23). A portion of the Ziracloy substrate was removed along with the white deposit. In some areas the depression is ~ 50 percent of the cladding thickness. The surface of the exposed Zircaloy at the defect site shown in Figure 3.3-29 indicates a brittle fracture, but it does not have the cleavage and fluting features of an SCC failure. A through-wall crack was also present at this site (Area B, Figure 3.3-28). However, it is not known if this crack was present prior to sectioning or whether it was created by the sectioning process. The surface of the crack near the outer surface contains a large amount of debris as shown in Figure 3.3-30. Several elements including calcium, zinc, cesium, uranium, and iron were found at isolated points on this surface. Only zirconium was detected on the exposed Zircaloy substrate on the inner surface.

3.3.3.2 Fractographic Examination. Several of the defects from Specimens 2K, 4K, and 8K were opened by three point bending in order to study the Zircaloy substrate and to determine the mode and extent of fracture. Prior to bending, the cladding was positioned in the bending apparatus such that the maximum stress was applied to the area of the defect. In some cases, the bending was done 90 degrees to the long axis of the rod. The defect sites investigated included the areas of circular cracking on Specimen 2K (Areas E and F of Figure 3.3-23), the circumferential cracks on Specimen 8K (Figure 3.3-21), and the large pits on Specimen 4K (Area A, Figure 3.3-13). The fracture surfaces of all the defects were similar in appearance, and only differed in the degree of the different fracture types.

The fracture surface corresponding to the circumferential cracks in Specimen 8K is shown in Figure 3.3-31. Two distinct fracture types can be delineated: a dark smooth surface which travels ~ 150 μm into the cladding, and a more irregular surface over the rest of the fracture. The fracture types can be seen more clearly in a higher magnification map of the area shown in Figure 3.3-32. The area of smooth fracture follows a circular arc and has a width of approximately 1.5 mm.

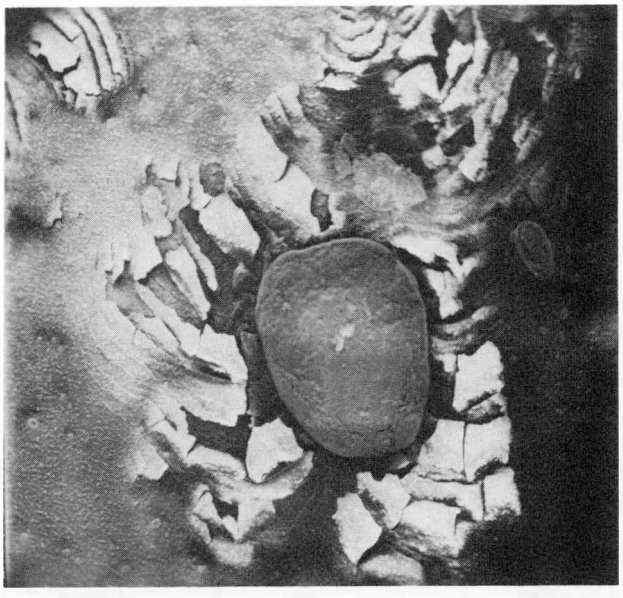

Figure 3.3-27 Surface Oxide Flaking Near Uranium-Rich Deposit (Area E, Figure 3.3-23), 60X, Negative Number MSD-204121

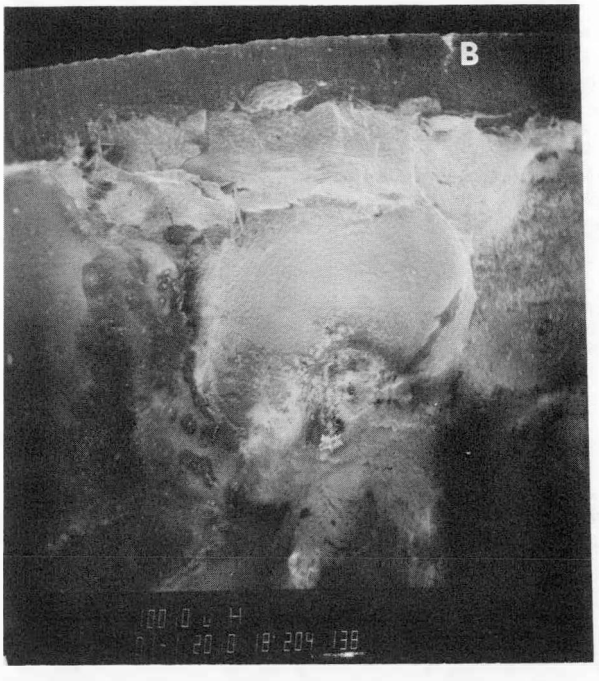

Figure 3.3-28 Defect Site of Specimen 2K (Area A, Figure 3.3-22 and Area 6, Figure 3.3-23). Area B Indicates a Through-wall Crack

Figure 3.3-29 Fracture Surface of Defect from Specimen 2K

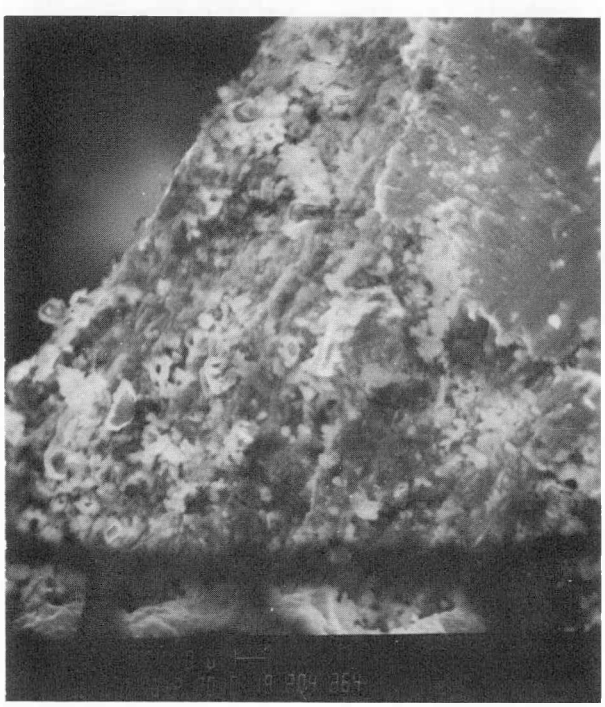

Figure 3.3-30. Through-Wall Crack Surface Near Outside of Specimen 2K

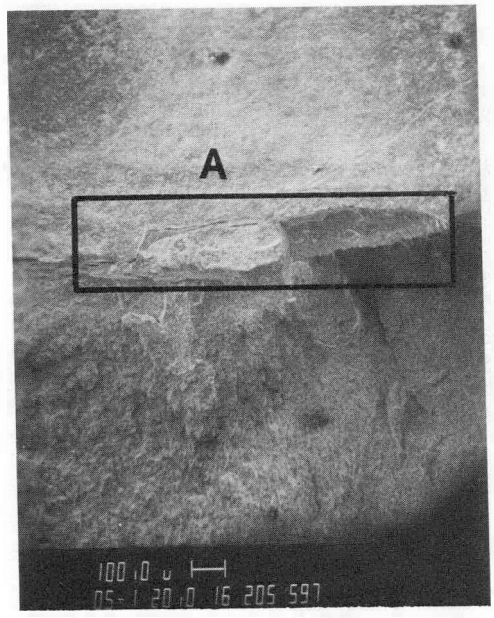

Figure 3.3-31 Fracture Along Circumferential Cracks in Specimen 8K (Fig. 3.3-21)

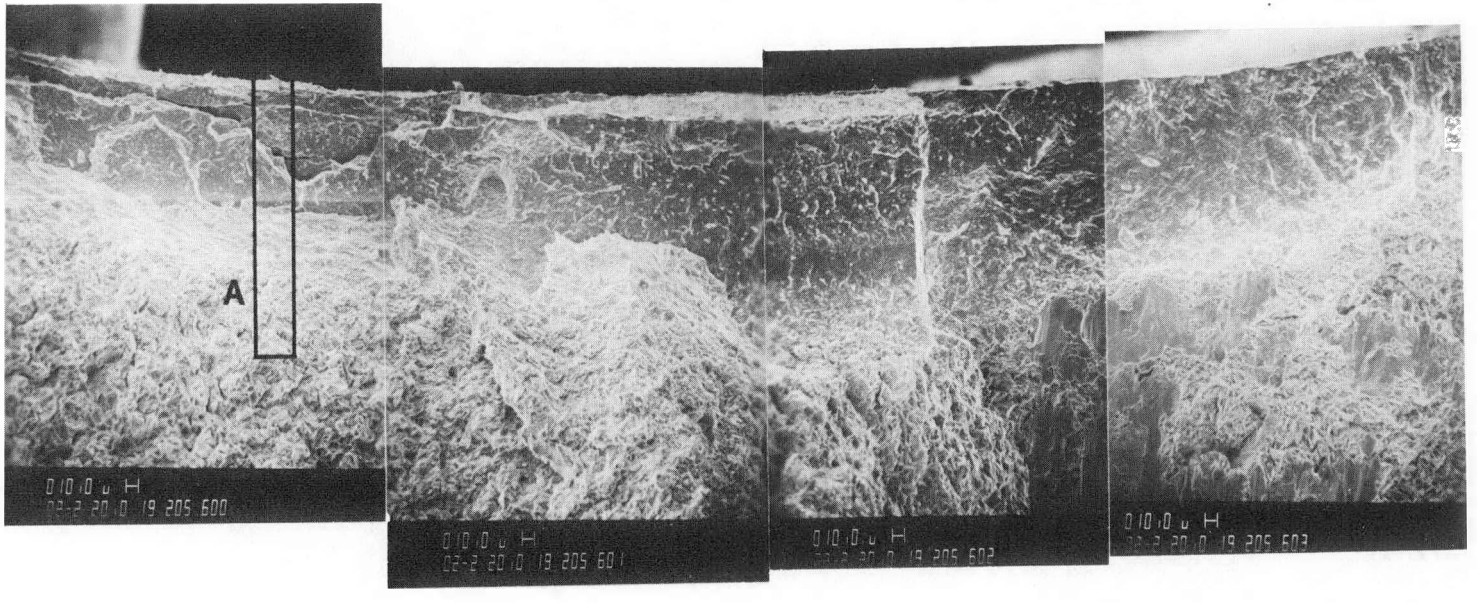

Figure 3.3-32 Fracture Map from Specimen 8K of Area A, Figure 3.3-31

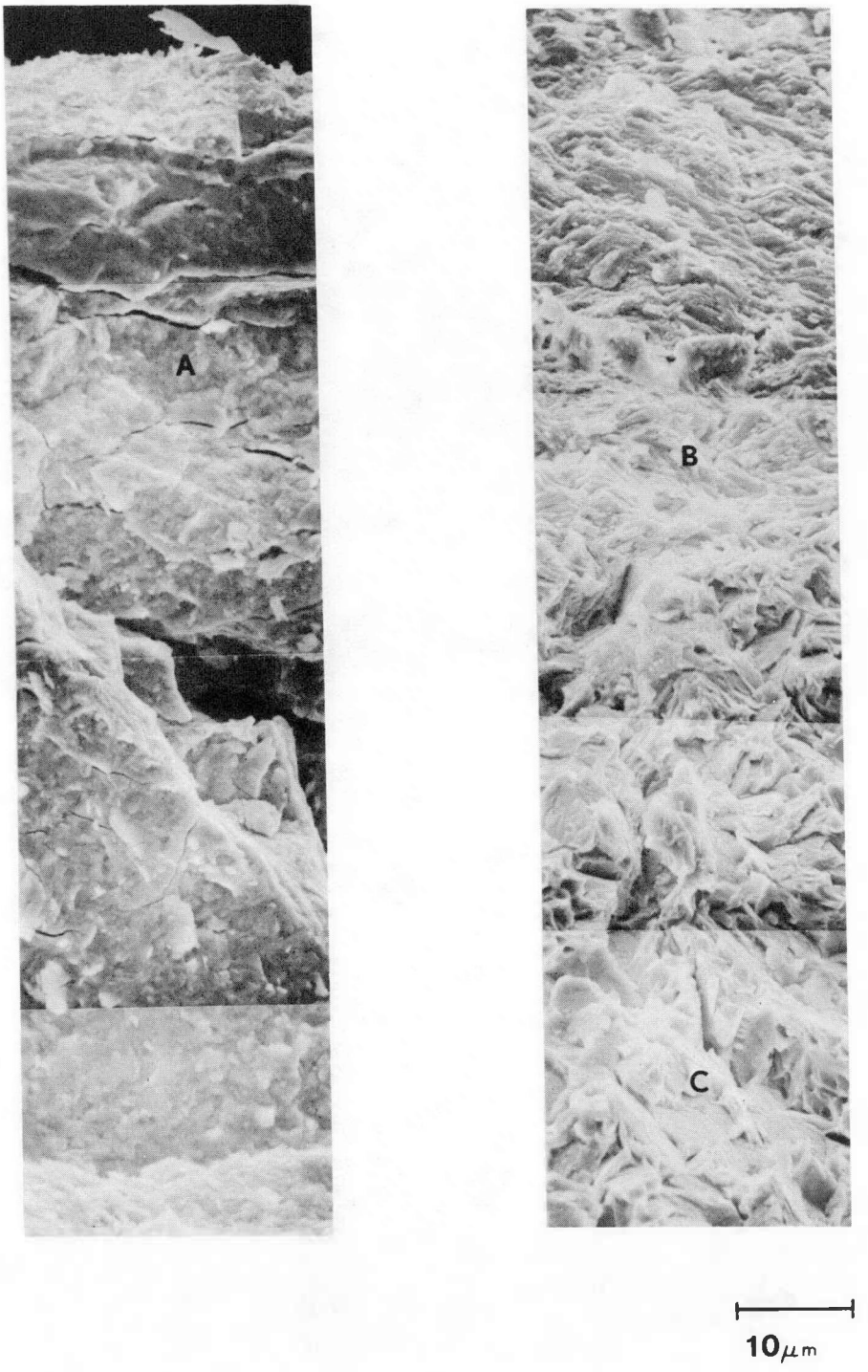

Figure 3.3-33 Fracture Map from Specimen 8K of Area A, Figure 3.3-32

The microstructure of the fracture surface from the inner surface towards the outer surface is shown in Figure 3.3-33 where several modes of fracture can be seen. Area A, adjacent to the inner surface, has a rounded appearance with some secondary cracking. Area B, ~ 100 μm from the inner surface has a more brittle character than Area A. Neither fracture surface showed any evidence of cleavage and fluting which is typical of SCC fractures in Zircaloy. Area C, below 150 μm from the inner surface, shows a mixed ductile-brittle fracture mode. Area C is representative of most of the fracture surface away from the inner surface and was undoubtedly created during the bending process.

The fracture surface exposed by three point bending of the pit and longitudinal crack of Specimen 4K is shown in Figure 3.3-34. Three fracture modes can be seen in a high magnification map of the area (Figure 3.3-35). These fracture modes correspond to those observed in Specimen 8K. Area A represents the area of undistinguished or rounded fracture, Area B represents the area of brittle fracture, and Area C represents the area of mixed ductile-brittle fracture. The microstructures of the fracture surface are shown in Figure 3.3-36. The undistinguished fracture penetrates ~ 250 μm from the inner surface. Below this point and continuing to the outer surface is the brittle fracture surface. Neither fracture showed evidence of cleavage and fluting. The remaining surface away from the pit was composed of the mixed-mode fracture.

The areas of circular cracks from Specimen 2K (Areas E and F of Figure 3.3-23) were also opened by three point bending, and the fractures were mapped in a similar manner to the two previous samples. The fracture modes observed were the same as those seen in Specimens 4K and 8K. The overall appearance of the fractures was close to that of the pit and longitudinal fracture of Specimen 4K. Because of the similarity of the fracture surfaces in both specimens, it is likely that they are both the result from the same mechanism.

During the fractographic examination, the zirconium-oxide layer on the inside surfaces was analyzed. Specimens used for the analysis were 2K, 4K, 8K, 14K, and 16K. The specimens were first split open in the axial direction to expose oxide layers in cross section. SEM photographs were taken at high magnification, and X-ray analysis was performed at various points along the cross sections. An example of the oxide appearance is shown in Figure 3.3-37, and Table 3.3-3 summarizes the results of the analysis. The oxide thickness varied between 1 and 4 μm, and the uranium, detected on the inner surface, generally penetrated less

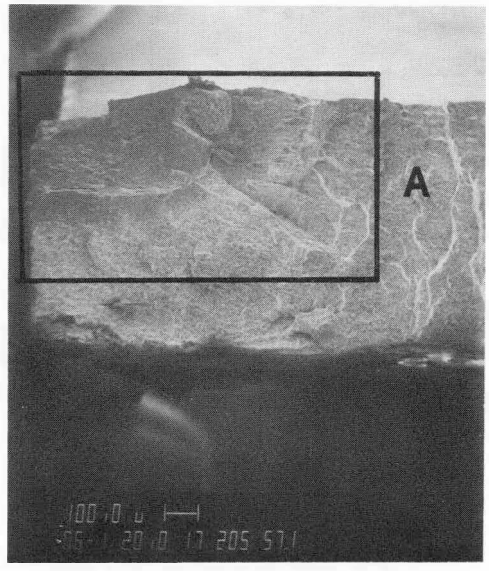

Figure 3.3-34 Fracture Through Pit and Longitudinal Crack of Specimen 4K, Figure 3.3-17

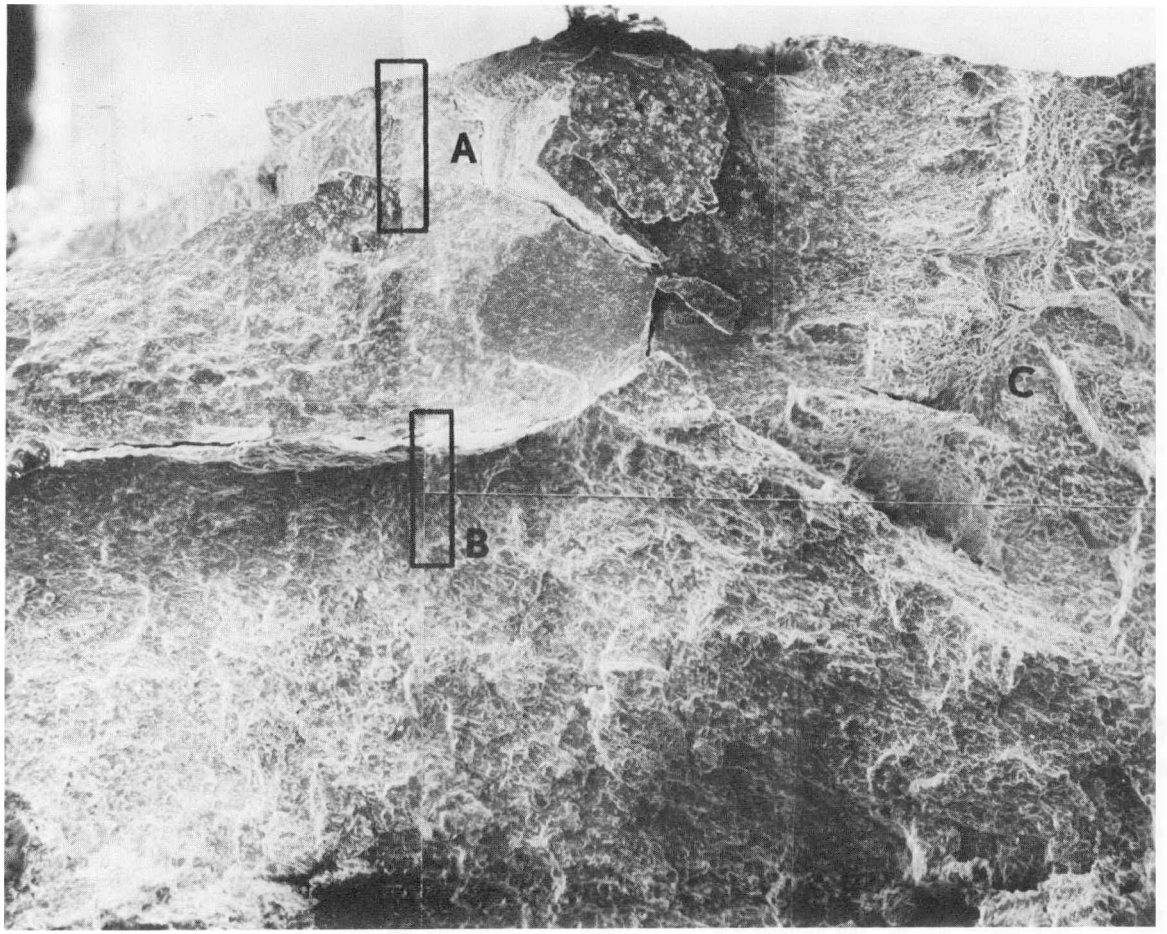

Figure 3.3-35 Fracture Map from Specimen 4K of Area A, Figure 3.3-34

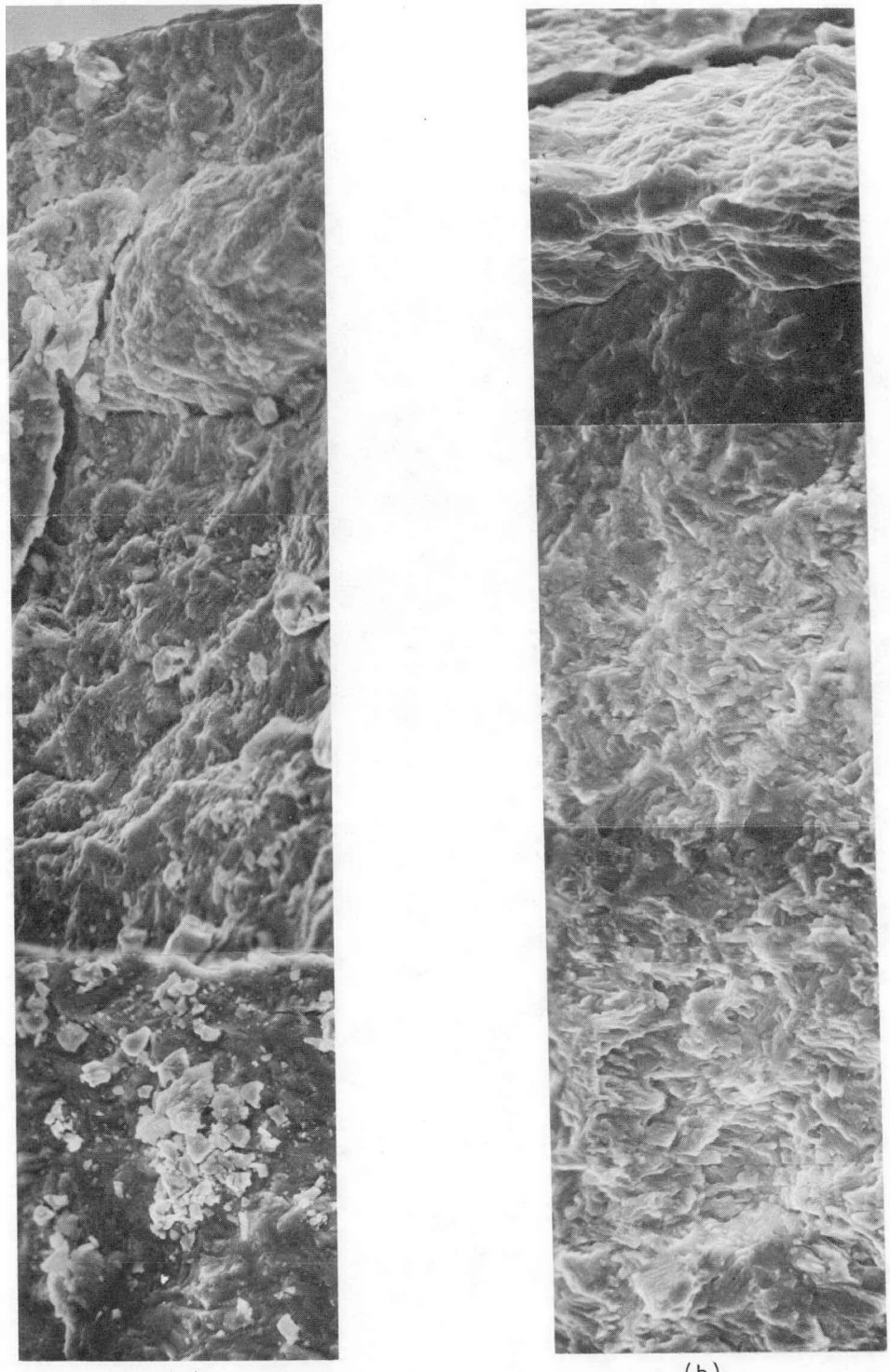

(a) (b)

Figure 3.3-36 Fracture Maps from Specimen 4K of (a) Area A, Figure 3.3-35, and (b) Area B, Figure 3.3-35

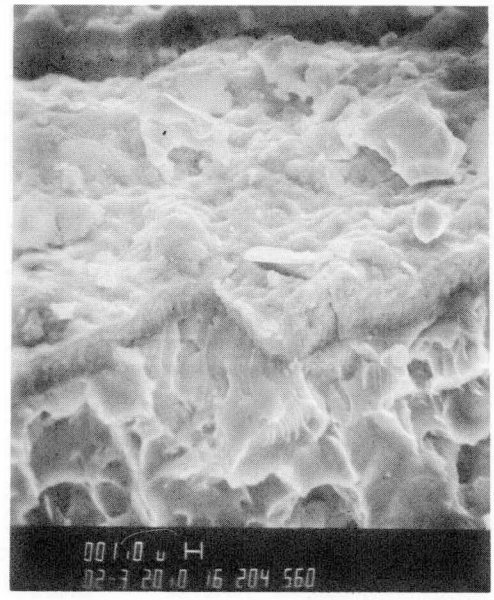

Figure 3.3-37 Surface Oxide of Specimen 14K

Table 3.3-3

Oskarshamn Oxide Characterization

Specimen	Element Failed	Defects Present	Oxide Thickness (μm)	Uranium Penetration (μm)	Oxide Separation from Substrate
2K	Yes	Yes	3.5-4	~ 2	Yes
4K	Yes	Yes	1.0-1.5	< 1	Yes
8K	Yes	Yes	1.5-2	< 1	No
14K	No	No	3.5-4	< 1	No
16K	Yes	No	1.5-2	< 1	No

than 1 μm. Specimen 2K, which had heavy uranium-containing deposits on the inner surface, had a uranium depth penetration of ~ 2 μm. The 1 μm depth penetration represents an upper limit, since the X-rays used for uranium analysis are generated from a depth of ~ 1 μm from the surface. Two specimens, 2K and 4K, showed oxide separation from the substrate. Both specimens came from rod 380/B7 which is believed to have had water ingress based on the observations made during the SEM examination of Specimen 2K. Both specimens also exhibited large, pit-type defects.

In contrast to the results from ANL, fracture surfaces examined by ASEA-Atom at Studsvik did exhibit features typical of SCC similar to the Dresden-3 samples. Figure 3.3-38 shows some examples of the fracture surfaces observed at Studsvik. Comparison of the Studsvik results (Figure 3.3-38) with those from Dresden-3 (Figure 3.2-26 and 3.2-30) show a greater proportion of intergranular fracture in the Oskarshamn samples. This is probably due to differences in heat treatment of the two claddings (fully recrystallized Oskarshamn cladding versus stress relieved Dresden-3 cladding).

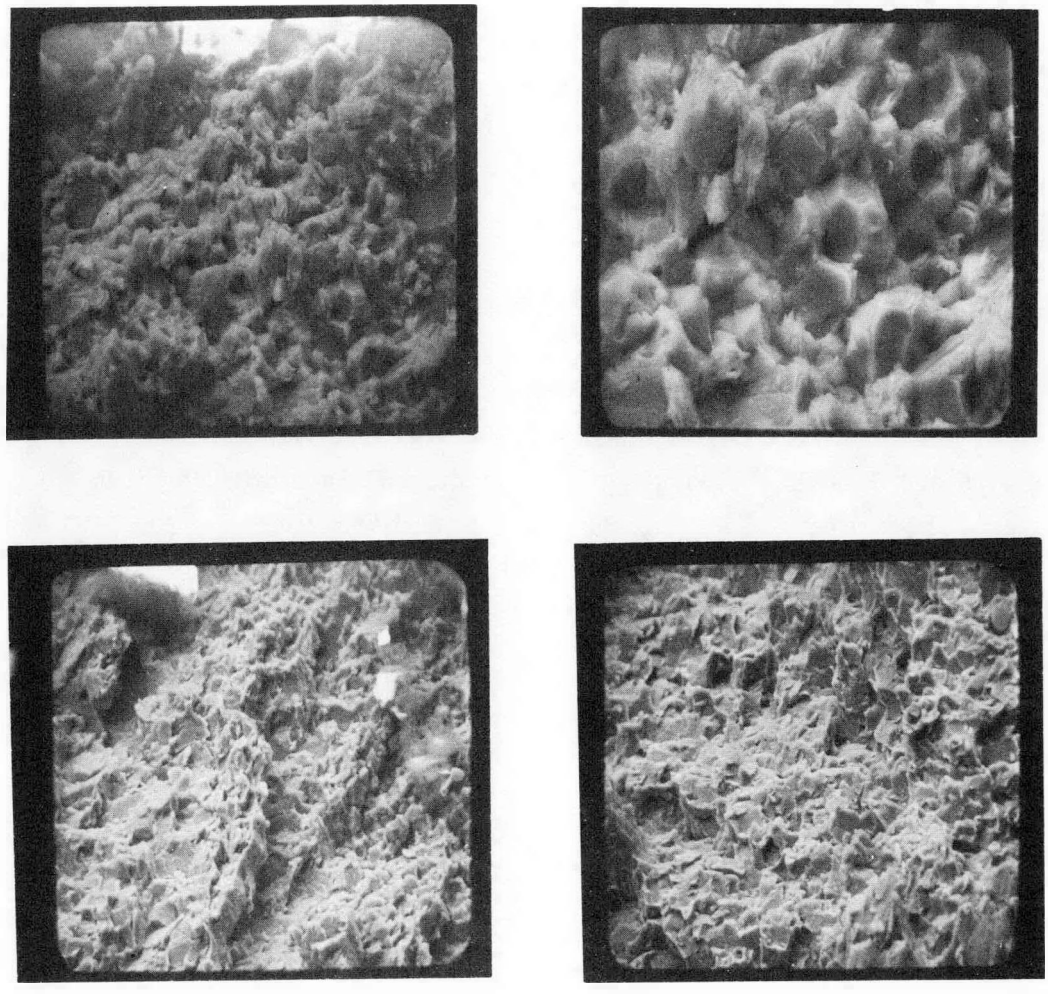

Figure 3.3-38 Appearance of Fracture Surface Near Clad Inner Surface of Oskarshamn-1 Fuel Rods

Section 4

GENERAL DISCUSSION

Fuel rods from Point Beach-1, Dresden-3, and Oskarshamn-1 reactors were examined in detail to locate and study incipient defects in the cladding. The results of the various examinations have been presented in Section 3 of this report. Key features of the results will be discussed in this section.

4.1 POINT BEACH-1 FUEL ROD STUDIES

4.1.1 Selection of Fuel Rods for Examination

During the Spring of 1974 postrefueling Cycle 3 startup of the Point Beach Unit 1 reactor a significant increase in radioactivity in the coolant occurred. The radioactivity first became significant during peak power escalation from 50 percent of full power of the reactor. The rate of power increase at the time the coolant activity became apparent exceeded 40 percent of full reactor power per hour. By comparing the operational data from the Point Beach Unit 1 reactor with data available at the time from other power reactors, it was tentatively concluded that the most probable cause of failure was that of pellet-clad interaction due to the rapid postrefueling startup. Region 4 of the Cycle 3 core of the Point Beach Unit 1 reactor was the only previously irradiated region in the reactor. At the end of Cycle 3, Point Beach personnel performed leak testing on this region of fuel; approximately one-half of the fuel assemblies were found to be leaking. Of these assemblies, significantly, all four assemblies which had been transferred to the spent fuel storage pit during the end of Cycle 2 refueling outage were found to be leaking. The observation led to the belief that the startup failures were due to a PCI mechanism, the influence of fuel assembly handling being attributed to associated pellet relocation in the fuel column and possible wedging of pellet fragments into the "cold" fuel clad diametral gap. The influence of fuel rod handling had previously been demonstrated by AECL (10). Of the other fuel assemblies found to be leaking, all experienced a power increase (beyond the Cycle 2 level) during the Cycle 3 startup. None of the assemblies which experienced both minor handling and no power increase gave leak indications.

Based on the above evaluation of the leak test data, fuel Assembly D-14 was selected for detailed examination in the present program. Thirteen removable rods from fuel Assembly D-40 were also selected. Both of these assemblies had been handled during the end of Cycle 2 refueling outage and both exhibited high activity in the leak testing. Thirty rods from Assembly D-14 together with the 13 removable rods from Assembly D-40 were selected for initial nondestructive screening in the BCL hot cells. From examination of these selected rods, it was anticipated that incipient cracks would be located in some of the unfailed rods for subsequent characterization.

The initial examinations on the 43 rods was undertaken utilizing an encircling coil eddy current system in the BCL hot cells. From an evaluation of the results, the 10 candidate rods were selected for further nondestructive examinations. The selection included rods with special features such as potential incipient defect signals at pellet interfaces. In addition, care was taken to ensure representation of typical power histories of the Region 4 fuel rods.

4.1.2 Nondestructive Examination Results

The 10 candidate fuel rods selected were subjected to a detailed nondestructive examination campaign which included gamma scanning, spiral profilometry, and eddy current test. The results of the gamma scans showed that most of the fuel rods contained small gaps in fuel stacks with the single largest gap being 0.62 cm (0.244 inch). From limited gamma scan data obtained on precharacterized identical removable rods after 1 and 2 cycles of irradiation (1) the net rate* of (isotropic) volume increase over the second cycle was determined to be approximately 0.15 v/o per 10,000 MWD/MTU. Thus, for the design life time of the fuel, the data indicate that the fuel was relatively stable.

Both gross gamma and Cs-137 gamma activity profiles showed activity depressions at pellet interfaces and gaps in the fuel stack. The similarity of the gross gamma and Cs-137 gamma activity suggests that extensive migration of the fission product cesium to pellet interfaces did not occur in these rods. The observation is contrary to that made on many Maine Yankee rods in which substantial Cs-137 peaking at the pellet interfaces was evident. It is inferred that operational

---

* Swelling minus densification.

temperatures in the fuel rods were low and were typical of commercial power reactor fuel rods. The metallographic examinations to be discussed later confirm this interpretation.

Fuel rod profilometry was performed on the 10 candidate rods which showed no apparent correlation between clad creepdown and rod average burnup over the range of 15,500 to 29,300 MWD/MTU. However, as is evident from the profilometry data shown in Figure 3.1-11 for a comparable fuel rod 037 creepdown of the cladding continued into the second cycle of irradiation (Reactor Cycle 3) implying that at the beginning of Reactor Cycle 3, hard uniform pellet-clad contact had not been established. The data also showed the rods to have variable ovalities, with the maximum ovality ranging from 0.11 to 0.25 mm (4.3 to 9.8 mils). The ovality existed over the full length of the fuel rods and appeared to be generally independent of the extent of clad creepdown.

The profilometry data also showed that all rods exhibited evidence of interpellet ridging over short axial segments. The extent of ridging was small, however, with the maximum diametral ridge height being 0.015 mm (0.6 mils). Through comparison of limited on-site profilometry data previously published (1), it is concluded that for the rods examined only a small change in ridge height occurred during the second cycle of irradiation (Reactor Cycle 3). Although the amount of clad ridging was small, it should be considered important since it represents a form of pellet-clad interaction. In addition to clad ridging, the profilometry data also showed that some rods exhibited sharp local diameter increases over the length of one pellet.

The 10 candidate rods were eddy current scanned using both the encircling coil and the probe coil techniques. Results from both techniques showed potential incipient defect indications in all the rods scanned; in general, the observations from both techniques were comparable. The probe coil system, however, detected a significant number of additional indications over the encircling coil system. Most potential incipient defects, as detected by the probe coil, appeared to span a large fraction of the cladding circumference.

The eddy current examinations indicated that many of the potential incipient defect signals appeared to be associated with interpellet gaps in the fuel column inferred from gamma scan. To test if the gaps "per se" were responsible for the

signals, an eddy current standard (containing wooden spacers to simulate various gaps) was provided by W and examined with the BCL eddy current system. From this work, it was concluded that the gaps "per se" were not responsible for the eddy current signals. Rather, it was inferred that the eddy current signals in the proximity of the interpellet gaps were due to either an incipient defect or to local deformation of the cladding associated with a locked pellet (cocked or wedged pellet). This interpretation tended to be supported by the profilometry data which indicated slight ridging and occasional slight bulging of the cladding in the immediate vicinity of the interpellet gaps.

4.1.3 Destructive Examination

From examination of all available nondestructive data, four rods were selected for fission gas puncture and analysis; one of the rods selected was a well characterized removable rod (045). The three standard rods selected from fuel Assembly D-14 (A-1, B-11, and M-14) represented a range of fuel rod burnups and power histories. The prime purpose of puncturing the rods was to confirm that the rods were unfailed. The data obtained ascertained the rod integrity and showed in all cases that the fission gas release was less than 1 percent of total generated. In comparison with fission gas release data from one cycle rods of identical design, the puncture data obtained from the present program tended to show only slight increase in fission gas release with continued irradiation through two cycles.

The low fission gas release of the one and two cycle rods tend to confirm the inference that the fuel operated at low temperatures during irradiation. Further, the low fission gas release data and the absence of any appreciable Cs-137 redistribution as evident from the gamma scan data tend to suggest that during the Cycle 3 startup, little volatile and corrosive fission product species would exist in the fuel rod free volume particularly at the low power level at which significant failures first became apparent. Thus, if stress corrosion cracking was the predominant failure mechanism during the Point Beach Unit 1, Cycle 3, startup, it would appear that little of the corrosive species is required.

Although no mechanical test data on the Zircaloy cladding was obtained under the present program, mechanical tests on representative one cycle (end of Reactor Cycle 2) cladding has been previously undertaken by Westinghouse (1). This data, summarized in Appendix C, represents the condition of the cladding (for the

higher burnup rods) immediately prior to the occurrence of the Cycle 3 startup failure indications. From these data, it is evident that, at temperatures typical of in reactor operation (343 C) the cladding had substantially hardened during irradiation, the 0.2 percent offset tensile yield stress being in excess of 490 MN/m^2 (71 ksi). Despite this hardening, however, substantial ductilities to failure (> 5 percent) remained. Thus, for pellet clad interaction to be responsible for the Point Beach Unit 1, Cycle 3, startup failures, it must be argued that a mechanism for substantial stress concentration and/or chemically assisted reduction in clad strength exists. It is believed that such stress concentration results from the relocation of pellet fragments into the fuel-clad diametral gap particularly when the coolant is depressurized and the fuel is subsequently handled.

Keeping in mind this postulated mechanism for the cause of the startup failures, two of the punctured rods, 045 and A-1, were selected for destructive sectioning and metallographic examination. Fuel rod 045, from the removable rod Assembly D-40, experienced little power increase during the Cycle 3 startup. Conversely, fuel rod A-1 experienced close to a fivefold increase in rod average power (end of Cycle 2 of 4.1 kw/m and beginning of Cycle 3 power of 18.9 kw/m) when the reactor was operating at full power. Both rods exhibited potential defect signals from the nondestructive examination worthy of further investigation.

For fuel rod 045, five sections of the fuel rod displaying suspect eddy current indications were metallographically examined: three of these were examined in detail. Two of the latter sections displayed adjacent axial gaps in the fuel column (symptomatic of pellet hang-up) and sharp local diametral increases of the clad diameter suggestive of the wedging of pellet fragments into the fuel-clad diametral gap. However, despite the detailed examination of some 64 surfaces on rod 045, resulting from careful grinding of the samples up to, and through the suspect defect areas, no evidence of an incipient cladding crack was detected. In all of the samples, fuel clad chemical bonding was evident. The bonding appeared to be similar to that observed on a high fission gas release Maine Yankee fuel rod (6). In two of the samples, pits were evident on the clad bore, which, in places, appeared to have a depth of up to ~ 15 μm.

All clad and fuel examinations on rod 045 indicated performance characteristics typical of those for a fuel rod irradiated in a pressurized water power reactor.

The Zircaloy-4 clad samples exhibited very low concentrations of hydride precipitate (apparently below ~ 80 ppm). The hydride precipitates were, in general, randomly oriented and uniformly distributed around the cladding circumference. The fuel pellets showed no evidence of equiaxed grain growth, confirming that the fuel had operated at low temperature ($\lesssim$ 1300 C) throughout its lifetime.

For fuel rod A-1, one metallographic section was prepared to examine the cause of a large probe signal; no encircling coil eddy current signal was evident at this location of the fuel rod. From examination of two transverse planes of the sample (from incremental grinding), however, it became evident that the cause of the probe eddy current signal was a large (~ 0.06 cm) metallic particle and not an incipient clad defect. The metallic particle is believed to have originated in the pellet during fabrication.

These metallographic examinations suggest that the eddy current indications (both encircling and probe) of potential cladding defects can be misleading. Extensive examination of samples obtained at the locations of eddy current indications revealed no cladding defects.

The eddy current results from the Maine Yankee Core 1 samples were very similar (6). Extensive examination of a large number of MaineYankee samples failed to locate any incipient cladding cracks and it was concluded that the source of most of the eddy current indications was the fuel clad bonding. Examination of incipient cracks subsequently identified in the Maine Yankee rods through other techniques (e.g., Cs-137 gamma peaking) indicated that the cracks were very tight, and that for these cracks the eddy current indications were not detectable. In contrast, detection in the program of incipient cracks in the failed Dresden rods KB-5249 and KE-2225, and in Oskarshamn rods was readily accomplished. However, for this work, the influence of a contaminating environment in the vicinity of the crack surfaces (due to ingressing water) and corrosion products may be the key to the success of locating the incipient defects; in nonfailed Dresden rods and Oskarshamn, no incipient defect signals were apparent.

4.1.4 Search for a Failed Fuel Rod

Consequently, effort in the present program was redirected, utilizing other available techniques, toward attempting to locate a failed fuel rod in the assembly. With this approach, it was anticipated that, following the successful identifica-

tion and characterization of a failed fuel rod, the search for an incipient defect in a nonfailed sister rod would be considerably simplified.

The search for a failed fuel rod was confined to fuel Assembly D-14 since it was known with certainty that the fuel assembly contained leaking fuel rods.* Initially, the search made use of experimental ultrasonic test equipment which had been used previously by W on short rods, in attempt to locate a failed fuel rod. Two campaigns were conducted at ultrasonic frequencies of 464 kHz and at 290 kHz. The equipment was calibrated using both a punctured and a nonfailed unirradiated fuel rod as a standard; in the second campaign, the standard calibration rods were swagged to simulate the effect of pellet-clad contact. Despite the subsequent puncture of 14 fuel rods, however, which were identified from the ultrasonic tests as having the potential for being failed, all 14 rods were found to be intact through measurement of rod internal pressure.

Because of these apparent difficulties in locating a failed fuel rod in Assembly D-14, it was decided to puncture a large number of rods from the fuel assembly and to measure their internal pressure to verify integrity and/or locate a failed fuel rod. Since it was not practical to puncture all rods in the assembly, it was decided that a total of 46 rods would provide a representative sample. To accommodate this task, BCL developed a technique to seal weld all punctured and nonfailed fuel rods; the technique was subsequently accepted by the operators of the WEPCO storage facility (GE Morris) for the ultimate retention of the fuel rods. The 46 rods (including the 17 rods already punctured) were selected to represent the following subgroup of rods which could be devined in the assembly:** burnup, power level, power increase, pellet group, and cladding lot. Assuming the 46 rods were truly representative of rods in the assembly, it was calculated that if 8 failed rods were assumed to exist in the assembly, the probability of locating at least 1 of them from the puncture campaign would be 93 percent or greater. Therefore, since more than 8 failed rods were presumed to exist in fuel Assembly D-14 (on the basis of coolant activity, choice of fuel assembly, etc.), the chances of success with this approach seemed high.

---

* That the assembly was leaking was again confirmed by the activity of the cask flush when the fuel assembly was transported off the BCL site on December 27, 1977.

** Only subgroups having 4 or more identical rods were considered.

The additional 29 rods required to form the total sample of 46 rods were selected, punctured, and pressure checked in an identical manner to that used on previous rods. The total range of all pressure readings obtained was only ± 14 percent of the mean pressure value of all rods, and none of the rods was judged to be failed. This range was considered reasonable in view of the variation of gas release and the variation of as-built rod free volumes, cladding creepdown, and other dimensional changes which influence the rod internal pressure.

4.1.5 Analysis of Puncture Data

In analyzing the puncture data from fuel Assembly D-14 by the identified subgroups of fuel rods viz: burnup, power level, power increase, pellet group and clad lot; it appears that with the possible exception of the low burnup subgroup of fuel rods (average burnup of 2,000-3,000 MWD/MTU at time of the Point Beach Unit 1 Cycle 3 startup), if 3 or more failed rods exist in the fuel assembly then their distribution within the assembly must be essentially random. Thus, on the basis of the rod puncture data, it is concluded that with 93 percent probability, the leaking fuel Assembly D-14 contained no more than 8 failed fuel rods; this estimated number of failed rods is less than that initially supposed.

This conclusion is strengthened considerably if it is also assumed that the rods originally screened via the encircling coil eddy current system, and not punctured in the various campaigns, are also unfailed. Since the worst (i.e., high failure potential) rods initially screened were punctured and shown to be intact, it is reasonable to assume also that none of these rods are failed. The consequences of pooling the two types of data are summarized in Table 4.1-1. As indicated in this table, the possibility of the low burnup subgroups (which are also the highest power and highest power swing subgroups) containing failed fuel rods is virtually eliminated. This observation is not inconsistent with the postulated mechanism of failure, since very little pellet fragmentation and subsequent relocation in handling would be expected in low power fuel rods; in addition, the released corrosive fission product inventory of the low power/low burnup fuel rods would be expected to be extremely small at the time of the cycle startup.

The magnitude of power change during the Cycle 3 startup is illustrated in Figure 4.1-1 for the 46 rods punctured. In this figure, the local power change during the startup is plotted for the peak power axial station of the fuel rod (64 percent from the rod bottom) when the reactor was at 70 percent full power;

Table 4.1-1

SUMMARY OF PERFORATION PROBABILITY ANALYSIS
OF PUNCTURED AND EDDY CURRENT TESTED RODS
(ASSUMING RODS TESTED BY ENCIRCLING COIL E.C. ARE INTACT)

Rod Subgroup Parameter	Parameter Range	Fuel Rods In Assembly	Fuel Rods Punctured	A Fuel Rods E.C. Tested	B Fraction Tested	C Probability of Three Perforated Rods Still In This Group
Beginning of Cycle 3 B.U. GWD/MTU	2-3	7	3	3	.85	0.0
	3-5	34	12	9	.61	0.05
	5-7	46	10	3	.28	0.36
	7-9	50	12	2	.28	0.36
	9-11	42	9	1	.24	0.43
Beginning of Cycle 3 Power	5.6-6.0	4	2	1	.75	0.0
	6.0-6.4	17	6	4	.60	0.05
	6.4-6.8	83	15	11	.31	0.32
	6.8-7.2	82	23	2	.30	0.33
Ratio of Average Power Increase BOC-3/EOC-2	4.6-3.8	4	2	2	1.0	0.0
	3.8-3.0	16	6	1	.44	0.01
	3.0-2.4	21	3	7	.48	0.12
	2.4-2.0	24	10	3	.54	0.08
	2.0-1.4	74	16	3	.26	0.40
	1.4-1.0	46	9	2	.24	0.43

(Continued on p 4-10)

Table 4.1-1 (Continued)

Rod Subgroup Parameter	Parameter Range	Fuel Rods In Assembly	Fuel Rods Punctured	A Fuel Rods E.C. Tested	B Fraction Tested	C Probability of Three Perforated Rods Still In This Group
Pellet Group	Gr. 19	18	3	1	.22	.45
	Gr. 8	15	5	2	.47	.48
	Gr. 15	15	2	2	.27	.48
	Gr. 12	14	4	2	.43	.15
	Gr. 13	13	2	1	.23	.42
	Gr. 22	13	2	1	.23	.42
	Gr. 20	12	2	-	.16	.54
	Gr. 30	9	0	2	.22	.42
	Gr. 42	9	2	-	.22	.42
	Gr. 14	8	3	-	.37	.17
	Gr. 17	6	3	1	.66	.1
	Gr. 31	5	2	-	.40	-
	Gr. 34	5	0	-	0.0	-
	Others (less than 4/Gr.	37	16	6	.59	-
Cladding Lot	5DJ 1948	39	8	2	.26	.40
	5AX 6460	26	3	3	.23	.44
	5DR 1946	25	10	3	.52	.1
	5Az 1773	21	4	-	.19	.51
	5EE 1946	18	3	3	.33	.27
	5BG 1816	13	2	1	.23	.42
	5BG 1802	6	3	-	.5	.05
	Others (less than 4/lot	31	13	6	.61	-

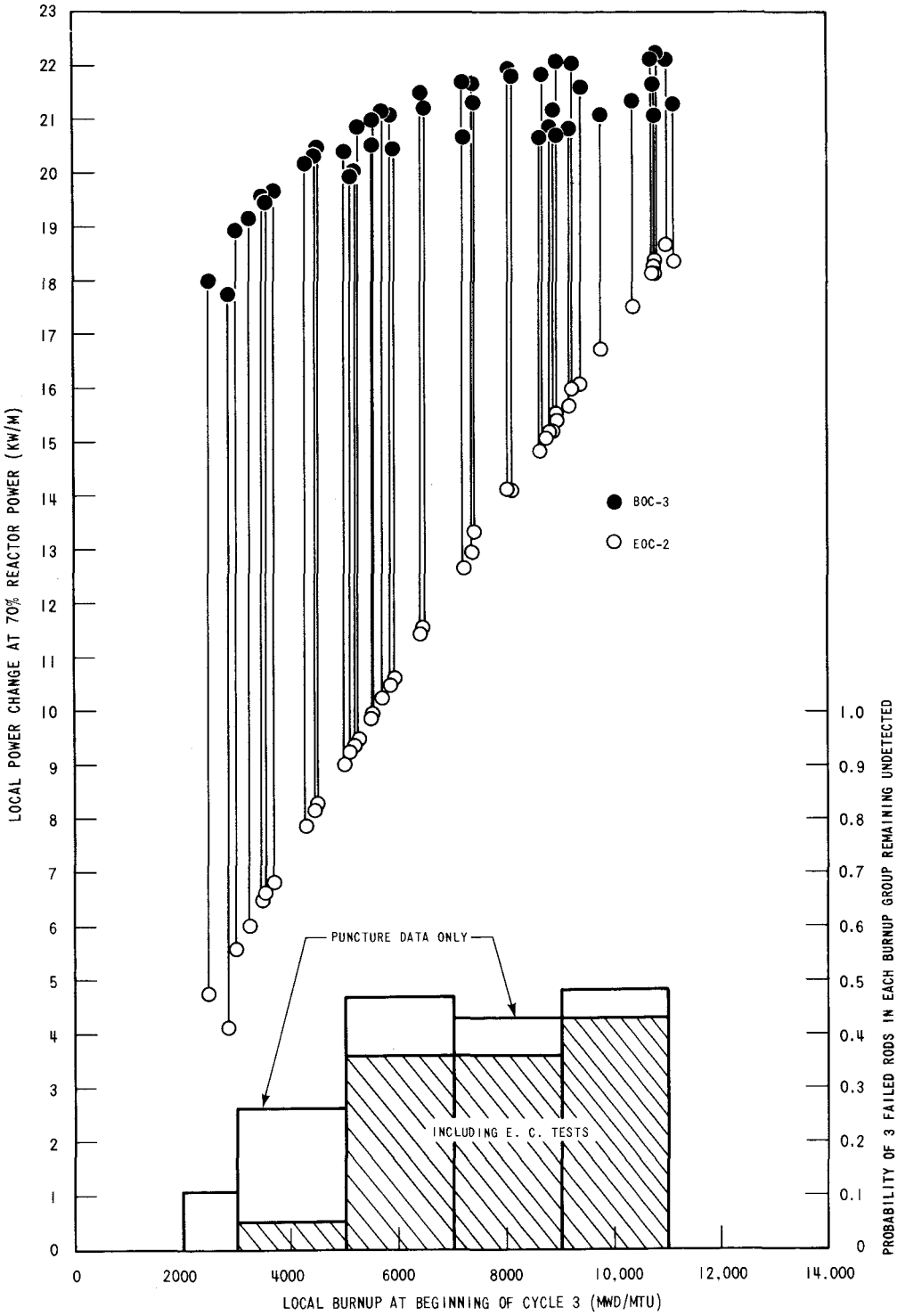

Figure 4.1-1 Power Increase During Cycle 3 Startup of Punctured Fuel Rods. Point Beach-1, Fuel Assembly D-14

as previously stated, the coolant activity first became significant during reactor power escalation from 50 percent to 70 percent of full power. The figure illustrates that at the time significant coolant activity was evident during the startup, the lowest burnup rods (local burnup of 2500 MWD/MTU) had experienced local power increases of approximately 18 kw/m (5.48 kw/ft); in contrast, the highest burnup rods (local burnups of 11,000 MWD/MTU) had experienced much lower local power increases of approximately 4/kw/m (1.2 kw/ft).

Included in Figure 4.1-1 for convenience is plotted (from Table 4.1-1) the probability of 3 perforated rods remaining undetected in a given burnup subgroup. Despite the wide range of power change duty demonstrated, the probability of 3 perforated rods remaining undetected in any burnup subgroup is small. If more than 3 failed rods are assumed to exist in the assembly, the probability that all rods are confined to a single burnup subgroup becomes even smaller. In view of the threefold difference in power increase between the rods irradiated to 5,000 MWD/MTU and 11,000 MWD/MTU burnup, respectively, at the time of the reactor postrefueling startup, the apparent independence of failure probability with burnup, and power swing, is striking. The combined data of Table 4.1-1 and Figure 4.1-1 tend to suggest that the failure probability in fuel Assembly D-14 is dependent only on absolute power level obtained during the startup (for the rapid rate of power change), since at any given reactor power, the absolute power level achieved is relatively insensitive to rod burnup.

The observation of apparent dependency of failure probability on achieved absolute power is consistent with the postulated mechanism for the startup failures. With this mechanism, under the ambient pressure/temperature conditions of the depressurized primary coolant circuit (and transfer canal, etc.), pellet fragments in the fuel column are assumed to become relocated during fuel assembly handling. The pellet fragments then become wedged in the fuel clad diametral gap of the "cold" fuel rods. Thus, since following refueling the cladding will tend to elastically collapse a small amount under the pressure of the primary coolant, on returning the reactor to power the pellet fragments will begin almost immediately to exert an outward force on the cladding. The magnitude of the force created during power escalation will therefore tend to be dependent only on the absolute linear heat rating of the fuel rods and the rate of power change during the postrefueling startup.

With this mechanism, low frequency random fuel rod failures are expected to occur in fuel assemblies which have been handled and subsequently returned to power rapidly; no change of operating power level is necessary to cause rod perforation under these circumstances. This is consistent with the Point Beach-1 end of Cycle 3 on-site observation of high leak test activity in all 4 Point Beach-1 assemblies which had been temporarily transferred to the spent fuel storgae pit during the end of Cycle 2 refueling outage. In contrast, fuel assemblies which are only lightly handled during a refueling outage are expected to experience only small relocation of fragmented pellets into the cold pellet-clad diametral gap. With these assemblies, the failure probability during rapid power escalation will thus be much reduced even in assemblies which achieve power levels higher than those previously experienced. This is also consistent with the Point Beach-1 end of Cycle 3 on-site leak test data. From these leak tests, only 14 fuel assemblies out of a total of 27 fuel assemblies which had experienced both light handling during the refueling outage and a power increase during the Cycle 3 startup were judged to contain perforated fuel rods; furthermore, none of the 7 fuel assemblies which experienced both light handling and no power change during the startup was failed. Hence, although no direct evidence for pellet-clad interaction being the cause of the Point Beach-1 Cycle 3 startup failures was obtained from this program, the indirect evidence obtained from representative fuel rods punctured from fuel Assembly D-14 appears to be strongly supportive and consistent with the postulated mechanism.

4.2 DRESDEN-3 FUEL RODS

4.2.1 Rod Selection

Available nondestructive techniques at the reactor site were unsuccessful in finding incipient PCI induced defects in unfailed fuel rods. The criterion used at the reactor site to determine whether a rod was "failed" was to seek the presence of liquid phase water within the fuel rod by an ultrasonic test. Since these rods could hold helium when they were punctured (4), it can be inferred that the selected rods which are now known to have failed must have resealed themselves during the reactor operation subsequent to the PCI event and before the end of Cycle 3. When the defects had resealed themselves, the sealed-in water probably reacted with the fuel and the cladding; and the water was no longer present as a liquid when the fuel rods were examined in the fuel pool.*

* Had the selection of these rods been for the purpose of reconstituting fuel bundles for further reactor service, all 9 of those with eddy current indications would have been rejected as potentially failed.

4.2.2 Eddy Current

Comments on the relative sensitivities of the encircling coil technique and the probe technique have already been made in Section 3.2.8.1. From this work we cannot infer that the eddy current techniques used either can or cannot detect an incipient PCI induced defect when the defect is unaffected by water ingress. Such a defect was not found in this study or in the examination of Oskarshamn fuel rods. Cordall, et al (21), also found that eddy current tests were able to detect through-wall defects in failed BWR fuel rods, but were unable to detect an incipient defect in an unfailed fuel rod.

A comparison of the BCL and ANL eddy current measurements on the same length of rod KG-0113 is shown in Table 3.2-3. The agreement of the two systems is good on strong eddy current signals, but the agreement is poor for weak signals. There are several potential reasons for the disagreement. First, the two devices operate on slightly different principles, and the methods for internal data analysis are different. Second, the response of the ANL system depends on the positions of the sampling points on the voltage signal waveform. The sampling points used for the measurements may be more sensitive to one form of defect than to another. Finally, the interpretation of weak eddy current signals can be expected to vary from one operator to another.

The last two points concerning the operation of the ANL system and the interpretation of data deserve special attention. To a large extent, the ability to detect a particular type of defect in a fuel rod is dependent on the availability of suitable standards for tuning the instrument. Ideally, the standards should simulate the rods to be tested as closely as possible. For example, if the system is to be used to locate narrow incipient cracks, then the standards should be sections of cladding containing narrow incipient cracks at known locations.

With such standards, the system could be tuned to detect and discriminate between different types of defects. However, in practice it is not possible to obtain realistic standards. In the case of the BCL system the standard used was produced by machining defects of known dimensions on the inner surface of an unirradiated piece of cladding. Unfortunately, such a standard does not include features such as fuel adhering to the cladding, pitting on the inner surface, or cracks that have been filled by fission or corrosion products. In practice, ANL does not calibrate the eddy current system with a defect standard. Rather, the sampling points

are established by the instrument being tuned to its maximum sensitivity for identifying the cladding inner and outer surfaces in sound cladding. Defects between these points are then qualitatively identifiable. For greater sensitivity and semiquantitative identification of defect size, a pulsed eddy current system with four sampling points would be more suited. In any case, interpretation of the data is difficult even after tuning the instrument with a standard. Thus it is not surprising that the agreement between the BCL system and the ANL system is poor for weak signals.

4.2.3 Fission Gas Release

As mentioned in Section 3.2.3 the fission gas analyses (Table 3.2-2) indicated that rod KD-0451 was definitely unfailed and KE-2225 was probably unfailed. The microscopic studies, however, have shown that KE-2225 had a through-wall crack (Figures 3.2-16, 19, 20). Therefore, it can be inferred that steam could have entered the fuel rod and that some of the fission gas and filler gas (He) could have escaped. Hence, the observed release rate of 0.64 percent for the fission gases in KE-2225 is not a reliable figure, although release fractions of that size are not unusual (22, 23). The relatively large amount of helium in rod KE-2225 (78.9 cc @ STP) indicates that very little gas could have escaped. By comparison the amount of helium is greater than that found in the unfailed rod, KD-0451.

The data for rod KD-0451 were not confused by any indication of rod failure and are considered valid. Because the power transient occurred in a region of the fuel that had low burnup, it is difficult to attribute the high release fraction (11.8 percent) to that power transient. It is more reasonable to attribute this release fraction to the rest of the power history of the rod through the end of Cycle 3 (average burnup = 13.4 GWd/t-U and peak burnup = 18.3 GWd/t-U). The source of the N_2 observed in the gas sample from KD-0451 is not known. If it were from air contamination during the puncture, some O_2 would have been observed, too. Perhaps, some air contamination had occurred during fabrication of that rod.

4.2.4 Deposits on the Inner Surface of Cladding and Chemical Interactions

As has been reported in previous studies of the chemical interactions between fuel and cladding (6, 24, 25) deposits on the inner surface of cladding tend to occur at sites adjacent to pellet-pellet interfaces and at fuel cracks. These deposits

tend to be rich in uranium and also contain fission products such as cesium and tellurium. There is evidence of fuel bonding with uranium-rich particles tightly bound to the inner surface of the cladding (Figures 3.2-54 and 74).

The deposits at pellet-pellet interfaces and at fuel cracks have a variety of features, but a salient feature has been described as "beads" or "nodules" (e.g., Figure 3. 2-37 and 3.2-73), and there are places where these nodules appear to have coalesced (Figure 3.2-40 and 3.2-45) to varying degrees. The deposits are rich in uranium and also contain cesium and tellurium. Comparing our results with those reported by Cubicciotti , et al. (24), the overall characteristics of of the deposits on the cladding were heavier than those observed on fuel from H. B. Robinson, and not as heavy as those from Maine Yankee.

From their analyses of the fuel specimens from the Maine Yankee and from H. B. Robinson reactors, Cubicciotti , et al. (24), suggested that the chemical interaction between the fuel and the Zircaloy cladding involved a phase rich in cesium and uranium. Davies, et al. (25), performed similar studies on fuel from Humboldt Bay, which was subsequently given a controlled power ramp in the GE Test Reactor, and they reported the presence of a ceramic phase rich in zirconium and cesium, which tended to bind the urania to the Zircaloy. In both of these studies the deposits tended to occur at sites on the cladding adjacent to pellet-pellet interfaces and cracks in the fuel. Here, too, the deposits follow that pattern. The chemical analysis of the present work, however, was not sufficient to determine the chemical compositions of the various phases.

4.2.5 Fractography

Fracture surfaces that could be attributed to PCI were observed only on specimens from rod KE-2225, which had suffered a through-wall crack. The fracture surface of the through-wall crack was sufficiently oxidized to obscure significant features. However, the part-through crack, at approximately the same axial location as the through-wall crack, was much cleaner, and several areas have the combination of cleavage and fluting which are characteristic of stress-corrosion cracking in Zircaloy (16, 26-28). These can be seen in Figures 3.2-26 and 30b. These results are in agreement with the earlier work by Davies, et al. (25), where the evidence for a stress-corrosion cracking power-ramped BWR fuel was not complicated by the possible ingress of water and consequential perturbations of the chemical system. In addition to the primary PCI induced fracture surfaces, some fracture surfaces appeared to be secondary defects; these probably occurred after the primary breach of the cladding.

It is also noteworthy that these cracks in KE-2225 were associated with little macroscopic plastic deformation. From profilometry data the macroscopic strain induced by the PCI event (25) was no greater than 0.07 percent. Such low level of macroscopic strain is consistent with other observations of PCI induced defects (29). As was mentioned in Section 3.2.9.3, the presence of a sizable quantity of helium in rod KE-2225 indicates that little of the internal gas had escaped. Therefore, the chemical changes brought about by ingress of water are likely to be small. Nonetheless, the finding of fractographic evidence for stress-corrosion cracking as the primary PCI mechanism is corrobrative but would not be deemed conclusive by itself.

4.2.6 Hydride Particles

Precipitation of zirconium hydride occurs in fuel cladding only during cooling from the service temperature when the concentration of hydrogen is below the solubility limit, ~ 100 ppm. For hydrogen concentrations above the solubility limit, precipitation can occur during reactor operation, or existing hydride particles can dissolve and reprecipitate in a manner that best relieves the local stress. Here, hydrides were observed by TEM, by backscattered SEM imaging, by metallography and by SEM fractography. The hydride morphology is that of platelet clusters arranged as long ribbons or stringers which are aligned parallel to the tube axis. The platelet width direction is aligned tangentially except in certain regions ahead of crack tips. Hence, there is evidence that the hydride orientations have been affected by the local stress fields of the PCI induced cracks. However, it appears that the stringer phenomenon is not associated with stress fields, because they were observed in the plenum region of the cladding as well as that over the fuel.

The fractographic features which were described as "quasi-cleavage" (Figure 3.2-28) or "flaky" (Figures 3.2-21 and 22b) are consistent with fractures through hydrided regions. The same is probably true of the "undistinguished area" and "brittle area" in Figure 3.2-83, but with less certainty.

That hydride particles should be aligned and clustered to form long ribbons or stringers in this cladding was a surprising observation. Proebstle, et al. (26), have documented the mechanism of hydride induced fuel rod failure, but their observations were of localized massive hydriding and not of stringers as were observed here. The hydride stringers phenomenon is not yet understood. In this work the hydrogen content of the cladding was not measured. However, from the

appearance of the metallographic photomicrographs, the total hydride content is not unusual; it is only the distribution of the hydrides that is remarkable. It appears that the hydrides had only a minor effect on the PCI event. While the presence of the hydrides affected the fracture morphologies, they did not confuse the analyses. Since the hydride stringers were present in both the unfailed rod as well as the failed one, their contribution to the susceptibility of the fuel to PCI was little or nothing.

A very similar distribution of hydrides was observed by Pasupathi (29) in irradiated cladding from Oconee-1.

4.2.7 TEM--Microstructural Evidence of Strain

The microstructures of this cladding are complex intrinsically because the initial condition is heavily cold worked (~ 70 percent) and then annealed to a state of partial recrystallization prior to irradiation. The TEM observations were complicated further by the unexpected presence of long hydride stringers. Partially "healed" dislocation channels in the region near the power transient and a mechanical twin are good evidence that the PCI event produced strains on a microscopic scale (Figures 3.2-61 and 3.2-65). The observation that dislocation channel traces are on planes of type $(10\bar{1}2)$ and $(10\bar{1}3)$ is unusal, but geometrically feasible for deformation by $\vec{a}$-type dislocations (18). These planes can also serve as twinning planes with the shear direction normal to a. In fact $(10\bar{1}2)$ is the most commonly observed twin system in α-phase zirconium alloys and its conjugate plane is of the same type. The planes of type $(10\bar{1}3)$ are twin planes in other hexagonal close-packed metals, and their conjugate twin planes are of the type $(10\bar{1}1)$, which contain no less than three geometrically feasible deformation modes: $<\vec{a}>$, $<\vec{c}+\vec{a}>$, and the twinning shear direction normal to $<\vec{a}>$. Thus, one might suppose that small "healed" mechanical twins could be mistaken for dislocation channels if the microstructure were so complex that the twin interfaces were not clearly visible. However, the conclusions relevant to the present study would remain unchanged. Either channels or twins indicate localized mechanical deformation. Furthermore, the TEM work here was done in dark field in which the orientation difference between twin and matrix would have been clearly seen, even if the twin was too small to produce an unambiguous selected area diffraction pattern. Hence, the inference that the features in Figure 3.2-61 are healed dislocation channels seems valid.

4.2.8 Pellet-Pellet Interface

Although the pellet-pellet interfaces that were examined did not provide evidence for local stress concentrations due to cesium-uranate formation, the grain boundary separations that were present in one of the sections are evidence for a thermal ramp occurring in the rod. Similar separations have been found in reactor ramp (27) and in postirradiation direct electrical heating (DEH) experiments (11). These latter experiments are conducted with heating rates in 20-30°C/s and result in fission gas-driven tearing of the grain boundaries. The filling of the pellet dishes in the Dresden rod indicates that this fuel motion, conceivably an instantaneous fuel swelling phenomenon, takes the path of least resistance. Whether this fuel motion can result in a stress concentration in the cladding adjacent to the pellet-pellet interface when the opposing pellets come into contact should be the subject of a detailed stress analysis.

4.3 OSKARSHAMN-1 CLADDING STUDIES

4.3.1 Clad Inner Surface Characterization

The inner surfaces of specimens without defects from both failed and unfailed rods had a very similar appearance in the SEM. Nodular or wormlike formations on the Zircaloy surface were observed in areas that were free of fuel deposits, and angular fuel particles of varying sizes were distributed over most of the surface. No obvious interaction of the fuel particles and the Zircaloy was observed, although uranium was detected over the entire inner surface of each specimen, even in areas that were free of fuel particles. Notably absent from these specimens were the linear deposits of fission products corresponding to fuel cracks and pellet-pellet interfaces which were observed in the Dresden-3 and Maine Yankee fuel rods (6). The small nodular deposits usually associated with these linear deposits were also absent. No defects, other than occasional oxide cracking, were observed. The one observable difference between the failed and unfailed rods was the color of the inner surfaces. The specimens from unfailed rods retained much of the original light metallic color while the specimens from failed rods had darkened to a deep blue or black.

Several elements, other than zirconium and uranium, were detected on the inside surfaces of the specimens. The elements identified were iron, nickel, chromium, zinc, chlorine, barium, and cesium, and with the exception of cesium, they were always observed in small individual particles. Unfortunately, no definite conclusions can be made regarding the relationship of these elements to PCI, because

of the possibility of contamination due to coolant ingress or contamination which occurred after removal from the reactor. Iodine and cadmium, two fission products that are known to induce SCC, were not detected.

The pit-type defects observed in Specimens 2K and 4K do not appear to be related to SCC phenomena but are more likely the result of internal hydriding. The pit surfaces of these circular defects do not contain any areas that are typical of SCC failures, but they do resemble sunburst hydrides in shape and geometry (30). The heavy uranium-containing deposits on Specimen 2K, which are believed to be a higher oxide of uranium because of their behavior in the SEM, are probably the result of coolant ingress following failure. The coolant would have also supplied hydrogen for hydriding the cladding.

Evidence suggests that the circumferential cracks observed in Specimen 8K are the result of pellet-clad interaction. First, the area where the cracks are found appears to be the location of a pellet-pellet interface. There are circumferential deposits at this point, including small uranium-rich nodular deposits with some cesium that are often oberved at pellet-pellet interfaces and fuel crack locations (6). Cladding defects are known to preferentially form at pellet-pellet interfaces. Second, the cracks are located in an area of a surface depression. Such a depression could have been produced by pellet hour-glassing. Other than the small nodules containing some cesium, there appeared to be no oxidation of fission-products with these cracks on the cladding surface.

There appeared to be little correlation between the surface deposits of fuel or fission products and the operating history of the fuel rods from which the specimens were taken. Linear fission-product deposits were found only on Specimen 8K and the rod from which it came, 383/A1, had the lowest linear heat rating before and during the ramp test and the greatest power decrease during the ramp test. Only the surface appearance of Specimen 2K, which exhibited extensive atypical uranium-containing deposits, might be attributed to its operating history and location rod 380/B7. This rod had the highest linear heat rating during the test and the greatest power increase during the test of any specimen examined. Also, its location near the bottom of the rod in the area of many defect signals suggests it was near the through-wall defect. Water ingress in this local region in the rod could account for the atypical appearance of the uranium-containing deposits.

4.3.2 Fractographic Characterization

All the fracture surfaces that corresponded to either pit-type or crack defects on the inner surface were similar in appearance. An undistinguished fracture was found adjacent to the inner surface, and a brittle fracture surface was observed below that. The undistinguished fracture surface and the brittle fracture surfaces are similar to the fractures observed by us in the Dresden-3 cladding. The brittle surface also resembles low temperature fractures of hydrided Zircaloy (31). This region may have been created at low temperature in-reactor or, perhaps, during the three point bending operation. The rest of the surfaces were a mixed ductile-brittle mode of fracture that could only have been produced by the three point bending operation. The amount of undistinguished and brittle fracture area was greatest in the vicinity of the circular cracks and pits on Specimens 2K and 4K, respectively, but these two fracture modes were also identified on the circumferential cracks on Specimen 8K.

The fractures that were observed on the Oskarshamn cladding do not appear to be SCC related. Cleavage and fluting, usually associated with SCC fractures of Zircaloy, were not observed on any surface, and fission products also were not detected on any surface. Instead, the fracture surfaces suggest that the defects are the result of internal hydriding. Thus, these defects probably do not represent the sites of primary cracking or failure but were most likely produced following the original failure of the rods. Even though the fracture surfaces associated with the small circumferential cracks in Specimen 8K resemble the other defects believed to be hydride in nature, the location of the cracks at a pellet-pellet interface and the surface depression in which they occurred suggest they were at least in part due to a pellet-cladding mechanical interaction.

Section 5

REFERENCES

1. E. H. Pilzer. Determination and Microscopic Study of Incipient Defects in Irradiated Power Reactor Fuel Rods. Westinghouse Data Package. Summary Report, WCAP-8863 and WCAP-8816, February 1977.

2. H. S. Rosenbaum. Data Package for BWR Fuel Rods Selected for Study in the Program "Determination and Microscopic Study of Incipient Defects in Irradiated Power Reactor Fuel Rods". Vol. 1 and 2, GE Report NEDC-23557, March 1977.

3. G. Vesturlund. Data Package for ASEA-Atom BWR Fuel Rods Selected for Study in the Program "Determination and Microscopic Study of Incipient Defects in Irradiated Power Reactor Fuel Rods". September 1977.

4. V. Pasupathi, V. W. Storhok, and J. S. Perrin. Interim Report on "Determination and Microscopic Study of Incipient Defects in Irradiated Power Reactor Fuel Rods." Battelle Report BCL-585-1, August 1977.

5. Planning Support Document for the EPRI Light Water Reactor Fuel Performance Program. EPRI-NP-370-SR, January 1977.

6. N. Fuhrman, V. Pasupathi, D. B. Scott, S. M. Temple, S. R. Pati, and T. E. Hollowell. Evaluation of Fuel Rod Performance in Main Yankee Core-1. Final Report, EPRI-NP-218, November 1976.

7. N. Fuhrman, V. Pasupathi, L. V. Corsetti. PCI Observation in a Combustion Engineering PWR. ANS Topical Meeting on Water Reactor Fuel Performance. St. Charles, Illinois, May 1977.

8. S. Junkrans and O. Varnild. ASEA-Atom Research on PCI. ANS Topical Meeting on Water Reactor Fuel Performance. St. Charles, Illinois, May 1977.

9. E. Smith and A. K. Miller. "Stress Corrosion Fracture of Zircaloy Cladding in Fuel Rod Subjected to Power Increases. I. A Model for Crack Propagation and the Failure Threshold Stress." Paper to be published in J. Nucl. Materials.

10. S. Aas. "Operating Conditions and Fuel Rod Behavior - A Review." Proceedings Joint Topical Meeting on Commercial Nuclear Fuel Technology Today, CNS ISSN 0068-8517, 75-CNA/ANS-100, 1975, pp 2-35.

11. S. M. Gehl, M. G. Seitz, and J. Rest. "Relationship Between Fission-gas Release and Microstructural Change During Transient Heating of Pressurized Water Reactor Fuel." To be published in the Proceedings of the American Nuclear Society Thermal Reactor Safety Meeting, Sun Valley, Idaho, July 31-August 5, 1977.

12. J. T. A. Roberts, et al. "SCC Model for PCI Failures in LWR Fuel Rods." Paper to be presented at the Fourth International Symposium on Zirconium in Nuclear Industry, June 1978, United Kingdom.

13. W. R. Smalley. Evaluation of Saxton Core III Fuel Materials Performance. WCAP-3385-57, July 1974.

14. J.A.L. Robertson. Improved Performance for UO_2 Fuel. AECL-4366, January 1973.

15. A. Sather. "Pulsed Eddy-Current Testing Apparatus for Use on Smooth and Ribbed Tubing." Materials Evaluation, 55, December 1977.

16. I. Aitchison and B. Cox. "Interpretation of Fractographs of SCC in Hexagonal Metals." Corrosion, 28, 1972, pp 83-87.

17. W. L. Bell. "Corduroy Contrast Observations in Neutron Irradiated Zirconium and Zircaloy." Journal of Nuclear Materials, 55, 1975, pp 14-22

18. H. S. Rosenbaum. "Nonbasal Slip in h.c.p. Metals and its Relation to Mechanical Twinning, in Deformation Twinning." R. E. Reed-Hill, J. P. Hirth, and H. C. Rogers, eds. AIME Metallurgical Society Conferences, Vol. 25, 1964, pp 43-75.

19. W. L. Bell. Discussion in "Zirconium in Nuclear Applications." J. H. Schemel and H. S. Rosenbaum, eds. ASTM STP 551, 1974, pp 199-200.

20. O. M. Katz. "Tetragonal Hydride in Low Hydrogen Content Zircaloy." Journal of Nuclear Materials, 36, 1970, p 335.

21. D. Cordall, R. M. Cornell, K. W. Jones, and J. S. Waddington. "Fuel Failures in the Dodewaard Boiling Water Reactor." Nuclear Technology, 34, 1977, pp 438-448.

22. F. H. Magerth, C. P. Ruiz, and U. E. Wolff. Zircaloy-Clad UO_2 Fuel Rod Evaluation Program. GE Report GEAP-10371, June 1971.

23. H. E. Williamson and D. C. Ditmore. Experience with BWR Fuel through September 1971. GE Report NEDO-10505, May 1972.

24. D. Cubicciotti, J. E. Sanecki, R. B. Strain, S. Greenberg, L. A. Neimark, and C. E. Johnson. The Nature of Fission - Product Deposits Inside Light-Water-Reactor Fuel Rods. SRI Report, November 1976.

25. J. H. Davies, H. S. Rosenbaum, J. S. Armijo, R. A. Proebstle, T. C. Rowland, J. R. Thompson, E. L. Esch, G. Romeo, and D. R. Rutkin. Irradiation Tests to Characterize the PCI Failure Mechanism. GE Report NEDO-21551, February 1977, also presented at ANS Topical Meeting on Water Reactor Fuel Performance, May 1977, St. Charles, Illinois.

26. B. Cox. Reviews on Coatings and Corrosion, 1, 1974, pp 275-321.

27. B. Cox and J. C. Wood. "Iodine Induced Cracking of Zircaloy Fuel Cladding." In Corrosion Problems in Energy Conversion and Generation. C. S. Tedman, ed. Electrochemical Society, 1974, pp 275-321.

28. W. T. Grubb. "Cadmium Metal Embrittlement of Zircaloy-2." Nature, 265, 1977, p 36.

29. V. Pasupathi, private communication.

30. R. A. Proebstle, J. H. Davies, T. C. Rowland, D. R. Rutkin, and J. S. Armijo. "The Mechanism of Defection of Zircaloy-Clad Fuel Rods by Internal Hydriding". Proceedings Joint Topical Meeting on Commercial Nuclear Fuel Technology Today, CNS ISSN 0068-8517, 75-CNA/ANS-100, 1975, pp 2-15

31. C. J. Simpson and J. Moerman. "Hydrogen Embrittlement of Zr-2.5 wt % NB." Effect of Hydrogen on Behavior of Materials. Edited by A. W. Thompson and J. M. Bunstein, 1975, p 428.

APPENDIX A

POINT BEACH UNIT 1, CYCLE 3
FUEL ASSEMBLY AND CORE COMPONENT DETAILS

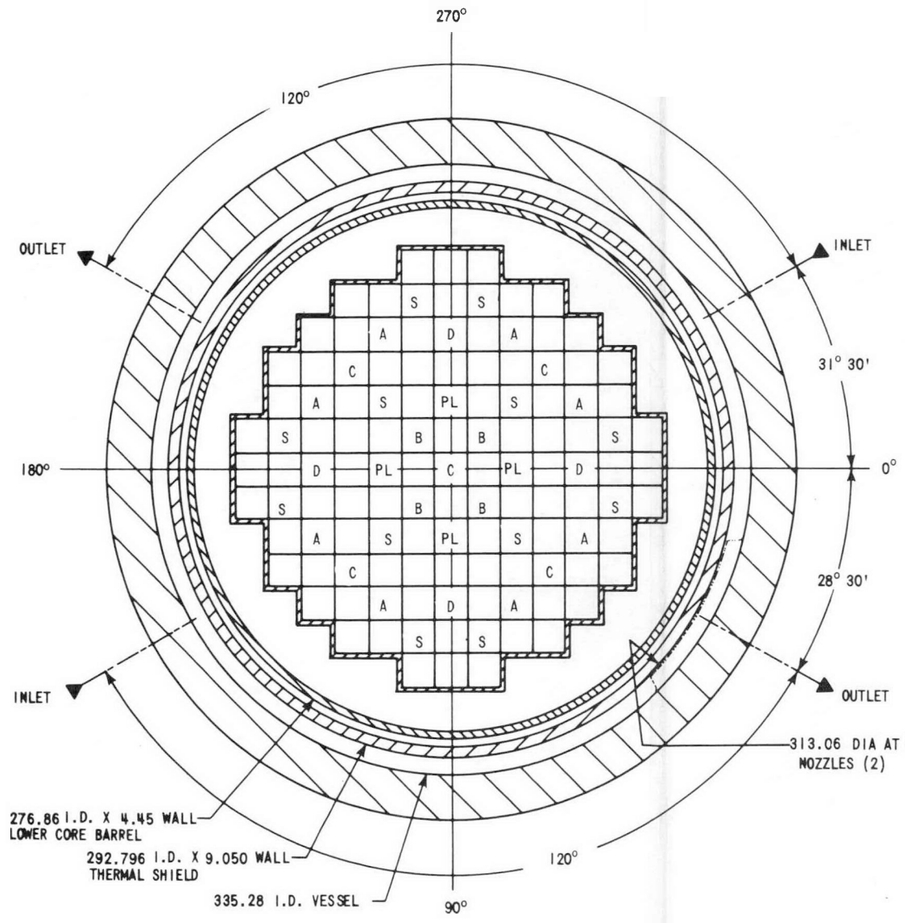

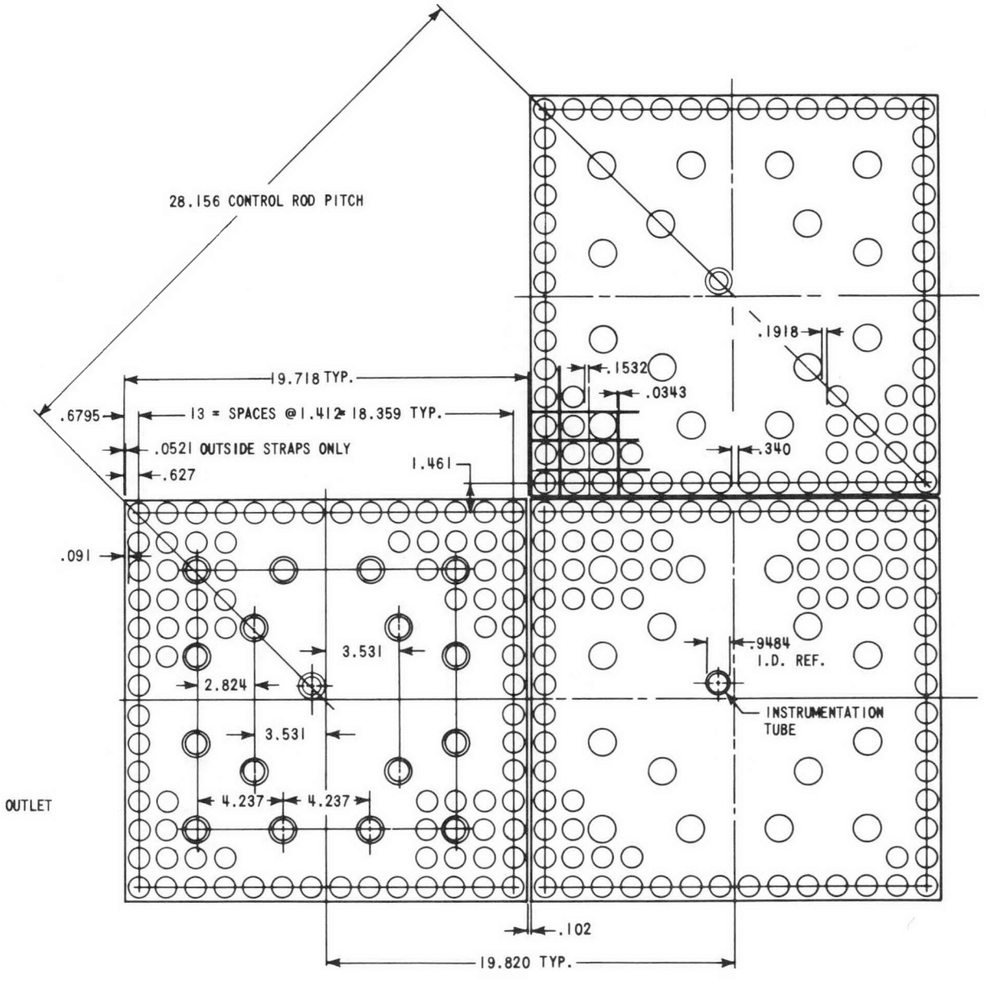

(ALL DIMENSIONS INDICATED AT 15 TO 21°C. DIMENSIONS ARE IN CENTIMETERS.

Figure A-1. Point Beach Unit 1, Core and Fuel Assembly Cross Section

Blank Page

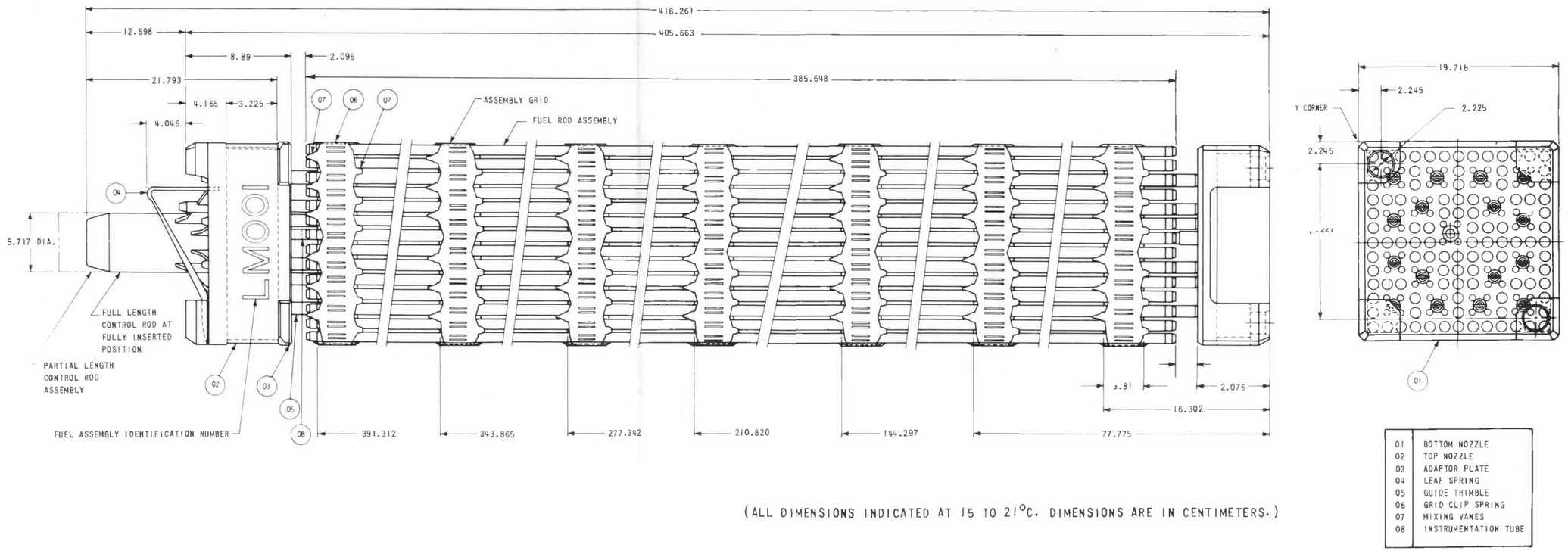

Figure A-2. Point Beach Unit 1 Fuel Assembly

Blank Page

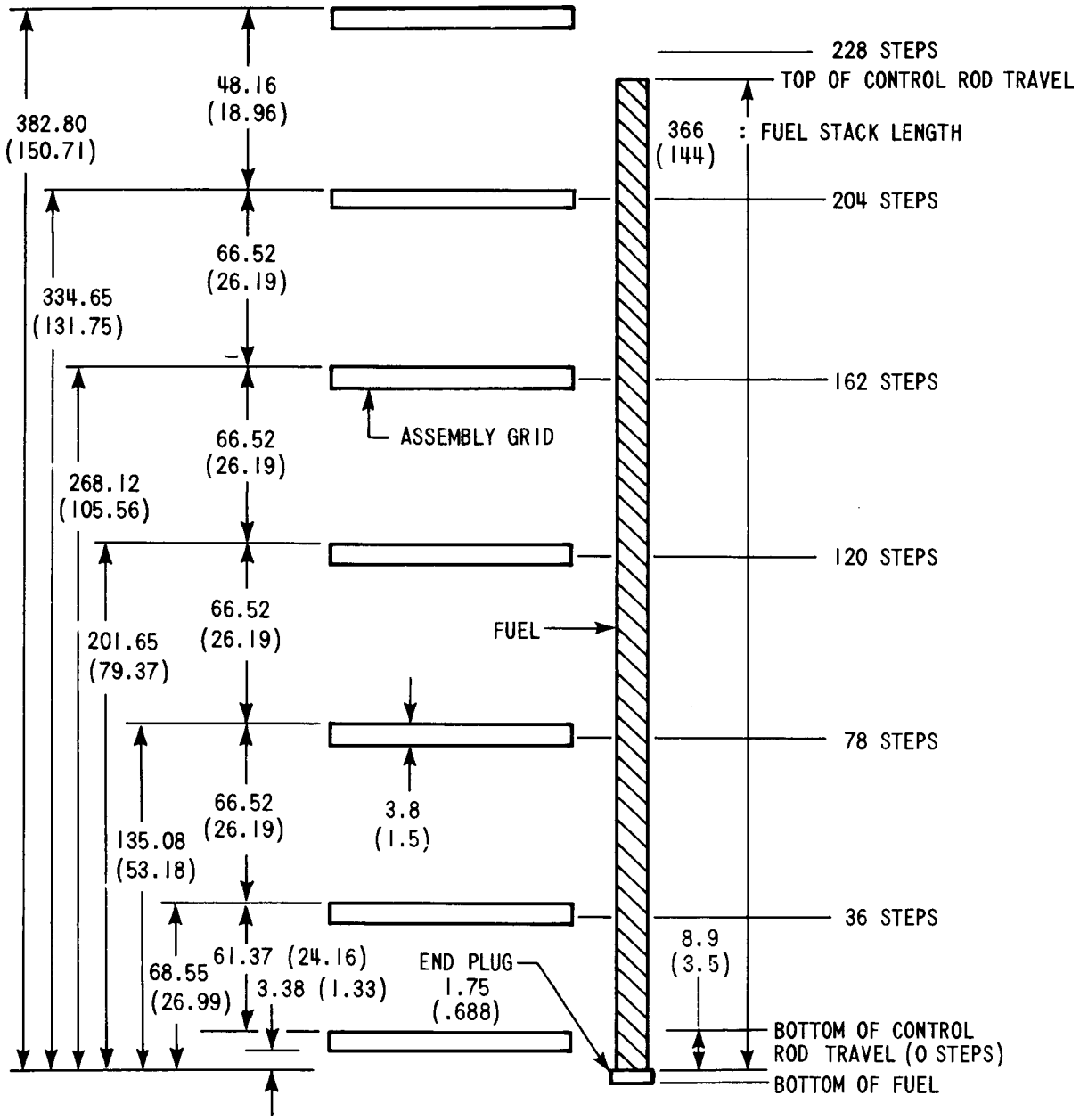

Figure A-3. Point Beach Unit 1, Cycle 3, Axial Grid Locations With Respect to Fuel and Control Rod Position (All Dimensions are Given in Centimeters, Inches are in Parenthesis)

APPENDIX B

POINT BEACH UNIT 1, CYCLES 2 AND 3
CORE LOADING AND OPERATIONAL DATA

Blank Page

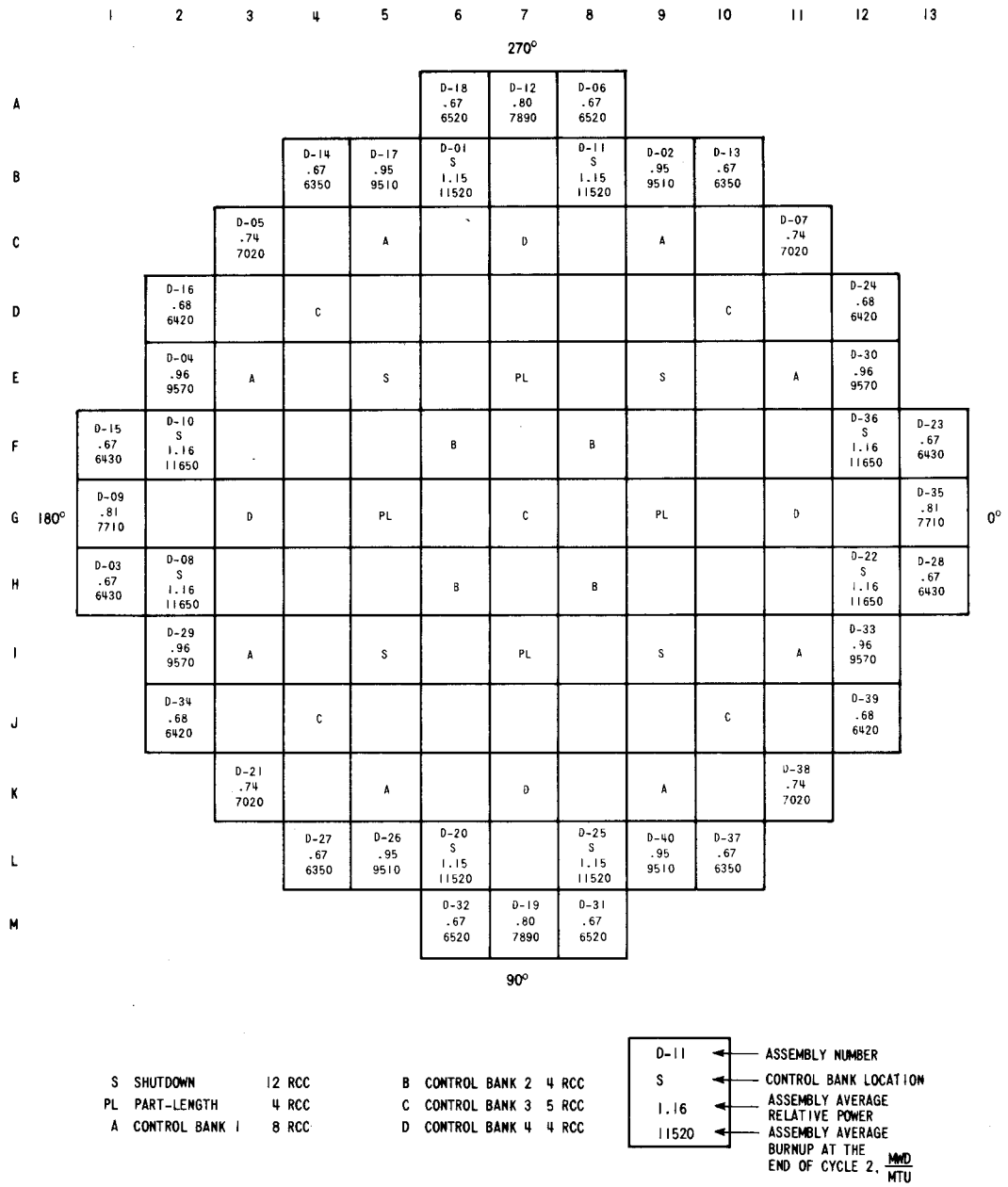

Figure B-1. Region 4 in Point Beach Unit 1, Cycle 2

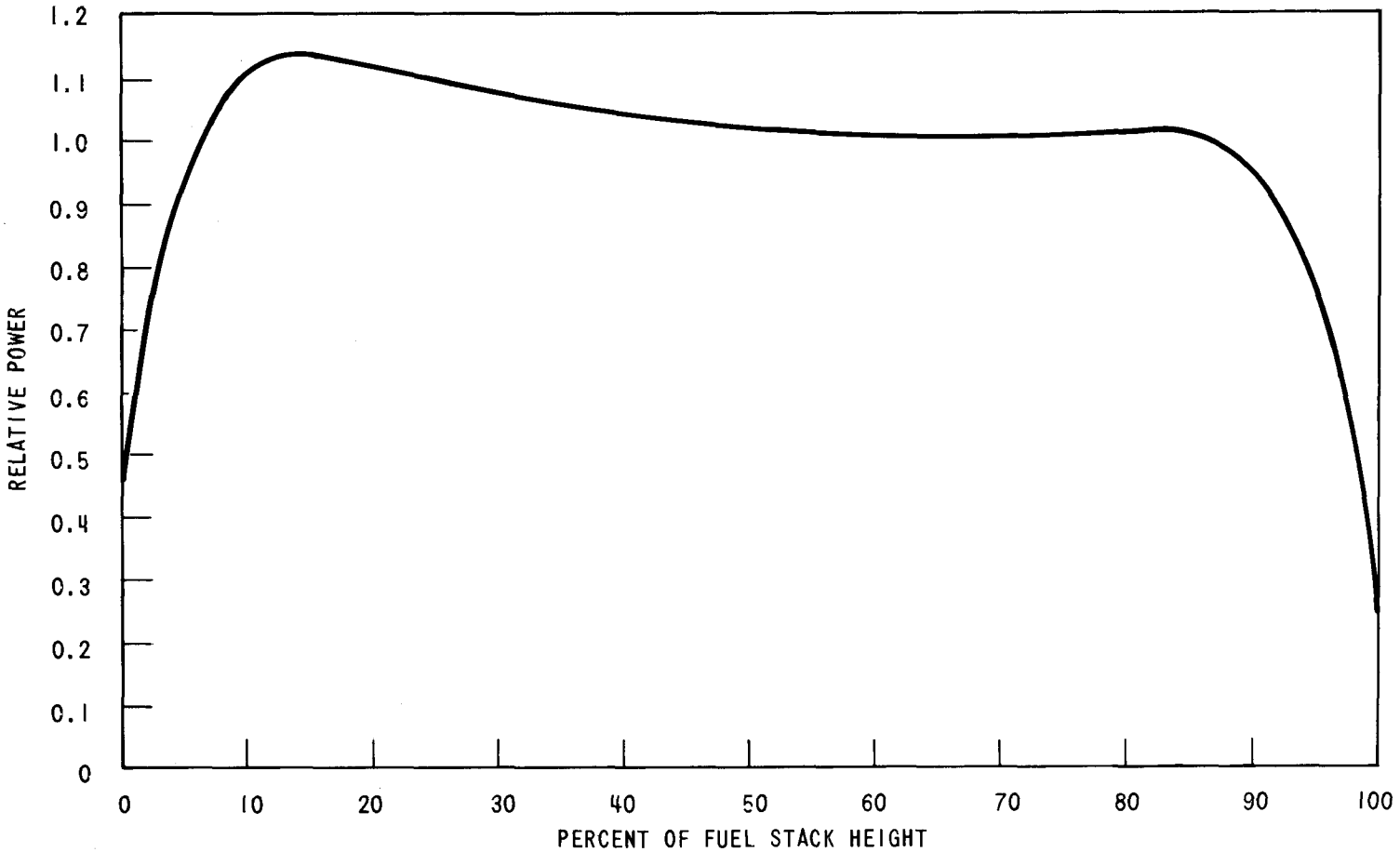

Figure B-2. Point Beach Unit 1: Relative Axial Power Distribution at the End of Cycle 2

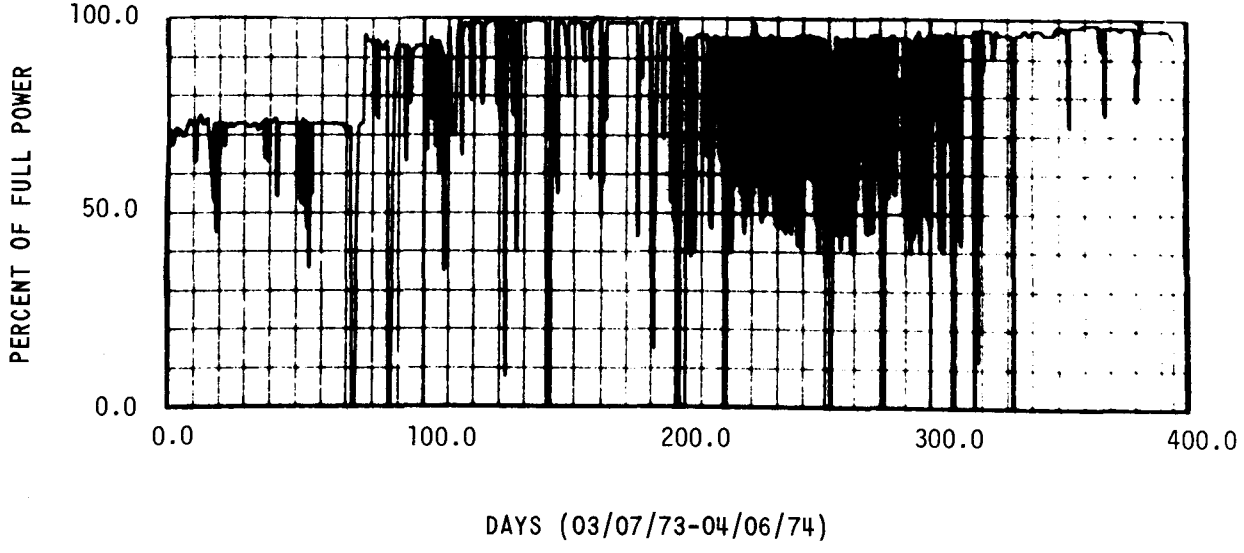

Figure B-3. Point Beach Unit 1: Cycle 2 Power History

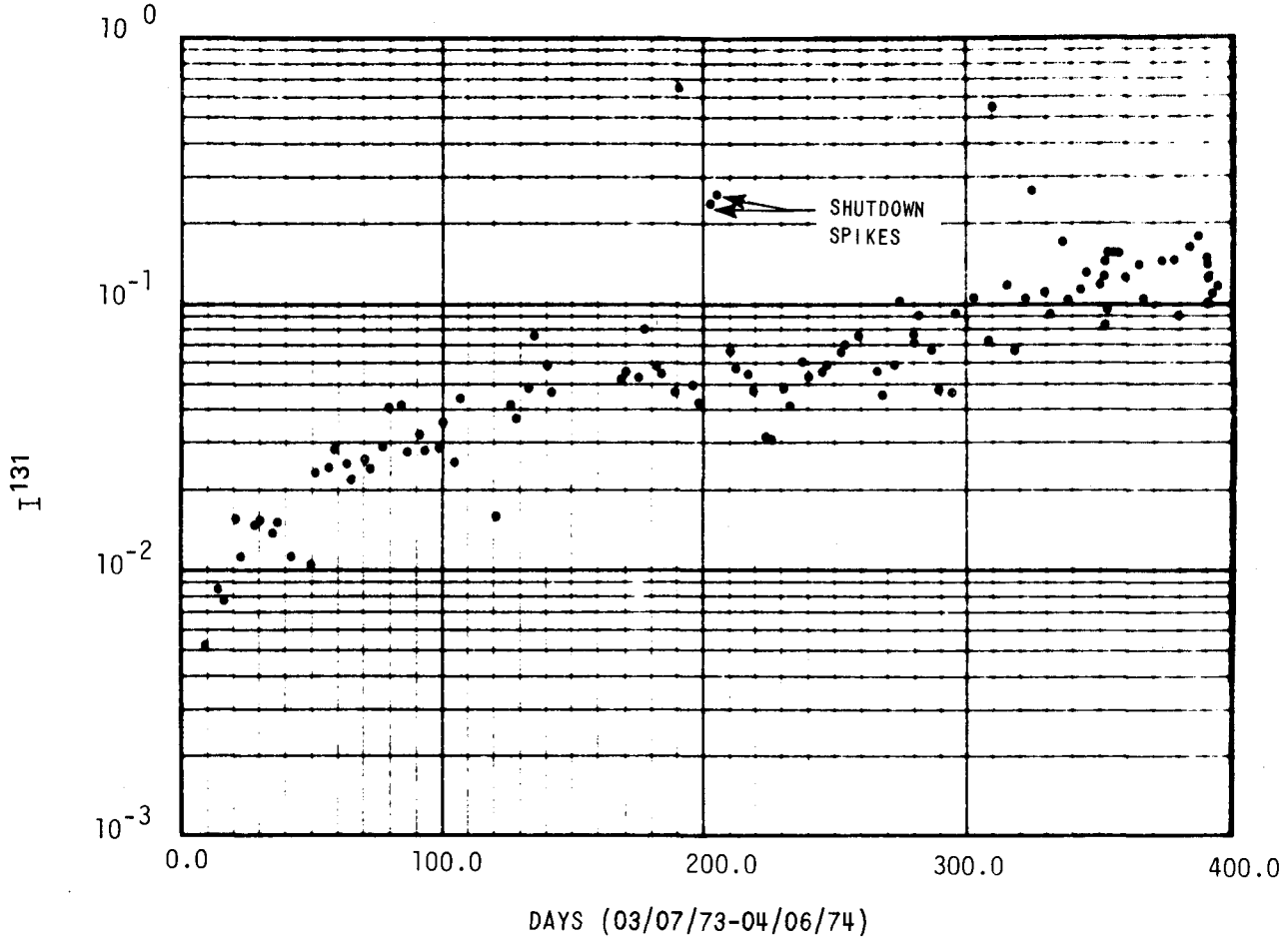

Figure B-4. Point Beach Unit 1: Cycle 2 I^{131} Coolant Activity

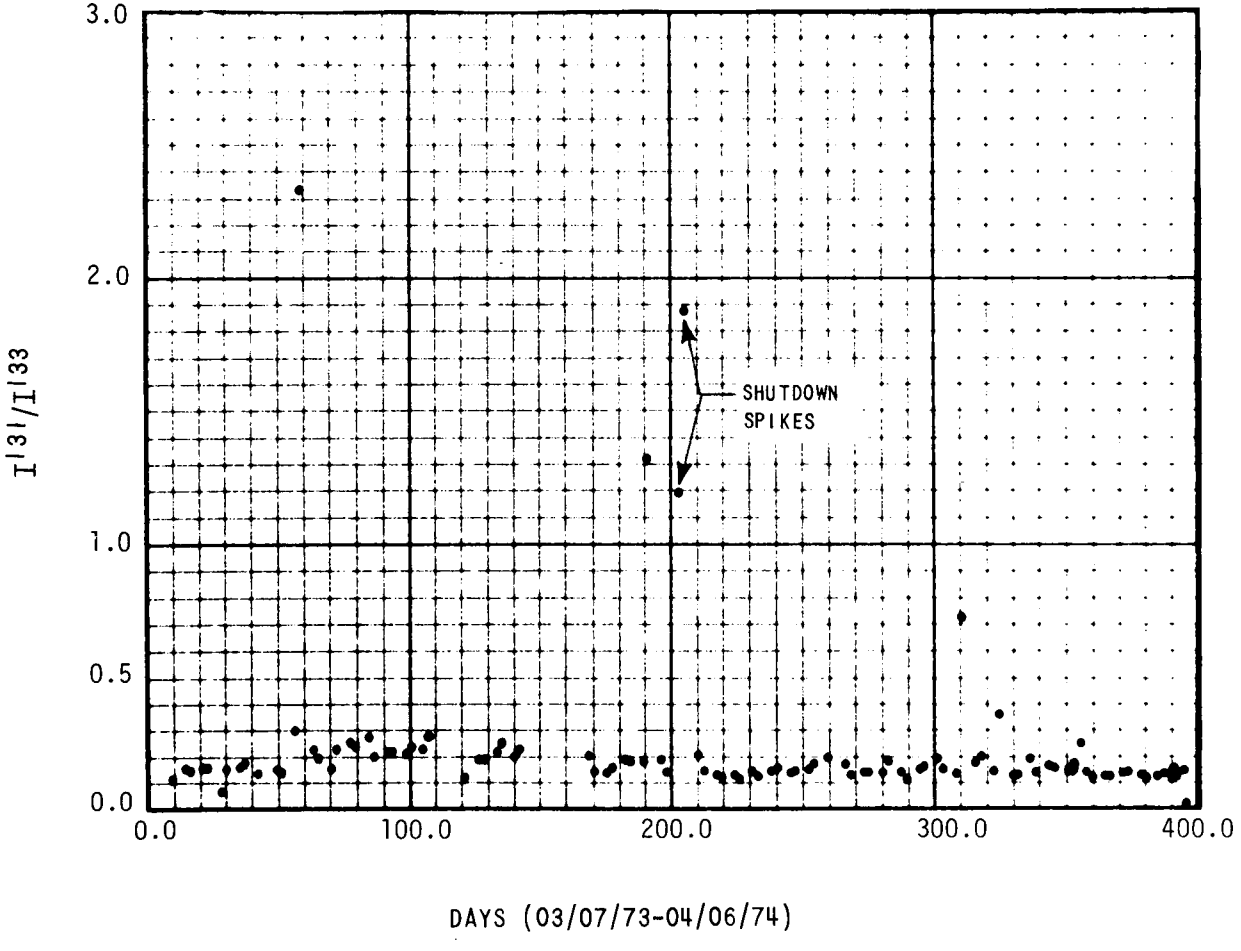

Figure B-5. Point Beach Unit 1: Cycle 2 I^{131}/I^{133} Coolant Activity Ratio

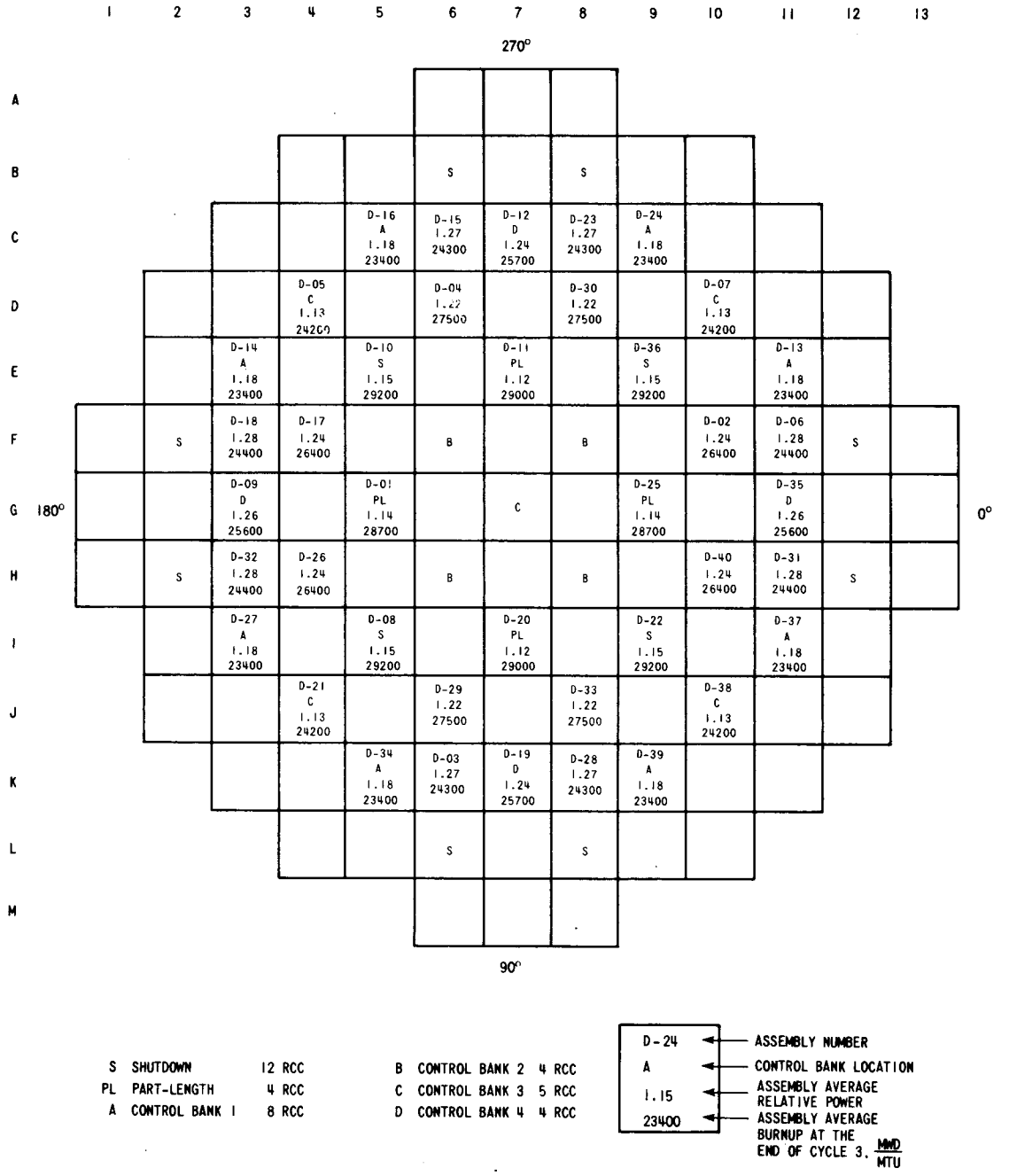

Figure B-6. Region 4 in Point Beach Unit 1, Cycle 3

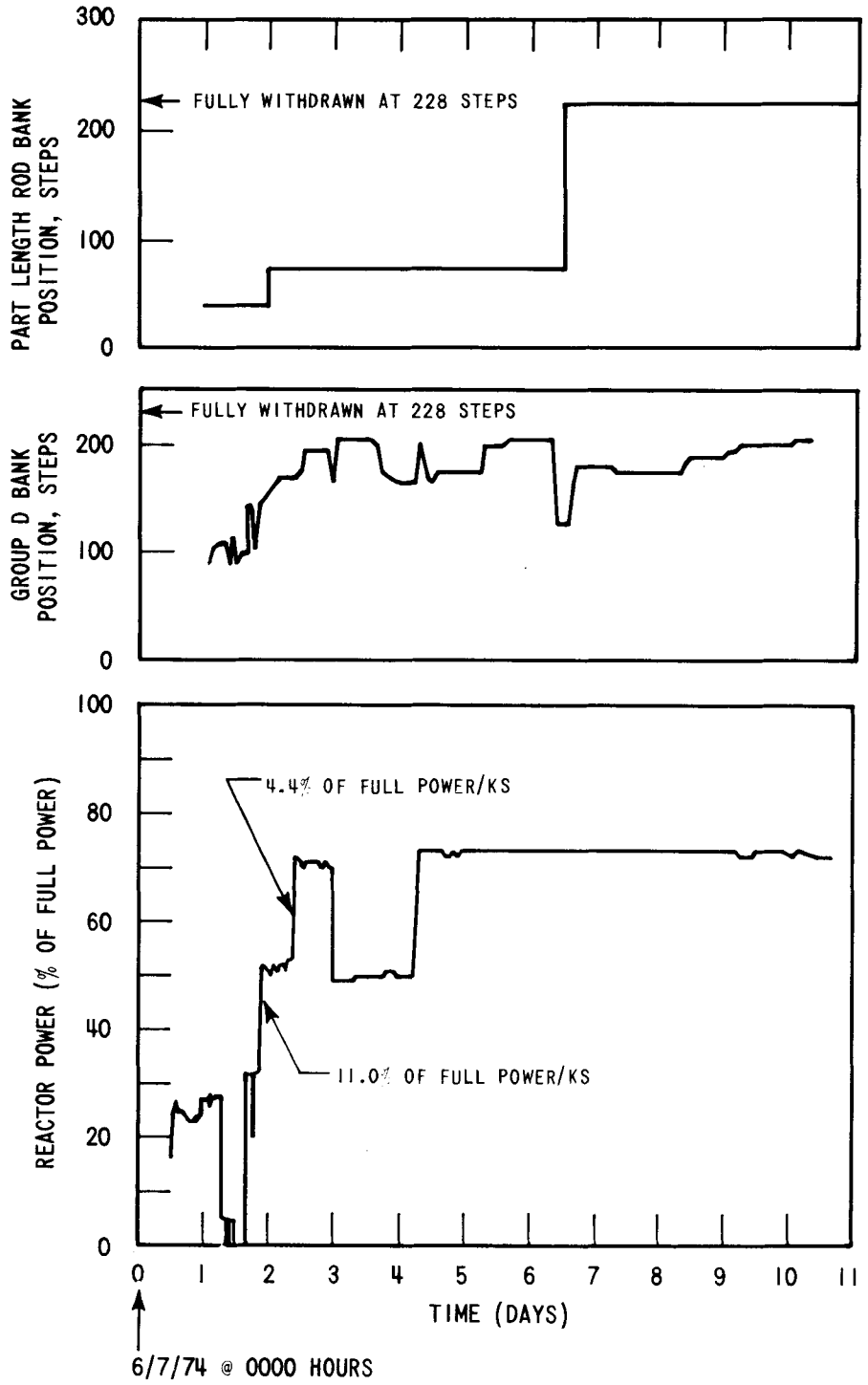

Figure B-7. Reactor Power and Control Rod Maneuvers During Point Beach Unit 1, Cycle 3 Startup

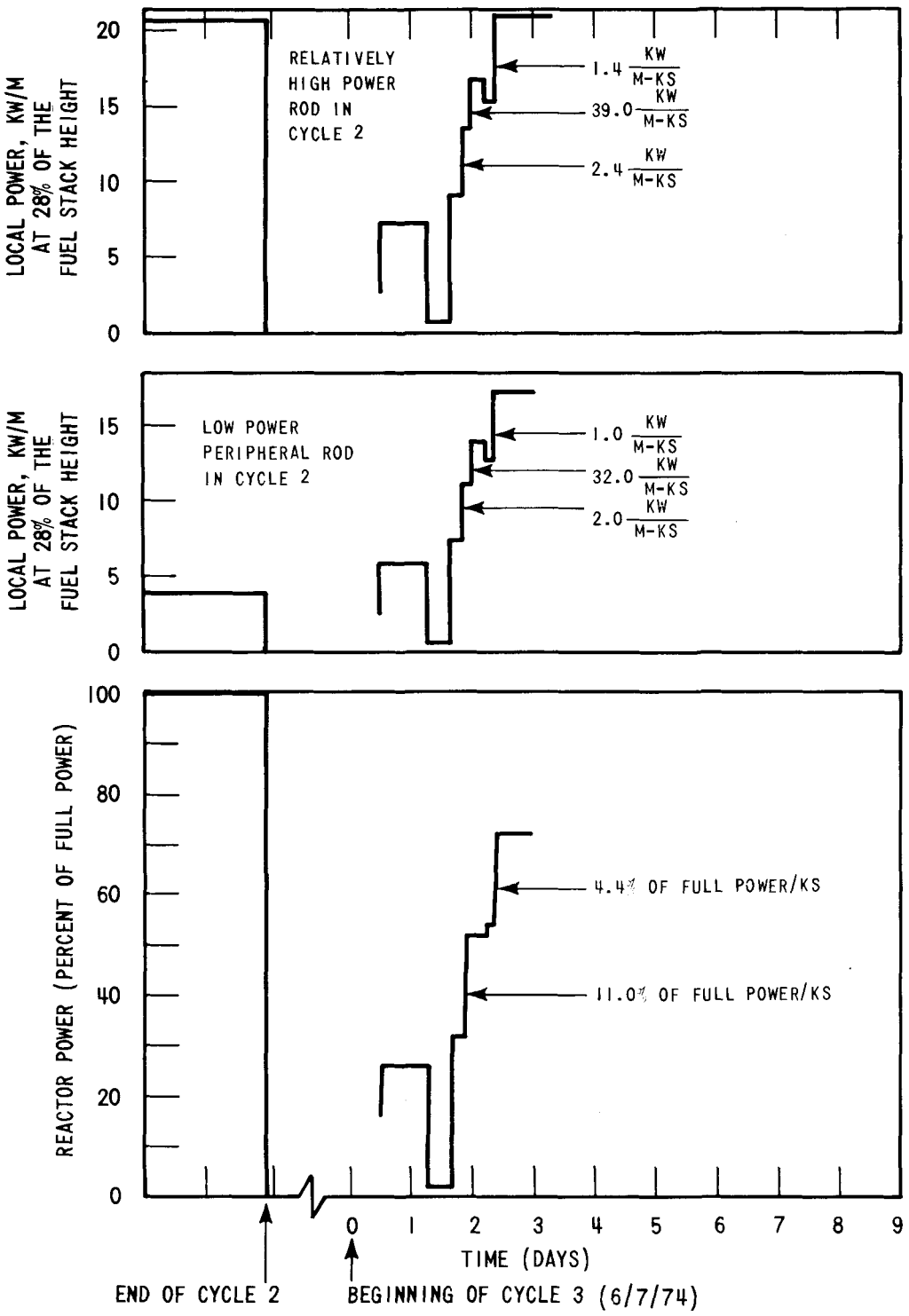

Figure B-8. Local Powers During Cycle 3 Startup

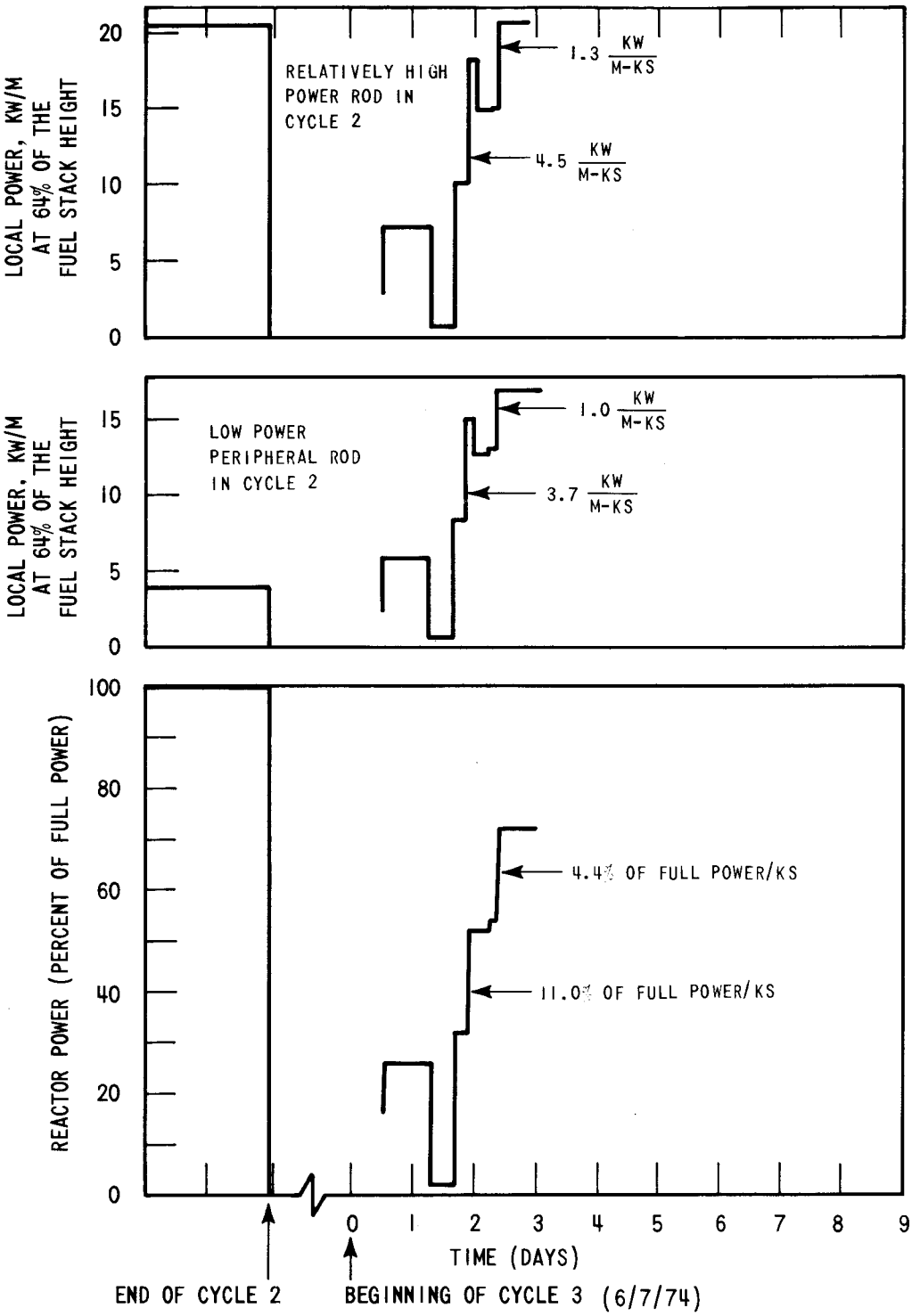

Figure B-9. Local Powers During Cycle 3 Startup

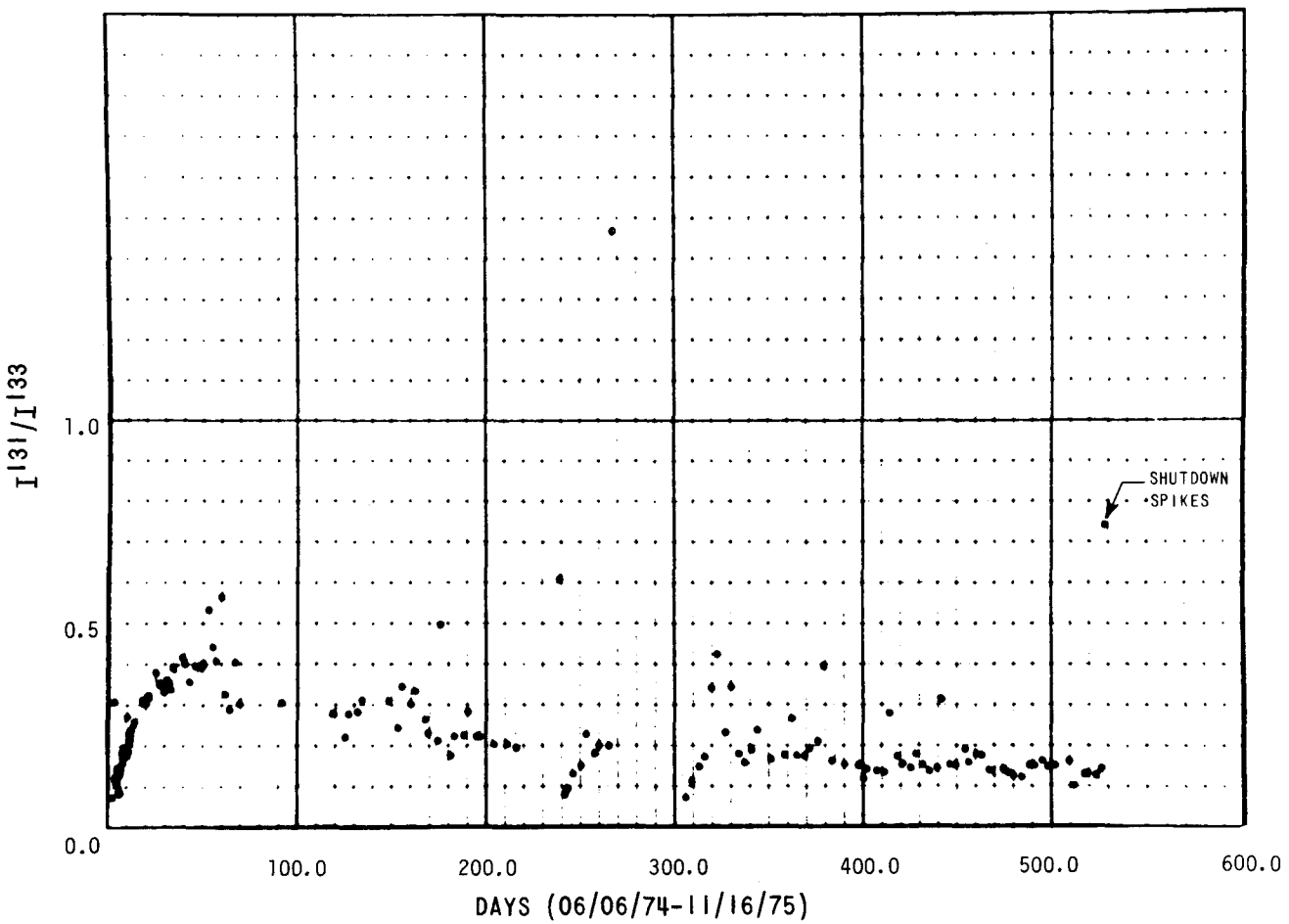

Figure B-10. Point Beach Unit 1: Cycle 3 I^{131}/I^{133} Coolant Activity Ratio

APPENDIX C

POINT BEACH UNIT-1, REGION 4
CHARACTERIZATION DATA

Blank Page

Table C-1

POINT BEACH UNIT 1, REGION 4, LEAK TEST RESULTS

Part A. Higher Distribution

Assembly Identification	Leak Test, I^{131} Corrected Activity, μCi/gm	Relative Power at BOC3(a)	Relative Power at BOC3(b)	Burnup at BOC3, MWD/MTU	Burnup at EOC3, MWD/MTU	Comment
D-03	3.8×10^{-3}	.67	1.27	6430	24,300	failed in cycle 2 due to a leaking baffle joint
D-31	3.5×10^{-3}	.67	1.28	6520	24,400	
D-14	1.9×10^{-3}	.67	1.18	6350	23,400	moved to spent fuel pit during cycle 2 to 3 refueling
D-40	1.7×10^{-3}	.95	1.24	9510	26,400	moved to spent fuel pit during cycle 2 to 3 refueling
D-34	1.4×10^{-3}	.68	1.18	6420	23,400	
D-18	1.2×10^{-3}	.67	1.28	6520	24,400	
D-26	1.2×10^{-3}	.95	1.24	9510	26,400	
D-19	1.2×10^{-3}	.80	1.24	7890	25,700	group D bank
D-20	1.0×10^{-3}	1.15	1.12	11,520	29,000	moved to spent fuel pit during cycle 2 to 3 refueling. Part-length rod bank
D-33	9.6×10^{-4}	.96	1.22	9570	27,500	
D-12	7.7×10^{-4}	.80	1.24	7890	25,700	group D bank
D-30	6.7×10^{-4}	.96	1.22	9570	27,500	
D-39	6.4×10^{-4}	.68	1.18	6420	23,400	moved to spent fuel pit during cycle 2 to 3 refueling
D-38	5.8×10^{-4}	.74	1.13	7020	24,200	
D-21	5.0×10^{-4}	.74	1.13	7020	24,200	
D-05	5.0×10^{-4}	.74	1.13	7020	24,200	
D-37	4.2×10^{-4}	.67	1.18	6350	23,400	
D-13	4.1×10^{-4}	.67	1.18	6350	23,400	

(Core Average Power is 5.70 kw/ft)

(a) End of Cycle 2.

(b) Beginning of Cycle 3.

Table C-1 (Continued)

Part B Lower Distribution

Assembly Identification	Leak Test, I^{131} Corrected Activity, μCi/gm	Relative Power at BOC3[a]	Relative Power at BOC3[b]	Burnup at BOC3, MWD/MTU	Burnup at EOC3, MWD/MTU	Comment
D-13	4.1×10^{-4}	.67	1.18	6350	23400	
D-01	3.1×10^{-4}	1.15	1.14	11520	28700	Part length rod bank
D-11	2.3×10^{-4}	1.15	1.12	11520	29000	Part length rod bank
F-16	1.5×10^{-4}	0	1.04	0	15500	Region 5 Assembly
D-16	1.1×10^{-5}	.68	1.18	6420	23400	
E-05	9.5×10^{-5}	0	1.06	0	14900	Region 6 Assembly
D-06	8.6×10^{-5}	.67	1.28	6520	24400	
D-36	5.1×10^{-5}	1.16	1.15	11650	29200	
D-29	3.4×10^{-5}	.96	1.22	9570	27500	
D-02	0	.95	1.24	9510	26400	
D-04	0	.96	1.22	9570	27500	
D-07	0	.74	1.13	7020	24200	
D-08	0	1.16	1.15	11650	29200	
D-09	0	.81	1.26	7710	25600	Group D Bank
D-10	0	1.16	1.15	11650	29200	
D-15	0	.67	1.27	6430	24300	
D-17	0	.95	1.24	9510	26400	
D-22	0	1.16	1.15	11650	29200	
D-23	0	.67	1.27	6430	24301	
D-24	0	.68	1.18	6420	23400	
D-25	0	1.15	1.14	11520	28700	Part length rod bank
D-27	0	.67	1.18	6350	23400	
D-28	0	.67	1.27	6430	24300	
D-32	0	.67	1.28	6520	24400	
D-35	0	.81	1.26	7710	25600	Group D Bank

FUEL ASSEMBLY D-14--CHARACTERIZATION DATA

Fabrication

The fuel rods in the Assembly D-14 represent 23 individual cladding lots and 38 individual pellet groups. Table C-2 shows grouping and numbers of sister rods per given combination of cladding lot and pellet group. Figure C-1 shows the identity and location of fuel rods loaded into the assembly. Representative mechanical proprietary data of as-fabricated cladding tubes is summarized in Table C-3; representative pellet data is summarized in Table C-4.

Operating Powers/Burnup

Figure C-2 illustrates average calculated rod power at the end of Cycle 2 for all rods loaded into the fuel assembly. Figure C-3 gives the average rod burnup at the end of Cycle 2. The average rod power at the beginning of Cycle 3 is given in Figure C-4 while Figure C-5 gives the average rod burnup at the end of Cycle 3.

Table C-2

NUMBER OF FUEL RODS PER GIVEN COMBINATION OF PELLET GROUP AND CLADDING LOT, ASSEMBLY D-14

Sister Rods		
Cladding Lot	Pellet Group	No. of Fuel Rods
5AW1794	11	2
5DR1946	12	14
5DJ1948	13	13
5DJ1948	14	8
5EE1946	15	12
5BA6469	16	1
5EE1946	17	6
5BR1798	18	1
5DR1946	8	3
5DJ1948	19	18
5AX6460	8	12
5AZ1773	20	12
5AH1698	3	1
5BR1802	21	1
5BG1816	22	13
5AZ6463	16	1
5BG1802	23	2
5BA6469	24	1
5BG1799	7	2
5BA1773	25	2
5BP1794	26	1
5BL1796	27	1
5BR1802	28	2
5DR1946	15	3
5BP1794	29	1
5AX6460	30	9
5DR1946	31	5
5AS1790	32	1
5BA1773	33	1
5AX6460	34	5
5AX1790	35	1
5BR1798	36	2
5AS1790	37	1
5BR1791	38	1
5BR1795	39	2
5BG1802	6	3
5BP1793	40	1
5AW1794	47	1
5BP1794	41	1
5AZ1773	42	9
5BA1776	43	1
5BG1802	28	1

Table C-3

AS FABRICATED CLADDING PROPERTIES

FUEL ASSEMBLY D-14

Mechanical Properties[a]	Mean Value
Ultimate tensile strength at 385°C (725°F) MN/m^2 (ksi)	4.60×10^2 (66.7)
Yield strength at 385°C (725°F) MN/m^2 (ksi)	3.58×10^2 (52.0)
Hot tensile elongation at 385°C (725°F) 5.1 cm (2 in.) gauge length, %	16.4
Hydride Data	**Mean Value**
H_2 content, ppm[a]	11.2
Hydride orientation[b,c] Fn no.	0.115

a. Based on two measurements per cladding lot

b. Based on three measurements per cladding lot

c. Hydride orientation factor, Fn, is defined as the ratio of the number of radial hydride platelets to the total number of hydride platelets.

Table C-4

AS FABRICATED FUEL PROPERTIES

FUEL ASSEMBLY D-14

Fuel Composition	
Isotope [a]	**Weight Percent**
U^{234}	0.024
U^{235}	3.035
U^{236}	0.015
U^{238}	96.926
Fuel Properties	**Mean Value**
Fuel density, % theoretical density [b]	93.919
H_2 content, ppm [c]	0.25
H_2O content, ppm [d]	6.1

a. Based on one measurement per 10 groups
b. Based on 35 measurements per group
c. Based on one measurement per group
d. Based on one measurement per four groups

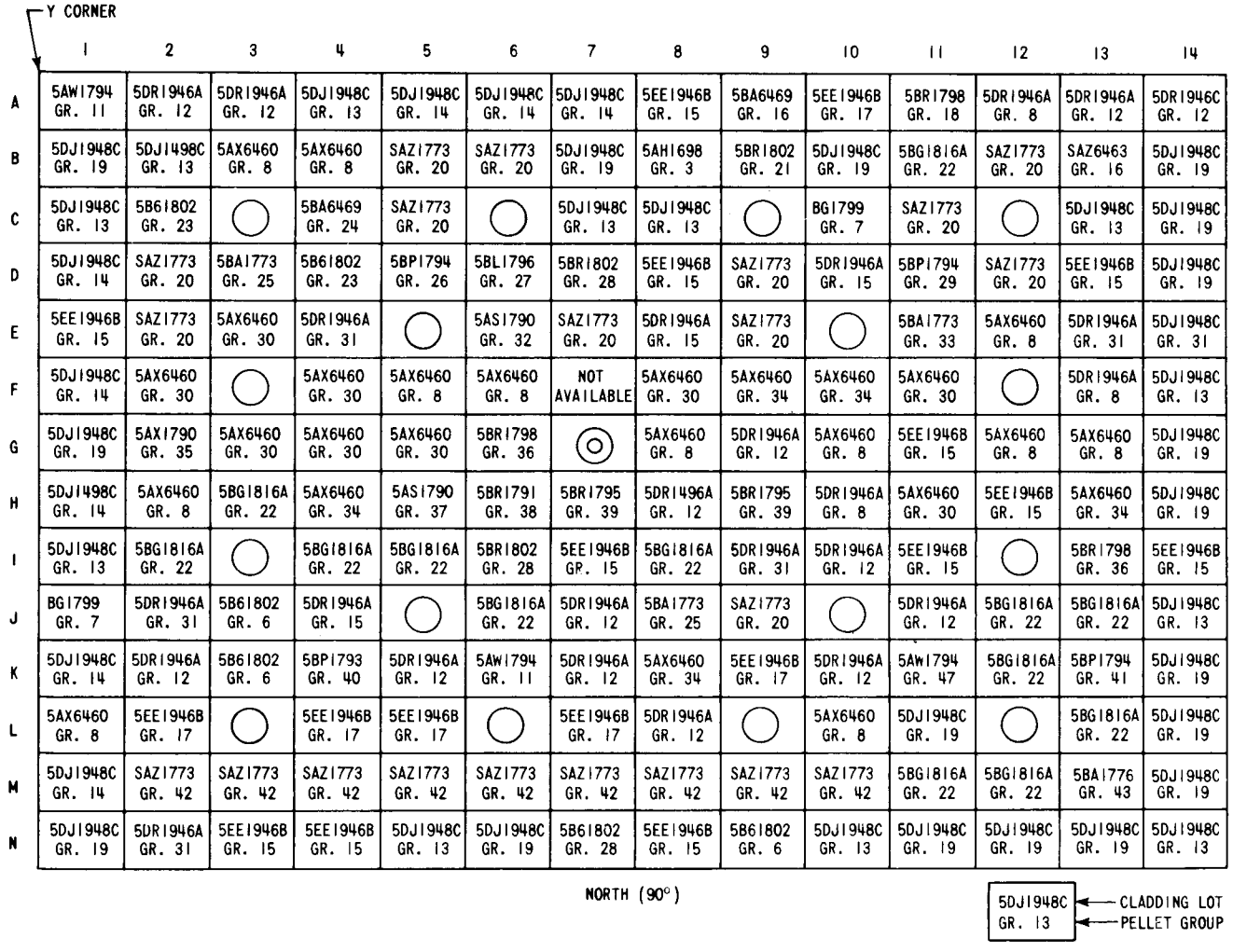

Figure C-1. Assembly D-14, Distribution of Clad Lots and Pellet Groups

Table C-5

PERTINENT FUEL ROD INFORMATION FOR THE SELECTED RODS OF ASSEMBLY D-14

Fuel Assembly	Rod	Rod Average Power EOC2 kw/m	Rod Average Power EOC2 [kw/ft]	Rod Average Power BOC3 kw/m	Rod Average Power BOC3 [kw/ft]	Power Increase BOC3/EOC2	Rod Average Burnup MWD/MTU BOC[a]	Rod Average Burnup MWD/MTU EOC3[b]	Cladding Lot	Fuel Group
D-14	A-1	4.10	[1.25]	18.9	[5.75]	4.6	1977	15563	5AW1794	11
"	K-6	16.1	4.90	23.3	7.11	1.5	8813	25149	5AW1794	11
"	A-4	5.57	1.70	20.0	6.12	3.6	2831	17310	5DJ1948	13
"	B-2	5.57	1.70	19.7	6.01	3.5	2823	16996	5DJ1948	13
"	A-2	4.62	1.41	19.3	5.89	4.2	2291	16221	5DR1946	12
"	A-3	5.15	1.57	19.8	6.05	3.9	2591	16914	5DR1946	12
"	E-3	9.31	2.84	22.0	6.73	2.3	4871	20580	5AX6460	30
"	F-2	8.82	2.69	21.5	6.56	2.4	4592	19792	5AX6460	30
"	A-10	7.84	2.39	21.4	6.53	2.7	4054	19462	5EE1946	17
"	K-9	17.8	5.43	23.4	7.14	1.3	9878	26374	5EE1946	17
"	A-9	7.57	2.31	21.4	6.52	2.8	3905	19288	5BA6469	16
"	C-4	8.26	2.52	21.7	6.62	2.6	4287	19892	5BA6469	24
"	D-3	8.43	2.57	21.7	6.61	2.6	4375	19893	5BA1773	25
"	J-8	15.8	4.81	22.1	6.75	1.4	8698	24314	5BA1773	25
"	G-6	12.5	3.80	21.7	6.61	1.7	6754	22103	5BR1798	36
"	I-13	17.5	5.34	22.7	6.91	1.3	9803	25967	5BR1798	36
"	A-11	8.10	2.47	21.5	6.57	2.5	4219	19721	5BR1798	18
"	B-11	9.84	3.00	21.7	6.63	2.2	5222	20927	5BG1816	22
"	I-2	10.8	3.30	22.1	6.74	2.0	5734	21182	5BG1816	22
"	K-11	18.2	5.56	23.0	7.01	1.3	10201	26479	5AW1794	47
"	A-8	7.18	2.19	21.0	6.42	2.9	3694	18858	5EE1946	15
"	E-1	6.62	2.02	20.0	6.12	3.0	3374	17456	5EE1946	15
"	B-3	6.46	1.97	20.7	6.33	3.2	3307	18261	5AX6460	8
"	B-4	6.89	2.10	20.5	6.26	3.0	3539	18322	5AX6460	8
"	B-1	4.75	1.45	19.1	5.83	4.0	2357	16055	5DJ1948	19
"	B-10	9.54	2.91	21.7	6.61	2.3	5035	20674	5DJ1948	19
"	A-12	8.43	2.57	21.8	6.64	2.6	4397	20060	5DR1946	8
"	F-13	15.2	4.63	22.5	6.85	1.5	8383	24550	5DR1946	8
"	E-11	14.1	4.30	23.1	7.06	1.6	7674	24354	5BA1773	33
"	H-3	11.5	[3.51]	22.5	[6.87]	2.0	6112	21962	5BG1816	22

a. Fast fluence (greater than 1 Mev) at BOC3 can be calculated as n/cm^2 = (Burnup at BOC3, MWD/MTU) x 1.69×10^{17}

b. Fast fluence (greater than 1 Mev) at EOC3 can be calculated as n/cm^2 = [(Burnup at EOC3, MWD/MTU) - (Burnup at BOC3, MWD/MTU)] x 1.85×10^{17} + (Burnup at BOC3, MWD/MTU) x 1.69×10^{17}

Table C-6

PERTINENT FUEL ROD INFORMATION FOR THE SELECTED RODS OF ASSEMBLY D-40

Fuel Assembly	Rod	Rod Average Power EOC2 kw/m	Rod Average Power EOC2 [kw/ft]	Rod Average Power BOC3 kw/m	Rod Average Power BOC3 [kw/ft]	Power Increase BOC3/EOC2	Rod Average Burnup MWD/MTU BOC[a]	Rod Average Burnup MWD/MTU EOC3[b]	Cladding Lot	Fuel Group
D-40	045	21.4	[6.52]	23.8	[7.25]	1.1	12348	29365	5BG1816	48
"	039	18.3	5.58	23.3	7.11	1.3	10376	26878	5BG1816	48
"	046	17.5	5.34	23.5	7.16	1.3	9894	26482	5BG1816	48
"	030	20.4	6.22	23.4	7.14	1.1	11658	28298	5BG1816	48
"	042	16.7	5.09	25.1	7.66	1.5	9303	26963	5BR1791	48
"	043	20.5	6.26	24.2	7.37	1.2	11701	28830	5BG1816	48
"	026	20.0	6.09	22.9	6.98	1.1	11494	27818	5BG1816	48
"	047	19.0	5.80	24.1	7.34	1.3	10850	28245	5BG1816	48
"	038	17.5	5.35	23.5	7.18	1.3	9947	26969	5BR1791	48
"	041	19.0	5.80	23.0	7.01	1.2	10931	27416	5BG1816	48
"	035	15.7	4.79	24.1	7.35	1.5	8805	26206	5BR1791	48
"	R-04	--	--	19.6	5.98	--	0	15017		
"	R-03	--	--	20.4	[6.21]	--	0	15891		

a. Fast fluence (greater than 1 Mev) at BOC3 can be calculated as n/cm^2 = (Burnup at BOC3, MWD/MTU) x 1.69×10^{17}

b. Fast fluence (greater than 1 Mev) at EOC3 can be calculated as n/cm^2 = [(Burnup at EOC3, MWD/MTU) - (Burnup at BOC3, MWD/MTU)] x 1.85×10^{17} + (Burnup at BOC3, MWD/MTU) x 1.69×10^{17}

Y CORNER	1	2	3	4	5	6	7	8	9	10	11	12	13	14
A	4.10 (1.25)	4.62 (1.41)	5.15 (1.57)	5.57 (1.70)	6.03 (1.84)	6.49 (1.98)	6.82 (2.08)	7.18 (2.19)	7.57 (2.31)	7.84 (2.39)	8.10 (2.47)	8.43 (2.57)	8.59 (2.62)	8.82 (2.69)
B	4.75 (1.45)	5.57 (1.70)	6.46 (1.97)	6.89 (2.10)	7.41 (2.26)	8.13 (2.48)	8.33 (2.54)	8.75 (2.67)	9.44 (2.88)	9.54 (2.91)	9.84 (3.00)	10.43 (3.18)	10.26 (3.13)	10.36 (3.16)
C	5.44 (1.66)	6.62 (2.02)	◯	8.26 (2.52)	8.95 (2.73)	◯	9.93 (3.03)	10.46 (3.19)	◯	11.41 (3.48)	11.70 (3.57)	◯	11.97 (3.65)	11.77 (3.59)
D	6.03 (1.84)	7.18 (2.19)	8.43 (2.57)	9.05 (2.76)	10.03 (3.06)	10.46 (3.19)	10.59 (3.23)	11.11 (3.39)	12.07 (3.68)	12.66 (3.86)	12.69 (3.87)	13.18 (4.02)	12.79 (3.90)	12.82 (3.91)
E	6.62 (2.02)	7.90 (2.41)	9.31 (2.84)	10.20 (3.11)	◯	11.28 (3.44)	11.38 (3.47)	11.90 (3.63)	12.98 (3.96)	◯	14.10 (4.30)	14.36 (4.38)	13.87 (4.23)	13.84 (4.22)
F	7.28 (2.22)	8.82 (2.69)	◯	10.85 (3.31)	11.48 (3.50)	11.67 (3.56)	12.26 (3.74)	12.79 (3.90)	13.31 (4.06)	14.33 (4.37)	14.92 (4.55)	◯	15.18 (4.63)	14.75 (4.53)
G	7.80 (2.38)	9.21 (2.81)	10.72 (3.27)	11.15 (3.40)	11.77 (3.59)	12.46 (3.80)	◎	14.23 (4.34)	14.10 (4.30)	14.52 (4.43)	15.15 (4.62)	16.07 (4.90)	15.57 (4.75)	15.54 (4.74)
H	8.33 (2.54)	9.87 (3.01)	11.51 (3.51)	11.93 (3.64)	12.56 (3.83)	13.21 (4.03)	14.49 (4.42)	15.11 (4.61)	14.85 (4.53)	15.38 (4.69)	15.97 (4.87)	16.92 (5.16)	16.36 (4.99)	16.26 (4.96)
I	8.92 (2.72)	10.82 (3.30)	◯	13.18 (4.02)	13.90 (4.24)	13.97 (4.26)	14.52 (4.43)	15.05 (4.59)	15.67 (4.78)	16.82 (5.13)	17.41 (5.31)	◯	17.51 (5.34)	17.02 (5.19)
J	9.31 (2.84)	11.08 (3.38)	12.92 (3.94)	14.07 (4.29)	◯	15.25 (4.65)	15.18 (4.63)	15.77 (4.81)	17.02 (5.19)	◯	18.20 (5.55)	18.33 (5.59)	17.64 (5.38)	17.51 (5.34)
K	9.77 (2.98)	11.64 (3.55)	13.54 (4.13)	14.27 (4.35)	15.51 (4.73)	16.07 (4.90)	15.97 (4.87)	16.56 (5.05)	17.80 (5.43)	18.36 (5.60)	18.23 (5.56)	18.79 (5.73)	18.10 (5.52)	17.97 (5.48)
L	10.23 (3.12)	12.56 (3.83)	◯	15.05 (4.59)	15.97 (4.87)	◯	17.11 (5.22)	17.67 (5.39)	◯	18.66 (5.69)	18.95 (5.78)	◯	19.02 (5.80)	18.36 (5.63)
M	10.69 (3.26)	12.62 (3.85)	14.33 (4.37)	14.82 (4.52)	15.57 (4.75)	16.62 (5.07)	16.72 (5.10)	17.21 (5.25)	18.13 (5.53)	18.03 (5.50)	18.36 (5.60)	19.11 (5.83)	18.66 (5.69)	18.36 (5.68)
N	11.54 (3.52)	13.11 (4.00)	14.26 (4.35)	15.02 (4.58)	15.67 (4.78)	16.33 (4.98)	16.75 (5.11)	17.18 (5.24)	17.70 (5.40)	17.97 (5.48)	18.26 (5.57)	18.59 (5.67)	18.66 (5.69)	18.85 (5.75)

NORTH (90°)

Figure C-2. Assembly D-14, Rod Average Power, kW/m, at the End of Cycle 2 (Figures in Parenthesis are kW/ft)

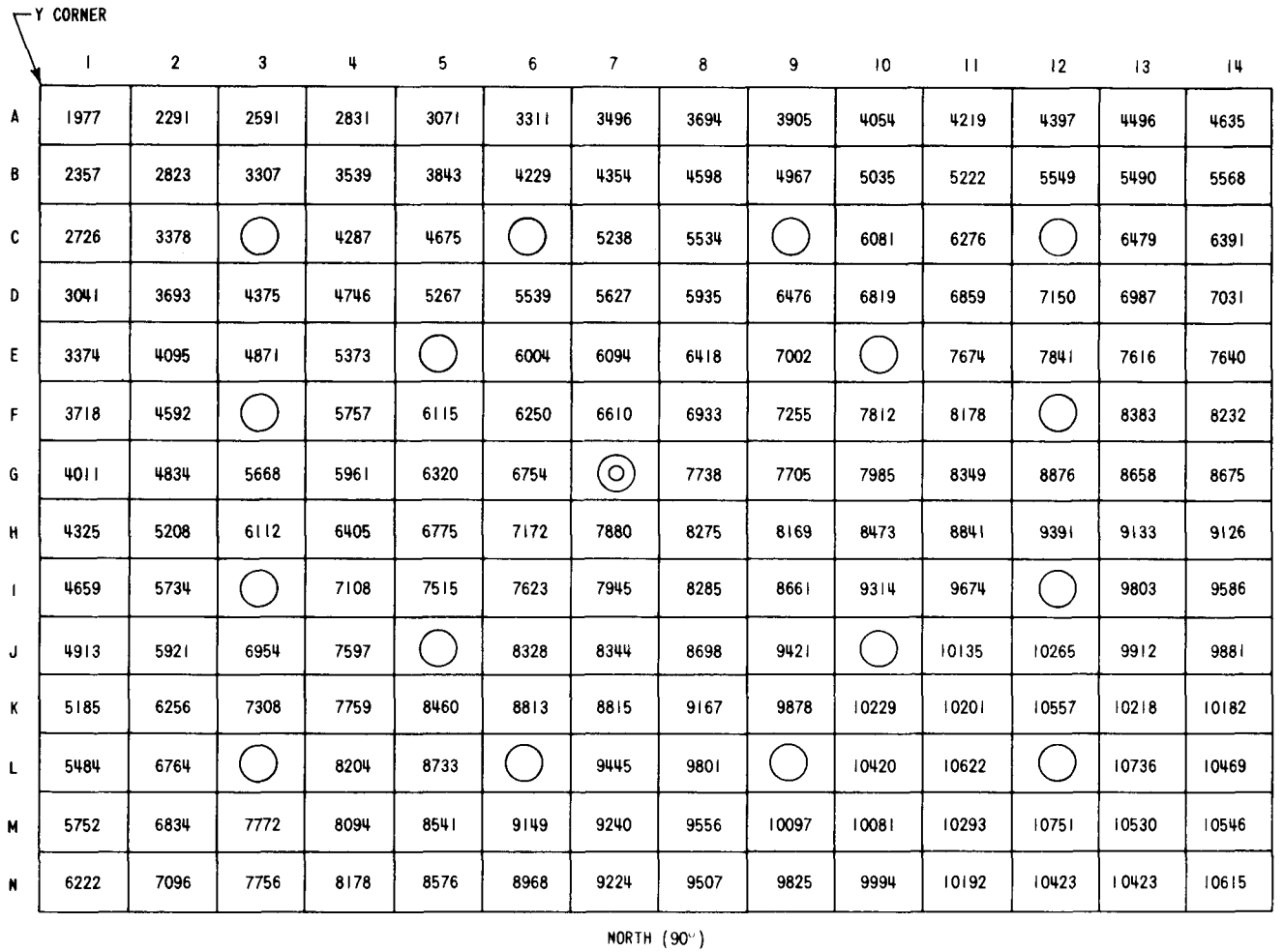

Figure C-3. Assembly D-14, Rod Average Burnup (MWD/MTU) at the End of Cycle 2

Y CORNER	1	2	3	4	5	6	7	8	9	10	11	12	13	14
A	18.85 (5.75)	19.31 (5.89)	19.84 (6.05)	20.07 (6.12)	20.36 (6.21)	20.75 (6.33)	20.85 (6.36)	21.05 (6.42)	21.38 (6.52)	21.41 (6.53)	21.54 (6.57)	21.77 (6.64)	21.74 (6.63)	22.00 (6.71)
B	19.11 (5.83)	19.70 (6.01)	20.75 (6.33)	20.52 (6.26)	20.82 (6.35)	21.57 (6.58)	21.21 (6.47)	21.38 (6.52)	22.10 (6.74)	21.67 (6.61)	21.74 (6.63)	22.39 (6.83)	21.84 (6.66)	21.97 (6.70)
C	19.54 (5.96)	20.66 (6.30)	◯	21.70 (6.62)	22.07 (6.73)	◯	22.26 (6.79)	22.46 (6.85)	◯	22.79 (6.95)	22.75 (6.94)	◯	22.52 (6.87)	22.10 (6.74)
D	19.74 (6.02)	20.43 (6.23)	21.67 (6.61)	21.64 (6.60)	22.43 (6.84)	22.36 (6.82)	21.67 (6.61)	21.77 (6.64)	22.75 (6.94)	23.02 (7.02)	22.49 (6.86)	22.85 (6.97)	21.97 (6.70)	21.93 (6.69)
E	20.07 (6.12)	20.72 (6.32)	22.07 (6.73)	22.43 (6.84)	◯	22.30 (6.80)	21.54 (6.57)	21.61 (6.59)	22.59 (6.89)	◯	23.15 (7.06)	22.98 (7.01)	21.93 (6.69)	21.80 (6.65)
F	20.46 (6.24)	21.51 (6.56)	◯	22.39 (6.83)	22.33 (6.81)	21.61 (6.59)	21.64 (6.60)	21.70 (6.62)	21.84 (6.66)	22.72 (6.93)	22.98 (7.01)	◯	22.46 (6.85)	21.80 (6.65)
G	20.59 (6.28)	21.15 (6.45)	22.33 (6.81)	21.70 (6.62)	21.57 (6.58)	21.67 (6.61)	◎	22.79 (6.95)	21.84 (6.66)	21.87 (6.67)	22.13 (6.75)	22.92 (6.99)	21.93 (6.69)	21.70 (6.62)
H	20.82 (6.35)	21.38 (6.52)	22.52 (6.87)	21.87 (6.67)	21.74 (6.63)	21.80 (6.65)	22.85 (6.97)	22.89 (6.98)	21.93 (6.69)	21.97 (6.70)	22.07 (6.73)	23.02 (7.02)	22.00 (6.71)	21.77 (6.64)
I	21.15 (6.45)	22.10 (6.74)	◯	22.92 (6.99)	22.79 (6.95)	22.00 (6.71)	21.97 (6.70)	22.00 (6.71)	22.10 (6.74)	22.98 (7.01)	23.21 (7.08)	◯	22.66 (6.91)	21.97 (6.70)
J	21.25 (6.48)	21.70 (6.62)	22.98 (7.01)	23.25 (7.09)	◯	22.98 (7.01)	22.10 (6.74)	22.13 (6.75)	23.05 (7.03)	◯	23.48 (7.16)	23.28 (7.10)	22.23 (6.78)	22.10 (6.74)
K	21.41 (6.53)	21.84 (6.66)	22.98 (7.01)	22.75 (6.94)	23.44 (7.15)	23.31 (7.11)	22.46 (6.85)	22.49 (6.86)	23.41 (7.14)	23.57 (7.19)	22.98 (7.01)	23.31 (7.11)	22.36 (6.82)	22.36 (6.82)
L	21.67 (6.61)	22.52 (6.87)	◯	23.18 (7.07)	23.38 (7.13)	◯	23.34 (7.12)	23.38 (7.13)	◯	23.48 (7.16)	23.38 (7.13)	◯	23.05 (7.03)	22.66 (6.91)
M	21.70 (6.62)	21.93 (6.69)	22.72 (6.93)	22.23 (6.78)	22.33 (6.81)	22.95 (7.00)	22.39 (6.83)	22.39 (6.83)	23.02 (7.02)	22.46 (6.85)	22.39 (6.83)	22.98 (7.01)	22.36 (6.82)	22.59 (6.89)
N	21.97 (6.70)	21.87 (6.67)	22.07 (6.73)	22.03 (6.72)	22.10 (6.74)	22.26 (6.79)	22.20 (6.77)	22.20 (6.77)	22.33 (6.81)	22.20 (6.77)	22.20 (6.77)	22.30 (6.80)	22.23 (6.78)	22.59 (6.89)

NORTH (90°)

Figure C-4. Assembly D-14, Rod Average Power, kW/m, at the Beginning of Cycle 3 (Figures in Parenthesis are kW/ft)

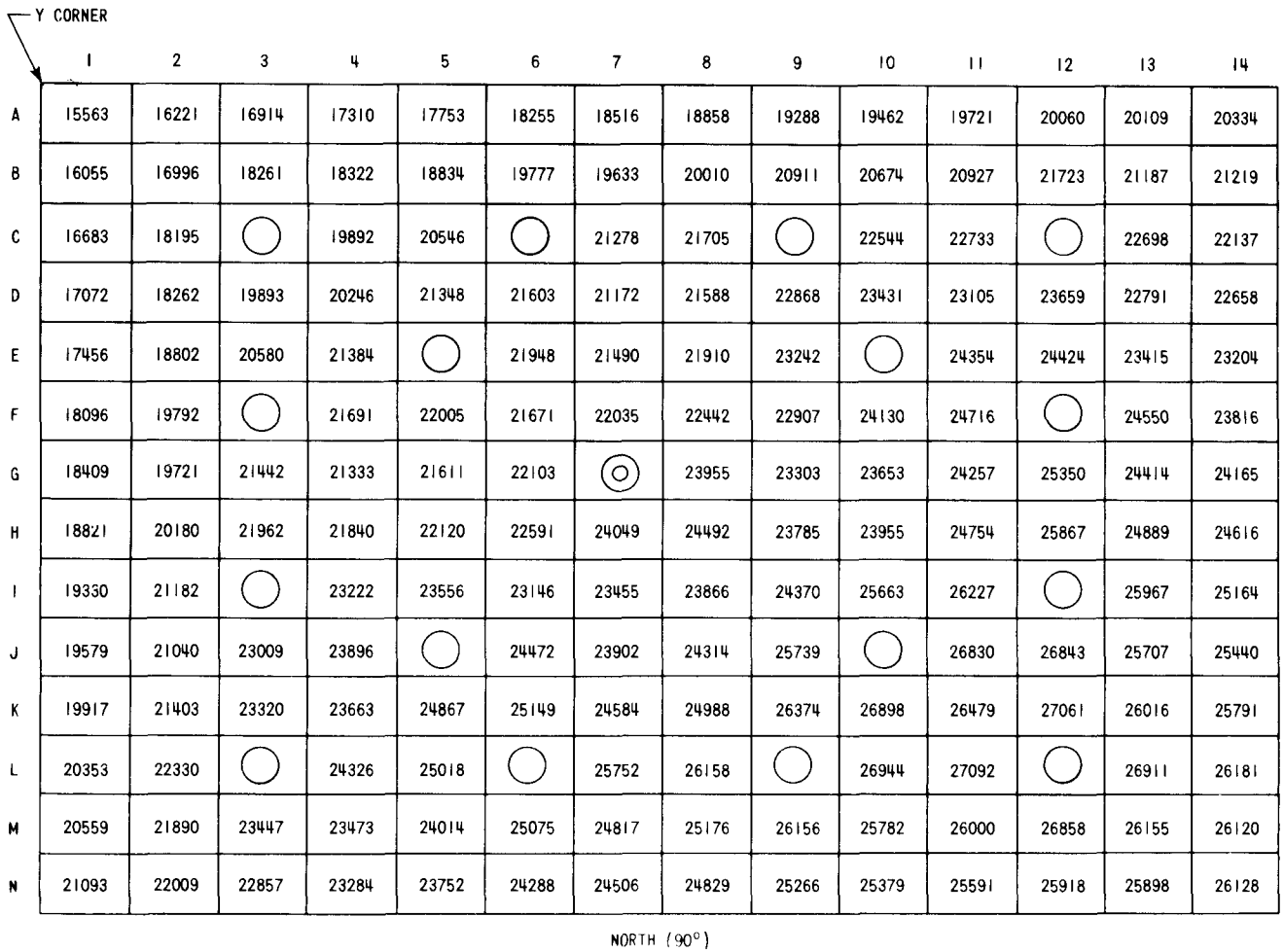

Figure C-5. Assembly D-14, Rod Average Burnup (MWD/MTU) at the End of Cycle 3

REMOVABLE ROD PREIRRADIATION CHARACTERIZATION

Table C-7 summarizes W characterization information available on the selected 13 removable rods prior to further examination at the BCL hot cell under this program. Of these rods, only rod 045 was selected for further examination in detail. The cladding of rod 045 was from Lot No. 5BG1816; tubes of this lot were also present in Assembly D-14. In rod fabrication the inner surface of the tubing was measured by air gauge; values are provided in Table C-8. The outer surface of the cladding was characterized by spiral profilometry an example of which is illustrated in Figure C-6 and tabulated in Table C-9. Ground pellets selected at random for length, diameter, and weight measurement were loaded at specific axial positions in the clad tube. Details are given in Table C-10.

Typical pellet microstructure for pellets in rod 045 are provided in Figures C-7 and 8. Plenum length of the loaded fuel rods was determined by X ray; plenum length and fuel rod length data for rod 045 is given in Table C-11.

Table C-7

SUMMARY OF PREIRRADIATION AND POSTIRRADIATION INFORMATION AVAILABLE ON REMOVABLE RODS SHIPPED TO BMI HOT CELL FACILITIES

Rod	Char.	Clad/Density	Rod Internal Pressure, MN/m^2 (psia)	No. of Cycles	EOC2 Postirradiation Examination	EOC3 Postirradiation Examination	E.C. Signals
047	√	Zr-4/94%	2.65 (385)	2 cycles		V; P; E.C.	1
045	√	Zr-4/94%	2.65 (385)	2 cycles		V; P; E.C.	1
035		Zr-4/94%	2.65 (385)	2 cycles		V; P; E.C.	13-centimeter questionable area
043	√	Zr-4/94%	2.65 (385)	2 cycles		V; P; E.C.	2
042		Zr-4/94%	2.65 (385)	2 cycles		V; P; E.C.	1
046	√	Zr-4/94%	2.65 (385)	2 cycles		V; P; E.C.	several
041	√	Zr-4/94%	2.65 (385)	2 cycles	γ	V; P; E.C.	1
038		Zr-4/94%	4.14 (600)	2 cycles		V; P; E.C.	1
039	√	Zr-4/94%	4.14 (600)	2 cycles	γ	V; P; E.C.	several
030	√	Zr-4/94%	2.65 (385)	2 cycles	γ	V	
026	√	Zr-4/94%	2.65 (385)	2 cycles			
R-03	L	Zr-4/95%	2.65 (385)	1 cycle (cycle 3)			
R-04	L	Zr-4/95%	2.65 (385)	1 cycle (cycle 3)			
037[a]	√	Zr-4/94%	2.65 (385)	2 cycles	V; L; P; γ	V; P; γ	

Legend:

Char. = characterization of preirradiated rods; measurements of clad ID; profilometry; dimensions and density of several traceable pellets in fuel stack; rod length; and full stack length

γ = γ scan
L = length measurements
P = profilometry
V = visualed
E.C. = eddy current
E.C. signal = suspect incipient crack signal

a. Rod was reinserted in the core for cycle 4 operation

Table C-8

ZIRCALOY-4 TUBE INSIDE DIAMETER OF THE REMOVABLE RODS
ROD NUMBER 045

Axial Locations Centimeters from Bottom of Tube	Inside Diameter at 0° Centimeters	Inside Diameter at 90° Centimeters	[Axial Locations Inches from Bottom of Tube]	[Inside Diameter at 0° Inches]	[Inside Diameter at 90° Inches]
15.24	0.9492	0.9492	[6.00]	[0.3737]	[0.3737]
45.72	0.9495	0.9487	18.00	0.3738	0.3735
76.20	0.9497	0.9487	30.00	0.3739	0.3735
106.68	0.9487	0.9489	42.00	0.3735	0.3736
137.16	0.9487	0.9484	54.00	0.3735	0.3734
167.64	0.9489	0.9489	66.00	0.3736	0.3736
198.12	0.9492	0.9479	78.00	0.3737	0.3732
228.60	0.9495	0.9479	90.00	0.3738	0.3732
259.08	0.9492	0.9482	102.00	0.3737	0.3733
289.56	0.9495	0.9492	114.00	0.3738	0.3737
320.04	0.9497	0.9487	126.00	0.3739	0.3735
350.52	0.9487	0.9495	138.00	0.3735	0.3738
368.30	0.9492	0.9497	[145.00]	[0.3737]	[0.3739]

Table C-9

ZIRCALOY-4 TUBE OUTSIDE DIAMETER OF THE REMOVABLE RODS

Rod Number 045

Axial Locations Centimeters From Bottom of Tube	Maximum Clad Diameter (cm)	Minimum Clad Diameter (cm)	Axial Location Inches From Bottom of Tube	Maximum Clad Diameter (in.)	Minimum Clad Diameter (in.)
15.24	1.0717	1.0703	6.0	0.42195	0.42138
38.72	1.0763	1.0708	18.0	0.42190	0.42160
76.20	1.0718	1.0706	30.0	0.42195	0.42150
106.68	1.0719	1.0707	42.0	0.42200	0.42155
137.16	1.0716	1.0705	54.0	0.42190	0.42145
167.64	1.0718	1.0707	66.0	0.42195	0.42155
198.12	1.0718	1.0706	78.0	0.42195	0.42150
228.60	1.0713	1.0709	90.0	0.42180	0.42160
259.08	1.0716	1.0704	102.0	0.42190	0.42140
289.56	1.0718	1.0709	114.0	0.42198	0.42160
320.04	1.0719	1.0705	126.0	0.42199	0.42145
350.52	1.0719	1.0705	138.0	0.42200	0.42146
368.30	1.0715	1.0705	145.0	0.42185	0.42145

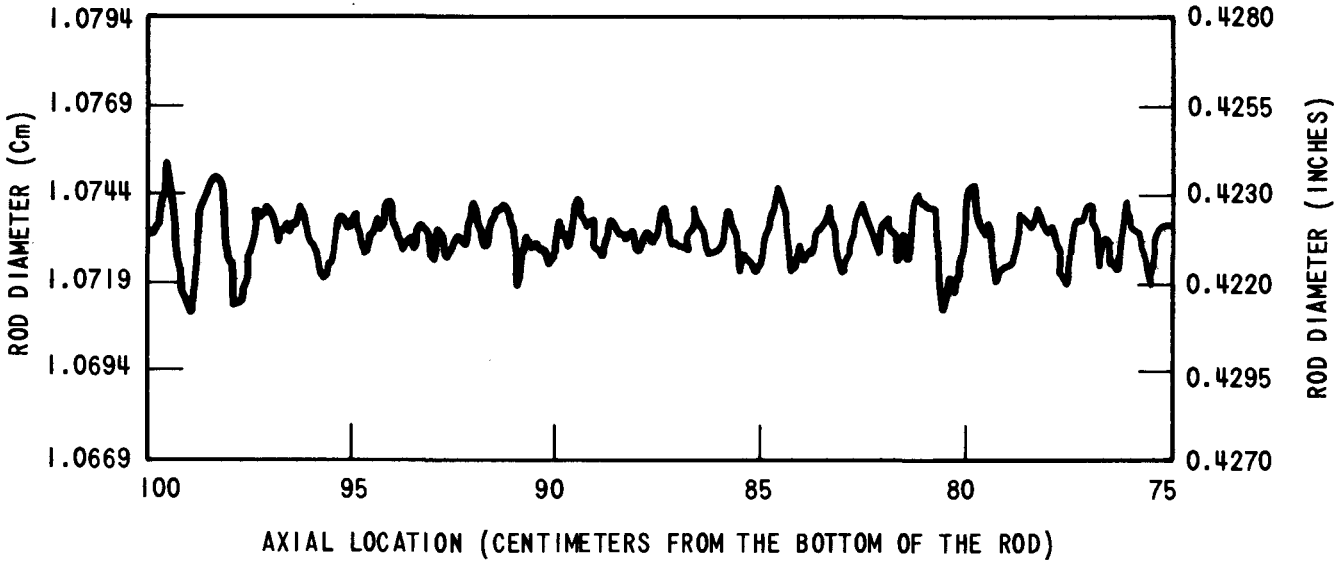

Figure C-6. Preirradiation Spiral Profilometry Trace, Rod 045

Table C-10

DIMENSIONAL ANALYSIS OF FUEL PELLETS OF REMOVABLE ROD 045

Pellet Number	Density Percent T.D.	Pellet Weight, gm	Pellet Diameter Centimeters	Pellet Length Centimeters	[Pellet Diameter Inches]	[Pellet Length Inches]
498-169	93.25	10.15	0.9296 to 0.9312	1.486	0.3660 to 0.3666	0.585
498-168	93.25	10.17	0.9294 to 0.9304	1.488	0.3659 to 0.3663	0.586
498-163	93.25	10.08	0.9294 to 0.9304	1.476	0.3659 to 0.3663	0.581
499-210	93.25	10.23	0.9296 to 0.9301	1.496	0.3660 to 0.3662	0.589
499-223	93.25	10.25	0.9289 to 0.9301	1.501	0.3657 to 0.3662	0.591
499-224	93.25	10.08	0.9294 to 0.9301	1.476	0.3659 to 0.3662	0.581
531-254	93.55	10.20	0.9299 to 0.9301	1.483	0.3661 to 0.3662	0.584
531-295	93.55	10.18	0.9296 to 0.9301	1.481	0.3660 to 0.3662	0.583
531-289	93.55	10.25	0.9296 to 0.9307	1.494	0.3660 to 0.3664	0.588
541-23	93.85	9.91	0.9291 to 0.9296	1.440	0.3658 to 0.3660	0.567
541-24	93.85	10.47	0.9294 to 0.9299	1.519	0.3659 to 0.3661	0.598
541-25	93.85	10.59	0.9296 to 0.9299	1.534	0.3660 to 0.3661	0.604
546-340	93.55	10.47	0.9301 to 0.9301	1.519	0.3662 to 0.3662	0.598
546-316	93.55	10.35	0.9276 to 0.9296	1.506	0.3652 to 0.3660	0.593
546-312	93.55	10.29	0.9299 to 0.9301	1.496	0.3661 to 0.3662	0.589
553-66	93.85	10.24	0.9289 to 0.9294	1.486	0.3657 to 0.3659	0.585
553-65	93.85	10.29	0.9291 to 0.9291	1.491	0.3658 to 0.3658	0.587
553-64	93.85	10.30	0.9291 to 0.9291	1.494	0.3658 to 0.3658	0.588

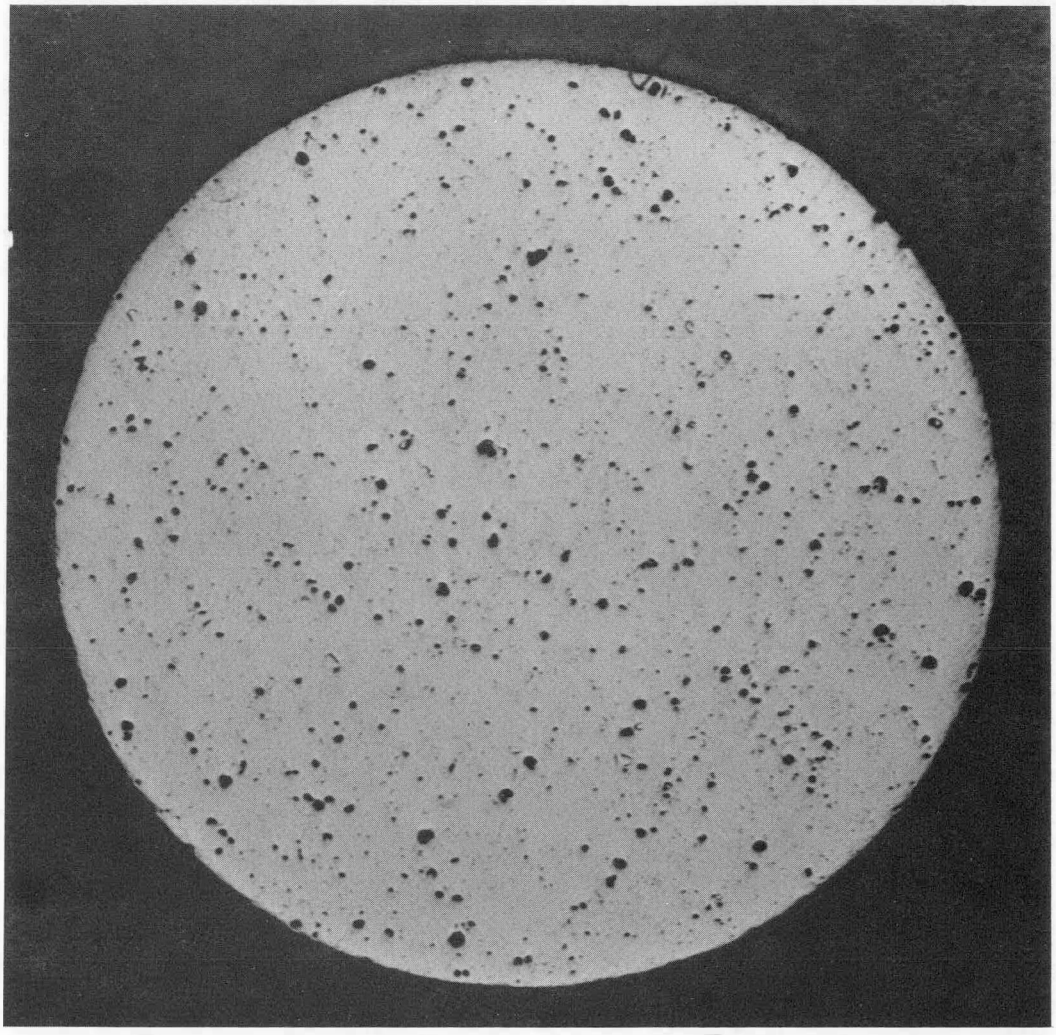

X15

FIGURE C-7. Transverse Macrostructure of a Fuel Pellet, Fuel Group 48

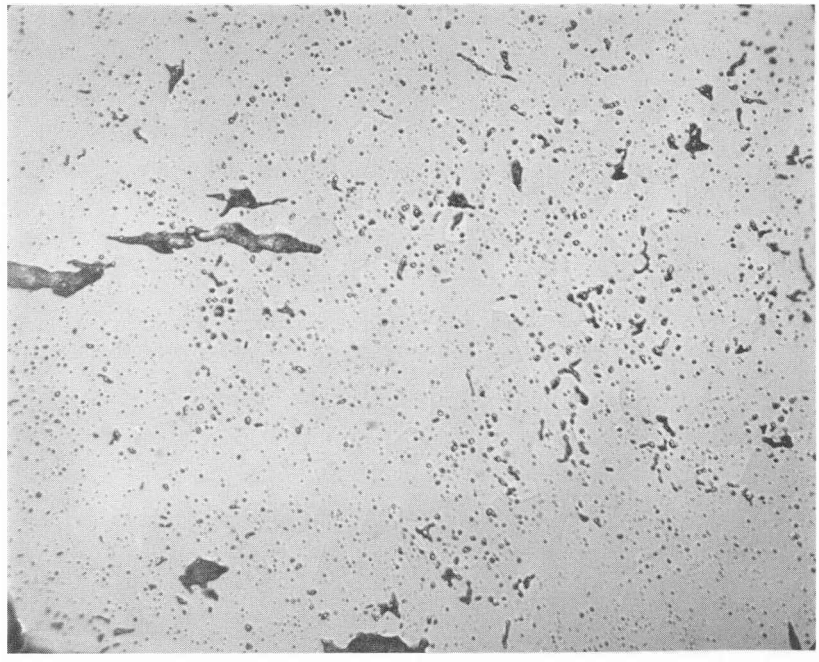

Figure C-8 Typical Microstructure of a Fuel Pellet in the As-Polished Condition Fuel Group 48

Table C-11

PLENUM LENGTH AND ROD LENGTH OF REMOVABLE RODS 045

Rod Number	Plenum Length Centimeters	Rod Length Centimeters	Plenum Length Inches	Rod Length Inches
045	15.596	387.497	6.140	152.558

REMOVABLE ROD--END OF CYCLE 2 HOT CELL
POST IRRADIATION CHARACTERIZATION

Several removable rods were examined by W at the BCL hot cells at the end of reactor Cycle 2 under a separate program. While none of the rods examined were of the standard Region 4 fuel rod design, some cladding and fuel rod data obtained are nevertheless pertinent to the present program and provide information on the condition of the fuel immediately prior to the Cycle 3 startup.

Several clad samples from typical fuel rods but having the same tubing lot as removable rod 045 were characterized for mechanical properties in the hot cells. The mechanical property data provided some indication of the ability of the clad to maintain high stresses generated during a power ramp. Table C-12 provides the tensile test data. It is to be noted that at temperatures typical of in-reactor operation and for neutron fluences in the range of $1.8 - 2.4 \times 10^{21}$ n/cm^2 (typical of one cycle of irradiation) the cladding yield strength has increased to a level in excess of 490 MN/m^2 (71 ksi), while the ductility to failure is maintained high. Further details of mechanical properties have been previously documented in Reference 1.

Fission gas release data for experimental fuel rods containing Region 4 fuel pellets and having representative power histories are summarized in Table C-13. The stable fission product gasses released provide some indication of the volatile corrosive fission products which may be expected. From this data, it is to be noted that the expected gas release (and hence corrosive fission product release) of all Region 4 fuel rods prior to the Cycle 3 startup was very low. The clad mechanical property data and fuel rod fission gas release data suggest that prior to the Point Beach Unit 1, Cycle 3, startup, the Region 4 fuel rods had good potential for sustaining rapid rates of the startup.

Other data obtained during the end of Cycle 2 examinations, such as profilometry and gamma scan data, are not reported in this section since comparable data was obtained in the present program for removable rod 045. These data are described in Section 3.1.4.2.2. The Cycle 2 data has been published in Reference 1.

Table C-12

343°C (650°F) TENSILE PROPERTIES OF ONE CYCLE ZIRCALOY-4 CLADDING

Rod and Sample No.	Clad Alloy Type	Axial Location, cm (in.) From the Bottom of the Rod	Fast Fluence,[a] $n/cm^2 \times 10^{-21}$	Avg.[b] Clad Temp., °C (°F)	0.2%[c] Yield Stress, MN/m^2 (ksi)	Ultimate[c] Stress, MN/m^2 (ksi)	Uniform[d] Elongation, %	Total[d] Elongation, %
007-30B	Zr-4	302 to 317 (119 to 125)	2.3	357 (674)	502 (72.9)	686 (99.6)	4.2	7.4
007-23	Zr-4	205 to 220 (81 to 87)	2.4	345 (654)	538 (78.1)	719 (104.4)	4.5	9.0
013-27	Zr-4	205 to 220 (81 to 87)	1.8	332 (631)	536 (77.9)	695 (100.9)	4.0	5.6
013-33	Zr-4	282 to 297 (111 to 117)	1.8	340 (645)	494 (71.8)	702 (102.0)	4.2	8.5

a. Based upon the nuclear design computer code.

b. Based upon the fuel performance computer code. Clad temperatures (midwall) are for the last 500 hours of last irradiation at the axial center of the samples.

c. Based upon cross-sectional areas calculated from on-site profilometry and measured preirradiation clad wall thickness.

d. Based upon a 10.16 cm (4 inch) gauge length.

Table C-13

FISSION GAS RELEASE OF THE REMOVABLE RODS

Rod	Avg. Power kw/m	(kw/ft)	Avg. Burnup MWD/MTU	Fission Gas Release % Release/Birth
8	18.4	(5.6)	11,150	0.29
11	22.0	(6.7)	13,350	0.26

APPENDIX D

POINT BEACH UNIT 1, CYCLE 3
HOT CELL DATA

Blank Page

Table D-1

POINT BEACH-1 ROD NDE DATA SUMMARY AT LOCATIONS
OF EDDY CURRENT INDICATIONS

Rod No.	Encircling Coil Location			Probe Coil Location				Gamma Scan	
	cm	in.	Strength	cm	in.	Orientation	Strength	Gross and Cs-137+	Profilometry *
045	46.80	18.44	W	48.50	19.10	225°	W	GAP @46.99 cm (18.5)	Irregular diameter trace
	--	--	--	53.30	21.00	270°	W	No Anomalies	Small diameter increase at @53.1 cm(20.9)0.01 mm (0.4 mils)
	--	--	--	14.30	36.40	135°	M	No Anomalies	Clad Ridging
	105.10	41.38	M	--	--	--	--	Small Gaps	No Anomalies
	--	--	--	121.00	47.70	135°	M	No Anomalies	0.013 mm (0.5 mil) diameter increase @120.9 cm (47.6)
	--	--	--	146.60	57.70	135-180°	M	GAP @145.8 cm (57.4)	No Anomalies
	--	--	--	161.50	63.60	135-360°	W	No Anomalies	Clad ridging and small diameter increase
	--	--	--	191.00	63.60	90-135°	M	No Anomalies	Clad ridging and small diameter increase
	210.20	82.75	M	--	--	--	--	GAP @210 cm (82.7)	No Anomalies
	--	--	--	217.40	85.60	315°	W	No Anomalies	No Anomalies
	--	--	--	223.30	87.90	270°	M	No Anomalies	No Anomalies
	--	--	--	239.50	94.30	225°	S	No Anomalies	No Anomalies
	--	--	--	245.90	96.80	315°	M	No Anomalies	Clad Ridging
	278.60	109.67	S	278.60	109.70	0-225°	S	GAP @278.6 cm (109.7) M	Sharp Diameter increase @278.6 cm (109.7), 0.023 mm (0.9 mils)
	290.60	114.40	S	291.30	114.70	90-180°	M	GAP @290.8 cm (114.5)	Clad ridging and small diameter increases in the area
	--	--	--	293.90	115.70	180°	S	No Anomalies	No Anomalies
	323.40	127.31	S	323.30	127.30	0-225°	S	No Anomalies	No Anomalies
	--	--	--	323.30	127.90	45-90°	W	No Anomalies	No Anomalies
	333.90	131.44	M	334.00	131.50	315°	M	GAP @335.3 (132.0)	No Anomalies
	342.70	134.94	M	--	--	--	--	GAP @342.9 cm (135.0)	No Anomalies

Table D-1 (Continued)

Rod No.	Encircling Coil Location			Probe Coil Location				Gamma Scan Gross and Cs-137+	Profilometry*
	cm	in.	Strength	cm	in.	Orientation	Strength		
039	93.30	36.75	M	93.50	36.80	45-90°	M	GAP @93.2 (36.7)	No Anomalies
	--	--	--	112.80	44.40	135°	S	No Anomalies	No Anomalies
	117.50	46.25	W	117.60	46.30	270°	W	GAP @117.6 (46.3)	No Anomalies
	--	--	--	150.90	59.40	135°	S	No Anomalies	No Anomalies
	203.50	80.13	M	--	--	--	--	GAP @203.7 (80.2)	No Anomalies
	206.70	81.38	W	208.30	82.00	135°	M	GAP @206.7 (81.38)	Diameter increase 0.01 (0.4 mils) @208.5 (82.1)
	--	--	--	219.20	86.30	135°	M	--	Diameter increase 0.02 (0.8 mils) @218.95 (86.2)
A-1	--	--	--	237.00	93.30	0-45°	S	No Anomalies	Large ovality area
	245.30	96.56	M	245.40	96.60	0-360°	M	No Anomalies	Large ovality area
	309.20	121.75	W	309.60	121.90	0-360°	M	GAP - possible broken pellet	Small diameter increase
	311.20	122.50	M	311.40	122.60	0-360°	M	GAP @311.4 (122.6)	High ovality - possible ridging
F-13	--	--	--	126.70	49.90	45-90°	M	No Anomalies	Evidence of clad ridging
	--	--	--	128.30	50.50	45°	W	No Anomalies	Evidence of clad ridging
	145.60	57.31	M	145.50	57.30	0-45°, 90-135°	M	GAP @145.5 (57.3) Small	Evidence of clad ridging
	154.70	60.80	W	--	--	--	--	GAP @156.0 (61.4)	Evidence of clad ridging
	--	--	--	212.10	83.50	315-0-90°	W	No Anomalies	No Anomalies
	214.40	84.40	M	215.40	84.80	0-135°	W	GAP @214.9 (84.6)	Diameter increase @214.9 (84.6) 0.02 (0.8 mils)
	--	--	--	226.10	89.00	270°	M	GAP @225.0 (88.6)	No Anomalies
	291.50	114.75	M	291.60	114.80	180-360°	W	GAP @ 291.3 (114.7)	No Anomalies
	328.30	129.25	W	328.30	129.30	90-180°	W	No Anomalies	No Anomalies
K-9	--	--	--	94.70	37.30	0-45°, 270°	S	GAP @93.2 (36.7)	Clad ridging in the area
	--	--	--	97.50	38.40	0-45°	W	No Anomalies	Clad ridging in the area
	321.90	126.75	M-S	321.90	126.80	0-360°	M	GAP @321.8 (126.7)	No Anomalies
	--	--	--	333.50	131.30	90°, 135°	M	No Anomalies	No Anomalies

Table D-1 (Continued)

Rod No.	Encircling Coil Location			Probe Coil Location				Gamma Scan Gross and Cs-137	Profilometry
	cm	in.	Strength	cm	in.	Orientation	Strength		
E-3	220.70	86.88	W	220.80	86.90	225°	W	CAP @220.75 (86.9)	Small change in rod diameter
	--	--	--	231.40	91.10	0-45°	W	No Anomalies	No Anomalies
	259.40	102.30	W	259.60	102.20	45°	W	No Anomalies	No Anomalies
	260.80	102.69	W	--	--	--	--	CAP @260.9 (102.7)	Ovality decrease to 0.013 (0.5 mils) from 0.13 (5 mils) @261.6 (103)
I-13	83.00	32.69	W	--	--	--	--	CAP @83.06 (32.7)	No Anomalies
	185.60	73.06	M	185.90	73.20	0-360°	M	CAP @186.4 (73.4)	No Anomalies
	230.60	90.80	W	--	--	--	--	CAP @230.6 (90.8)	No Anomalies
	--	--	--	234.20	92.20	0-360°	M	CAP @234.2 (92.2)	Sharp increase in diameter @234.2, (92.2), 0.04 (1.5 mils)
B-11	--	--	--	59.30	23.60	0-45°	W	No Anomalies	No Anomalies
	119.50	47.06	M	119.40	47.00	135°	W	No Anomalies	No Anomalies
	--	--	--	120.70	47.50	0-360°	W	No Anomalies	No Anomalies
	150.80	59.38	S	151.10	59.50	0-360°	M	No Anomalies	Possible clad ridging
	155.40	61.19	M	155.70	61.30	0-360°	M	No Anomalies	Possible clad ridging
	158.40	62.38	S	158.80	62.50	0-360°	M	No Anomalies	Possible clad ridging
	168.90	66.50	W	--	--	--	--	CAP @169.7 (66.8)	Possible clad ridging
	171.90	67.69	M	--	--	--	--	CAP @171.96 (67.7)	No Anomalies
	207.80	81.81	S	208.30	82.00	0-360°	M	CAP @208.3 (82.0)	Possible ridge @209.0 (82.3)
	231.80	91.25	M	232.70	91.60	45-315°	W	CAP @231.9 (91.3)	Diameter increase @233.4 (91.9), 0.015 (0.6 mils)
	--	--	--	261.60	103.00	45-90°	W	No Anomalies	No Anomalies
	296.40	116.69	M	--	--	--	--	No Anomalies	No Anomalies
	297.90	117.30	W	297.20	117.00	180-225°	W	CAP @297.9 (117.3) Very Small	No Anomalies
	319.10	125.63	S	319.50	125.80	0-360°	M	No Anomalies	No Anomalies
	330.80	130.25	S	331.50	130.50	0-360°	M	CAP @331.5 (130.5)	Maximum ovality @332.7 (131)

Table D-1 (Continued)

Rod No.	Encircling Coil Location			Probe Coil Location				Gamma Scan Gross and Cs-137	Profilometry*
	cm	in.	Strength	cm	in.	Orientation	Strength		
A-9	--	--	--	278.90	109.80	225°	W	GAP @278.9 (109.8)	Very low ovality region
	279.10	109.88	W	279.90	110.20	0-360°	W	No Anomalies	Possible ridging
	--	--	--	297.80	117.20	0°	W	No Anomalies	No Anomalies
	301.60	118.75	W	301.80	118.80	225-90°	W	GAP @301.75 cm (118.8 in.)	No Anomalies
	--	--	--	335.90	132.20	90°	W	No Anomalies	No Anomalies
K-6	--	--	--	29.20	11.50	225-270°	W	No Anomalies	Evidence of clad ridging
	--	--	--	52.10	20.50	135-270°	W	No Anomalies	Sharp diameter increase @48.5 (19.1), 49.8 (19.6), 50.8 (20), 51.8 (20.4)
	126.50	49.81	W	126.70	49.90	45-270°	W	GAP @126.7 (49.9)	No Anomalies
	--	--	--	134.10	52.80	270-315°	W	No Anomalies	No Anomalies
	--	--	--	146.80	57.80	270-315°	W	No Anomalies	Evidence of clad ridging
	--	--	--	148.60	58.50	0°	W	No Anomalies	Evidence of clad ridging
	--	--	--	224.50	88.40	90°, 135°	W	No Anomalies	Evidence of clad ridging
	228.60	90.00	M	228.10	89.80	0-360°	M	GAP @228.6 (90.0)	Evidence of clad ridging
	240.30	94.60	W	239.80	94.40	315-0°	M	GAP @239.3 (94.2)	Evidence of clad ridging
	--	--	--	277.60	109.30	90°, 180°, 225°	M	No Anomalies	Sharp diameter increase @278.6 cm (109.7)
	--	--	--	308.40	121.40	225°	M	No Anomalies	Clad ridging
	--	--	--	313.70	123.50	0-45°	M	No Anomalies	Sharp diameter increase @313.7 (123.5), 0.03 mm (1.2 mils)
	--	--	--	333.30	131.20	180-270°	W	No Anomalies	Small diameter increase @334.3 (131.6), 0.01 (0.4 mils)

Note: All locations are from bottom of the rod.

*Location of Anomalies from Rod Bottom cm (in.).

Table D-2

INITIAL PUNCTURE AND FISSION GAS RELEASE DATA

Rod	Assembly	Pre-Punch Pressure, PSIA	Puncture Temperature, ° C	Initial Punched Pressure, PSIA	Expanded Punched Pressure, PSIA
045	D-40	20.02	24.3	37.76	26.25
B-11	D-14	20.08	24.0	39.41	27.58
A-1	D-14	20.02	21.5	36.92	25.88
M-14	D-14	20.4	23.3	37.17	25.80

PROCEDURE FOR TESTING THE INTERNAL PRESSURE
OF POINT BEACH UNIT 1, REGION 4, FUEL RODS

The BCL equipment used in the puncture campaign for testing the internal pressure of fuel rods, and hence, ascertaining their integrity, was the same as that used in the measurement of total gas content and total free volume in the fuel rod. The system has been described in detail previously (4). In the pressure test campaign, however, neither the total volume of gas, nor the free volume in the fuel rods, was measured. Rather, the approach adopted was to confirm the gas pressure in the fuel rod by measuring the pressure initially in the puncture chamber immediately after puncturing, and again following release of the gas to the expansion chamber. Table D-2 illustrates the range of pressures obtained by this approach for the four rods examined in detail in the program. Variations in fission gas release in the range observed has little effect on the pressure reading. It was determined that for expected ambient temperatures in the hot cell, measurements of initial punched pressure close to, or in the range of 35.76 psia, and measurement of expanded punched pressure close to, or in the range of 25.03 to 28.06 psia, would acceptably indicate the presence of a nonfailed fuel rod.

Measurements on all 46 rods from Assembly D-14 are summarized in Table D-3. Utilizing the above criteria, none of the rods was judged to be failed.

Table D-3

FUEL ROD PUNCTURE RESULTS PRESSURE READINGS*

Number	Rod	Initial Pressure Readings, PSIA	Expanded Pressure Readings, PSIA
1	C-10	36.92	25.71
2	M-2	37.90	26.41
3	K-13	38.70	26.95
4	I-13	40.23	28.23
5	H-10	37.08	25.90
6	J-1	38.30	26.81
7	C-4	37.41	26.12
8	J-11	38.15	26.66
9	E-9	37.10	25.89
10	I-9	37.17	25.95
11	F-13	37.39	26.10
12	A-1	36.92	25.58
13	B-11	39.41	27.58
14	H-9	37.70	26.23
15	G-12	37.58	26.17
16	K-11	38.00	26.49
17	M-14	37.17	25.80
18	E-4	36.18	25.24
19	D-7	37.38	25.82
20	G-2	37.20	25.91
21	D-4	37.40	26.12
22	J-7	37.81	26.39
23	M-7	38.85	27.18
24	K-14	35.57	24.51
25	L-10	36.73	25.61
26	A-6	36.68	25.52
27	D-10	36.37	25.42
28	J-3	38.03	26.57
29	E-11	37.98	26.52
30	J-4	36.84	25.70
31	K-5	38.12	32.68
32	K-10	37.15	25.80
33	L-5	37.40	26.10
34	L-4	36.82	25.71
35	B-1	37.11	25.93
36	A-4	36.98	25.81
37	A-5	37.18	25.98
38	B-3	36.85	25.77
39	C-2	37.49	26.20
40	A-7	37.29	26.00
41	A-10	37.29	26.01
42	B-6	37.28	25.99
43	B-9	37.30	26.02
44	C-7	37.03	25.79
45	D-6	37.52	26.20
46	H-3	37.29	26.00

* Average puncture temperature ranged from 21.5° C to 26°C.

APPENDIX E

IMAGING OF ZIRCONIUM HYDRIDE IN ZIRCALOY WITH BACKSCATTERED ELECTRONS

Blank Page

Appendix E

IMAGING OF ZIRCONIUM HYDRIDE IN ZIRCALOY WITH BACKSCATTERED ELECTRONS

U. E. Wolff

When metallurgical specimens are exmained in the SEM by standard imaging techniques, i.e., with secondary electrons and a dectector located off-axis, one obtains an image with predominantly topographical information. If the specimen is a polished metallographic section, one is usually unsuccessful in detecting second phases unless a relief-producing etch has been used. In particular, hydrides in Zircaloy have not been observed in this mode.

However, backscattered electrons (BSE) combined with a special detector can be used to obtain compositional information as described in the following.

If a beam of electrons impinges on a target a certain fraction is backscattered. That fraction η is a function of the atomic number of the target as shown (E1) in Figure E-1. Contrast can therefore be obtained if different regions of the specimen surface consist of materials of different atomic numbers. If these regions are not "pure" elements, an effective or mean atomic number $\bar{Z}$ can be computed according to Birks (E2) as

$$\bar{Z} = \frac{\Sigma Z_i^2 x_i}{\Sigma Z_i x_i}$$

where x_i is the atomic fraction of element i with Atomic Number Z_i.

For zirconium hydride, the effective $\bar{Z}$ would thus be approximately 39, and the difference in η read from Figure E-1 for Zr and ZrH would be approximately 1.5 percent. According to Colby (E3) differences in η of 1 percent should be detectable with BSE, and this has been confirmed by our ability to image hydrides in the present case.

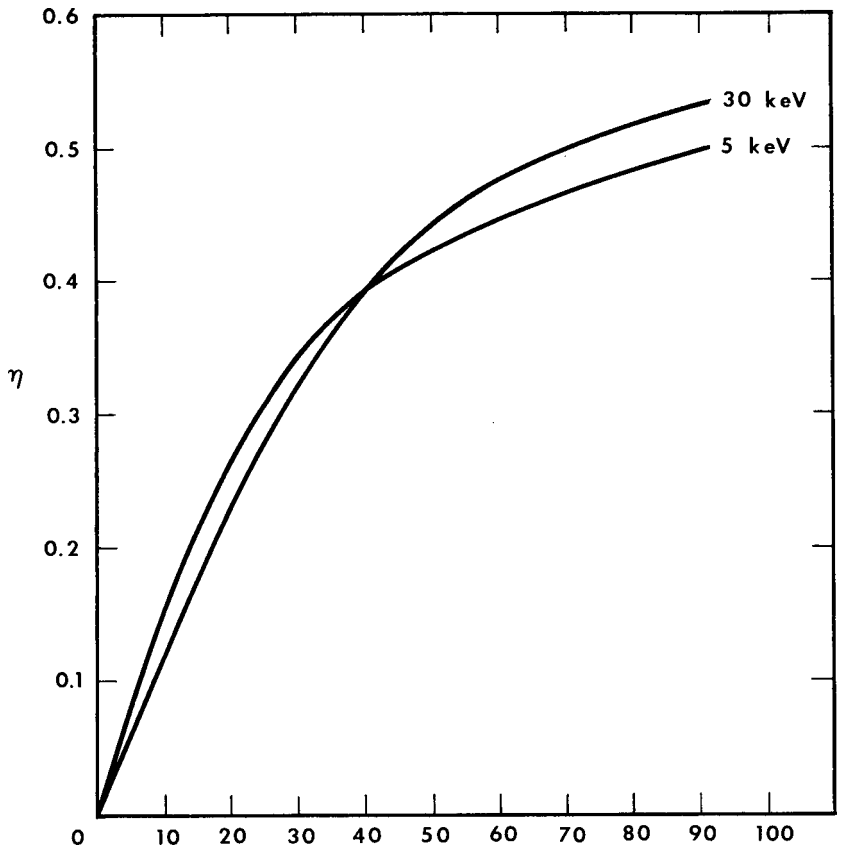

Figure E-1. Backscattered Electron Yield Versus Atomic Number [After Colby (E1)]

Since the absence of a field, backscattered electrons travel in straight lines, the BSE fraction detected is a function not only of the mean atomic number but also of the topography of the emitting surface. These two effects cannot be separated with a single detector. Kimoto and Hashimoto (E4) have described a BSE detector arrangement consisting of two solid state detectors mounted symmetrically under the objective lens pole piece of the SEM. Figures E-2 and E-3 taken from their paper, illustrate the principle of the detector system. With a flat specimen surface normal to the electron beam both detectors receive the same topographical signal with intensity variations (contrast) produced only by compositional differences (atomic number effect). If, on other hand, the specimen surface has topographical features the BSE's are not reflected symmetrically and the two detectors "see" different images. As illustrated in Figure E-2, when the signals of the two detectors are added, the compositional contribution to the signals is enhanced while the topographical contributions are essentially cancelled. When the two signals are subtracted the reverse is true.

The BSE detector system used in the present work incorporates the described arrangement, namely the solid state detector pair, an amplifier, and a switching arrangement for adding or subtracting the two signals (Figure E-3). The output of the amplifier modulates the intensity of the oscilloscope of the SEM producing an image of the area scanned by the primary beam.

Figure 3.2-68 in the main body of this report confirms that the hydrides are imaged because of their atomic number difference and not because of topographical relief.

REFERENCES

E1. J. W. Colby. "Backscattered and Secondary Electron Emission as Ancillary Techniques in Electron Probe Analysis". Electron Probe Microanalysis. Ed. A. J. Tousimis and L. Marton. Academic Press, New York, 1969, p 179.

E2. L. S. Birks. Electron Probe Microanalysis. Interscience Publ., New York, 1963, p 140.

E3. J. W. Colby. Loc. cit., pp 190-192.

E4. S. Kimoto and H. Hashimoto. "Stereoscopic Observation in Scanning Microscopy Using Multiple Detectors". The Electron Microprobe. Ed. T. D. McKinley, K.F.J. Heinrich, and D. B. Wittry. John Wiley & Sons, New York, 1966, pp 480-489.

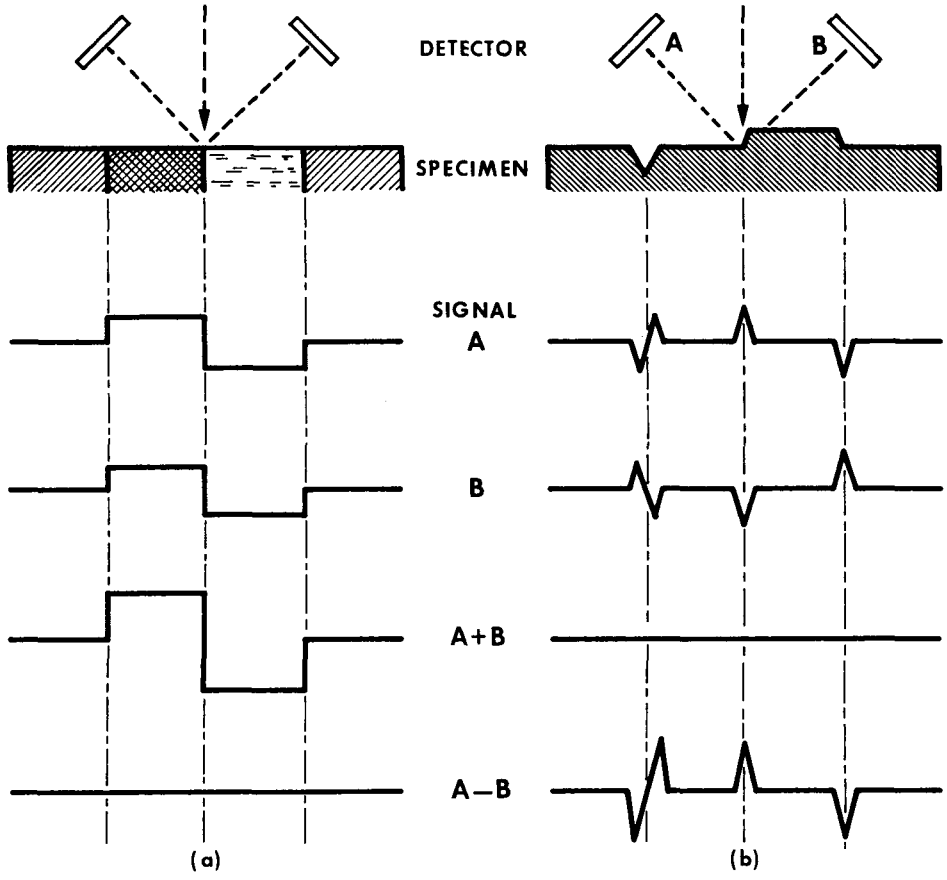

Figure E-2. Schematic of Paired Backscattered Electron Signals from Simple Specimens [After Kimoto and Hashimoto (E4)]

(a) Composition differences

(b) Topographical features.

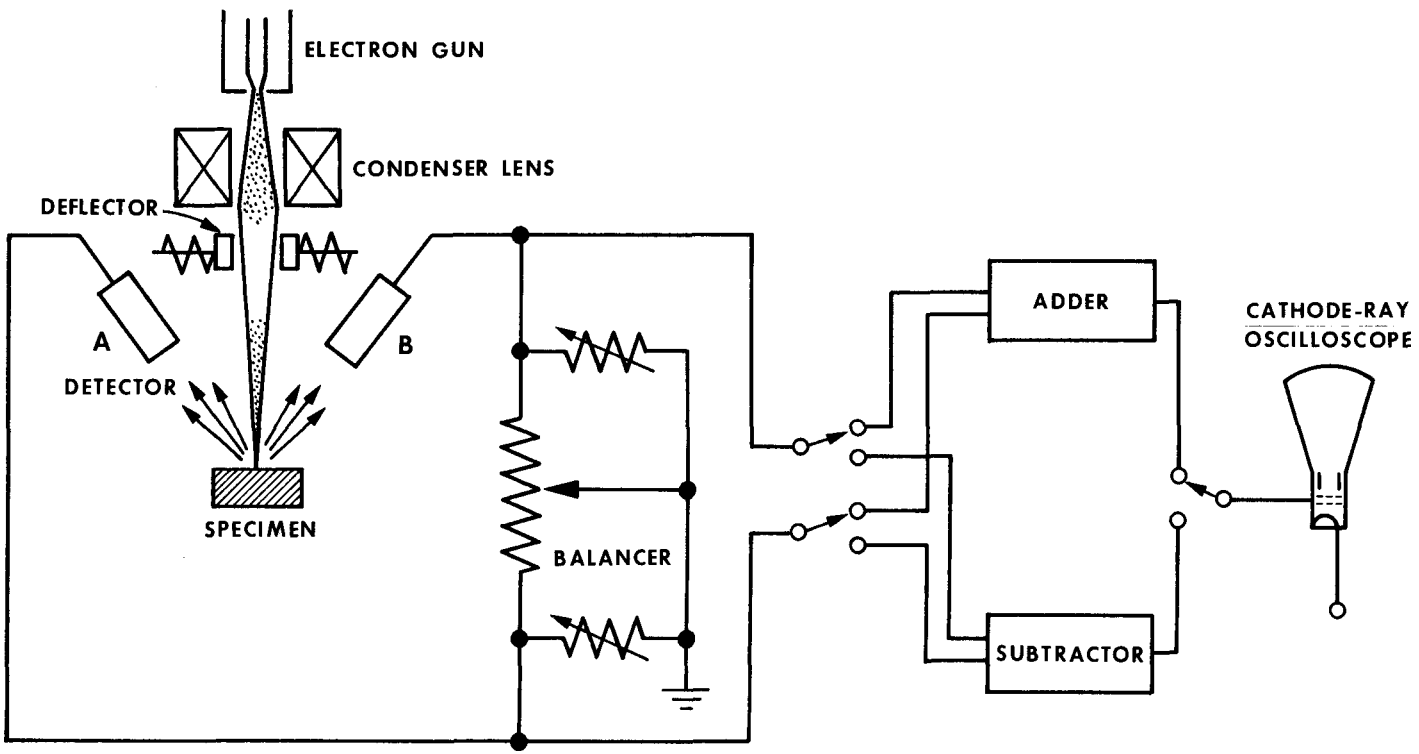

Figure E-3. Schematic of Solid State Pair Detector and Associated Electronics [After Kimoto and Hashimoto (E4)]